Struktur und Dynamik weicher Materie: Von zweidimensionalen Flüssigkristallen zu makromolekularer Diffusion durch Gele

Inaugural-Dissertation

zur Erlangung des Doktorgrades
der Mathematisch-Naturwissenschaftlichen Fakultät
der Heinrich-Heine-Universität Düsseldorf

vorgelegt von

Christoph Ernst Sitta
aus Hagen (Westfalen)

Düsseldorf, Januar 2018

aus dem Institut für Theoretische Physik II: Weiche Materie
der Heinrich-Heine-Universität Düsseldorf

Gedruckt mit der Genehmigung der
Mathematisch-Naturwissenschaftlichen Fakultät der
Heinrich-Heine-Universität Düsseldorf

Referent: Prof. Dr. Hartmut Löwen

Korreferent: Jun.-Prof. Dr. Raphael Wittkowski

Tag der mündlichen Prüfung: 27.11.2017

Abstract

Soft condensed matter is an interesting yet also demanding research area in modern physics, due to its many connections to biology, chemistry or medicine. Many systems in those related disciplines are of high importance for human life and their understanding can be enhanced by insight into the underlying physical mechanisms. Examples are the diffusion of enzymes within cells or the flow of blood within narrow channels. But also technical applications like the genetic fingerprint or liquid crystal displays (LCDs) rely on soft matter systems.

This dissertation focuses on two complex systems, which are connected to these two technical applications. When determining the genetic fingerprint, small DNA fragments diffuse in an electric field through a gel matrix. Although commonly used, the underlying mechanisms in the diffusion of macromolecules through gels are still under discussion and similarly, fundamental properties of gels like the mean pore size are still controversly discussed. Such topics are the main issue of the first part of this dissertation. By combination of three complementary experimental techniques and additional simulations, information about the dynamics of different macromolecules in the gel is obtained, which allows for conclusions about the underlying structure of the gel by deducing its pore size distribution.

The second part investigates different aspects of the behavior of a liquid containing anisotropic colloidal hard particles. Depending on the particles' shapes, their density, or other parameters, these particles can form different patterns. Such liquid crystals are the basis for LCDs and therefore of great importance. Additional interesting effects can be observed at the boundaries between liquids and hard walls, as the lotus effect is only one well known example. This work deals with colloidal systems, which are confined to two dimensions. Even though our world is three dimensional, this restriction is more than just a mathematical gimmick as processes on surfaces are effectively taking place in two dimensions. This dissertation focuses especially on dispersions of rodlike and rectangular colloidal particles, since their shape anisotropy allows for many interesting effects. Using simulations and density functional theory calculations, their phase behavior in various environments is investigated, including flat and curved surfaces and the presence or absence of walls or external fields. Furthermore, the interfacial free energies in the presence of walls are calculated.

The results presented in this thesis provide fundamental insights into the behavior of both two dimensional systems of anisotropic particles and the diffusion of macromolecules in gels and will help guide future research.

Kurzfassung

In der modernen Physik ist das Gebiet der *weichen Materie* durch seine vielen Schnittstellen zur Biologie, Chemie oder Medizin ein sowohl interessantes als auch anspruchsvolles Forschungsgebiet. Viele Systeme, die in angrenzenden Disziplinen von höchster Bedeutung für den Menschen sind, lassen sich durch Erkenntnisse über die zugrunde liegenden physikalischen Vorgänge besser verstehen. Beispiele sind die Diffusion von Enzymen in Zellen oder das Flussverhalten von Blut in engen Kanälen. Auch für technische Anwendungen, wie bei der Bestimmung des genetischen Fingerabdruckes oder bei LCD-Bildschirmen, bilden Systeme der weichen Materie die Grundlage.

In dieser Arbeit wird der Schwerpunkt auf zwei komplexe Systeme gelegt, die mit den beiden letztgenannten technischen Anwendungen in enger Verbindung stehen. Bei der Bestimmung des genetischen Fingerabdruckes diffundieren DNA-Fragmente bei angelegtem elektrischem Feld durch eine Gel-Matrix. Obwohl die Diffusion von Makromolekülen durch Gele in vielen Anwendungen eine Rolle spielt, sind viele Vorgänge hierbei noch nicht restlos erforscht. Ebenso werden viele Eigenschaften der Gele, wie beispielsweise ihre mittlere Porengröße, immer noch kontrovers diskutiert. Als erster Schwerpunkt dieser Dissertation wird unter Verwendung von computergestützten Simulationen und drei unterschiedlicher experimenteller Techniken die Dynamik von Makromolekülen in einem Gel durch Berechnung der Diffusionskoeffizienten untersucht. Dadurch werden Rückschlüsse auf die Struktur des Gels durch Bestimmung der Porengrößenverteilung ermöglicht.

Der zweite Teil dieser Arbeit untersucht verschiedenste Aspekte des Verhaltens richtungsabhängiger, kolloidaler, harter Teilchen. Je nach Teilchenform, Teilchendichte und anderen Parametern können diese durch ihr kollektives Verhalten unterschiedliche Strukturen bilden. Solche Flüssigkristalle bilden die Grundlage von LCD-Bildschirmen und sind daher von großer Relevanz. An Grenzflächen zwischen harten Wänden und Flüssigkeiten treten weitere interessante Effekte auf, von denen der Lotus-Effekt der wohl bekannteste ist. Diese Arbeit beschäftigt sich mit solchen kolloidalen Systemen in zwei Dimensionen. Auch wenn die reale Welt dreidimensional ist, ist die Einschränkung auf zwei Dimensionen mehr als nur eine mathematische Spielerei. Schließlich sind alle Prozesse, die auf Oberflächen stattfinden, effektiv zweidimensional.

Im Rahmen des zweiten Teils dieser Arbeit wird dabei ein Schwerpunkt auf Flüssigkeiten mit stäbchenförmigen oder rechteckigen Teilchen gelegt, da diese im Gegensatz zu Scheiben eine Orientierungsabhängigkeit vorweisen und so durch ihre Form weitere interessante Effekte ermöglichen. Unter Verwendung von Simulationen

und Dichtefunktionaltheorierechnungen wird das Phasenverhalten dieser Flüssigkeiten unter verschiedenen Bedingungen betrachtet. Im Speziellen werden die Einflüsse der Oberflächenkrümmung, eines externen Feldes oder von Wänden auf das jeweilige System untersucht und dabei auch die Oberflächenspannungen in der Anwesenheit von Wänden berechnet.

Die in dieser Dissertation präsentierten Ergebnisse liefern grundlegende Einblicke in das Verhalten von anisotropen Teilchen in zwei Dimensionen sowie in die Diffusion von Makromolekülen in Gelen und können als Basis für zukünftige Forschungsprojekte dienen.

Eidesstattliche Versicherung

Ich versichere an Eides Statt, dass die Dissertation von mir selbständig und ohne unzulässige fremde Hilfe unter Beachtung der „Grundsätze zur Sicherung guter wissenschaftlicher Praxis an der Heinrich-Heine-Universität Düsseldorf“ erstellt worden ist.

Düsseldorf, _____ _____

Vorwort

Die Inhalte dieser Dissertation beruhen auf den folgenden vier Publikationen in internationalen wissenschaftlichen Fachjournalen mit anerkannten Begutachtungsverfahren (peer review), zu denen ich während meiner Arbeit am *Institut für Theoretische Physik II: Weiche Materie* der *Heinrich-Heine-Universität Düsseldorf* zwischen Mai 2013 und September 2017 beigetragen habe.

I. D. Sandrin*, D. Wagner*, **C. E. Sitta***, R. Thoma, S. Felekyan, H. E. Hermes, C. Janiak, N. de Sousa Amadeu, R. Kühnemuth, H. Löwen, S. U. Egelhaaf & C. A. M. Seidel, *Diffusion of macromolecules in a polymer hydrogel: from microscopic to macroscopic scales*, Phys. Chem. Chem. Phys. **18**, 12860 (2016)

II. **C. E. Sitta**, F. Smallenburg, R. Wittkowski & H. Löwen, *Hard rectangles near curved hard walls: Tuning the sign of the Tolman length*, J. Chem. Phys. **145**, 204508 (2016)

III. R. Wittmann*, **C. E. Sitta***, F. Smallenburg & H. Löwen, *Phase diagram of two-dimensional hard rods from fundamental mixed measure density functional theory*, J. Chem. Phys. **147**, 134908 (2017)

IV. **C. E. Sitta**, F. Smallenburg, R. Wittkowski & H. Löwen, *Liquid crystals of hard rectangles on flat and cylindrical manifolds*, Phys. Chem. Chem. Phys. (2018), DOI: 10.1039/C7CP07026H

* Diese Autoren haben in gleichem Maß zur jeweiligen Publikation beigetragen und teilen die Erstautorschaft.

Danksagung

An dieser Stelle möchte ich mich bei allen bedanken, die zum Gelingen dieser Dissertation beigetragen und mich in den vergangenen Jahren unterstützt haben.

Zuerst ist dies mein Betreuer Prof. Dr. Hartmut Löwen, der mir die Gelegenheit zur Promotion durch die Mitarbeit an mehreren interessanten Projekten seines Lehrstuhls erst ermöglicht und mich dabei stets tatkräftig unterstützt hat. Als nächstes danke ich meinem Co-Betreuer und Zweitgutachter Jun.-Prof. Dr. Raphael Wittkowski, der mir in den Projekten zur Dichtefunktionaltheorie zur Seite stand und mir bei Problemen stets weiterhelfen konnte. Dank gebührt natürlich auch allen Co-Autoren meiner Veröffentlichungen. Allen voran Dr. Frank Smallenburg, ohne dessen Simulationen drei Publikationen nicht in dieser Form möglich gewesen wären, aber auch Prof. Dr. Stefan U. Egelhaaf, der mich schon während meines vorausgegangenen Studiums betreute und dabei ständig ansprechbar war, sowie Prof. Dr. Claus A. M. Seidel, Dr. René Wittmann, Dr. Deborah Sandrin, Dr. Dana Wagner und Dr. Ralf Kühnemuth.

An dieser Stelle dürfen auch nicht die Menschen vergessen werden, die im Hintergrund für einen reibungslosen Ablauf am Institut sorgen, als da wären Herr Joachim Wenk, Frau Claudia Stader und Frau Karin Wildhagen. Dazu danke ich meinen Kollegen an unserem Lehrstuhl. Hier durfte ich tolle Menschen kennenlernen, auf die ich mich jederzeit verlassen konnte, mit denen ich mich sowohl fachlich als auch persönlich austauschen und in unseren gemeinsamen Spielerunden auch einfach mal abschalten konnte.

Zuletzt danke ich ganz besonders meiner Familie und allen meinen Freunden für die ständige, bedingungslose Unterstützung, die ich stets erfahren durfte.

Inhaltsverzeichnis

Kapitel 1

Einleitung

In der Physik befasst sich der Bereich der *weichen Materie* mit einer Vielzahl unterschiedlicher Systeme und Teilchen, wie beispielsweise Polymeren, Gelen, Tensiden, Flüssigkristallen oder auch biologischen Zellbestandteilen wie DNA oder Proteinen.[1–4] Damit befindet sich die weiche Materie im Grenzgebiet zur Chemie, Medizin und Biologie.

Wichtige Systeme in der weichen Materie sind kolloidale Dispersionen.[2;5] Diese bestehen aus mindestens zwei Komponenten unterschiedlicher Größenordnung, nämlich einer *dispersen Phase*, die sich in einem *Dispersionsmedium*, beispielsweise Wasser, befindet. Die disperse Phase besteht dabei aus Teilchen, auch *Kolloide* genannt, die mindestens einige Nanometer groß sind.[4] So können zum einen Quanteneffekte vernachlässigt werden und zum anderen sind die Teilchen wesentlich größer als die Moleküle des Dispersionsmediums, sodass Letzteres als Kontinuum dargestellt werden kann. Gleichzeitig dürfen Kolloide höchstens etwa 10 Mikrometer groß sein, damit die thermische Energie immer noch die Gravitation überwiegt und dadurch die Brownsche Bewegung, also die scheinbar zufällige Bewegung durch Stöße mit Molekülen des Dispersionsmediums, sichtbar ist.[5]

Wie der Name schon impliziert, haben Systeme in der weichen Materie neben der gemeinsamen Größenordung der relevanten Teilchen eine Gemeinsamkeit darin, dass sie sich bei externen Kräften relativ leicht verformen lassen.[4] Aufgrund der Vielzahl der auftretenden Teilchen sind zur Beschreibung dieser Systeme Methoden der statistischen Physik nötig, da die Berechnung der Bewegung jedes einzelnen Moleküls zu komplex wäre. Durch die Interaktion vieler Teilchen sind die auftretenden Strukturen dabei sowohl komplex als auch interessant und durch technische Anwendungen für den menschlichen Alltag relevant. So sind Flüssigkristalle ein zentraler Baustein von LCD-Bildschirmen, aber auch lebenswichtige Substanzen wie Milch oder Blut fallen unter kolloidale Systeme und motivieren zu ihrer Erforschung.[1]

Die dieser kumulativen Dissertation zugrunde liegenden Veröffentlichungen haben sich mit zwei komplexen Systemen aus dem Bereich der weichen Materie befasst, nämlich mit der Diffusion von Makromolekülen durch Gele sowie mit zweidimensionalen Flüssigkristallen. Beide Systeme werden in den folgenden Kapiteln vorgestellt.

1.1 Diffusion in Hydrogelen

Stellt man die scheinbar einfache Frage, ob man wisse, was ein „Gel“ sei, so wird diese Frage meist bejaht werden, da Assoziationen zu „Alltags-Gelen“ wie beispielsweise Götterspeise oder Haargel hergestellt werden. Fragt man unabhängig davon, ob man generell zwischen *flüssig* oder *fest* unterscheiden könne, wird diese Frage ebenso bejaht werden. Fragt man jedoch, ob ein Gel flüssig oder fest sei, so wird es komplexer und Antworten wie „beides“ oder „weder noch“ scheinen auf einmal zulässig.

Als erstes System befasst sich diese Arbeit mit Hydrogelen. Dabei handelt es sich um dreidimensionale Netzwerke aus (festen) Polymeren, deren Zwischenräume mit (flüssigem) Wasser gefüllt sind. Für kleine Moleküle, wie beispielsweise Wasser, sind solche Netzwerke durchlässig. Dies gilt jedoch nicht zwangsläufig für Makromoleküle, also größere, aus sich wiederholenden Bausteinen aufgebaute Teilchen wie Polymere oder Proteine.

Die Diffusion von solchen Makromolekülen in Gelen ist in vielerlei Hinsicht interessant.* Zum einen spielt sie eine Rolle in technischen Analyseverfahren, wie bei der Gelelektrophorese, die u.a. zur Bestimmung des genetischen Fingerabdrucks verwendet wird,[6] aber auch bei der Gel-Chromatographie,[7] der Expansions-Mikroskopie,[8] bei biologischen Mikrochips in der Genetik[9] oder bei der Untersuchung von Diffusion in Biofilmen[10]. Neben diesen Anwendungen in Analyseverfahren ergibt sich eine weitere Relevanz in medizinischen und pharmazeutischen Fragestellungen, wie bei Kontaktlinsen[11] oder der kontrollierten Abgabe[12–16] bzw. Flusskontrolle[17] pharmazeutischer Wirkstoffe, aber auch bei technischen Verfahren wie beispielsweise der Ölrückgewinnung[18;19] oder der Entwicklung saugfähiger Stoffe[14;20]. Trotz dieser vielfältigen Anwendungen und ausgiebiger Forschung auf diesem Gebiet sind viele Antworten auf grundlegende Fragestellungen noch unbekannt, da bei der Bewegung von Makromolekülen durch Gele viele Effekte gleichzeitig auftreten können. Beispiele hierfür sind chemische oder elektrische Wechselwirkungen zwischen dem Makromolekül und dem Gel, eine mögliche Einwicklung des Makromoleküls durch die Polymerketten, ein Siebeffekt durch die Maschen des Polymernetzwerks oder Fluktuationen der Porengrößen im Gel durch die Flexibilität der Polymerketten.[21–27] Selbst grundlegende Charakteristika wie die mittlere Porengröße im Gel sind häufig nicht bekannt.

Verschiedenste Methoden und Instrumente zur Bestimmung der mittleren Porengröße sind u.a. mit der Chromatographie,[28] der Thermoporometrie,[29] der Elektrophorese,[23;30–32] der Rasterelektronenmikroskopie,[33–35] der Rasterkraftmikroskopie,[36] der Transmissionselektronenmikroskopie[29] oder dem neuen *fluorescence correlation spectroscopy super-resolution optical fluctuation imaging*[37] bekannt. Allerdings unterscheiden sich die Ergebnisse verschiedener Methoden für vergleichbare Gele oft signifikant um teilweise mehr als das tausendfache,[28;30–35;38] sodass die mittlere Porengröße in Gelen immer noch ein kontrovers diskutierter Bestandteil aktueller Forschung

*Siehe auch die Einleitung in Veröffentlichung I, an die Teile dieses Abschnittes angelehnt sind.

ist.[38]

Allerdings werden nicht nur die Phänomenologien und die experimentellen Verfahren vielfältig und kontrovers diskutiert. Auch in der theoretischen Beschreibung von Hydrogelen gibt es eine Vielzahl verschiedener theoretischer Modelle[39;40] und Simulationsansätze[41–53] mit unterschiedlichen Vor- und Nachteilen.

Um einen Beitrag zur aktuellen Forschung auf diesem Gebiet zu leisten, werden in Veröffentlichung I die Diffusionskoeffizienten sowohl für Wasser als auch für mehrere unterschiedlich große Makromoleküle innerhalb einer Gelprobe ermittelt.[54] Diese Daten erlauben Rückschlüsse auf die mittlere Porengröße im Gel. Dabei werden mit der *Multiparameter Fluorescence Image Spectroscopy* (MFIS),[55;56] der Makroskopischen Transmissions Bildgebung (engl. *macroscopic transmission imaging* (MTI))[57;58] und der Kernspinresonanzspektroskopie (NMR)[59;60] drei unterschiedliche experimentelle Verfahren kombiniert und die Ergebnisse mit Brownsche Dynamik Simulationen (siehe auch Kap. 1.3.1) verglichen.[54]

Durch die Übereinstimmung der Resultate unterschiedlicher Verfahren erlangen die gefundenen Ergebnisse eine besonders hohe Validität und wurden bereits von anderen Arbeitsgruppen für ihre Forschung weiterverwendet.[61;62]

1.2 Anisotrope Teilchen auf zweidimensionalen Mannigfaltigkeiten

Auch wenn wir in einer dreidimensionalen Welt leben, haben zweidimensionale Systeme eine große Bedeutung. Alles, was sich auf Oberflächen abspielt, findet effektiv in einem zweidimensionalen System statt. Solange Menschen zu Fuß gehen, bewegen sie sich auf der Erdoberfläche näherungsweise auf einer zweidimensionalen Mannigfaltigkeit. Deshalb werden solche Systeme relevant, wenn es beispielsweise darum geht, Massenpaniken zu untersuchen[63;64] oder die Bewegung von Menschen auf Konzerten zu modellieren[65]. Auch im kleineren, kolloidalen Maßstab sind zweidimensionale Systeme relevant, beispielsweise im Flüssig-Mosaik-Modell von Zellmembranen.[66]

In dieser Arbeit werden Systeme aus monodispersen, kolloidalen, anisotropen, harten Teilchen betrachtet, die sich auf einer zweidimensionalen Mannigfaltigkeit frei bewegen und drehen können. Dabei meint „monodispers“, dass alle Teilchen die gleiche Größe haben und „anisotrop“, dass diese Teilchen im Gegensatz zu kreisrunden Scheiben eine Orientierungsabängigkeit vorweisen. Konkret handelt es sich im Rahmen dieser Arbeit bei diesen Teilchen entweder um gewöhnliche Rechtecke (in Veröffentlichung II und Veröffentlichung IV) oder um Rechtecke mit abgerundeten Kappen an zwei gegenüberliegenden Seiten (in Veröffentlichung III), welche im Folgenden als „Stäbchen“ bezeichnet werden. Beide Teilchensorten sind in Abb. 1.1 skizziert.

Auf zwei Dimensionen eingeschränkt können reale Teilchen wie DNA-Helizes[67] oder stäbchenförmige Viren[68;69] in guter Näherung durch solchen Formen beschrieben wer-

den. Bei der Untersuchung dieser Systeme werden in dieser Arbeit zwei Schwerpunkte gesetzt:

Einerseits wird das *Phasenverhalten* sowohl von Stäbchen (in Veröffentlichung III) als auch von Rechtecken (in Veröffentlichung IV) untersucht und dabei im letzteren Fall auch auf den Einfluss externer Felder und/oder gekrümmter Oberflächen (beides in Veröffentlichung IV) eingegangen. Auf der anderen Seite wird der Einfluss von Wänden auf ein solches System durch die Bestimmung der *Oberflächenspannungen* (in Veröffentlichung II) ermittelt. Auf beide Aspekte wird in den folgenden Unterkapiteln weiter eingegangen.

1.2.1 Phasenverhalten

Um in diese Thematik einzuleiten, sei zunächst wieder ein Problem aus dem alltäglichen Leben vorgestellt:

Sollen Würstchen auf einem Grill zubereitet werden, so ist es wünschenswert, dass sich diese nicht überlappen. Auf dem Rost betrachtet man effektiv ein zweidimensionales System harter Stäbchen. Ist der Grill sehr groß und sollen nur zwei Würstchen zubereitet werden, so ist die *Dichte* der Würstchen auf dem Rost sehr gering und man könnte sie mit zufälliger Orientierung auf zufällige Stellen des Rosts legen, ohne dass ihre relative Position oder Orientierung zueinander in einer besonderen Beziehung stehen müssten. Will man auf diesem Rost jedoch sehr viele Würstchen gleichzeitig zubereiten und dabei annähernd die ganze Grillfläche füllen (hohe Dichte), so würde man sie intuitiv parallel ausrichten, um den Platz ohne Überlappung abzudecken. Durch die Anwesenheit vieler Teilchen ist dann von außen eine Struktur gut erkennbar.

Ähnliches passiert auch selbstständig in viel kleinerem Maßstab. So können Kollektive kolloidaler Teilchen viele verschiedene Strukturen (oder auch *Phasen*) annehmen. Solche Phasen können stabil, meta-stabil oder instabil sein, wobei diese Arbeit sich auf stabile Gleichgewichtsphasen konzentriert.

Welche Phase jeweils im Gleichgewicht vorliegt, ist allerdings eine komplexe Fragestellung, denn sie hängt von vielen Faktoren ab. Einen großen Einfluss auf die vorliegende Struktur haben die Eigenschaften der einzelnen Teilchen: Wie ist die Form der Teilchen? Gibt es nur eine Teilchensorte oder Mischungen verschiedener Teilchen? Wie ist die Teilchen-Teilchen-Wechselwirkung (hart oder weich, anziehend oder abstoßend, ...)? Sind sie passiv oder bewegen sie sich aktiv?[†]

Allerdings spielen auch andere Faktoren eine Rolle: Wie viele Teilchen gibt es, d.h. wie groß ist die Teilchendichte? Gibt es externe Potentiale, die bestimmte Orientierungen oder Positionen begünstigen? Ist die Oberfläche, auf der die Teilchen liegen, eben oder gekrümmt?

Im Folgenden wird ein Überblick über die in dieser Arbeit relevanten Phasen

[†]Im Falle aktiver Teilchen kann man zwar beispielsweise durch Schwarmbildungen Strukturen erkennen, allerdings würde man nicht mehr von einer Gleichgewichtsphase sprechen.

anisotroper Teilchen in zwei Dimensionen gegeben. Dabei sei erwähnt, dass es gerade in drei Dimensionen durchaus noch mehr flüssigkristalline Phasen gibt.[70–75]

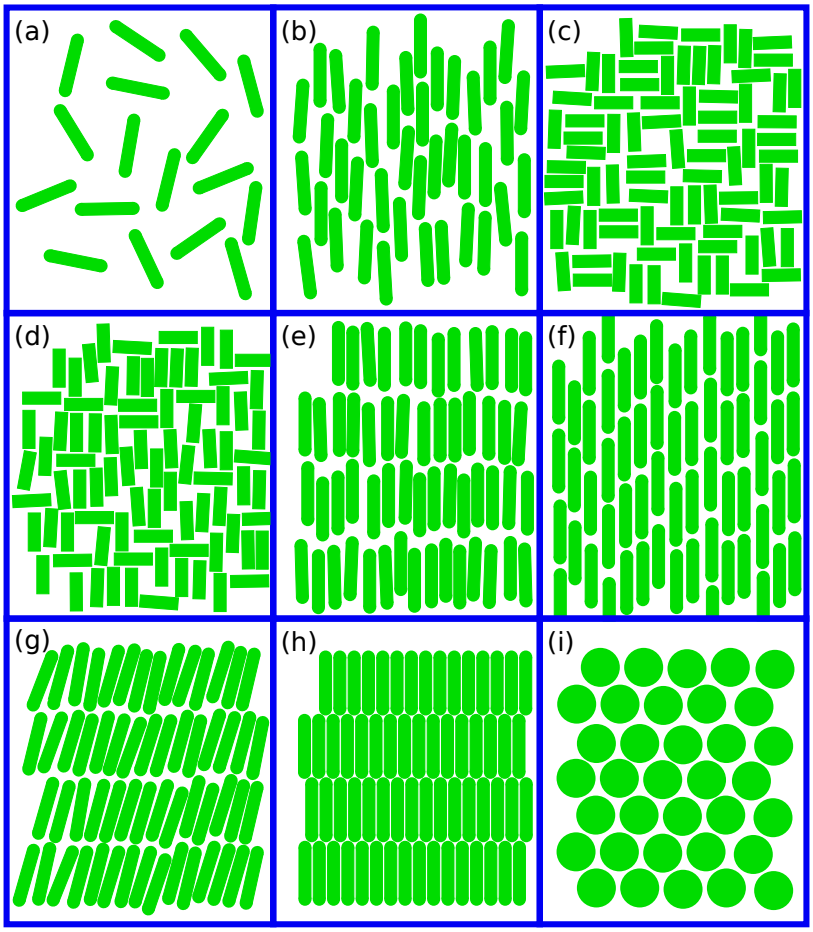

Abbildung 1.1: Skizzen zur Veranschaulichung unterschiedlicher flüssigkristalliner Phasen. (a) isotrop, (b) nematisch, (c) tetratisch, (d) binematisch, (e) smektisch A, (f) kolumnar, (g) smektisch C, (h) Kristall anisotroper Teilchen, (i) Kristall isotroper Teilchen.

In Abbildung 1.1 sind die unterschiedlichen Phasen durch Skizzen veranschaulicht. Für geringe Teilchendichten sind sowohl die Teilchenorientierungen als auch ihre Positionen zufällig. Dabei sind alle Orte und Orientierungen gleich wahrscheinlich. Diese *isotrope Phase* ist in Abb. 1.1(a) abgebildet.

Betrachtet man Teilchen mit einem großen Länge-Breite-Verhältnis, so findet man ab einer bestimmten Dichte eine *nematische Phase*, in der die Teilchenorientierung nicht mehr gleichverteilt, sondern entlang einer Achse ausgerichtet ist. Dadurch liegen benachbarte Teilchen tendenziell parallel zueinander. Dabei ist eine räumliche strukturelle Ordnung der Teilchenpositionen nur kurzreichweitig, sodass sich kaum

Vorhersagen über die Positionen nächster oder gar übernächster Nachbarn treffen lassen. Diese Phase ist in Abb. 1.1(b) veranschaulicht.

Die *tetratische Phase* ähnelt der nematischen Phase insofern, als dass die Orientierungsverteilung nicht gleichverteilt ist und sie auch keine langreichweitige Ordnung der Teilchenpositionen zeigt. Wie in Abb. 1.1(c) deutlich wird, besteht der Unterschied zur nematischen Phase darin, dass die Teilchenausrichtung nun entlang zweier zueinander senkrechter Achsen überwiegt und daher benachbarte Teilchen dazu neigen, sich entweder parallel oder senkrecht zueinander anzuordnen. Diese Phase wird nur für Rechtecke und nicht für Stäbchen beobachtet, da die abgerundeten Kappen der Stäbchen diese Phase verhindern.

Eine Mischphase zwischen der tetratischen und nematischen Phase kann mit der *binematischen Phase* auftreten, wenn beispielsweise in einem System mit tetratischer Phase ein externes Feld angelegt wird, das die Ausrichtung entlang einer der beiden tetratischen Achsen leicht bevorzugt. Wie in Abb. 1.1(d) erkennbar ist, sind weiterhin die meisten Teilchen entlang einer der beiden senkrecht zueinander liegenden Achsen orientiert, wobei nun die Ausrichtung entlang der vertikalen Achse überwiegt. Auch hier gibt es keine langreichweitige räumliche Struktur.

Für hohe Teilchendichten hingegen bildet sich ein Flüssigkristall, der eine räumliche Struktur der Teilchenpositionen zeigt. Diese räumliche Ordnung kann auf eine Raumrichtung beschränkt sein, sodass die Teilchenpositionen in der anderen Raumrichtung weiter keine langreichweitige Struktur zeigen. In diesem Fall bildet sich ein Streifenmuster und man unterscheidet je nach mittlerer Orientierung der Teilchen innerhalb dieser Streifen die folgenden Phasen:

Sind die einzelnen Teilchen senkrecht zu den Streifen ausgerichtet (siehe Abb. 1.1(e)), so wird diese Struktur als *smektische A Phase* bezeichnet. Wenn die gemeinsame Orientierung der Teilchen entlang der Streifen ist, spricht man von einer *kolumnaren Phase* (siehe Abb. 1.1(f)). Ist die mittlere Orientierung der Teilchen weder senkrecht noch parallel zu den Streifen, wird sie als *smektische C Phase* bezeichnet (siehe Abb. 1.1(g)).

Andererseits können die Teilchenpositionen aber auch in beiden Raumrichtungen geordnet sein. In diesem Fall spricht man von einer *kristallinen Phase* und ein Beispiel hierfür ist in Abb. 1.1(h) für Stäbchen und in Abb. 1.1(i) für Scheiben skizziert.

Um das Verhalten unterschiedlicher harter Teilchen zu untersuchen, wurde bereits eine Vielzahl an Experimenten[76–78], Simulationen[73;79–87] und Dichtefunktionaltheorierechnungen[73;87–101] konzipiert und durchgeführt. Auch wenn viele Veröffentlichungen sich auf drei Dimensionen konzentrieren, gibt es doch auch mehrere Untersuchungen zweidimensionaler Systeme.[81–83;87;89–91;93;95;97;102–104] Hier liegt der Schwerpunkt meist auf ebenen Oberflächen, aber auch gekrümmte Oberflächen wurden für verschiedene Systeme betrachtet.[105–122]

Allerdings gibt es trotz dieser Vielzahl an Studien noch viele ungeklärte Fragen, von denen manche im Rahmen dieser Dissertation untersucht werden. So wurde eine tetratische Phase zwar für harte Rechtecke in Simulationen und Experimenten beob-

achtet,[76–78;82–84;89–91;93;97;100] allerdings gab es bis zu den hier vorgestellten Ergebnissen in Veröffentlichung IV keine systematische Auswertung eines Phasendiagramms für harte Rechtecke mittels einer Dichtefunktionaltheorie, die eine stabile tetratische Phase ermöglicht. Darüber hinaus fehlte es bisher an systematischen Studien über das Verhalten harter Rechtecke sowohl in der Ebene als auch auf einer Zylinderoberfläche bei angelegtem externem Potential, welches in Veröffentlichung IV untersucht wird. Des Weiteren war zwar ein Phasendiagramm für Stäbchen in zwei Dimensionen bekannt,[81] allerdings wurde dort nicht der Übergang zwischen der smektischen und kristallinen Phase aufgelöst. Diese Lücke wird ebenfalls im Rahmen dieser Arbeit in Veröffentlichung III geschlossen.

1.2.2 Oberflächenspannung

Wenn eine Flüssigkeit in Kontakt mit einer Wand tritt, kann es zu vielen verschiedenen Effekten kommen. So kann der Kontaktwinkel zwischen der Wand und einem Flüssigkeitstropfen, je nach Beschaffenheit der Wandoberfläche und der Flüssigkeit, variieren.[123;124] Anschaulich bedeutet das, dass ein Wassertropfen sich auf einer festen Oberfläche in einem Extremfall vollständig ausbreiten könnte oder aber auch im anderen Extremfall komplett abperlt (auch bekannt als Lotus-Effekt[125–127]).

Stellt man sich eine Flüssigkeit mit nadelförmigen Kolloiden vor, so ist anschaulich klar, dass alle Nadeln, die sich mit ihrem Schwerpunkt sehr nahe an der Wand befinden, parallel zu ihr ausgerichtet sein müssen, damit es zu keiner Überlappung mit der Wand kommt. Dadurch entwickeln sich in der Nähe der Wand Strukturen. Darüber hinaus kann eine Wand eine Keimbildung, wie sie beispielsweise für einen Gefriervorgang nötig ist, unterstützen.[128–130]

Betrachtet man die nähere Umgebung von Teilchen in einer Flüssigkeit weit weg von der Wand, so finden sich in allen Richtungen benachbarte Teilchen. Betrachtet man jedoch die nähere Umgebung eines Teilchens direkt an der Wand, so finden sich in Richtung der Wand keine benachbarte Teilchen. Diese Asymmetrie an der Grenzfläche führt zu einer Differenz $\Omega_{\text{Wand}} - \Omega_0$ zwischen den Energien in einem System mit (Ω_{Wand}) und einem System ohne Wand (Ω_0). Normiert auf die Wandlänge L_{Wand} ergibt diese Energiedifferenz (hier betrachtet im großkanonischen Ensemble) die physikalisch wichtige Größe der *Oberflächenspannung*:

$$\gamma = \frac{\Omega_{\text{Wand}} - \Omega_0}{L_{\text{Wand}}} \,. \tag{1.1}$$

Diese Oberflächenspannung γ ist von der Beschaffenheit der Wand abhängig. Insbesondere hängt sie in der Regel auch von ihrer Krümmung ab. Werden gekrümmte Wände betrachtet, so kann für schwache Krümmungen folgende Näherung für die Oberflächenspannung gemacht werden:[131]

$$\gamma(R) = \gamma(\infty)\Big(1 - \frac{2\ell_{\text{T}}}{R} + \mathcal{O}(R^{-2})\Big) \,. \tag{1.2}$$

Dabei bezeichnet R den Krümmungsradius, $\gamma(\infty)$ die Oberflächenspannung für eine gerade Wand (also $R \to \infty$) und ℓ_T die sogenannte *Tolman-Länge*[131]. Dem Vorzeichen der Tolman-Länge kommt dabei eine besondere Bedeutung zu. Bei einem negativen Vorzeichen „kostet“ die gekrümmte Wand das System mehr Energie, als es bei einer geraden Wand der Fall wäre. Umgekehrt ist eine gekrümmte Wand bei einem positiven Vorzeichen energetisch günstiger für das System als eine gerade Wand, was bei einer verformbaren Wand zu einer Krümmung führen würde.

In der Vergangenheit wurden bereits diverse Studien bezüglich der Tolman-Länge und der Oberflächenspannung an gekrümmten Wänden durchgeführt.[132–151] Jedoch wurden dabei keine frei drehbaren anisotropen Teilchen betrachtet, sondern nur Scheiben (in zwei Dimensionen) bzw. Kugeln (in drei Dimensionen). Veröffentlichung II schließt diese Lücke. Dabei findet sich übereinstimmend in analytischen Rechnungen, Dichtefunktionaltheorierechnungen und Monte-Carlo-Simulationen eine bislang unbekannte Abhängigkeit des Vorzeichens der Tolman-Länge sowohl von der Teilchendichte als auch von dem Länge-Breite-Verhältnis der Teilchen.

1.3 Methoden

Da es sich bei den meisten Systemen in der weichen Materie um komplexe Vielteilchensysteme handelt, sind diese oft nur unter starken Näherungen für analytische Rechnungen zugänglich. Hier gibt es jedoch durch die Möglichkeit computergestützter Rechnungen und Simulationen alternative Ansatzpunkte. Im Rahmen dieser Arbeit werden zwar analytische Rechnungen in Veröffentlichung II durchgeführt, jedoch beruhen die meisten Ergebnisse auf numerischen Methoden. In den folgenden Unterkapiteln werden die für diese Arbeit relevanten Methoden vorgestellt.

1.3.1 Simulation

Teilchenaufgelöste Simulationen sind ein wichtiger Bestandteil der modernen Forschung. Durch den technischen Fortschritt lassen sich immer größere und komplexere Systeme untersuchen. Ihre Einsatzmöglichkeiten sind vielfältig. Zum einen sind ihre Ergebnisse eine hervorragende Referenz, wenn es darum geht, neue Theorien zu testen. In diesem Zusammenhang werden in Veröffentlichung II, Veröffentlichung III und Veröffentlichung IV Monte-Carlo-Simulationen durchgeführt, um die Vorhersagen der hier verwendeten Dichtefunktionaltheorien zu testen. Zum anderen ermöglichen Simulationen eine Hilfestellung bei der Erstellung von Experimenten und erlauben es, Vorhersagen über reale experimentelle Systeme zu treffen sowie physikalische Größen aus ihnen zu extrahieren.

In diesem Zusammenhang werden in Veröffentlichung I Brownsche Dynamik Simulationen durchgeführt, um u.a. die durchschnittliche Porengröße eines Hydrogels zu

bestimmen. Eine gute Übersicht über diese und weitere numerische Simulationsmethoden bietet das Buch von Allen und Tildesley.[152]

Im Folgenden wird nur auf die von mir angewandte Methode der *Brownsche Dynamik Simulationen* (BD-Simulationen) eingegangen.

Brownsche Dynamik Simulationen

Wie in Kapitel 1 erwähnt, zeichnen sich kolloidale Systeme durch die unterschiedlichen Größenordnungen der dispersen Phase und der Teilchen des Dispersionsmediums aus. Während die kolloidalen Teilchen der dispersen Phase viel größer sind, ist ihre Bewegung viel langsamer als die der Moleküle des Dispersionsmediums. Dies hat für die Simulation solcher Systeme weitreichende Konsequenzen. Bei der Brownschen Bewegung kommt es zu einer Bewegung der Kolloide durch eine Vielzahl von Stößen mit den Molekülen des Dispersionsmediums. Würde man die Trajektorie eines dieser Kolloide exakt beschreiben wollen, indem man die exakten Trajektorien aller Moleküle des Dispersionsmediums[‡] und ihre Stöße mit dem Kolloid berechnet, so wäre der Rechenaufwand viel zu hoch, als dass in einer vertretbaren Zeit Ergebnisse möglich seien. Darüber hinaus sind die einzelnen Trajektorien der Moleküle des Dispersionsmediums meist nicht von Interesse, wenn man die Eigenschaften der Kolloide untersuchen will. Brownsche Dynamik Simulationen sind eine Möglichkeit, mit dieser Problematik umzugehen. Sie beruhen mathematisch auf der Langevin Gleichung, welche die Bewegung eines Teilchens i wie folgt beschreibt:[153]

$$m_i \frac{\mathrm{d}^2 \vec{r}_i}{\mathrm{d}t^2} = -\zeta \frac{\mathrm{d}\vec{r}_i}{\mathrm{d}t} + \vec{F}_i(\vec{r}_i, t) + \vec{f}_{i,\mathrm{ran}}(t)\,. \tag{1.3}$$

Dabei bezeichnet m_i die Masse des Teilchens i am Ort $\vec{r}_i$ und ζ den Reibungskoeffizienten des Teilchens im Medium. Die Kraft $\vec{F}_i(\vec{r}_i, t)$ umfasst alle Beiträge der zum Zeitpunkt t auf das Teilchen wirkenden Kräfte. Diese können sowohl aus externen Feldern als auch aus Teilchen-Teilchen-Wechselwirkungen stammen.[§] Bis zu dieser Stelle ist die Gleichung komplett deterministisch und analog zur Netwon'schen Mechanik. Den Unterschied macht der Term $\vec{f}_{i,\mathrm{ran}}(t)$ aus, welcher die Zufallsbewegung durch die Brownsche Bewegung über eine Gauß-verteilte Zufallskraft modelliert, die auf das Teilchen wirkt. Diese Kraft ist im zeitlichen Mittel ungerichtet und ihre Amplitude hängt von der Temperatur T und dem Medium ab. Beide Eigenschaften lassen sich mathematisch durch

$$\begin{aligned} \langle \vec{f}_{i,\mathrm{ran}}(t) \rangle &= \vec{0}, \\ \langle \vec{f}_{i,\mathrm{ran}}(t) \vec{f}_{j,\mathrm{ran}}(t') \rangle &= 2 k_\mathrm{B} T \zeta \delta_{ij} \delta(t' - t) \boldsymbol{\delta}, \end{aligned} \tag{1.4}$$

[‡]Abhängig vom betrachteten System wären tausende oder auch viele Milliarden Moleküle zu simulieren.

[§]Je nach Darstellung werden diese Kräfte auch alternativ über den Gradienten eines Potentials mit $\vec{F}_i(\vec{r}_i, t) = -\vec{\nabla}_{\vec{r}_i} U_i(\vec{r}_i, t)$ dargestellt.

darstellen,[¶] wobei k_B die Boltzmannkonstante, δ_{ij} das Kronecker-Delta, $\delta(t'-t)$ die Delta-Distribution und $\boldsymbol{\delta}$ den Einheitstensor zweiter Ordnung bezeichnet.[152;154]

Im Gegensatz zur Bewegung von Teilchen im Vakuum wird die Bewegung von Kolloiden in Flüssigkeiten sehr stark von der Reibung beeinflusst. Dadurch kommt eine Bewegung in den meisten Medien rasch zum Erliegen, falls keine permanente Kraft auf das Kolloid einwirkt. Dieser überdämpfte Fall rechtfertigt daher die Annahme

$$|m_i \frac{\mathrm{d}^2\vec{r}_i}{\mathrm{d}t^2}| \ll |\zeta \frac{\mathrm{d}\vec{r}_i}{\mathrm{d}t}|\,, \tag{1.5}$$

sodass der Trägheitsterm auf der linken Seite von Gleichung (1.3) vernachlässigt werden kann.[‖] Schreibt man nun in Gleichung (1.3)

$$\frac{\mathrm{d}\vec{r}_i}{\mathrm{d}t} = \frac{\vec{r}_i(t+\Delta t) - \vec{r}_i(t)}{\Delta t} \tag{1.6}$$

als Differenzenquotienten und löst nach $\vec{r}_i(t+\Delta t)$ auf, ergibt sich eine numerische Lösung der stochastischen Differentialgleichung nach dem Euler-Verfahren:[152;154]

$$\vec{r}_i(t+\Delta t) = \big(\vec{F}_i(\vec{r}_i,t)\Delta t + \vec{f}_{i,\mathrm{ran}}(t)\sqrt{\Delta t}\big)/\zeta + \vec{r}_i(t)\,. \tag{1.7}$$

Mit ihr lässt sich die Bewegung aller Teilchen sukzessiv in Zeitschritten Δt bestimmen, da alle Positionen $\vec{r}_i(t)$ und Kräfte zum aktuellen Zeitpunkt t auf der rechten Seite von Gleichung (1.7) bekannt sind. Dabei muss Δt hinreichend groß gewählt werden, um eine Lösung der Gleichung in akzeptabler Zeit zu ermöglichen, gleichzeitig jedoch hinreichend klein, um eine korrekte Integration der Bewegungsgleichung zu gewährleisten. Um zu testen, ob Δt ausreichend klein gewählt wurde, sollte daher überprüft werden, ob die Simulationsergebnisse von einer Verringerung des Zeitschrittes unabhängig sind.

Aus den so bestimmten Teilchentrajektorien lassen sich anschließend makroskopische Größen des Systems berechnen. In Veröffentlichung I wurden auf Basis der simulierten Trajektorien in drei Dimensionen die Diffusionskonstanten der Makromoleküle über folgende Relation bestimmt:[152;155]

$$D = \frac{1}{6}\lim_{\tau\to\infty}\frac{\mathrm{d}\langle\vec{r}^{\,2}(\tau)\rangle}{\mathrm{d}\tau}\,. \tag{1.8}$$

Dabei bezeichnet $\langle\vec{r}^{\,2}(\tau)\rangle$ das mittlere Verschiebungsquadrat (engl. *mean squared displacement*) der Teilchen in einem ausreichend großen Zeitintervall τ.

[¶] Je nach Darstellung wird die zweite Gleichung auch mit dem Diffusionskoeffizienten $D = k_\mathrm{B}T/\zeta$ geschrieben.

[‖] Charakterisiert wird das Verhältnis der Trägheit zur Reibung auch über die Reynolds-Zahl, welche im überdämpften Fall sehr klein ist.

1.3.2 Dichtefunktionaltheorie (DFT)

Neben der im vorherigen Kapitel vorgestellten Möglichkeit, ein System teilchenaufgelöst zu beschreiben, indem die Trajektorien aller relevanten Teilchen berechnet werden, gibt es auch die Möglichkeit einer Dichtefeldbeschreibung. Dies meint, dass der aktuelle Zustand eines Systems durch die Einteilchendichte $\rho(\vec{r})$ charakterisiert wird, welche proportional zur Wahrscheinlichkeit ist, ein Teilchen am Ort $\vec{r}$ zu finden. Diese Beschreibung lässt sich ebenso für Mischungen verschiedener Teilchensorten anwenden, indem für jede Teilchensorte α ein eigenes Dichtefeld $\rho_\alpha(\vec{r})$ angegeben wird. Zudem können weitere Freiheitsgrade, wie beispielsweise der Orientierungswinkel φ anisotroper Teilchen, als Argument in das Dichtefeld eingehen. Da sich diese Arbeit mit monodispersen, anisotropen Teilchen in zwei Dimensionen befasst, wird im Folgenden ein Dichtefeld $\rho(\vec{r},\varphi)$ angenommen und dabei der Index α zur hier nicht relevanten Unterscheidung unterschiedlicher Teilchensorten weggelassen, um die Lesbarkeit zu erleichtern. Die Wahrscheinlichkeit $\bar{\rho}(\vec{r})$, ein Teilchen mit beliebiger Orientierung am Ort $\vec{r}$ zu finden, ergibt sich dann durch die Integration über alle Winkel φ:**

$$\bar{\rho}(\vec{r}) = \int_0^{2\pi} \mathrm{d}\varphi\, \rho(\vec{r},\varphi)\,. \tag{1.9}$$

Eine Methode, um das Gleichgewichtsdichteprofil $\rho_0(\vec{r},\varphi)$ eines Systems zu bestimmen, ist die in den 1970er Jahren entwickelte klassische Dichtefunktionaltheorie,[156–158] deren Grundzüge in Analogie zu der in den 1960er Jahren entwickelten quantenmechanischen Dichtefunktionaltheorie[159–161] stehen, für welche Walter Kohn 1998 mit dem Nobelpreis für Chemie ausgezeichnet wurde.[162] Im Rahmen der klassischen Dichtefunktionaltheorie kann gezeigt werden, dass ein Energiefunktional $\Omega[\rho]$ existiert, welches folgende Eigenschaften besitzt:[158]

- Es wird durch das Gleichgewichtsdichteprofil ρ_0 minimiert, d.h. $\Omega[\rho] \geq \Omega[\rho_0]$.
- Der Wert dieses Energiefunktionals für das Gleichgewichtsprofil $\Omega[\rho_0]$ entspricht dem großkanonischen Potential Ω des Systems.

Die erste Eigenschaft wird auch in dem folgenden Variationsprinzip zusammengefasst:[158;163]

$$\left.\frac{\delta\Omega[\rho]}{\delta\rho(\vec{r},\varphi)}\right|_{\rho=\rho_0} = 0\,. \tag{1.10}$$

** Alternativ kann man den Zusammenhang zwischen $\bar{\rho}(\vec{r})$ und $\rho(\vec{r},\varphi)$ auch über eine Mittelung über alle Orientierungen durch $\bar{\rho}(\vec{r}) = (\int_0^{2\pi}\mathrm{d}\varphi\ \rho(\vec{r},\varphi))/(\int_0^{2\pi}\mathrm{d}\varphi\,) = \int_0^{2\pi}\mathrm{d}\varphi\ \rho(\vec{r},\varphi)/(2\pi)$ definieren. Diese Darstellung ist äquivalent zur Interpretation über eine Integration (Gl. (1.9)) und die dazu konsistenten Gleichungen ergeben sich durch eine Substitution von $\rho(\vec{r},\varphi)$ durch $\rho(\vec{r},\varphi)/(2\pi)$ in den folgenden Gleichungen. Im Gegensatz zu Veröffentlichung II und Veröffentlichung IV haben wir in Veröffentlichung III die Darstellung über eine solche Mittelung verwendet, um Konsistenz zu den vorherigen Veröffentlichungen meines Co-Autors Dr. René Wittmann zu gewährleisten.

Für ein gegebenes externes Potential V_{ext} ist das Energiefunktional $\Omega[\rho]$ eindeutig[158] und kann geschrieben werden als

$$\Omega[\rho] = \mathcal{F}[\rho] + \int_{\mathbb{R}^2} \mathrm{d}^2 r \, \rho(\vec{r}, \varphi)(V_{\text{ext}}(\vec{r}, \varphi) - \mu) \,, \tag{1.11}$$

wobei $\mathcal{F}[\rho]$ das Funktional für die intrinsische freie Helmholtz Energie, μ das chemische Potential und Λ die thermische De-Broglie-Wellenlänge bezeichnet.

Für den Fall eines idealen Gases, d.h. keine Teilchen-Teilchen-Wechselwirkungen, ist $\mathcal{F}_{\text{id}}[\rho]$ exakt bekannt[158] und durch

$$\mathcal{F}_{\text{id}}[\rho] = \beta^{-1} \int_{\mathbb{R}^2} \mathrm{d}^2 r \int_0^{2\pi} \mathrm{d}\varphi \, \rho(\vec{r}, \varphi) \big(\ln(2\pi\Lambda^2 \rho(\vec{r}, \varphi)) - 1 \big) \tag{1.12}$$

für anisotrope Teilchen gegeben, wobei $\beta^{-1} = k_{\text{B}} T$ die thermische Energie mit der Boltzmann-Konstante k_{B} und der Temperatur T bezeichnet.

Setzt man Gl. (1.12) für $\mathcal{F}[\rho]$ in Gl. (1.11) ein, so ergibt sich nach Gl. (1.10) die Gleichgewichtsdichteverteilung

$$\rho_0(\vec{r}, \varphi) = e^{\beta(\mu - V_{\text{ext}}(\vec{r}, \varphi))} / (2\pi\Lambda^2) \,. \tag{1.13}$$

Ohne externes Potential stellt sich also eine *isotrope Phase* mit einer homogenen (d.h. von der Position und Teilchenorientierung unabhängigen) Gleichgewichtsdichteverteilung

$$\rho_0(\vec{r}, \varphi) = \rho_0 = e^{\beta\mu} / (2\pi\Lambda^2) = \text{konst.} \tag{1.14}$$

ein.

Werden andere Systeme als ein ideales Gases betrachtet, so wird $\mathcal{F}[\rho] = \mathcal{F}_{\text{id}}[\rho] + \mathcal{F}_{\text{exc}}[\rho]$ üblicherweise als Summe aus dem exakten idealen-Gas-Term $\mathcal{F}_{\text{id}}[\rho]$ und einem korrigierenden Überschussterm $\mathcal{F}_{\text{exc}}[\rho]$ (engl. *excess term*) dargestellt. $\mathcal{F}_{\text{exc}}[\rho]$ ist jedoch nur in den seltensten Fällen exakt bekannt. Eine Ausnahme bildet das Percus-Funktional,[164] welches das Tonks-Gas[165] monodisperser, harter Teilchen in einer Raumdimension beschreibt. Relevant für diese Arbeit ist das zweidimensionale Onsager-Funktional[166]

$$\beta\mathcal{F}_{\text{Ons}}[\rho] = -\frac{1}{2} \int_{\mathbb{R}^2} \mathrm{d}^2 r \int_0^{2\pi} \mathrm{d}\varphi \, \rho(\vec{r}, \varphi) \int_{\mathbb{R}^2} \mathrm{d}^2 r' \int_0^{2\pi} \mathrm{d}\varphi' \rho(\vec{r}\,', \varphi') f(\vec{r} - \vec{r}\,', \varphi, \varphi') \tag{1.15}$$

mit der Mayer-Funktion

$$f(\vec{r} - \vec{r}\,', \varphi, \varphi') = \begin{cases} -1 \,, & \text{wenn Teilchen mit den Koordinaten} \\ & (\vec{r}, \varphi) \text{ und } (\vec{r}\,', \varphi') \text{ überlappen,} \\ 0 \,, & \text{sonst,} \end{cases} \tag{1.16}$$

dessen dreidimensionales Äquivalent den Grenzfall unendlich langer Nadeln und verschwindender Dichte ebenfalls exakt beschreibt. Zur Beschreibung aller anderen Systeme muss $\mathcal{F}_{\text{exc}}[\rho]$ möglichst gut genähert werden. Dazu wurden in den vergangenen Jahrzehnten verschiedene Ansätze entwickelt, von denen mit der *local density approximation* (LDA),[167] der *weighted density approximation* (WDA)[168–170] oder der *Ramakrishnan-Yussouff approximation* (RY)[171] hier einige genannt seien. Für Details zu diesen und weiteren Ansätzen sei auf die entsprechenden Veröffentlichungen und die Übersichtsartikel in den Referenzen [163, 172, 173, 174] verwiesen.

Fundamental Measure Theory (FMT)

Von Bedeutung für diese Arbeit ist vor allem die 1989 von Rosenfeld entwickelte sogenannte *fundamental measure theory* (FMT).[175††] FMT beruht auf der Idee, die Mayer-Funktion (Gl. (1.16)) mit Hilfe von gewichteten Dichten (engl. *weighted densities*) zu zerlegen. Während die Mayer-Funktion noch von den Positionen zweier Teilchen abhängt und gerade bei Mischungen verschiedener Teilchensorten immer unterschiedlich aussieht, sind die gewichteten Dichten nur noch von Einteilchendichten abhängig. Darüber hinaus haben diese einen direkten Bezug zur Geometrie der Teilchen (Volumen, Oberfläche, etc.). Dadurch vereinfacht sich u.a. die Beschreibung von Mischungen verschiedener Teilchensorten. Während die ursprüngliche Version von Rosenfelds FMT noch einzelne Nachteile hatte, da u.a. der Gefrierpunkt harter Kugeln nicht korrekt vorhergesagt wurde,[163] wurden diese im Laufe der Jahre durch verschiedene Arbeiten behoben.[178–180]

Im Folgenden wird nun detaillierter auf die mathematischen Inhalte der FMT eingegangen: Die beschriebenen gewichteten Dichten $n_i(\vec{r})$ erhält man durch die orientierungsintegrierte Kreuzkorrelation $\star$ der Einteilchendichte $\rho(\vec{r},\varphi)$ mit den geometrischen Gewichtungsfunktionen $\omega^{(i)}(\vec{r},\varphi)$:‡‡

$$\begin{aligned} n_i(\vec{r}) &= \int_0^{2\pi} \mathrm{d}\varphi \, [\rho \star \omega^{(i)}](\vec{r},\varphi) \\ &= \int_0^{2\pi} \mathrm{d}\varphi \int_{\mathbb{R}^2} \mathrm{d}^2 r' \, \rho(\vec{r}\,',\varphi)\, \omega^{(i)}(\vec{r}\,' - \vec{r},\varphi)\,. \end{aligned} \tag{1.17}$$

In Anlehnung an Rosenfelds Formulierung der geometrischen Gewichtungsfunktionen in drei Dimensionen,[175] lauten die skalaren Gewichtsfunktionen in zwei Dimensionen

††Eine alternative Version wurde ein Jahr darauf von Kierlik und Rosinberg veröffentlicht,[176] welche jedoch äquivalent zu Rosenfelds FMT ist.[177]

‡‡In der Literatur wird diese Operation irreführenderweise auch oft als Faltung bezeichnet. Allerdings unterscheidet sich die Kreuzkorrelation $[g \star h](x) = \int \mathrm{d}x' \, g(x')h(x'-x)$ zwischen zwei Funktionen $g(x)$ und $h(x)$ von einer Faltung $[g * h](x) = \int \mathrm{d}x' \, g(x')h(x-x')$, außer in dem Fall, dass beide Funktionen $g(x)$ und $h(x)$ gerade sind. In diesem Zusammenhang befindet sich in Rosenfelds ursprünglicher Formulierung[175] ein Vorzeichenfehler.[177]

für frei drehbare anisotrope Teilchen:[90;181]

$$\begin{aligned}
\omega^{(2)}(\vec{r},\varphi) &= \Theta\big(|\vec{R}(\hat{\vec{r}},\varphi)| - |\vec{r}|\big)\,, \\
\omega^{(1)}(\vec{r},\varphi) &= \frac{\delta\big(|\vec{R}(\hat{\vec{r}},\varphi)| - |\vec{r}|\big)}{\vec{n}(\hat{\vec{r}},\varphi)\cdot\hat{\vec{r}}}\,, \\
\omega^{(0)}(\vec{r},\varphi) &= \frac{K(\hat{\vec{r}},\varphi)}{2\pi}\,\omega^{(1)}(\vec{r},\varphi)\,,
\end{aligned} \tag{1.18}$$

wobei $\delta(x)$ die Delta-Distribution und $\Theta(x)$ die Heaviside-Stufenfunktion bezeichnen. Der Vektor vom Mittelpunkt eines Teilchens mit Orientierung φ entlang des Einheitsvektors $\hat{\vec{r}} = \vec{r}/|\vec{r}|$ zu seinem Rand ist mit $\vec{R}(\hat{\vec{r}},\varphi)$ bezeichnet. Des Weiteren ist $\vec{n}(\hat{\vec{r}},\varphi)$ der Normalenvektor und $K(\hat{\vec{r}},\varphi)$ die lokale Krümmung an der Stelle des Teilchenrandes $\vec{R}(\hat{\vec{r}},\varphi)$. Diese Größen sind in Abbildung 1.2 veranschaulicht.

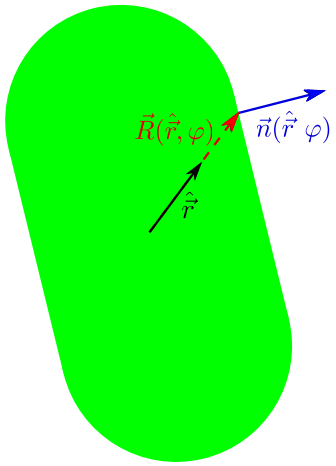

Abbildung 1.2: Veranschaulichung der Größen $\vec{R}(\hat{\vec{r}},\varphi)$, $\hat{\vec{r}} = \vec{r}/|\vec{r}|$ und $\vec{n}(\hat{\vec{r}},\varphi)$ für ein Stäbchen in zwei Dimensionen. $\vec{R}(\hat{\vec{r}},\varphi)$ zeigt bei einem Teilchen mit Orientierung φ von seinem Teilchenmittelpunkt entlang der Richtung $\hat{\vec{r}}$ bis zu seinem Rand. Der Normalenvektor des Randes an dieser Stelle ist $\vec{n}(\hat{\vec{r}},\varphi)$.

Die geometrischen Gewichtungsfunktionen haben jeweils konkrete geometrische Bedeutungen. So lässt sich $\omega^{(2)}(\vec{r},\varphi)$ beispielsweise mit

$$\omega^{(2)}(\vec{r},\varphi) = \begin{cases} 1\,, & \text{für alle Orte } \vec{r} \text{ innerhalb eines Teilchens} \\ & \text{im Koordinatenursprung mit Orientierung } \varphi, \\ 0\,, & \text{sonst,} \end{cases} \tag{1.19}$$

übersetzen. Bei der Berechnung von $n_2(\vec{r})$ entspricht die Kreuzkorrelation also einer (orientierungsintegrierten) Integration der Einteilchendichte $\rho(\vec{r},\varphi)$ über die Fläche eines an $\vec{r}$ zentrierten Teilchens mit Orientierung φ. Im Umkehrschluss folgt daraus, dass $n_2(\vec{r})$ die Bedeutung der lokalen Packungsdichte hat. Analog zur Einschränkung der Integration auf eine Teilchenfläche durch $\omega^{(2)}(\vec{r},\varphi)$, schränkt $\omega^{(1)}(\vec{r},\varphi)$ die Integration auf den Rand eines Teilchens am Koordinatenursprung mit Orientierung φ ein und $\omega^{(0)}(\vec{r},\varphi)$ wiederum gewichtet diesen Rand noch mit der lokalen Krümmung.

Im Falle harter Rechtecke, wie sie in Veröffentlichung II und Veröffentlichung IV untersucht wurden, beträgt die Krümmung jedoch entweder 0 (an den Seiten) oder ∞ (an den Ecken). Folglich wird aus $K(\hat{\vec{r}},\varphi)$ effektiv eine Delta-Distribution, wodurch bei der Berechnung von $n_0(\vec{r})$ über alle Ecken summiert wird. Für frei drehbare Rechtecke mit Länge L und Breite D lauten dann die relevanten geometrischen Gewichtsfunktionen:[90;182;183]

$$\omega^{(0)}(\vec{r},\varphi) = \frac{1}{4}\delta\Big(\frac{D}{2} - |x_\varphi|\Big)\delta\Big(\frac{L}{2} - |y_\varphi|\Big)\,, \tag{1.20}$$

$$\omega^{(1x)}(\vec{r},\varphi) = \frac{1}{2}\delta\Big(\frac{D}{2} - |x_\varphi|\Big)\Theta\Big(\frac{L}{2} - |y_\varphi|\Big)\,, \tag{1.21}$$

$$\omega^{(1y)}(\vec{r},\varphi) = \frac{1}{2}\Theta\Big(\frac{D}{2} - |x_\varphi|\Big)\delta\Big(\frac{L}{2} - |y_\varphi|\Big)\,, \tag{1.22}$$

$$\omega^{(2)}(\vec{r},\varphi) = \Theta\Big(\frac{D}{2} - |x_\varphi|\Big)\Theta\Big(\frac{L}{2} - |y_\varphi|\Big)\,. \tag{1.23}$$

Dabei sind x_φ and y_φ durch $x_\varphi = x\cos(\varphi) - y\sin(\varphi)$ und $y_\varphi = x\sin(\varphi) + y\cos(\varphi)$ definiert.

Verschiedene Ansätze zur Erweiterung von Rosenfelds FMT wurden u.a. mit dem White-Bear Funktional,[184;185] dem White-Bear mark II Funktional,[186] der *extended deconvolution fundamental measure theory* (edFMT)[92;94] oder der *fundamental mixed measure theory* (FMMT)[99] vorgestellt, allerdings außer der edFMT noch nicht in zwei Dimensionen angewandt. Eine solche Adaption für zwei Dimensionen der FMMT wird in Veröffentlichung III vorgenommen. Daher wird in der Folge kurz auf ihre Grundideen eingegangen.

Fundamental Mixed Measure Theory (FMMT)

In der ursprünglichen FMT gehen nur gewichtete Dichten $n_i(\vec{r})$ ein, die durch Kreuzkorrelationen der Dichte mit Gewichtsfunktionen $\omega^{(i)}(\vec{r}\,' - \vec{r},\varphi)$ bestimmt werden,

welche jeweils nur von der Position und Orientierung *eines* Teilchens abhängen. Folglich wird bei ihrer Berechnung auch nur einmal über alle Orte und Orientierungen integriert (siehe Gl. (1.17)). In der FMMT gehen nun mit den gemischten gewichteten Dichten auch Terme nächst höherer Ordnung der Form

$$N(\vec{r}) = \int_{\mathbb{R}^2} \mathrm{d}^2 r' \int_{\mathbb{R}^2} \mathrm{d}^2 r'' \int_0^{2\pi} \mathrm{d}\varphi' \int_0^{2\pi} \mathrm{d}\varphi'' \rho(\vec{r}', \varphi') \, \rho(\vec{r}'', \varphi'') \, \Omega(\vec{r} - \vec{r}', \vec{r} - \vec{r}'', \varphi', \varphi'') \quad (1.24)$$

ein. Hier hängt die gemischte Gewichtungsfunktion $\Omega(\vec{r} - \vec{r}', \vec{r} - \vec{r}'', \varphi', \varphi'')$ von den Positionen $\vec{r}', \vec{r}''$ und den Orientierungen φ', φ'' *zweier* Teilchen ab. Somit muss auch zwei mal über alle Positionen und Orientierungen integriert werden.

Beim Vergleich von Gl. (1.24) mit dem Onsager-Funktional (Gl. (1.15)) fällt sofort ihre gemeinsame Struktur auf. Bei niedrigen Dichten reduziert sich die FMMT wegen ihrer Herleitung exakt auf das Onsager-Funktional. Dieses entspricht, im Gegensatz zu drei Raumdimensionen, in zwei Raumdimensionen allerdings nicht mehr dem exakten Funktional für $\mathcal{F}_{\mathrm{exc}}$ bei niedrigen Dichten, ermöglicht jedoch eine gute Ausgangsbasis.

Die gemischte Gewichtsfunktion hängt in der FMMT mit

$$\begin{aligned} &\Omega(\vec{r}', \vec{r}'', \varphi', \varphi'') = \\ &\frac{\arccos\left(\vec{n}(\hat{\vec{r}}', \varphi') \cdot \vec{n}(\hat{\vec{r}}'', \varphi'')\right)}{2\pi} \left|\vec{n}(\hat{\vec{r}}', \varphi') \times \vec{n}(\hat{\vec{r}}'', \varphi'')\right| \, \omega^{(1)}(\vec{r}', \varphi') \, \omega^{(1)}(\vec{r}'', \varphi'') \end{aligned} \quad (1.25)$$

weiterhin von den aus der FMT bekannten Gewichtungstermen einzelner Teilchen ab, was ihre Berechnung im Vergleich zur Mayer-Funktion erleichtert. Die Definitionen in Gl. (1.25) sind hierbei analog zu Kapitel 1.3.2. Für weitere Details sei auf die Herleitung in Veröffentlichung III verwiesen.

Bei all den verschiedenen Ansätzen für eine Dichtefunktionaltheorie-basierte Beschreibung kolloidaler Flüssigkeiten sei betont, dass es sich in der Regel jeweils nur um Näherungen der nicht exakt bekannten Energiefunktionale handelt und in diesem aktiven Forschungsfeld ständig neue Funktionale vorgestellt werden. Auch diese Arbeit leistet neue Beiträge in diesem Forschungsgebiet: In Veröffentlichung IV wurde ein für ein System paralleler harter Rechtecke hergeleitetes FMT-Funktional[187;188] modifiziert und in ein neues Funktional eingearbeitet, wodurch das Phasenverhalten für frei drehbare Rechtecke in Übereinstimmung mit Simulationen beschrieben wurde. In Veröffentlichung III wird die für drei Dimensionen schon ausführlich diskutierte FMMT[99;189] in ihrer zweidimensionalen Version hergeleitet und implementiert. Ihre Qualität wird dort im Beispielsystem harter Stäbchen getestet und mit Simulationsergebnissen verglichen.

Kapitel 2

Publikationen

Dieser kumulativen Dissertation liegen die folgenden vier Publikationen zugrunde, welche in internationalen wissenschaftlichen Fachjournalen mit anerkannten Begutachtungsverfahren (peer-review) veröffentlicht wurden:

I. D. Sandrin*, D. Wagner*, **C. E. Sitta***, R. Thoma, S. Felekyan, H. E. Hermes, C. Janiak, N. de Sousa Amadeu, R. Kühnemuth, H. Löwen, S. U. Egelhaaf & C. A. M. Seidel, *Diffusion of macromolecules in a polymer hydrogel: from microscopic to macroscopic scales*, Phys. Chem. Chem. Phys. **18**, 12860 (2016)

II. **C. E. Sitta**, F. Smallenburg, R. Wittkowski & H. Löwen, *Hard rectangles near curved hard walls: Tuning the sign of the Tolman length*, J. Chem. Phys. **145**, 204508 (2016)

III. R. Wittmann*, **C. E. Sitta***, F. Smallenburg & H. Löwen, *Phase diagram of two-dimensional hard rods from fundamental mixed measure density functional theory*, J. Chem. Phys. **147**, 134908 (2017)

IV. **C. E. Sitta**, F. Smallenburg, R. Wittkowski & H. Löwen, *Liquid crystals of hard rectangles on flat and cylindrical manifolds*, Phys. Chem. Chem. Phys. (2018), DOI: 10.1039/C7CP07026H

In Veröffentlichung I und Veröffentlichung III haben sich alle Autoren auf eine geteilte Erstautorschaft der mit * gekennzeichneten Autoren geeinigt. Alle Publikationen werden in diesem Kapitel einzeln aufgeführt und mein eigener Beitrag jeweils explizit angegeben.

Veröffentlichung I Diffusion of macromolecules in a polymer hydrogel: from microscopic to macroscopic scales

D. Sandrin*, D. Wagner*, C. E. Sitta*, R. Thoma, S. Felekyan, H. E. Hermes, C. Janiak, N. de Sousa Amadeu, R. Kühnemuth, H. Löwen, S. U. Egelhaaf & C. A. M. Seidel,

Diffusion of macromolecules in a polymer hydrogel: from microscopic to macroscopic scales,
Phys. Chem. Chem. Phys. **18**, 12860 (2016),
veröffentlicht durch *The Royal Society of Chemistry*.

Digital Object Identifier (DOI): 10.1039/C5CP07781H

* Diese Autoren haben in gleichem Maß zur Publikation beigetragen und teilen die Erstautorschaft.

Stellungnahme zum eigenen Beitrag

H.E.H., N.A., R.K., H.L., S.U.E. und C.A.M.S. haben die Idee für das Forschungsprojekt entwickelt und es betreut.
D.S., D.W. und R.T. haben die experimentellen Proben vorbereitet.
Die Experimente wurden von D.S. und R.K. (MFIS), D.W. (MTI) und R.T. (NMR) durchgeführt.
S.F. hat die Programme zur MFIS-Auswertung entwickelt.
D.S., D.W., R.T., S.F., N.A. und R.K. haben die experimentellen Daten analysiert.
Ich habe die Brownsche Dynamik Simulation implementiert und durchgeführt sowie Abb. 9 erstellt.
Alle Autoren haben die Ergebnisse interpretiert und das Manuskript geschrieben.

Lizenzhinweise und Copyright

PCCP

PAPER

View Article Online
View Journal | View Issue

Cite this: *Phys. Chem. Chem. Phys.*, 2016, **18**, 12860

Diffusion of macromolecules in a polymer hydrogel: from microscopic to macroscopic scales†

D. Sandrin,‡[a] D. Wagner,‡[b] C. E. Sitta,‡[c] R. Thoma,[d] S. Felekyan,[a] H. E. Hermes,[b] C. Janiak,[d] N. de Sousa Amadeu,[d] R. Kühnemuth,*[a] H. Löwen,*[c] S. U. Egelhaaf*[b] and C. A. M. Seidel*[a]

Received 16th December 2015,
Accepted 17th March 2016

DOI: 10.1039/c5cp07781h

www.rsc.org/pccp

To gain insight into the fundamental processes determining the motion of macromolecules in polymeric matrices, the dynamical hindrance of polymeric dextran molecules diffusing as probe through a polyacrylamide hydrogel is systematically explored. Three complementary experimental methods combined with Brownian dynamics simulations are used to study a broad range of dextran molecular weights and salt concentrations. While multi-parameter fluorescence image spectroscopy (MFIS) is applied to investigate the local diffusion of single molecules on a microscopic length scale inside the hydrogel, a macroscopic transmission imaging (MTI) fluorescence technique and nuclear magnetic resonance (NMR) are used to study the collective motion of dextrans on the macroscopic scale. These fundamentally different experimental methods, probing different length scales of the system, yield long-time diffusion coefficients for the dextran molecules which agree quantitatively. The measured diffusion coefficients decay markedly with increasing molecular weight of the dextran and fall onto a master curve. The observed trends of the hindrance factors are consistent with Brownian dynamics simulations. The simulations also allow us to estimate the mean pore size for the herein investigated experimental conditions. In addition to the diffusing molecules, MFIS detects temporarily trapped molecules inside the matrix with diffusion times above 10 ms, which is also confirmed by anisotropy analysis. The fraction of bound molecules depends on the ionic strength of the solution and the charge of the dye. Using fluorescence intensity analysis, also MTI confirms the observation of the interaction of dextrans with the hydrogel. Moreover, pixelwise analysis permits to show significant heterogeneity of the gel on the microscopic scale.

1. Introduction

The motion of macromolecules through disordered matrices is of great importance in analytical and preparatory techniques (chromatography,[1] expansion microscopy,[2] genomics,[3] biofilms[4]) as well as in biomedical (imbibition,[5] controlled drug delivery,[6–9] flow control,[10] implantable devices,[9] contact lenses,[11] cellular and tissue engineering[12,13]) and technical applications (enhanced oil recovery[14,15]). From a fundamental point of view, precise measurements for model systems are needed to reveal the underlying transport principles.[16–19] It is known that the presence of obstacles slows down the transport and that this is more pronounced for larger molecules. However, the basic underlying mechanisms and their effects are not yet completely understood. In particular, the motion of particles through a gel matrix represents an intricate problem as the gel matrix can respond to the particle motion. A nontrivial dependence of the diffusion behavior on both the host and the guest, *i.e.* the gel and the diffusing particles, is expected. The behavior of the host is mainly characterized by a typical pore size. However, topological constraints resulting from the nontrivial and dynamically changing connectivity of the pores[20] also have an impact on the diffusion of the guest molecules. This connectivity is expected to result in a wide spread in the translocation rate of the individual particles. The translational rate is also influenced by the structural properties of the guest molecules

[a] *Institut für Physikalische Chemie II, Molekulare Physikalische Chemie, Heinrich-Heine-Universität, Universitätsstr. 1, 40225 Düsseldorf, Germany. E-mail: ralf.kuehnemuth@hhu.de, cseidel@hhu.de*
[b] *Institut für Experimentelle Physik der Kondensierten Materie, Heinrich-Heine-Universität, Universitätsstr. 1, 40225 Düsseldorf, Germany. E-mail: stefan.egelhaaf@hhu.de*
[c] *Institut für Theoretische Physik II: Weiche Materie, Heinrich-Heine-Universität, Universitätsstr. 1, 40225 Düsseldorf, Germany. E-mail: hlowen@hhu.de*
[d] *Institut für Anorganische Chemie und Strukturchemie, Heinrich-Heine-Universität, Universitätsstr. 1, 40225 Düsseldorf, Germany*

† Electronic supplementary information (ESI) available. See DOI: 10.1039/c5cp07781h

‡ These authors have contributed equally to this work.

such as hydrodynamic radius, shape, molecular weight or charge distribution. The significance of sieving, entanglements, (chemical) interactions, partitioning, oscillation of pores *etc.* is still controversially discussed.[21–27] In addition, the average size of the pores is also under debate.[23,28–34]

It is accepted that the mesh sizes in polymer hydrogels depend on the specific gel preparation such as (I) the mass concentration of polymeric material in the reaction solution, [T], and (II) the weight fraction of cross-linker, C_R, but the absolute average size of the pores is subject to debate.[23,28–34] Considering hydrogels (0.035 g ml^{-1} $\leq$ [T] $\leq$ 0.065 g ml^{-1}, $0.02 \leq C_R \leq 0.05$) with similar compositions to the one studied here ([T] = 0.04 g ml^{-1}, C_R = 0.035), different methods give very different results for the pore sizes (please note that the numbers given for [T] and C_R, multiplied by 100, correspond to the parameters %T and %C, respectively, which were used in the above publications). The reported pore sizes range from 2.00–2.25 nm (chromatography[28]) through 5–9 nm (electrophoresis studies in the 1960s and 1980s[29,30]) and 60–156 nm (electrophoresis studies in 1991[23,31]) up to values of 2–20 μm (for the largest pores found by scanning electron microscopy[32–34]). This also complicates any systematic study of particle diffusion in a well-characterized model system, which however is important to understand the principles of translocation and to test theoretical approaches.

Here we study polymeric dextran molecules diffusing through a polyacrylamide hydrogel without interfering with the sample during the measurements. We use dextrans as tracer particles, because they have a good water solubility, low toxicity, relative inertness and are flexible polymers. Moreover, they are commercially available over a broad range of molecular weights and hence sizes. Most dextrans can be also obtained as derivatives labelled with fluorescent dyes (fluorescein sodium salt (FLU), Alexa Fluor 488 (A488), tetramethylrhodamine (TMR)). The molecular weight of the dextrans is varied between M_w = 3 kDa to 2000 kDa. For comparison the diffusion of free dyes, FLU, A488 and TMR is studied in our hydrogel, too. To investigate the interactions of the particles with the hydrogel in more detail, we study the influence of solution conditions like pH-value, salt and tracer particle concentrations. Using three complementary methods, multiparameter fluorescence image spectroscopy (MFIS), macroscopic transmission imaging (MTI) with fluorescence detection and nuclear magnetic resonance (NMR), we measure the long-time diffusion coefficient of the fluorescently labelled and unlabelled probe particles, respectively. MFIS also allows us to detect the heterogeneity of the gel. The data are compared to a model by Ogston[35] which predicts the dynamical hindrance in a network of randomly distributed fibers due to geometric confinement. The Ogston model provides a simple analytical formula for the particle dynamics *via* an effective excluded volume. Another theoretical approach is to perform computer simulations. As modeling a hydrogel on an atomic basis over huge length- and timescales is computational unaffordable, various different model assumptions including different degrees of molecular details have been used in the past.[36–48] The most detailed model for the gel matrix was used by Linse and coworkers[36–39] and Holm and coworkers[40–42] who resolved the monomers of the polymer chains connecting the nodes explicitly within a bead-spring model. Within their approach the swelling behavior of the gels was explored but the diffusion of tracer particles within the gel network was not addressed. In a more coarse-grained approach, the matrix was described by either a static network of points,[43] rods,[43,44] or chains[45] or as fluctuating network of spheres[46,47] which indeed allows for the computation of tracer diffusion. Following the latter coarse grained approach of Zhou and Chen,[47] we perform Brownian dynamics (BD) simulations representing three different levels of complexity to resolve the different physical effects that are operating in the hydrogel. Our simulation study provides a simple and systematic framework, taking into account the flexibility of the matrix particles, the effective dextran–matrix excluded volume and finding strong indications for effective attractive interactions. Our combined results provide a consistent picture of polymers diffusing through a hydrogel matrix and may serve to test more quantitative theories and other experimental approaches.

2. Materials and methods

2.1. Samples

2.1.1. Hydrogel: a polymer matrix in an aqueous environment. The polyacrylamide (PAAm) hydrogels were formed by copolymerization of acrylamide (AAm, monomer) with the tetrafunctional cross-linking agent *N*,*N*′-methylenebis(acrylamide) (BIS), using ammonium peroxodisulphate (APDS) and tetramethylethylenediamine (TEMED) as redox initiators. The monomer and cross-linker were both purchased from Sigma-Aldrich, APDS from Roth and TEMED from Merck. All components were used without further purification. AAm, BIS and APDS were separately dissolved in deionized and filtered water and cooled to 4 °C. The individual solutions were then mixed at a low temperature. The reaction mixture contained 75 mg of AAm, 2.71 mg of BIS, 6 mg of APDS and 10 μl of TEMED in a total volume of 2 ml which corresponds to a molar ratio of cross-linker to monomer of 1 : 60. The total monomer concentration, defined as the mass concentration of AAm and BIS in the total reaction volume, is [T] = 0.04 g ml^{-1} and the weight fraction of cross-linker with respect to the total mass of the polymeric material (AAm and BIS) is C_R = 0.035.

After mixing, the solution was transferred to Teflon molds and allowed to warm up and react at room temperature. After one to two hours, polymerization was complete and the hydrogel was transferred into a larger container filled with deionized water. The gel was left for five days to ensure that the hydrogel swells to equilibrium. The excess water was exchanged daily to wash out residual chemicals that had not reacted in the gelation process.[49]

Discs with a radius $R_d \approx 0.3$ cm were cut from the hydrogels using a simple stamp. In corresponding MTI and MFIS experiments, samples cut from one gel block were used. For the NMR measurements, the gelation process was carried out in cylindrical

Teflon molds ($R_d \approx 0.5$ cm, height 5 cm). The hydrogels were then transferred into a container filled with deuterium oxide.

The hydrogel was characterized by determining the polymer volume fraction in the fully swollen state, φ, the average molecular weight between cross-linking points, M_c, and the mesh size, ξ. The polymer volume fraction of the hydrogel in the swollen state φ was calculated directly from eqn (1):[50,51]

$$\varphi = \frac{V_p}{V_{gel}} = \frac{m_p \rho_{H_2O}}{m_p \rho_{H_2O} + m_{H_2O} \rho_p} \quad (1)$$

where V_p is the volume of the dry polymer (PAAm), V_{gel} is the volume of the hydrogel after equilibrium swelling, m_p is the mass of the polymer, m_{H_2O} is the mass of water in the swollen gel and ρ_p and ρ_{H_2O} are the densities of polymer and water, respectively.

The mass of the fully swollen hydrogel was measured after removing the liquid on the surface of the hydrogel with a pipette. It was then dried at 40 °C under vacuum for at least 6 h until constant weight was reached to determine m_p. The experiment was repeated for different pieces of hydrogel, and the mass fraction was converted into volume fraction using the known polymer density (ρ_p = 1.3 g cm^{-3}).[52]

The theoretical molecular weight of the polymer between cross-links M_c is related to the degree of cross-linking in the hydrogel, X (*i.e.*, the molar ratio of cross-linker to monomer) and the molecular weight of the repeating units ($M_{r,AAm}$ = 71.1 g mol^{-1}):[51,53]

$$M_c = \frac{M_r}{2X} \quad (2)$$

The mesh size, ξ, which characterizes the space between macromolecular chains can be calculated using:[50,54,55]

$$\xi = \varphi^{-1/3} \zeta \left(\frac{C_n 2 M_c}{M_r} \right)^{1/2} \quad (3)$$

where C_n is Flory's characteristic ratio ($C_{n,AAm}$ = 2.72) and ζ is the carbon–carbon bond length (ζ = 0.154 nm).[56] This calculation assumes ideal solvent quality, homogeneous cross-linking densities and Gaussian distribution of chain lengths.

We characterized the polyacrylamide hydrogels as used in these experiments, *i.e.* in water and in a 20 mM potassium carbonate buffer at pH 10. The results are shown in Table 1.

2.1.2. Diffusing polymeric guest molecules. The dextrans (Table 2) and free dyes were purchased from Invitrogen. For the NMR experiments, unlabelled dextrans were dissolved in deuterium oxide with a purity of 99.9% from Deutero GmbH. For the remaining experiments, dextrans conjugated with Alexa Fluor 488 (A488) or tetramethylrhodamine (TMR) were dissolved in deionized water. To exclude fluorescence blinking due to protonation–deprotonation dynamics, dextrans labelled with fluorescein (FLU) were prepared in potassium carbonate buffer at pH = 10, (20 mM) and the fluorescence measurements were conducted after addition of 100 μM Trolox (Sigma-Aldrich) to avoid photobleaching of the dye.

Table 1 Polymer volume fraction in the swollen state (φ), molecular weight of the polymer between cross-links (M_c) and mesh size (ξ) for the PAAm hydrogel in water and in potassium carbonate buffer 20 mM at pH 10. The errors are the standard errors of repeated measurements of the polymer volume fraction

	PAAm in water	PAAm pH 10
φ	0.0390 ± 0.0004	0.0150 ± 0.0001
M_c [g mol^{-1}]	2141	2141
ξ [nm]	5.7 ± 0.1	7.8 ± 0.1

Table 2 Overview of dyes and dextrans of different molecular weights, M_w, as obtained from manufacturer (for labelled dextrans already including the dye) and their naming convention. The dextrans were either unlabelled or conjugated with one of three different dyes: Alexa Fluor 488, tetramethylrhodamine and fluorescein. For more detailed information see S1.1 and S1.2 (ESI)

M_w [kDa]	Unlabelled	Alexa fluor 488	Tetramethylrhodamine	Fluorescein
0.33				FLU
0.39			TMR	
0.53		A488		
3	D3	A488-D3	TMR-D3	FLU-D3
10	D10	A488-D10	TMR-D10	FLU-D10
40	D40		TMR-D40	FLU-D40
70			TMR-D70	
500				FLU-D500
2000			TMR-D2000	

To investigate the local environment and possible probe–polymer interactions inside the gel matrix, we measured the most polar dye attached to one of the smaller dextrans, A488-D10 under five different conditions: (i) H_2O, (ii) aqueous $KClO_4$ solution (10 mM, 20 mM, 40 mM, and 60 mM), (iii) aqueous KCl solution (20 mM), (iv) aqueous potassium carbonate buffer (20 mM) at pH = 7, and (v) at pH = 10.

2.1.3. Addition of polymeric guest molecules to the hydrogel. For MFIS experiments, each hydrogel disc was placed in a chambered cover glass (Lab-Tek™, Thermo Fisher Scientific, USA), incubated with guest molecule solution (400 μl in total) and allowed to reach equilibrium before the measurement was started (2 to 7 days depending on dextran size). When electrolyte solutions were used, the solution was exchanged approximately every 12 h during the incubation period to ensure defined concentrations.

In the MTI experiments, the initial particle concentration in the hydrogel was 0 and the concentration in the surrounding solution was varied between 0.1 and 10 μM. The hydrogel matrix was contacted with the particle (dye or dextran) solution at the beginning of the experiments and the diffusion of guest molecules from the solution into the hydrogel was studied.

For NMR measurements, the hydrogel cylinders were incubated with concentrated amino dextran solution in deuterium oxide for at least 48 h. The samples were then carefully transferred into NMR tubes ensuring that the gel texture was not destroyed. Concentrations below 1 mM were used in order to avoid aggregation. Bubbles were successfully avoided.

2.2. Measurement methods

2.2.1. Multiparameter fluorescence image spectroscopy (MFIS). All measurements were conducted on a confocal fluorescence microscope (FV1000 Olympus, Hamburg, Germany),

which had been modified to allow time-resolved experiments.[57,58] A488 and FLU were excited using a polarized pulsed diode-laser (LDH-D-C-485, PicoQuant, Berlin, Germany) at 485 nm, while for TMR a supercontinuum laser (SuperK Extreme, NKT Photonics, Birkerød, Denmark) at 555 nm was employed. Laser light was directed into a 60× water immersion objective (NA = 1.2) by a dichroic beam splitter and focused into the sample close to the diffraction limit. The light emitted was collected by the same objective and separated into two polarizations (parallel and perpendicular) relative to the excitation beam. The fluorescence signal was further divided into two spectral ranges (BS 560, AHF, Tübingen, Germany). Bandpass filters for A488/FLU and TMR fluorescence (HC 520/35 and HC 607/70, AHF), were placed in front of the detectors. The signal from single photon sensitive detectors (PDM50-CTC, Micro Photon Devices, Bolzano, Italy and HPMC-100-40, Becker&Hickl, Berlin, Germany, respectively) was recorded photon-by-photon with picosecond accuracy (HydraHarp400, PicoQuant) and analyzed using custom software (LabVIEW based). The temperature during all measurements was 22.5 ± 0.5 °C and the concentration of the dextrans was adjusted between 0.05 and 3 nM, depending on their different degree of labelling.

The sample was mounted on a piezo-controlled x–y scanner (P-733.2CL, Physik Instrumente, Karlsruhe, Germany) and moved perpendicular to the optical axis. It was moved in a stepwise manner to permit multiparameter fluorescence detection at defined locations. The pixel size is defined by the step size of the scan (in our experiments 10.00 μm) while photons are collected from the confocal detection volume only (V_{det} = 0.55 fl). The integration time per pixel was 30 min and the complete image contains 18 pixels (probed spots).

2.2.2. Macroscopic transmission imaging (MTI). The macroscopic transmission imaging experiments were performed using a custom-built imaging apparatus similar to that described previously.[59] The sample was illuminated by a parallel beam of light from an LED lamp (CoolLED, center wavelength of 490 nm) whose wavelength was chosen to excite the fluorescent particles in the sample. Using a dichroic mirror that transmits wavelengths above and reflects wavelengths below 502 nm, the transmitted light was split into excitation light (bright-field transmission image) and emitted light from the fluorophores (fluorescence image). The images were then focused onto separate CCD cameras. Additional fluorescence filters (excitation filter: 480/25, emission filter: longpass LP 520) were applied. The hydrogel discs were placed between two horizontally held glass plates with a fixed distance between the plates of 1.5 mm using aluminum spacers. This distance was chosen to ensure that the gels were compressed as little as possible but still in contact with both glass plates. The particle solution was added around the gel discs and allowed to diffuse into the gel matrix. The image collection time was varied between 5 s at the beginning and up to 300 s at the end of a measurement. Images were collected for 3 to 72 h. The sample cells were sealed to ensure that the solvent did not evaporate and measurements were performed at room temperature (23 °C).

2.2.3. Nuclear magnetic resonance (NMR). A Bruker AVANCE DRX-500 NMR spectrometer operating at 500 MHz for ^{1}H was used. The spectrometer was equipped with a Bruker Great 1/10 gradient amplifier and a Bruker selective inverse (SEI) probe with *z*-gradient coils. The gradient amplitudes were calibrated using dodecane, 1-pentanol and water as standard samples.[60] The temperature sensor was calibrated using methanol as described by van Geet.[61] All diffusion measurements were acquired by using stimulated echo with bipolar gradient pulses (pulse program name STEBPGP).[62,63] This sequence was also followed by a WATERGATE sequence to suppress the water signal.[64,65]

In each experiment, the magnetic field gradient strength of the bipolar pulses was linearly arrayed along 16 values from 10 to 60 G cm^{-1} while all other parameters were kept constant. The gradient pulse length, δ and the diffusion delay, Δ_N, were chosen such that the echo signal was suppressed considerably.

The diffusion coefficients of unlabelled aminodextrans in hydrogels and in deuterium oxide were measured at 23 °C in NMR sample tubes of 5 mm diameter. Dextran concentrations depended on the dextran's molecular weight and varied from 3.0 M for the 3 kDa dextran to 0.3 M for the 40 kDa dextran to avoid agglomeration in solution. We performed several diffusion measurements with each sample, varying the key parameters δ and Δ_N. Our experience showed that this is a good practice which helps identifying artifacts affecting the experiments or errors in the processing routines. The diffusion delays, Δ_N were chosen between 0.1 and 2.0 s and the gradient pulse widths, δ were between 600 and 1400 μs. Several combinations of Δ_N and δ were applied within those ranges. Later examination revealed high agreement among all those measurements, indicating good reproducibility.

2.3. Analysis methods

2.3.1. Multiparameter fluorescence image spectroscopy (MFIS). The recorded MFIS data can be correlated to yield correlation curves (fluorescence correlation spectroscopy, FCS, is part of the MFIS). Those fluorescence correlation curves that were measured inside the hydrogel usually exhibited multiple overlapping bunching terms in the time regime of the diffusion process. To establish the number of independent species, *M*, needed in the model function to reproduce the data, we fitted a distribution of diffusion coefficients applying the maximum entropy method (MEMFCS).[66] Having determined *M* we then fitted a model function containing *M* diffusion terms (eqn (4)):

$$G(t_c) = 1 + \frac{1}{N}\sum_{i=1}^{M} x_i \left(\left(1+\frac{t_c}{t_{d,i}}\right)\sqrt{1+\frac{t_c}{(z_0/\omega_0)^2\cdot t_{d,i}}}\right)^{-1} \times \left(1 - A_T + A_T \cdot e^{-\frac{t_c}{t_T}}\right) \quad \text{with} \quad \sum_{i=1}^{M} x_i = 1 \tag{4}$$

For species with identical brightness, x_i represents their true molecular fractions. In this case, *N* is the number of molecules in the singlet state in the detection volume element and t_c is the correlation time. The model assumes a three-dimensional Gaussian-shaped volume element with spatial distribution of

the detection probabilities $w(x,y,z) = \exp(-2(x^2 + y^2)/\omega_0^2) \exp(-2z^2/z_0^2)$. The $1/e^2$ radii in x and y or in z direction are denoted by ω_0 or z_0, respectively. The characteristic diffusion time is $t_d = \omega_0^2/4D$, with the translational diffusion coefficient D. The confocal detection volume, V_{det} is calculated as follows: $V_{det} = \pi^{3/2} z_0 \omega_0^2$.

Basic photophysical processes such as triplet transitions which result in temporary dark states are accounted for by an additional bunching term. Here A_T and t_T represent the triplet population and the triplet relaxation time.

The correlation curves for A488- and TMR-dextrans in water and most FLU-dextrans in carbonate buffer were fitted pixel by pixel, the remaining samples image-integrated. At mean irradiances in the focus of 1.2 kW cm^{-2}, A488- and TMR-samples did not exhibit noticeable triplet populations ($A_T < 0.01$), only fluorescein showed fluorescence bunching in the µs regime at even lower irradiances of 0.4 kW cm^{-2}. For pixelwise analysis, error bars for t_d (and equivalently for D) were calculated as standard error of the mean while for single point (*i.e.* solution) or image integrated measurements a bootstrapping procedure was applied.

Diffusion coefficients can be derived from the extracted diffusion times (t_d) provided that the size and shape of the confocal detection volume element are characterized. In practice, a photostable reference dye with known diffusion properties is used to calibrate the system. In the present case, we chose rhodamine 110 (Rh110). Thus all presented diffusion coefficients derived from FCS are based on the reported value of $D_{Rh110} = (4.3 \pm 0.3) \times 10^{-6}$ cm^2 s^{-1} at 295.65 K in dilute aqueous solutions.[67] The characteristic diffusion time of Rh110 in deionized water was $t_d = 30$ µs with day-to-day variations of less than 5%. Due to increased aberrations with changes in the refractive index upon addition of salt, a systematic increase of t_d was observed (*e.g.* $t_d = 33$ µs for Rh110 in 20 mM potassium carbonate buffer at pH 7 and pH 10, respectively). The longer wavelength required for the TMR experiments caused an increase in focus area $\pi\omega_0^2 = t_d 4\pi D$ and thus of t_d of about 30%, as expected from the changed diffraction limit.

A variety of possible artifacts have been reported that could cause uncertainties in translational diffusion measurements by FCS.[68] In particular optical saturation effects are known to distort the detection volume element and thus alter the observed average dwell times of the fluorophores. These effects have been minimized by keeping the excitation power low and by performing reference measurements under identical conditions. Low excitation power also diminishes the probability of photobleaching. Successful minimization of this effect is confirmed by the observation of extremely slow diffusing molecules with dwell times of up to 1 s.

A further possible artifact, focal distortions due to a refractive index mismatch (below 0.01, see S1.6, ESI†) is estimated to result in a small corresponding error in D (below 1%[69]). This is supported by the good agreement of the FCS data with the independent MTI and NMR results (see below). Additionally, the possible refractive index mismatch between solution and hydrogel was checked using FCS and found to be negligible. No readjustment of the correction collar setting on the objective was required after switching the sample from pure water to hydrogel (see S1.6, ESI†).

The steady state anisotropy, r, which is another parameter detected by MFIS is defined *via* the intensities of the fluorescence signal polarized parallel ($F_\parallel$) and perpendicular ($F_\perp$) with respect to the excitation polarization. As described by Koshioka *et al.*,[70] the fluorescence signal recorded with a confocal microscope is slightly depolarized by the objective due to its high numerical aperture. To account for this experimental artifact, correction factors l_1 and l_2 have been introduced:[70]

$$r = \frac{GF_\parallel - F_\perp}{(1 - 3l_2)GF_\parallel + (2 - 3l_1)2F_\perp} \quad (5)$$

The correction factors l_1 and l_2 as well as the factor G, that compensates for the slightly different detection efficiencies of the two detection channels, were determined experimentally using the reference dyes enhanced green fluorescent protein (EGFP)[58] or rhodamine 110 and TMR, respectively, ($l_1 = 0.0308$, $l_2 = 0.0368$, $G = 0.99$). In detail, the G-factor is defined as the ratio of the detection efficiencies between perpendicular and parallel polarized fluorescence light. The fluorescence signal F is obtained from the detected signal by subtracting the appropriate background (scattering) measured in clean water or an unloaded gel.

2.3.2. Macroscopic transmission imaging (MTI). We found a linear relation between fluorescence intensity and concentration in the concentration range of 0.1 to 10 µM for all samples. Thus, we can directly determine the relative change in concentration from the image intensity. Especially for the larger dextran molecules, equilibration between the hydrogel and the surrounding solution takes several days. However, for most samples, it was found that measurement times of about 24 h were sufficient to allow diffusion coefficients to be extracted from the data. Some additional longer measurements were performed to capture the long time behavior. Even though the dyes used were relatively photostable and the incident intensity was reduced as much as possible, some photobleaching could be seen for these long measurement times. Thus, a photobleaching correction as described in ref. 71 and 72 was applied: the change in the normalized intensity F of an area in the solvent far outside the hydrogel, where no significant change in the concentration is expected, could be fitted with a double exponential function:

$$\frac{F(t)}{F(t=0)} = Pe^{-pt} + Qe^{-qt} \quad (6)$$

The intensity of the region of interest in the gel of every image was then corrected by dividing the original value by the one extracted from the bleach curve.

The hydrogel discs had a quasi-two-dimensional geometry and homogeneous radial diffusion was observed. Thus, by azimuthally averaging all pixels that are a certain distance away from the gel–reservoir interface, a concentration profile for every time step could be determined. Comparison of the concentration profiles with diffusion equations, including appropriate boundary conditions, yields diffusion coefficients (see Section 3.2.1).

The hydrogels were fully swollen and in equilibrium before the measurements and no change in the hydrogel size was expected. However, for some samples we observed a decreasing gel radius of up to 6% within the first hours of the experiments in the bright-field transmission images and the change in radius was taken into account in the analysis. The reason for this is not clear. A change in temperature or an expansion of the sample cell and with that a slight increase in sample thickness might play a role.[73]

2.3.3. Nuclear magnetic resonance (NMR). As is usual practice, the diffusion coefficients D were obtained by fitting the echo amplitudes (integral of the signals between 2.8 and 4.4 ppm) to the following equation:[74,75]

$$\frac{E_i}{E_0} = \exp\left[-D(\gamma g_i \delta)^2 \left(\Delta_N - \frac{\delta}{3} - \frac{\tau_N}{2}\right)\right] \quad (7)$$

where E_i and E_0 are the echo intensities at increment i and with zero gradient applied, γ is the gyromagnetic ratio, g_i is the gradient amplitude at increment i, δ is the gradient pulse width, Δ_N is the diffusion delay and τ_N is the delay between the two magnetic field gradient pulses laying at one side of the echo pulse sequence. For the purpose of comparison, the diffusion coefficients measured in D_2O were recalculated for H_2O using the known viscosities of both solvents.[76]

2.4. Models for Brownian dynamics simulations

Brownian dynamics simulations were used to calculate the diffusion coefficients of dextran particles within the polymer network. Inspired by previous investigations,[46,47] we considered simple models of effective spheres for the matrix particles and the dextrans. For this, we used a microscopic model resolving the matrix explicitly and coarse-graining the diffusing polymer coil as an effective soft sphere. There are further underlying model assumptions: (i) the polymer matrix is not resolved on the monomer level, (ii) the matrix structure is derived from a periodic structure, and (iii) explicit hydrodynamic interactions caused by the solvent are ignored.

In order to obtain a systematic insight, the flexibility of the polymer matrix and the softness of the dextran–matrix interaction were modeled on three different levels. A schematic illustration of the models is shown in the Results section (see Section 3.2.2 and Fig. 9). On the first level (also referred to as model 1 in the following), the matrix particles were fixed on a periodic simple-cubic lattice with lattice constant a providing static steric obstacles for the diffusing dextran molecules. For simplicity, the latter were modeled as effective spheres. On this crude level any fluctuations in the pore sizes were neglected. The repulsive steric interaction between an obstacle i at position $\vec{s}_i$ and another particle j (either tracer or obstacle) at position $\vec{s}_j$, separated by the distance s_{ij}, was modeled as in ref. 47 with a truncated and shifted repulsive Lennard Jones potential (also known as WCA-potential):

$$U_s(s_{ij}) = 4\varepsilon_s\left[\left(\frac{\sigma_{ij}}{s_{ij}}\right)^{12} - \left(\frac{\sigma_{ij}}{s_{ij}}\right)^{6} + \frac{1}{4}\right] \quad (8)$$

where $\varepsilon_s = 1k_BT$ ($\sim 4.05 \times 10^{-21}$ J at 20 °C) and the additive diameter $\sigma_{ij} = 2R_{obst}$ for the obstacle–obstacle-interaction and $\sigma_{ij} = R_{obst} + R_h$ for the interaction between a matrix obstacle and a tracer of radius R_h. The cutoff was set at the potential's minimum at $l_{ij} = 2^{1/6}\sigma_{ij}$.

For the second level (model 2), we introduced fluctuating matrix particles. The network connectivity was ensured by coupling neighboring matrix particles by harmonic springs. For the harmonic spring potentials, we used Hooke's law:

$$U_{sp}(s_{ij}) = 0.5k(s_{ij} - s_{0,ij})^2 \quad (9)$$

for two matrix particles i and j with their distance at rest $s_{0,ij}$. Setting $k = 2k_BT/(2R_{h,D3})^2$ (~ 0.6 mJ m^{-2}) allowed the dextran D3 to push a gap of its own diameter $2R_{h,D3}$ through two neighboring matrix particles in rest positions when overcoming an energy of $1k_BT$. This parameter is kept fixed in all simulations. Moreover the matrix particles were exposed to thermal fluctuations and repelled each other and the dextran particles *via* steric interactions as in model 1 (eqn (8)). To broaden the pore size distribution, the matrix particles were randomly shifted up to half the lattice constant a in each direction with respect to their initial positions before attaching undistorted springs between neighboring matrix particles.

At a third level of modeling, two different extensions were tested by changing the dextran–matrix interactions. In model 3a, we replaced the WCA potential for the steric interactions with a softer effective Gaussian potential which is a good model for penetrating polymer coils of different architecture:[77–79]

$$U_G(s_{ij}) = \varepsilon_G \exp\left(-\frac{s_{ij}^2}{2b^2}\right) \quad (10)$$

with $b^2 = (R_i + R_j)^2/(2\ln(\varepsilon_G/(k_BT)))$. This relation keeps the potential at $s_{ij} = R_i + R_j$ for $1k_BT$. We used $\varepsilon_G = 12k_BT$ (for more details see S11, ESI†).

In model 3b, an attractive shell with the size of a typical fluorescent dye's radius ($R_{D0} = 0.55$ nm) was added to the steric repulsion to account for a possible weak sticking of the dextrans to the matrix using a cosine function for a smooth transition:

$$U_{sp}(s_{ij}) = \begin{cases} 4\varepsilon_s\left[\left(\frac{\sigma_{ij}}{s_{ij}}\right)^{12} - \left(\frac{\sigma_{ij}}{s_{ij}}\right)^{6} + \frac{1}{4}\right] - \varepsilon_a & s_{ij} \le l_{ij} \\ -\frac{\varepsilon_a}{2}\left[\cos\left(\frac{\pi(s_{ij} - l_{ij})}{R_{D0}}\right) + 1\right] & l_{ij} < s_{ij} \le l_{ij} + R_{D0} \\ 0 & l_{ij} + R_{D0} \le s_{ij} \end{cases} \quad (11)$$

We obtained $\varepsilon_a = 3.0 \pm 0.3\ k_BT$ as fitted value in both investigated systems. This value seems reasonable as it should cause a significant slowdown of the dextrans' motion while still allowing a thermal escape out of the shells.

By tracking the tracer's trajectories, the mean square displacements can be calculated as:

$$\Delta s^2(t) = \langle(\vec{s}(t_0 + t) - \vec{s}(t_0))^2\rangle \quad (12)$$

For a given sufficiently large elapsed time t, the long-time diffusion coefficients could then be extracted as:[80,81]

$$D = \lim_{t\to\infty} \frac{1}{6}\frac{\mathrm{d}}{\mathrm{d}t}\Delta s^2(t) \qquad (13)$$

such that the hindrance factors are D/D_0.

For a given value of a, which sets the mean pore size, the hindrance factors for all tracer particles were calculated and this set of simulation data was compared to the experimental data. An optimal value for a was found by the best fit, using a as the single fitting parameter. Only in model 3b, ε_a was used as a second fitting parameter. For more technical details, see S11 (ESI†).

3. Results and discussion

The different experimental techniques used here allowed us to estimate the precision of the measurements in different ways. In MTI and NMR, the experiments are conducted by averaging over one gel, calculating therefore the dispersion of the data between different gels.

In MFIS we are able to detect two kinds of dispersion of the data: (i) we measured different spots within the same gel (pixelwise analysis) and (ii) we executed measurements between different gels (different data points in Fig. 12b).

It is known that the hydrogels in practice always exhibit an inhomogeneous cross-link density distribution, causing spatial heterogeneity.[82,83] The scattering of experimental data from various independent measurements, beyond the shot noise limits of the single measurements, indicates the heterogeneity in the gel structure. Spatial heterogeneity on the macroscopic scale is detected by pixelwise analysis. Different locations within the same gel display slightly different results. These feature were visible in all MFIS studies reported below.

3.1. Several populations of guest molecules detected by MFIS

FCS. In contrast to the single diffusion times observed in solution, for most of the gel samples we have observed that up to three independent diffusion times are needed to fit the FCS curves. Differently diffusing species, extending from free molecules just hindered by the limiting pore size ($t_d \sim 410$ μs) up to temporarily trapped particles ($t_d > 10$ ms) were found (SI2–4, ESI†). Fig. 1a displays a set of image-integrated correlation curves for A488-D10 at different electrolyte conditions which reveal the decreasing fraction of slowly diffusing temporarily trapped particles for increasing salt concentration. Temporary sticking and accumulation of the probe molecules in the hydrogel are indicated by time trace analysis (Fig. 4a). Such tracer–hydrogel interactions already have been studied in the past, showing different effects depending on the chemical structure of the gel, the solvent and the nature of the tracer.[21,25,27]

Interestingly, Vagias and coworkers[21] also found interactions between the hydrogel and different tracers when employing FCS. Although they used another hydrogel than in our study, the different fluorescence intensity between gel and solution is clearly shown by them.

A simple binding model was applied to describe the observed equilibrium fractions of mobile and trapped probe molecules (x_{bound}), where f_{free} is the activity coefficient for free molecules and K_d' the effective binding constant (see S1.7, ESI†):

$$x_{bound} = \frac{f_{free} K_d'}{1 + f_{free} K_d'} \qquad (14a)$$

It was assumed that the activity of the freely diffusing (mobile) species is most affected by the ionic strength of the solvent. The Debye–Hückel equation[84] describes the dependency of the activity coefficient, f_{free}, on the charge, Z_i, the effective radius of the ion, R_i, and the ionic strength, I, in the limit of low salt concentrations:

$$f_{free} = 10^{-\frac{AZ_i^2\sqrt{I}}{1+BR_i\sqrt{I}}} \qquad (14b)$$

with tabulated values[84] for the constants $A = 0.507$ mol$^{-1/2}$ dm$^{3/2}$ and $B = 3.28$ nm^{-1} mol$^{-1/2}$ dm$^{3/2}$ for aqueous solution at 22.5 °C. A combination of eqn (14a) and (14b) can be fit to the equilibrium fraction of trapped molecules as a function of the ionic strength. The fit shown in Fig. 1b yields $Z_i \approx 3$, which is in good agreement with the estimated mean number of

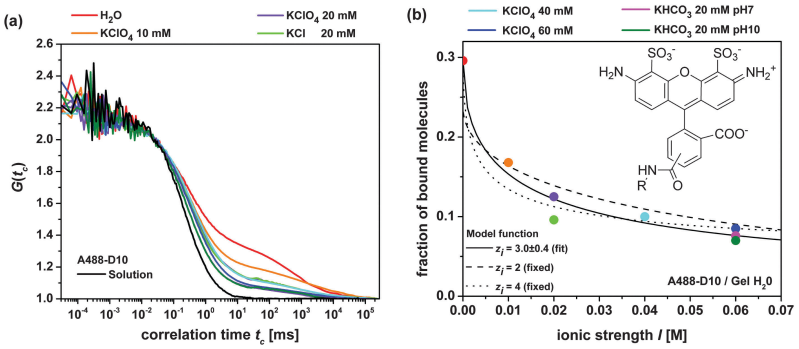

Fig. 1 (a) Image-integrated normalized correlation curves for A488-D10 in hydrogels at different salt conditions, (b) decreasing fraction of slow, temporarily bound molecules for A488-D10 in the hydrogel with increasing ionic strength I. A fit of eqn (14) yields $Z_i = 3.0 \pm 0.4$; $K_d' = 0.42 \pm 0.03$; $R_i = (0.7 \pm 0.5)$ nm. The inset shows one possible mesomeric structure and charge distribution of Alexa488.

charges per labelled dextran, estimated as follows. D10 samples have ~5 labelling sites per molecule. The specified mean degree of labelling (DoL_{av}) of the investigated A488-D10 samples is 1, if the unlabelled dextran molecules are also considered. However, considering only labelled dextrans in a first approximation of random labelling, we can expect around 1.5 dyes per labelled and thus detected dextran (for more details of this calculation, see S1.3, ESI†), which corresponds to a mean charge Z_i(A488-D10) ≈ 3. For the higher salt concentrations, the Debye length κ^{-1} is of the order of the macromolecule's dimension (κ^{-1} ≈ 1.4 nm for I = 0.05 M), producing conditions beyond some of the approximations made to derive eqn (14b). Nevertheless, the fit shown in Fig. 1b describes the experimental data sufficiently well.

The analysis reveals that mainly the presence or screening of charges determine the sticking behavior of the probe molecules and not the kind of anion as suggested by the Hofmeister series.[85,86] In particular, perchlorate, chloride or hydrogen carbonate ions at the same ionic strength had a comparable influence on the diffusion properties of the studied samples (see Fig. 1b).

Fluorescence anisotropy. To compare the restricted motion of A488-D10, TMR-D10 and FLU-D10 in the hydrogel to its behavior in solution, we performed measurements of steady state anisotropy r and time resolved anisotropy $r(t)$ for each pixel. For this, a possible distribution of r due to the heterogeneous environment needed to be separated from shot-noise broadening. Thus, a plot of r *vs.* number of detected photons, N_F, was analyzed (Fig. 2a), and the mean anisotropy, $\langle r \rangle$ was calculated:[87]

$$r = \langle r \rangle \pm \frac{1}{3}\frac{(2+\langle r \rangle)\sqrt{(1-\langle r \rangle)(1+2\langle r \rangle)}}{\sqrt{N_F}} \qquad (15)$$

It is clear that, on average, A488-D10 exhibits a higher anisotropy in the gel than in aqueous solution. This can be attributed to a temporary trapping of the solute in the matrix network. The plotted values for r in the gel are pixel-averages where about 30% of molecules were trapped for this sample (Fig. 1b). During the measurement time of 1800 s, many probe transits are averaged, so that the anisotropy reports on the average trapping probability. In our samples different pixels display different anisotropies, so that the width of the distribution significantly exceeds the shot-noise broadening as found in the solution measurement. This can only be explained by the spatial heterogeneity of the hydrogel.

To study probe–polymer interactions inside the gel matrix, r measurements where performed for A488-D10 under different conditions ($KClO_4$ 10 mM, 20 mM, 40 mM, 60 mM; KCl 20 mM; potassium carbonate buffer pH 7, 20 mM and pH 10, 20 mM, for TMR-D10 and FLU-D10 in H_2O, in potassium carbonate buffer 20 mM pH 10 and in Tris buffer 50 mM pH 7.5). The 2D r–N_F plots for all conditions are shown in S7 (ESI†). Fig. 3 shows the relation of the ratio of r in the hydrogel to r in different aqueous electrolyte solution and the fraction of trapped particles, x, which is directly calculated from FCS curves by applying eqn (4) (for values see Table S8, ESI†).

In a two-component system the additive behavior of anisotropies predicts a linear dependence of r_{gel} on the fraction of the trapped species x: $r_{gel} = xr_{trapped} + (1 - x)r_{sol}$. To take into account different initial solution anisotropies of the differently labeled probe molecules relative anisotropies r_{gel}/r_{sol} are plotted in Fig. 3. By fitting a line to the data and using r_{sol} = 0.037 (Fig. 2) we estimate mean $r_{trapped}$ = 0.10 ± 0.01 for A488-D10. This is much less than the fundamental anisotropy of A488 (r_0 = 0.37) which would be expected for the completely immobilized dye. The low density of labels renders energy transfer between identical chromophores an unlikely cause for the reduced anisotropy, leaving partial mobility of the dye even in the trapped environment as most probable explanation.

Fluorescence time traces. Time-traces of A488-D10 at low concentration in the hydrogel were investigated to further analyze the sticking behavior (Fig. 4a). Temporary sticking and accumulation of the probe molecules in the hydrogel are indicated by relatively long dwell times (up to seconds) and count rates which are significantly above average, both of

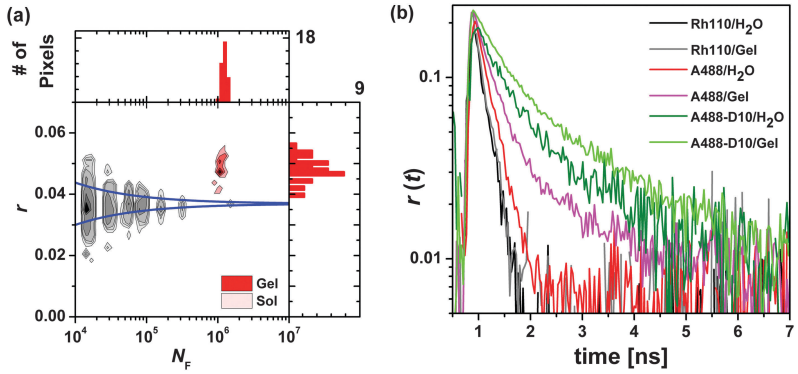

Fig. 2 (a) Anisotropy r *vs.* photon number N_F in different time windows for A488-D10 in water (gray contour lines) and in hydrogel (red contour lines) with one-dimensional projections for the gel data. The time window for the gel data was 1800 s. The theoretical shot-noise limits of r are calculated with eqn (15) with $\langle r \rangle$ = 0.037 (blue lines). (b) Anisotropy decays, $r(t)$ for Rh110, A488 and A488-D10 in H_2O and gel/H_2O.

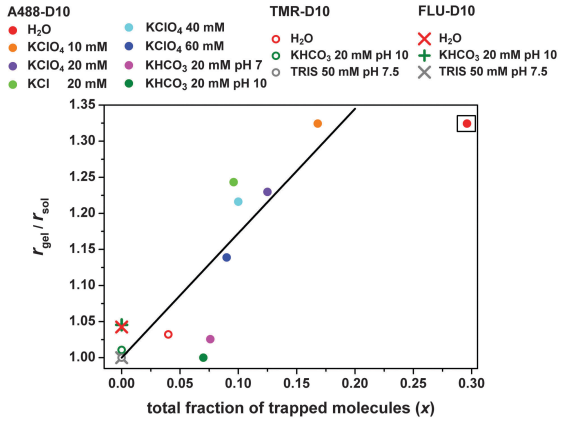

Fig. 3 Average anisotropy ratio, r_{gel}/r_{sol} as a function of the fraction of trapped particles derived from FCS measurements for A488-D10 (see Fig. 1), TMR-D10 and FLU-D10. Linear extrapolation (without H_2O value) yields $r_{gel}/r_{sol} = 2.7 \pm 0.3$ for $x = 1$.

which are not observed for molecules freely diffusing in solution (Fig. 4a). A strong correlation between the fraction of the trapped molecules is revealed by the slow decay between 10 ms and several seconds and the mean count rate for this time range in the corresponding fluorescence correlation curves (Fig. 4b).

The interaction of A488-D10 with the matrix is revealed by several different observations: first, a reduction of the fluorescence lifetime ($\tau_{gel}/\tau_{sol} \approx 0.95$), mainly attributed to quenching since a change in radiative lifetime due to refractive index differences between gel and solvent is expected to only account for 1/3 of the effect ($\tau_{r(gel)}/\tau_{r(sol)} \approx 0.987$, see S1.6, ESI†),[88,89] and, second, an increased anisotropy ($r_{sol} = 0.037$, $r_{gel} = 0.049$) with broadened distribution inside the gel (see Fig. 2 and 3). Third, the apparent brightness B_{app} of A488-D10 in the hydrogel, obtained as the ratio of detected count rate to the apparent number of particles N (taken from the FCS amplitude, eqn (4)), is significantly lower than B measured in solution ($B_{app}/B \approx 0.37$) which is not consistent with the weak dynamic quenching indicated by the small change in fluorescence lifetime. One possible explanation could be that a fraction of the molecules are trapped on a longer time scale (>1 min) which results in a virtually uncorrelated background reducing the correlation amplitude. Taking long term trapping into account for the highly interacting A488-D10, an effective concentration of trapping sites in the range from 10 to 50 nM can be deduced for low salt conditions (detailed discussion in the S1.4 and S1.5, ESI†). The observation of systematically higher fluorescence intensities inside the loaded gel than in the surrounding solution supports the idea of the enrichment of probe molecules in the gel (for details see S1.1 and S6, ESI†).

3.2. Mobile guest molecules

3.2.1. Experimental results

MFIS. As already discussed, the analysis of FCS correlation curves as displayed in Fig. 1a revealed different populations of guest molecules with differing diffusion times. In this section, we only consider the freely diffusing species with the smallest diffusion time. With MFIS, the hydrogel was studied in deionized water as well as in 20 mM potassium carbonate buffer at pH 10. Significantly different results were found for the two experimental conditions. These differences can be explained by a solvent dependent degree of swelling of the hydrogel (see sample details, Section 2.1.1). The diffusion coefficients from FCS experiments are shown in Table 3.

MTI. Fig. 5a shows an example set of fluorescence images at the beginning and the end of an MTI experiment of A488-D10 diffusing into a hydrogel disc. Due to the influx of fluorescent particles into the polymer hydrogel, the fluorescence intensity inside the hydrogel increases with time. A higher intensity inside the hydrogel is clearly visible at the end of the measurement. This indicates enhanced fluorescence of the dyes inside the gel and/or an attraction of the dye to the hydrogel. As expected, a variation of the particle concentration between 0.1 μM and 10 μM did not change the diffusion coefficient.

In these experiments the two faces of the hydrogel discs were not accessible to the solvent. Thus, the samples can be described as infinitely long cylinders in a reservoir of dye or dextran in solution, *i.e.* a quasi two-dimensional geometry with radial diffusion. Assuming azimuthally homogeneous diffusion, for every fluorescence image, the azimuthally averaged

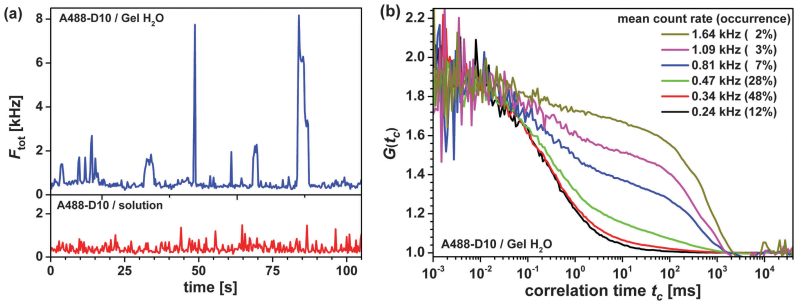

Fig. 4 (a) Fluorescence time traces (sum of perpendicular and parallel channel) for a single pixel in the image of A488-D10 in solution and in the gel in water conditions, (b) correlation curves of count rate selected subsets of the trace (for details see S5, ESI†).

Table 3 Diffusion coefficients of free dye and dextran conjugates in solution, D_{sol}, and in the hydrogel, D_{gel}, at 22.5 °C

Sample	Dye[a]	M_w[b] [kDa]	R_h[c] [nm]	D_{sol} [10^{-6} cm^2 s^{-1}]	D_{gel} [10^{-6} cm^2 s^{-1}]
Free dye	A488	0.53	0.56	3.69 ± 0.05	2.7 ± 0.1
	TMR	0.39	0.56	3.45 ± 0.07	2.6 ± 0.1
	FLU	0.33	0.54	4.33 ± 0.09	3.9 ± 0.1
D3	A488	3	1.7 ± 0.1	1.05 ± 0.02	0.59 ± 0.02
	TMR			1.13 ± 0.02	0.62 ± 0.02
	FLU			1.45 ± 0.03	1.24 ± 0.04
D10	A488	10	3.1 ± 0.2	0.64 ± 0.01	0.32 ± 0.02
	TMR			0.99 ± 0.02	0.47 ± 0.02
	FLU			0.60 ± 0.02	0.54 ± 0.02
D40	TMR	40	6.0 ± 0.3	0.38 ± 0.01	0.10 ± 0.01
	FLU			0.32 ± 0.01	0.18 ± 0.03
D70	TMR	70	7.9 ± 0.4	0.33 ± 0.01	0.083 ± 0.004
D500	FLU	500	20 ± 2	0.107 ± 0.002	0.04 ± 0.02
D2000	TMR	2000	40 ± 4	0.068 ± 0.002	—
	FLU			0.060 ± 0.001	—

[a] A488 and TMR samples measured in deionized water, FLU in 20 mM potassium carbonate buffer at pH10. [b] Molecular mass M_w as obtained from manufacturer. [c] Hydrodynamic radii R_h for free dyes are calculated from reported diffusion coefficients *via* Stokes–Einstein equation.[90–93] R_h of dextran conjugates are obtained from a fitted Flory scaling law to our MFIS and NMR data (see Fig. 8). Errors for D_{sol} and D_{gel} are standard errors of the averages from multiple measurements, errors for R_h are 68% confidence intervals ($\pm 1\sigma$) from the fit.

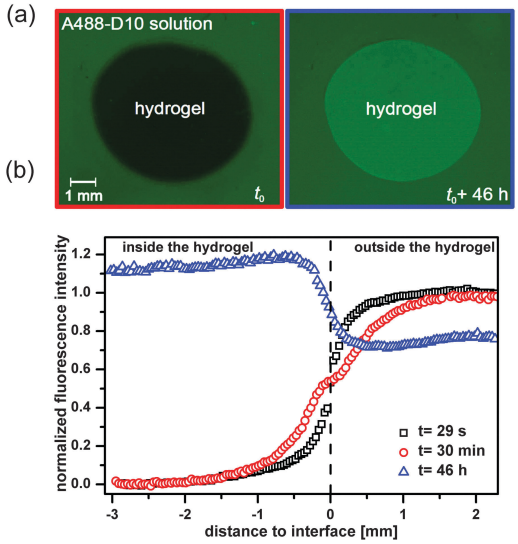

Fig. 5 (a) Example fluorescence images at the beginning (t_0) and the end of an experiment, (b) intensity–distance profiles for 29 s, 30 min and 46 h after contacting a cylindrical polymer hydrogel with A488-D10 solution.

intensity profiles were determined. Typical intensity–distance profiles for three times are displayed in Fig. 5b. The 46 h data illustrate that the fluorescence intensity in the gel is higher than in solution.

Diffusion equations for radial diffusion in an infinite cylinder with radius R_d suspended in an infinite reservoir with a diffusion coefficient D_{gel} yield a radial concentration profile $c(s,t)$ of the diffusing substance with the radial position s inside the infinite cylinder:[94]

$$c(s,t) = c_\infty + \left(\frac{c_i - c_\infty}{2D_{gel}t}\right) e^{-\frac{s^2}{4D_{gel}t}} \int_0^{R_d} e^{-\frac{s'^2}{4D_{gel}t}} I_0\left(\frac{ss'}{2D_{gel}t}\right) s' ds' \quad (16)$$

with the modified Bessel function of the first kind of order zero, I_0, and the initial and final concentrations c_i and c_∞, respectively.

Analysis of the complete concentration profiles is nontrivial because if the hydrogel edge is not perfectly perpendicular, this can lead to scattering and edge effects which will influence the shape of the measured concentration profiles. We thus first considered a more robust approach and analyzed the temporal increase in concentration in the center of the hydrogel. To enhance statistics, we averaged over an area of 0.2 mm by 0.2 mm in the center of the hydrogel. This area is small compared to the overall size of the gel ($R_d \approx 3.5$ mm). One typical dataset for the increase of A488-D10 in the center of a cylindrical hydrogel is shown in Fig. 6.

From eqn (16) an expression for $s = 0$ was derived:[94]

$$c(t) = c_i + (c_\infty - c_i) e^{-\frac{R_d^2}{4D_{gel}(t+t_0)}} \quad (17)$$

An imperfectly perpendicular hydrogel edge and potential scattering from the gel edge will lead to a broadened start profile (Fig. 5). This was accounted for by adding a time-offset t_0 in eqn (17). This equation was fitted to the time evolution of the intensity in the center of the hydrogel. This resulted in very good agreement with the data (see Fig. 6). As the gel radius plays an important role in the determination of D_{gel}, we fitted all datasets with both the initial and the final radius (given in Section 2.3.2) and estimated D_{gel} to be between the values we get from these fits (Table 4).

Since the reservoir in the experiments was finite, the above model does not perfectly describe the experimental conditions. In the experiments, the volume of the solution surrounding the

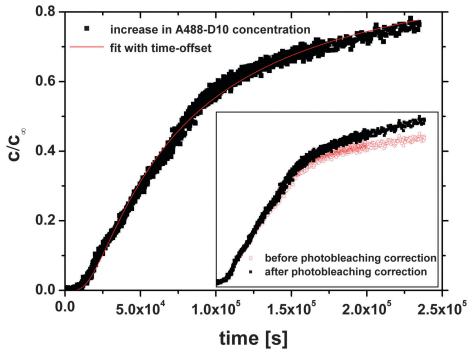

Fig. 6 Increase in A488-D10 concentration in the center of a hydrogel disc with time. The inset shows the original data (open circles) and the data after a photobleaching correction has been applied (closed squares).

Table 4 Diffusion coefficients of A488 free dye and dextran conjugates in the hydrogel at 23 °C measured by MTI. Errors for D_{gel} are standard errors of the averages from multiple measurements

Sample	Dye	D_{gel} [10^{-6} cm^2 s^{-1}]
Free dye	A488	3.2 ± 0.1
D3	A488	0.73 ± 0.02
D10	A488	0.42 ± 0.01

gel was about 11 times the cylinder volume. This should result in a homogeneous final dye concentration $c_\infty \approx 0.92c_i$ in both the gel and reservoir. This has not been observed (Fig. 5). Thus we considered a second model; diffusion into a cylinder from a stirred solution of limited volume.[94] The fitting results from this model were compared to those from the above model (eqn (16)). The second model was found to describe the data for short and intermediate measurement times, but failed to describe the long time behavior. The model suggests that saturation between cylinder and reservoir should be achieved much faster than seen in the experiments. This discrepancy could be due to an attractive interaction between the hydrogel and the diffusing molecules as indicated by the MFIS experiments. In line with this idea is the observation that for all measurements with Alexa-labelled particles, the fluorescence intensity of the hydrogel was higher than that of the surrounding solution at the end of the measurement (Fig. 5). If the particles are attracted to the hydrogel, they will preferentially diffuse into the gel even after the concentration difference between gel and reservoir is balanced. This corresponds to a larger effective reservoir as described by eqn (16), which is based on an infinite reservoir.

NMR. Diffusion coefficients of unlabelled dextrans in D_2O and inside the hydrogel were extracted from the NMR measurements using eqn (7) to fit the echo amplitudes. For D40 in the hydrogel, one typical decay curve and the corresponding fit using eqn (7) is shown in Fig. 7 (for more details see S10, ESI†).

Very good agreement between experimental data and the fit can be observed. The resulting diffusion coefficients (average of three measurements with varying gradient length) are shown in Table 5.

Summary. Although all applied techniques probe different length scales of the sample, for the same conditions they yield

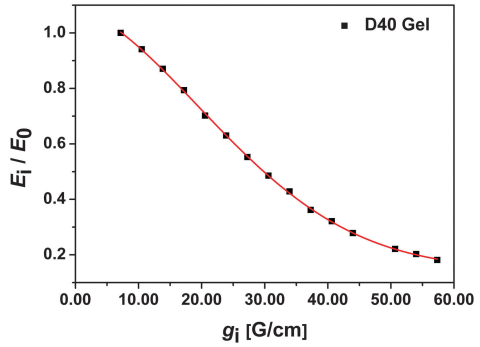

Fig. 7 NMR data and fit using eqn (7) for unlabelled dextrans (40 kDa) in the hydrogel. The data was normalized.

Table 5 Diffusion coefficients of unlabelled dextran in solution, $D_{solution}$, and in the hydrogel, D_{gel}, at 23 °C measured by NMR

Sample	Dye	R_h[a] [nm]	$D_{solution}$ [10^{-6} cm^2 s^{-1}]	D_{gel} [10^{-6} cm^2 s^{-1}]
D3	unl.	1.7 ± 0.1	1.37 ± 0.01	0.80 ± 0.01
D10	unl.	3.1 ± 0.2	1.158 ± 0.003	0.38 ± 0.01
D40	unl.	6.0 ± 0.3	0.451 ± 0.003	0.110 ± 0.003

[a] Hydrodynamic radii R_h from $D_{solution}$ (free dye) or fitted power law (dextran conjugates, from experimental data, see Table 3). Errors for $D_{solution}$ and D_{gel} are standard errors of the averages from multiple measurements, errors for R_h are 68% confidence intervals ($\pm 1\sigma$) from the fit.

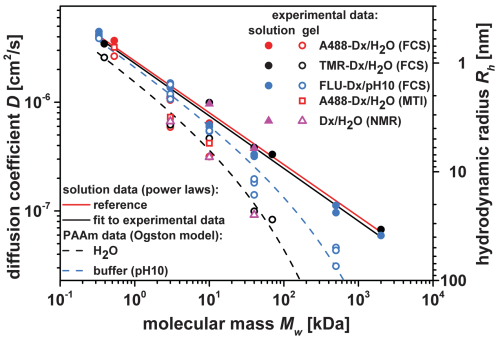

Fig. 8 Experimental diffusion coefficients D at 22.5 °C and (for solution data) hydrodynamic radii R_h for equivalent spheres as estimated by the Stokes–Einstein equation. Solution data (filled symbols) were approximated by the Flory scaling law (red line, R_h [nm] = (1.01 ± 0.07) × (M_w [kDa])$^{0.48\pm0.02}$), and compared to reference data (black line, R_h [nm] = (0.96 ± 0.13) × (M_w [kDa])$^{0.48\pm0.04}$, see S9, ESI†).[90,95,96] Dashed lines represent fits of the Ogston model (black: H_2O, blue: buffered solution at pH 10; for parameters see Table 6) to the gel data (open symbols).

remarkably consistent diffusion coefficients, which are displayed in Fig. 8. Fits to the Flory scaling law were used to determine the hydrodynamic radii R_h (also see S9, ESI†) of the dextrans in solution. As expected, the diffusion coefficients of all our guest molecules decay markedly with increasing molecular weight and the results for all methods agree quantitatively. The heterogeneity in the gel structure is indicated by the scatter of the gel data around the fit curve from various independent measurements beyond the shot noise limit.

3.2.2. Comparison with Ogston theory. Besides adsorption or temporary binding phenomena, the hindrance of diffusion, *i.e.* a reduction of the macroscopic diffusion coefficient inside the matrix with respect to the bulk diffusion coefficient is a fundamental property characterizing the transport behavior of particles within the matrix. Diffusion of solutes inside the pores has been approximated by many models.[97–99] Here we applied a simple fiber network theory. This model goes back to Ogston *et al.*[35] and describes a hydrogel as a network of randomly distributed fibers. Based on this model, the hindrance factor is

$$H = \exp\left(-\sqrt{\varphi\left(1+\frac{R_h}{R_f}\right)^2}\right) \quad (18)$$

where R_f is the radius and φ the volume fraction of the fibers in the gel and R_h the hydrodynamic radius of the diffusing species.

The important assumptions behind this model are known: (i) the solute/fiber interaction is purely hard-sphere in nature, (ii) the fibers are infinitely long and were placed randomly in the matrix, and (iii) the solute concentration is very low, so that solute–solute interactions are negligible in both phases. It is clear that such approach can only be a crude approximation of the real physical effects that are governing the translocation in the matrix in our system. Nevertheless, Ogston's model yields a convenient and simple analytic expression to analyze fundamental trends. Moreover, such approach implies the use of effective parameters, permitting in terms of the volume fraction (φ), to obtain reasonable results in comparison to the experimental values as estimated from analysis of the swelling behavior (see Section 2.1.1).

As expected and shown in Fig. 8, the diffusion coefficient D decreases with dextran size, with the decrease being more pronounced in the gel. Thus, the hindrance factor, $H = D_{gel}/D_{sol}$, will also decrease with increasing hydrodynamic radius R_h of the dextrans (see Fig. 12).

Dashed lines in Fig. 8 represent the curves calculated with the Ogston model (eqn (18)) using the fit parameters listed in Table 6.

Table 6 Results from fitted model function with standard errors and the experimentally determined polymer volume fraction (φ in the swollen hydrogel)

		TMR-Dx/H_2O	FLU-Dx/pH 10
	φ (exp.)	0.0390 ± 0.0004	0.0150 ± 0.0001
Fiber network	φ	0.06 ± 0.03	0.005 ± 0.007
model (eqn (18))	R_f [nm]	1.4 ± 0.5	1.3 ± 1.1

The agreement with our data is already very good. Using newer, comparable models (such as the Amsden-model[97]) did not noticeably improve agreement with our data (thus not shown in Fig. 8).

3.2.3. Comparison with Brownian dynamics simulations. While the Ogston model provides a simple analytical formula to describe the trends for the dextran dynamics with an effective excluded volume, we now apply our Brownian dynamics simulations (see Section 2.4) for a more detailed modeling approach. Different approaches to model a hydrogel have been used in previous works. When investigating the swelling behavior of a gel, Linse and coworkers[36–39] and Holm and coworkers[40–42] resolved the individual monomers of the gel network. However the dynamics of tracer particles through the network was not performed within this level of modelling. Addressing tracer motion within monomer-resolved modelling requires much more computational resources in particular for long-time diffusion. Also the fitting procedure would require several sets of runs. Therefore we leave monomer resolved studies to future work. Instead we decided to follow the more coarse-grained approach by Zhou and Chen.[47] This type of modeling provides a simple and systematic framework in which to include different physical effects, namely the mobility of the matrix particles (*i.e.* fluctuations in the matrix structure), the effective dextran–matrix excluded volume, and sticky attractions. The matrix-dextran interactions are expected to play a key role in spreading the delay times of the diffusive process of the dextran molecules through the matrix. Fig. 9 shows schematic two-dimensional representations of the three-dimensional simulations on the three different levels that were used to explain the experimental data.

In qualitative terms, one would expect increasing agreement between the simulation and experimental data as we increase

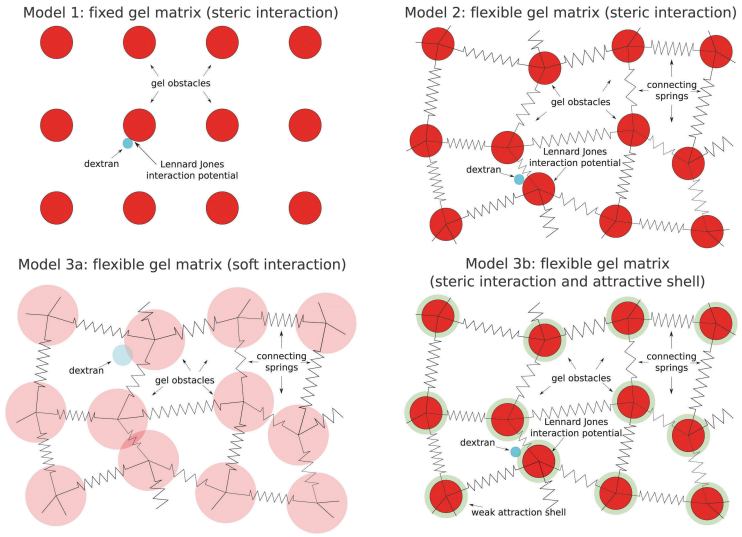

Fig. 9 Four models for the dextran–matrix system. Model 1: fixed gel matrix (steric interaction, eqn (8)), model 2: flexible gel matrix (steric interaction, eqn (8)), model 3a: flexible gel matrix (soft interaction, eqn (10)) and model 3b: flexible gel matrix (steric interaction and attractive shell, eqn (11)). The sketches illustrate two-dimensional representations of the three-dimensional models used for the simulations.

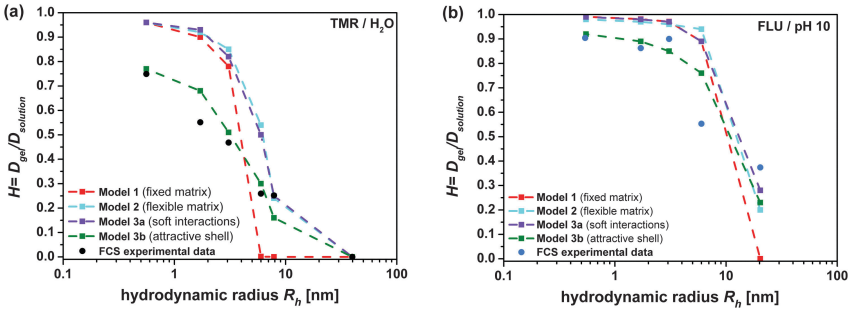

Fig. 10 Comparison between FCS experimental data and Brownian dynamic simulations with 4 different models for TMR-dextran in water conditions (a) and FLU-dextran in 20 mM potassium carbonate buffer at pH 10 (b).

the level of complexity. This is indeed what is observed and displayed in Fig. 10, where the different simulation results are compared to FCS data. In model 1, hard matrix particles are fixed on simple cubic lattice sites, providing a uniform matrix with just one pore size. This results in a very sharp drop in the hindrance factor when the dextran's size is increased to this pore size. Introducing elastically connected matrix particles (model 2) broadens the pore size distribution and leads to a slower decrease of the hindrance factors with dextran size, as expected. However, this decrease is still too sharp compared to the experimental data. Softening the interactions by changing the interaction potentials from WCA to a Gaussian potential (model 3a) shows an even lower, yet still too distinct decrease, of the hindrance factor with increasing dextran size. The agreement is still unsatisfactory. Especially the hindrance of the smaller dextrans is too weak in the previous approaches. When these small dextrans collide with matrix particles, they can easily find another way to pass due to their small size.

The introduction of an attractive contribution in the matrix-guest interaction (model 3b) is found to be crucial to describe the observed slow decay with increasing dextran sizes. If the smaller dextrans collide with matrix particles in this model, they can still find another path to pass. However, they are more likely to first become stuck resulting in a slowdown even for small dextrans.

Model 3b is the only one which includes a repulsive interaction and an attractive shell and it is the best representation of our experimental data. Additional simulations performed within model 3b using a Gaussian softened core showed a similar fit quality as that with a WCA-core. The results show that, within the framework of the model classes considered here, an effective attraction is needed to describe the spreading of the dynamics correctly given the statistical uncertainties of the experimental data. The origin of this attraction still needs to be resolved. For specific simulation parameters see the Table S11 (ESI†).

3.3. Estimation of the average pore size

The theoretical study permits an estimation of the average pore size of the investigated hydrogel in the two experimental environments. We optimized for the *a priori* unknown average pore size by fitting the simulated hindrance factors to the experimental data. Since the positions of all matrix particles in the BD-simulation are known, one can estimate the size of a specific pore in the gel as the center-to-center distance of two neighboring matrix-particles minus the matrix-particle-diameter. The decision which matrix particle pairs have to be counted as 'neighbors', is subject to a certain degree of arbitrariness. We chose to consider all particle pairs that are connected with springs, therefore possibly overestimating the correct value by neglecting close, but unconnected, matrix particle-pairs. Fig. 11 shows this distribution for both investigated conditions calculated using model 3b.

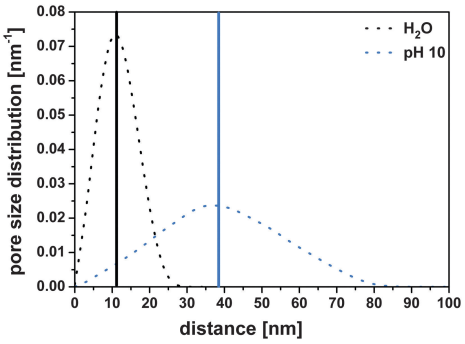

Fig. 11 The distribution of the free space between connected matrix particles (dots) in the BD simulation and the average pore size (bars) of the polymer matrix in both experimental conditions. It is based on the final set of parameters after the fit within the applied model 3b. Black dots correspond to H_2O, blue dots to 20 mM potassium carbonate buffer at pH 10 (for details see text).

We obtained an average value of 11 ± 1 nm for gels in water and 38 ± 3 nm for gels in buffer at pH 10 for the final set of parameters after the fit. While this average pore size is an output from fitting the simulated hindrance factors to the experimental data, the shape of the distribution is rather an input as the width of this distribution (standard deviation σ = 5 nm for water, σ = 16 nm for pH 10 in Fig. 11) scales with the average value as defined in the models. The average values are in the same order of magnitude as calculated from swelling experiments, where we estimated 5.7 nm and 7.8 nm, respectively, assuming ideal solvent quality, homogeneous cross-linking densities and Gaussian distribution of chain lengths (see Section 2.1.1). In H_2O both results differ by less than a factor of 2.

We now compare the results of our gel ([T] = 0.04 g ml^{-1}, C_R = 0.035), obtained in water conditions, with literature values for gels with similar composition. Significant discrepancy between pore size values resulting from scanning electron microscopy SEM (10–20 μm)[32–34] and swelling analysis (2.0 nm) was reported.[33] When using SEM, the structure of the gel may become damaged during the freeze-drying processes, resulting in systematically too large pore sizes. In our study, we measured under native conditions without disturbing the gel matrix structure thus circumventing this problem.

In gel electrophoresis with DNA as a cylindrical tracer molecule,[23,30,31] pore sizes between 5.9 and 133 nm are reported for gels with similar composition to ours. The hydrodynamic radius of the DNA was not measured directly but calculated using different models which is known to be an intrinsic problem. Approximating DNA by a sphere becomes more reasonable for shorter DNA molecules. Therefore it is notable, that the electrophoresis study using the shortest DNA[30] matches our result the best.

Very early work of polyacrylamide gels, using electrophoresis of proteins[29] in phosphate buffer, pH 7 ([T] = 0.06 g ml^{-1}, C_R = 0.05) and chromatography of proteins[28] in water ([T] = 0.065 g ml^{-1}, C_R = 0.02) agree well with our results, yielding 8.5 nm and 2.25 nm, respectively. In addition, recent studies[96] based on dynamic light scattering revealed mesh sizes of the same order of magnitude for polyacrylamide hydrogels of about 15 nm and for poly(*N*-isopropylacrylamide) of about 19 nm.

4. Combined results and conclusions

All data for the hindrance factor H obtained from the three different and independent methods we have applied are displayed and compared to Brownian dynamics simulations performed with model 3b in Fig. 12. For the MTI measurements, the average values of D_{sol} from NMR and MFIS were used to scale the data, as they could not be measured with this technique.

We have shown that the long time diffusion coefficients of dextran molecules moving in solution and in a polyacrylamide gel matrix determined on different length scales by using multiparameter fluorescence image spectroscopy (MFIS), macroscopic transmission imaging (MTI) and nuclear magnetic resonance (NMR) are consistent. The measured diffusion coefficients decrease with increasing molecular weight and fall on a master curve. This supports the reliability of our data set, which might thus serve as possible calibration data for future experiments and theories.

In addition, although our results could be described by the Ogston model (Fig. 12), a more realistic model of a flexible gel matrix was applied to describe the experimental data and to estimate the average pore size in the gel. The simulated average pore sizes of 11 nm (water) and 38 nm (pH 10) agree reasonably well with estimations from swelling theory of 5.7 nm and 7.8 nm, respectively. Within the experimental error bars and the limitations of the applied models, our results for the gel equilibrated in water are in good agreement with published studies employing comparable globular macromolecular probes (2.25 nm[28] or 8.5 nm[29]) as well as with light scattering investigations (15 nm)[96] in native gels with similar composition.

Combining experiments and simulations enabled us to achieve a better understanding of the effects determining the diffusion of molecules in the gel network. Moreover, using the MFIS method, a significant interaction between hydrogel and macromolecules was observed, in particular for A488 samples. The MTI results support the idea of the attractive interaction of Alexa-labelled particles and the gel, showing that the fluorescence intensity in the hydrogel was higher than that of the surrounding solution at the end of the measurements. This suggests to use uncharged dyes or, in case of charged dyes, to add a sufficiently high salt concentration for future investigations.

The heterogeneity inside a single hydrogel sample was probed on a length scale of 10 μm in anisotropy experiments by comparing different pixels and hence different positions in the hydrogel (Fig. 2). Furthermore, for the experiments at pH 10, the scattering of data from various independent samples in Fig. 12b was significantly beyond shot noise limits (or other experimental uncertainties), revealing a heterogeneity, which persisted over the complete measurement times.[82,83]

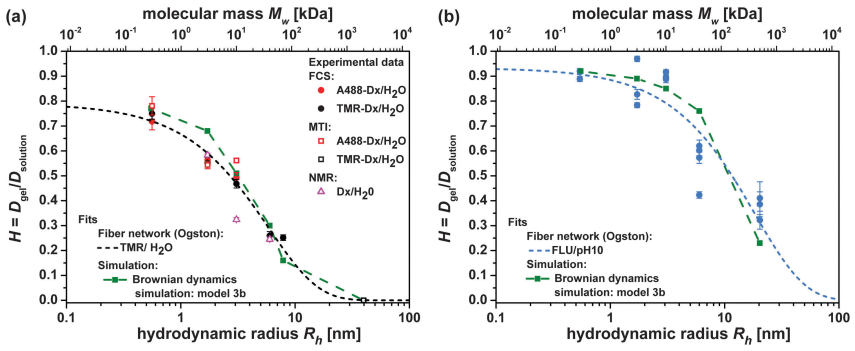

Fig. 12 Hindrance factors $H = D_{gel}/D_{sol}$ of dextrans in hydrogel. A488 (red), TMR (black) and unlabelled samples (magenta) measured in deionized water (a), FLU labelled samples (blue) measured in 20 mM potassium carbonate buffer at pH 10 (b). Experimental data: FCS (filled circles); MTI (open squares); NMR (open triangles); fitted model function: fiber network (eqn (18), dashed black and blue lines, parameters Table 6) and Brownian dynamics simulation (green points). The errors are the standard errors of repeat measurements.

Despite our application of a wide range of methods and the general consistency of the results we have obtained, open questions remain. For example, while the hindrance factor in the limit of small tracer particle sizes tends to 1 in our FLU/pH 10 system, it seems to approach ~ 0.8 in our TMR/H_2O system (Fig. 12). A value close to 1 might still be approached for smaller tracer particles in our H_2O system, but we could not investigate these in our study due to experimental limitations. If one assumes that there really is a difference for smaller tracer molecules, the question whether this is due to different swelling in different environments or caused by different interactions of the matrix with different dyes cannot be answered with certainty yet.

For future studies, the diffusion of the same dextran molecules with the same dyes in differently crosslinked matrices should be explored systematically in order to distinguish between different modes governing the translocation.

Abbreviations

Mass concentration of polymeric material in total volume	[T]
Weight fraction of cross-linker with respect to the total mass of the polymeric material	C_R
Diffusion time	t_d
Gel disk radius	R_d
Volume dry polymer	V_p
Volume gel after swelling	V_{gel}
Mass	m
Water density	ρ_{H_2O}
Polymer density	ρ_p
Polymer volume fraction in the swollen state	φ
Molecular weight of the polymer between cross-links points	M_c
Molecular weight of the repeating units	M_r
Polymer mesh size	ξ
Cross-linking degree in the hydrogel	X
Carbon–carbon bond length	ζ
Flory characteristic ratio	C_n
Numerical aperture	NA
Detection volume in MFIS	V_{det}
Temperature	T
Diffusion coefficient	D
Gradient pulse width	δ
Diffusion delay	Δ_N
FCS fit model function	$G(t_c)$
Triplet time	t_T
Triplet amplitude	A_T
Correlation time	t_c
Confocal volume radius in x and y	ω_0
Confocal volume radius in z	z_0
Detection probability	$w(x,y,z)$
Number of molecules	N
Molecular fraction	x_i
Position coordinates	x, y, z
Fluorescence intensity	$F, F_\parallel, F_\perp$
Polarization correction factors	l_1, l_2
Fluorescence anisotropy of species i	r_i
G-Factor	G
Intensity fit parameters in MTI	P, p, Q, q
Echo intensities	E_i, E_0
Gyromagnetic ratio	γ
Gradient amplitude at increment i	g_i
Delay between pulses	τ_N
Boltzmann constant	k_B
Lattice constant	a
Distance in simulations models	$s_{i,j}$
Radius	R
Hydrodynamic radius	R_h
Matrix particle radius	R_{obst}
Position of particles in simulations models	$\vec{s}$
Mean square displacement	Δs^2
Time, reference time	t, t_0
Potential between i and j particles	$U_{i,j}$
Energy steric constant	ε_s
Energy Gaussian constant	ε_G
Energy attractive constant	ε_a
Constant in simulations models	b
Additive diameter	$\sigma_{i,j}$
Position of minimum in simulations models	$l_{i,j}$
Hindrance factor	H
Charge	Z_i
Effective binding constant	K_d'
Ionic strength	I
Effective ion radius	R_i
Activity	a_i
Concentration	c_i
Activity coefficient	f_i
Debye–Hückel constants	A, B
Debye length	κ^{-1}
Photon number	N_F
Fluorescence lifetime of species i	τ_i
Radiative lifetime of species i	$\tau_{r,i}$
Bessel function	I_0
Radial position inside an infinity cylinder for MTI fit	s, s'
Fiber radius	R_f

Acknowledgements

C. J., H. L., S. U. E., and C. A. M. S. gratefully acknowledge partial financial support from the Strategic Research Fund of the HHU. Additional funding was given to D. W. by BioSoft and to C. E. S. and H. L. by the ERC Advanced Grant INTERCOCOS (grant agreement 267499).

References

1 S. T. Balke, A. E. Hamielec, B. P. LeClair and S. L. Pearce, *Ind. Eng. Chem. Prod. Res. Dev.*, 1969, **8**, 54–57.
2 F. Chen, P. Tillberg and E. Boyden, *Science*, 2015, **347**, 543–548.

3 V. E. Barsky, A. M. Kolchinsky, Y. P. Lysov and A. D. Mirzabekov, *Mol. Biol.*, 2002, **36**, 437–455.
4 T.-O. Peulen and K. J. Wilkinson, *Environ. Sci. Technol.*, 2011, **45**, 3367–3373.
5 S. Brahim, D. Narinesingh and A. Guiseppi-Elie, *Biomacromolecules*, 2003, **4**, 1224–1231.
6 N. Murthy, Y. X. Thng, S. Schuck, M. C. Xu and J. M. J. Fréchet, *J. Am. Chem. Soc.*, 2002, **124**, 12398–12399.
7 P. Gupta, K. Vermani and S. Garg, *Drug Discovery Today*, 2002, **7**, 569–579.
8 R. Morita, R. Honda and Y. Takahashi, *J. Controlled Release*, 2000, **68**, 115–120.
9 S. Sershen and J. West, *Adv. Drug Delivery Rev.*, 2002, **54**, 1225–1235.
10 D. T. Eddington and D. J. Beebe, *Adv. Drug Delivery Rev.*, 2004, **56**, 199–210.
11 O. Wichterle and D. Lim, *Nature*, 1960, **185**, 117–118.
12 H.-W. Kang, Y. Tabata and Y. Ikada, *Biomaterials*, 1999, **20**, 1339–1344.
13 A. S. Hoffman, *Adv. Drug Delivery Rev.*, 2002, **54**, 3–12.
14 A. Z. Abidin, T. Puspasari and W. A. Nugroho, *Procedia Chem.*, 2012, **4**, 11–16.
15 R. Zolfaghari, A. A. Katbab, J. Nabavizadeh, R. Y. Tabasi and M. H. Nejad, *J. Appl. Polym. Sci.*, 2006, **100**, 2096–2103.
16 A. Meller, *J. Phys.: Condens. Matter*, 2003, **15**, R581.
17 A. Milchev, *J. Phys.: Condens. Matter*, 2011, **23**, 103101.
18 R. Metzler and J. Klafter, *Phys. Rep.*, 2000, **339**, 1–77.
19 F. Höfling and T. Franosch, *Rep. Prog. Phys.*, 2013, **76**, 046602.
20 K. Mecke, *Acta Phys. Pol., B*, 1997, **28**, 1747–1782.
21 A. Vagias, R. Raccis, K. Koynov, U. Jonas, H.-J. Butt, G. Fytas, P. Košovan, O. Lenz and C. Holm, *Phys. Rev. Lett.*, 2013, **111**, 088301.
22 L. Haggerty, J. H. Sugarman and R. K. Prud'homme, *Polymer*, 1988, **29**, 1058–1063.
23 D. L. Holmes and N. C. Stellwagen, *Electrophoresis*, 1991, **12**, 253–263.
24 M. Kremer, E. Pothmann, T. Rössler, J. Baker, A. Yee, H. Blanch and J. M. Prausnitz, *Macromolecules*, 1994, **27**, 2965–2973.
25 J. Tong and J. L. Anderson, *Biophys. J.*, 1996, **70**, 1505–1513.
26 S. M. Russell and G. Carta, *Ind. Eng. Chem. Res.*, 2005, **44**, 8213–8217.
27 A. Stellwagen and N. C. Stellwagen, *Biopolymers*, 1990, **30**, 309–324.
28 J. S. Fawcett and C. J. O. R. Morris, *Sep. Sci.*, 1966, **1**, 9–26.
29 M. P. Tombs, *Anal. Biochem.*, 1965, **13**, 121–132.
30 N. C. Stellwagen, *Biochemistry*, 1983, **22**, 6186–6193.
31 D. L. Holmes and N. C. Stellwagen, *Electrophoresis*, 1991, **12**, 612–619.
32 R. Rüchel and M. D. Brager, *Anal. Biochem.*, 1975, **68**, 415–428.
33 L. M. Lira, K. A. Martins and S. I. C. D. Torresi, *Eur. Polym. J.*, 2009, **45**, 1232–1238.
34 Z. Blank and A. C. Reimschuessel, *J. Mater. Sci.*, 1974, **9**, 1815–1822.
35 A. G. Ogston, B. N. Preston and J. D. Wells, *Proc. R. Soc. London, Ser. A*, 1973, **333**, 297–316.
36 S. Schneider and P. Linse, *Macromolecules*, 2004, **37**, 3850–3856.
37 S. Edgecombe, S. Schneider and P. Linse, *Macromolecules*, 2004, **37**, 10089–10100.
38 S. Schneider and P. Linse, *J. Phys. Chem. B*, 2003, **107**, 8030–8040.
39 S. Schneider and P. Linse, *Eur. Phys. J. E: Soft Matter Biol. Phys.*, 2002, **8**, 457–460.
40 B. A. F. Mann, K. Kremer, O. Lenz and C. Holm, *Macromol. Theory Simul.*, 2011, **20**, 721–734.
41 B. A. Mann, C. Holm and K. Kremer, *J. Chem. Phys.*, 2005, **122**, 154903.
42 B. A. Mann, R. Everaers, C. Holm and K. Kremer, *EPL*, 2004, **67**, 786.
43 P. A. Netz and T. Dorfmüller, *J. Chem. Phys.*, 1997, **107**, 9221–9233.
44 H. Pei, S. Allison, B. M. H. Haynes and D. Augustin, *J. Phys. Chem. B*, 2009, **113**, 2564–2571.
45 L. Johansson and J. E. Löfroth, *J. Chem. Phys.*, 1993, **98**, 7471–7479.
46 P. Licinio and A. V. Teixeira, *Phys. Rev. E: Stat. Phys., Plasmas, Fluids, Relat. Interdiscip. Top.*, 1997, **56**, 631–634.
47 H. Zhou and S. B. Chen, *Phys. Rev. E: Stat., Nonlinear, Soft Matter Phys.*, 2009, **79**, 021801.
48 K. Kremer, *Comput. Mater. Sci.*, 1998, **10**, 168–174.
49 R. Messing, N. Frickel, L. Belkoura, R. Strey, H. Rahn, S. Odenbach and A. M. Schmidt, *Macromolecules*, 2011, **44**, 2990–2999.
50 D. A. Carr and N. A. Peppas, *Macromol. Biosci.*, 2009, **9**, 497–505.
51 F. Ganji, S. Vasheghani-Farahani and E. Vasheghani-Farahani, *Iran. Polym. J.*, 2010, **19**, 375–398.
52 H. Durchschlag and P. Zipper, in *Ultracentrifugation*, ed. M. D. Lechner, Steinkopff, 1994, ch. 3, vol. 94, pp. 20–39.
53 J. Jovanovic and B. Adnadjevic, *Polym. Bull.*, 2007, **58**, 243–252.
54 M. K. Krušić, M. Ilić and J. Filipović, *Polym. Bull.*, 2009, **63**, 197–211.
55 A. M. Lowman and N. A. Peppas, *Macromolecules*, 1997, **30**, 4959–4965.
56 A. Thakur, *Chem. Biochem. Eng. Q.*, 2011, **25**, 181.
57 S. Weidtkamp-Peters, S. Felekyan, A. Bleckmann, R. Simon, W. Becker, R. Kühnemuth and C. A. M. Seidel, *Photochem. Photobiol. Sci.*, 2009, **8**, 470–480.
58 Y. Stahl, S. Grabowski, A. Bleckmann, R. Kühnemuth, S. Weidtkamp-Peters, K. G. Pinto, G. K. Kirschner, J. B. Schmid, R. H. Wink, A. Hülsewede, S. Felekyan, C. A. M. Seidel and R. Simon, *Curr. Biol.*, 2013, **23**, 362–371.
59 D. Wagner, M. Börgardts, C. Grünzweig, E. Lehmann, T. J. J. Müller, S. U. Egelhaaf and H. E. Hermes, *Rev. Sci. Instrum.*, 2015, **86**, 093706.
60 M. Holz, S. R. Heil and A. Sacco, *Phys. Chem. Chem. Phys.*, 2000, **2**, 4740–4742.
61 A. L. van Geet, *Anal. Chem.*, 1970, **42**, 679–680.

62 D. H. Wu, A. D. Chen and C. S. Johnson, *J. Magn. Reson., Ser. A*, 1995, **115**, 260–264.
63 G. Wider, V. Dötsch and K. Wüthrich, *J. Magn. Reson., Ser. A*, 1994, **108**, 255–258.
64 V. Sklenar, M. Piotto, R. Leppik and V. Saudek, *J. Magn. Reson., Ser. A*, 1993, **102**, 241–245.
65 M. Piotto, V. Saudek and V. Sklenář, *J. Biomol. NMR*, 1992, **2**, 661–665.
66 P. Sengupta, K. Garai, J. Balaji, N. Periasamy and S. Maiti, *Biophys. J.*, 2003, **84**, 1977–1984.
67 P. O. Gendron, F. Avaltroni and K. J. Wilkinson, *J. Fluoresc.*, 2008, **18**, 1093–1101.
68 J. Enderlein, I. Gregor, D. Patra, T. Dertinger and U. B. Kaupp, *ChemPhysChem*, 2005, **6**, 2324–2336.
69 J. Enderlein, I. Gregor, D. Patra and J. Fitter, *Curr. Pharm. Biotechnol.*, 2004, **5**, 155–161.
70 M. Koshioka, K. Sasaki and H. Masuhara, *Appl. Spectrosc.*, 1995, **49**, 224–228.
71 N. B. Vicente, J. E. Diaz Zamboni, J. F. Adur, E. V. Paravani and V. H. Casco, *J. Phys.: Conf. Ser.*, 2007, **90**, 012068.
72 L. Hodgson, P. Nalbant, F. Shen and K. Hahn, *Methods Enzymol.*, 2006, **406**, 140–156.
73 D. Wagner, J. Burbach, C. Grünzweig, E. Lehmann, S. U. Egelhaaf and H. E. Hermes, unpublished work.
74 W. S. Price, *Concepts Magn. Reson.*, 1997, **9**, 299–336.
75 C. S. Johnson Jr., *Prog. Nucl. Magn. Reson. Spectrosc.*, 1999, **34**, 203–256.
76 F. J. Millero, R. Dexter and E. Hoff, *J. Chem. Eng. Data*, 1971, **16**, 85–87.
77 P. G. Bolhuis, A. A. Louis, J. P. Hansen and E. J. Meijer, *J. Chem. Phys.*, 2001, **114**, 4296–4311.
78 A. A. Louis, P. G. Bolhuis, E. J. Meijer and J. P. Hansen, *J. Chem. Phys.*, 2002, **117**, 1893–1907.
79 J. Dzubiella, A. Jusufi, C. N. Likos, C. von Ferber, H. Löwen, J. Stellbrink, J. Allgaier, D. Richter, A. B. Schofield, P. A. Smith, W. C. K. Poon and P. N. Pusey, *Phys. Rev. E: Stat., Nonlinear, Soft Matter Phys.*, 2001, **64**, 010401.
80 M. P. Allen and D. J. Tildesley, *Computer Simulation of Liquids*, Oxford Science Publications, Oxford University Press, 1989.
81 B. J. Alder, D. M. Gass and T. E. Wainwright, *J. Chem. Phys.*, 1970, **53**, 3813–3826.
82 M. Y. Kizilay and O. Okay, *Macromolecules*, 2003, **36**, 6856–6862.
83 A. M. Hecht, R. Duplessix and E. Geissler, *Macromolecules*, 1985, **18**, 2167–2173.
84 P. Debye and E. Hückel, *Phys. Z.*, 1923, **24**, 185–206.
85 F. Hofmeister, *Arch. Exp. Pathol. Pharmakol.*, 1888, **24**, 247–260.
86 K. D. Collins and M. W. Washabaugh, *Q. Rev. Biophys.*, 1985, **18**, 323–422.
87 C. Eggeling, PhD dissertation, Georg-August-Universität zu Göttingen, 1999.
88 J. Stejskal and J. Horská, *Makromol. Chem.*, 1982, **183**, 2527–2535.
89 D. Toptygin, *J. Fluoresc.*, 2003, **13**, 201–219.
90 Z. Zhang, E. Nadezhina and K. J. Wilkinson, *Antimicrob. Agents Chemother.*, 2011, **55**, 1075–1081.
91 A. W. Moore Jr. and J. W. Jorgenson, *Anal. Chem.*, 1993, **65**, 3550–3560.
92 Z. Petrášek and P. Schwille, *Biophys. J.*, 2008, **94**, 1437–1448.
93 E. P. Petrov, T. Ohrt, R. G. Winkler and P. Schwille, *Phys. Rev. Lett.*, 2006, **97**, 258101.
94 J. Crank, *The Mathematics of Diffusion*, Clarendon Press, Oxford, 2nd edn, 1975.
95 T. Kihara, J. Ito and J. Miyake, *PLoS One*, 2013, **8**, e82382.
96 S. Lehmann, S. Seiffert and W. Richtering, *J. Am. Chem. Soc.*, 2012, **134**, 15963–15969.
97 B. Amsden, *Macromolecules*, 1998, **31**, 8382–8395.
98 L. Masaro and X. X. Zhu, *Prog. Polym. Sci.*, 1999, **24**, 731–775.
99 B. A. Westrin, A. Axelsson and G. Zacchi, *J. Controlled Release*, 1994, **30**, 189–199.

Electronic Supplementary Material (ESI) for Physical Chemistry Chemical Physics.

SUPPORTING INFORMATION

Diffusion of macromolecules in a polymer hydrogel: from microscopic to macroscopic scales

D. Sandrin, [1,*] D. Wagner, [2,*] C. E. Sitta, [3,*] R. Thoma, [4] S. Felekyan, [1] H. E. Hermes, [2] C. Janiak, [4] N. de Sousa Amadeu, [4] R. Kühnemuth, [1,†] H. Löwen, [3,‡] S. U. Egelhaaf, [2,§] C. A. M. Seidel [1,¶]

[1] *Institut für Physikalische Chemie II, Molekulare Physikalische Chemie,*

Heinrich-Heine-Universität, Universitätsstr. 1, 40225 Düsseldorf, Germany

[2] *Institut für Experimentelle Physik der kondensierten Materie,*

Heinrich-Heine-Universität, Universitätsstr. 1, 40225 Düsseldorf, Germany

[3] *Institut für Theoretische Physik II: Weiche Materie,*

Heinrich-Heine-Universität, Universitätsstr. 1, 40225 Düsseldorf, Germany

[4] *Institut für Anorganische Chemie und Strukturchemie,*

Heinrich-Heine-Universität, Universitätsstr. 1, 40225 Düsseldorf, Germany

(Dated: February 26, 2016)

*these authors have contributed equally to this work

† ralf.kuehnemuth@hhu.de; corresponding author

‡ hlowen@hhu.de; corresponding author

§ stefan.egelhaaf@hhu.de; corresponding author

¶ cseidel@hhu.de; corresponding author

Materials and Methods

S1. *Dextran samples & hydrogel – fluorescence properties and quantitative FCS*

S1.1. *Manufacturers details of fluorescent samples*

Samples	**Degree of labelling**	**Number of lysines**	**Number of amines[a]**	**Charge[b]**	**Absorption Max [nm]**	**Emission Max [nm]**	**Quantum yield[c]**
A488-D3	1	0	≥ 1	a	495	517	0.6
A488-D10	1	10	≥ 2.5	a	494	516	0.6
FLU-D3	1	0	≥ 1	a	497	523	0.5
FLU-D10	2	0	≥ 2.5	a	496	521	0.5
FLU-D40	5	0	≥ 5	a	496	521	0.5
FLU-D500	86	58	≥ 50	a	496	521	0.2
TMR-D3	1	0	≥ 1	a	560	584	0.7
TMR-D10	3	0	≥ 2.5	n	559	586	0.5
TMR-D40	8	0	≥ 5	n	560	586	0.6
TMR-D70	10	0	≥ 10	n	560	585	1
TMR-D2000	138	456	not specified	not specified	560	583	0.8

Table S1. The table shows the manufacturers specification of dye-labelled dextran conjugates (data sheets of used sample batches, Invitrogen). [a] Specified for unlabelled aminodextrans. [b] a: anionic, n: neutral. [c] Fluorescence quantum yield Φ_F determined relative to fluorescein at pH 8.0 (FLU and A488; $\Phi_F^{\mathrm{FLU}} = 0.925 \pm 0.015$ [1]) or relative to 5-(and-6)-carboxytetramethylrhodamine (TMR).

S1.2. *Investigation of partial quenching (quantum yield and fluorescence lifetime)*:

For the sample A488-D10 the partial quenching of the labels as indicated in table S1 was investigated applying time-correlated single photon counting (TCSPC, table S2).

fl. lifetime (species fraction)	τ_1 [ns] (x_1)	τ_2 [ns] (x_2)	τ_3 [ns] (x_3)	τ_4 [ns] (x_4)	τ_5 [ns] (x_5)	χ^2	τ_x [ns]
A488 / H_2O	4.125 (0.978)	0.459 (0.022)	/	/	/	1.13	4.045
A488-D10 / H_2O	4.125 (0.742)	2.459 (0.104)	0.932 (0.066)	0.260 (0.089)	/	1.30	3.400
A488-D10 / H_2O (corr.)	4.125 (0.548)	2.459 (0.077)	0.932 (0.049)	0.260 (0.065)	0 (0.262)	1.30	2.511

Table S2. Lifetime components of A488 and A488-D10 in H_2O (FT300, PicoQuant, Berlin; excitation: 485 nm, emission: 517-523 nm, magic angle, photons recorded: total 5×10^8, peak channel 10^6 photons, T=20 °C). τ_x: species averaged fluorescence lifetime.

While free A488 decays almost mono-exponentially its D10-conjugate exhibits at least four lifetime components, indicating dynamic quenching of a subset of the labels. Albeit, the obtained species averaged lifetimes, $\tau_x = \sum x_i \tau_i$, of conjugated and free dye are not consistent with the determined corresponding fluorescence quantum yields, Φ_F. According to the ratio of the quantum yields of the labelled dextran ($\Phi_F^{\text{A488–D10(exp)}} = 0.57$, measured versus Rhodamine 110, $\Phi_F^{\text{Rh110}} = 0.85$,[2] consistent with manufacturers information $\Phi_F^{\text{A488–D10(man)}} = 0.6 \times 0.925 = 0.56$) and the A488 dye free in aqueous solution ($\Phi_F^{\text{A488}} = 0.92$, Invitrogen online) a ratio of the species averaged fluorescence lifetimes of $\tau_x^{\text{A488–D10}} / \tau_x^{\text{A488}} \equiv \Phi_F^{\text{A488–D10}} / \Phi_F^{\text{A488}} = 0.57 / 0.92 = 0.62$ is expected. Thus a fraction of completely (statically) quenched labels of x_5 = 0.262 can be deduced (last row in table S2; $\tau_x^{\text{A488–D10,corr}} / \tau_x^{\text{A488}} = 2.511 / 4.045 = 0.62$). The resulting unquenched fraction then is $x_1^{\text{A488–D10}} / x_1^{\text{A488}} = 0.560$ and the remaining fraction of $1 - 0.560 - 0.262 = 0.179$ represents the partially (=dynamically) quenched dyes. For sake of simplicity, in the following the partially quenched fraction will be ignored and instead an effective totally quenched portion of x_q = 0.38 and a corresponding fluorescent portion of x_f = 1- x_q = 0.62 will be assumed.

S1.3. *The effective degree of labelling* (DoL_{eff}):

The fluorescently labelled dextrans (as provided by Invitrogen, their specifications being summarized in table S1) are produced by exposing aminodextrans with an average number n_a of free amino groups to amine-reactive dye conjugates. Except for the A488 conjugates, once the dye has been added, the unreacted amines on the dextran are capped to yield a neutral or anionic dextran. Some of the samples carry additional lysines. Due to the applied labelling procedure, for any average degree of labelling, DoL_{av}, a distribution, $P(n_d)$, of the number of dyes per dextran molecule, n_{d}, is anticipated, i.e. even samples with a $DoL_{\text{av}} = 1$ will contain unlabelled as well as higher $(n_a \geq n_d > 1)$ labelled molecules. In case of random labelling, the distribution of n_{d} can be approximated by the binomial distribution:

$$P(n_d, n_a, DoL_{av}) = \frac{n_a!}{n_d!(n_a - n_d)!}\left(\frac{DoL_{av}}{n_a}\right)^{n_d}\left(1 - \frac{DoL_{av}}{n_a}\right)^{n_a - n_d} \qquad \text{(S1)}$$

For many labelled dextrans the fluorescence quantum yield is significantly reduced as compared to the free dye. Assuming only static quenching of the dyes (on the time scale of the experiment) three different distributions can be defined: (1) the distribution of dextrans $P(n_t)$ containing any number n_t of dyes (fluorescent or quenched) in the range of $n_a \geq n_t \geq 0$, (2) the distribution of dextrans $P(n_f)$ carrying n_f fluorescent (non-quenched) dyes, and (3) the distribution of dextrans containing any dye (fluorescent or quenched) under the condition that at least one fluorescent dye is present, $P(n_{t(f)})$. While $P(n_t) = P(n_d)$, $P(n_f)$ can easily be obtained from eq. S1 by replacing DoL_{av} with $DoL_{\text{av}} \times x_f$. The fluorescent fraction of the dyes x_f is approximated by the relative quantum yield of the labelled dextran as compared to the corresponding free dye, $x_f = \Phi_F^{\text{dextran}} / \Phi_F^{\text{free dye}}$ (see S1.2). The third distribution, $P(n_{t(f)})$, is obtained for $n_a \geq n_{t(f)} > 0$ from $P(n_t)$ by randomly distributing quenched dyes among the labelled dextrans, i.e. multiplying a second binomial distribution with $P(n_t)$ and adding the probabilities for all species with the same n_t that contain at least one fluorescent label. The unlabelled fraction is $P(n_{t(f)} = 0) = P(n_f = 0)$.

By omitting the corresponding unlabelled fractions ($n_t = 0$, $n_f = 0$ or $n_{t(f)} = 0$, respectively), three different effective degrees of labelling, DoL_{eff}^{x}, can be calculated from the obtained distributions using eq. S2:

$$DoL_{eff}^{x} = \sum_{n_x=1}^{n_a} n_x P(n_x) \Big/ \sum_{n_x=1}^{n_a} P(n_x) \qquad \text{(S2)}$$

with $x = t, f$ or $t(f)$, as defined above.

For A488-D10, the sample investigated in greatest detail in the current study, this will be shown in the following (table S3). For this sample $DoL_{av} = 1$ as determined by the manufacturer and $x_f = 0.62$ for the fluorescent fraction of the labels (see lifetime analysis S1.2) was assumed. Since the number of initial amino groups (n_a) per dextran could not be obtained from the manufacturer an average number of n_a=5 was estimated (being the mean $<n_a>$ for the currently available 18 batches of unlabelled aminodextrans D10 as specified on the manufacturers homepage). Choosing n_a=4 or n_a=6 does not significantly change the following considerations.

n_x	0	1	2	3	4	5	DoL^x_{eff}	x_f
$P(n_t)$	0.328	0.410	0.205	0.051	0.006	3×10^{-4}	1.49	1
$P(n_f)$	0.515	0.365	0.104	0.015	0.001	3×10^{-5}	1.28	0.62
$P(n_{t(f)})$	0.515	0.254	0.175	0.048	0.006	0.003	1.60	0.62

Table S3. Expected distribution of probabilities of labelled dextrans D10 ($P(n_t)$) assuming random labelling and a binomial distribution of the labels number, n_t, as well as corresponding distributions taking the fluorophores partial static quenching into account ($P(n_f)$ and $P(n_{t(f)})$. DoL_{av}=1, available labelling sites n_a=5. x_f is the fluorescent (non-quenched) fraction of the dyes. DoL^x_{eff} with $x = t, f, t(f)$ are the effective degrees of labelling considering all labels and labelled dextrans, only fluorescent labels and fluorescently labelled dextrans and all labels but only fluorescent dextrans, respectively.

The estimation of $DoL^{t(f)}_{eff}$ assumed only static quenching for the partially quenched sample and thus presents a border case, but can be justified by the fact that, according to fluorescence lifetime analysis, the fraction of completely quenched dyes significantly exceeds the dynamically quenched portion (26% vs. 18%). The distribution of the total number of labels ($P(n_t)$ or $P(n_{t(f)})$) is relevant for the estimation of average ionic charges carried by the label. Here $P(n_{t(f)})$ yields the higher number of the two but might be an overestimation, since partial quenching of the individual fluorophores was excluded. Thus the true value of $DoL^{t(f)}_{eff}$ as required to estimate the molecular charge due to labelling is expected to be in between the lower and upper limits as calculated via $P(n_t)$ and $P(n_{t(f)})$, respectively.

The distribution of fluorescent labels, $P(n_f)$, has implications on the molecular brightness as observed by FCS as will be shown in S1.4.

S1.4. *Implications of the distribution of molecular brightnesses for quantitative FCS*:

In FCS the molecular brightness B is estimated by dividing the detected fluorescence count rate F by the observed number of fluorescent molecules, N_{tot}, simultaneously present in the confocal detection volume element, $B = F/N_{tot}$. In case of identical brightness of all particles N_{tot} can directly be obtained from the amplitude of the correlation function (eq. 4 main document, $N_{tot}=N$ for negligible triplet population). A distribution of brightnesses as discussed above would increase the observed amplitude, i.e. yielding an apparent (or effective) number of molecules N_{eff} (eq. S3).[3]

$$N_{eff} = N_{tot}\left(\sum_{n_f} n_f P(n_f)\right)^2 \Big/ \sum_{n_f} n_f^2 P(n_f) \qquad \text{(S3)}$$

Applying eq. S3 to the numbers in the table S3 yields N_{eff}=0.856 N_{tot}. With $DoL_{eff,\ f.}$=1.28 an effective molecular brightness $B^{A488\text{-}D10}/B^{A488}$=1.28/0.856=1.5 is predicted and fully confirmed by experiment ($B^{A488\text{-}D10}$≈6.8 kHz/molecule, B^{A488}≈4.5 kHz/molecule; → $B^{A488\text{-}D10}/B^{A488}$ =1.5). Ignoring the distribution of labels would falsify the determined molecular concentrations by almost 15 % and the corresponding brightnesses by 50 %. To derive the total number of dextran molecules, N_{dex}, in the confocal volume in addition the non-fluorescent labels portion needs to be considered ($P(n_f=0)$ = 0.515, table SI 3): $N_{dex}=N_{eff}\cdot(0.856)^{-1}\times\ (1\text{-}0.515)^{-1}=2.41\cdot N_{eff}$. Comparing the concentrations of a series of A488-D10/H_2O solutions (not shown) as determined by FCS (confocal detection volume element V_{det}=0.55 fl) and its extinction (71,000 $cm^{-1}M^{-1}$ at 496 nm, Invitrogen) we find $N_{dex}(exp)$=2.9 N_{eff}, consistent with the estimated number within the anticipated uncertainties of the confocal volume determination (±15 %), the measured quantum yield (± 10 %), the average degree of labelling (manufacturers specification) and the approximations made by calculating the dye distributions.

The experimental confirmation of the estimated effective brightness justifies the assumption made above of a random distribution of the quenched labels. An alternative scenario, e.g. quenching due to dye-dye interaction, might be indicated by the similarity of the estimated portion of the singly labelled dextrans ($P(n_t=1)$ =0.41, corresponding to 61 % of the labelled molecules) and the fraction of unquenched dye as determined by TCSPC (56 %). This would lead to an expected effective molecular brightness of the dextran A488-D10 close to the free dye brightness and is not consistent with our FCS results.

S1.5. *Effect of immobile fluorophores on molecular brightness in FCS*:

In a stationary confocal measurement, i.e. keeping the location of the confocal volume fixed, the number of fluorophores that are immobile on the time scale of the experiment, N_{immob}, will not contribute to fluctuations of the fluorescence, provided temporary dark state population is negligible. In that case their fluorescence, F_{immob}, can be considered like uncorrelated background. This would reduce the correlation amplitude, $1/N_{mob}$ (the inverse number of diffusing fluorescent particles) corresponding to the fluorescence, F_{mob}, of mobile fluorophores and yield an apparent amplitude, $1/N_{app}$[3].

$$N_{mob} = N_{app}\left(\frac{F_{mob}}{F_{mob}+F_{immob}}\right)^2 = N_{app}\left(\frac{F_{mob}}{F_{tot}}\right)^2 \tag{S4}$$

$F_{tot}=F_{mob}+F_{immob}$ is the total fluorescence, $N_{tot}=N_{mob}+N_{immob}$ the total number of fluorescent particles. For brightness $B_{mob}=B$ of mobile and $B_{immob}=n_iB$ of immobile particles follows (with $n_i>0$):

$$N_{mob} = N_{app}\left(\frac{N_{mob}}{N_F}\right)^2 = N_{app}\left(\frac{N_{mob}}{N_{mob}+n_iN_{immob}}\right)^2 = N_{app}\left(\frac{N_{mob}}{n_iN_{tot}-(n_i-1)N_{mob}}\right)^2.$$

Here N_F is the equivalent total number of fluorophores with brightness B. With the apparent brightness $B_{app}=\frac{F_{tot}}{N_{app}}$ we get

$$B = \frac{F_{mob}}{N_{mob}} = \frac{F_{tot}}{n_iN_{tot}-(n_i-1)N_{mob}} = B_{app}\frac{N_{app}}{n_iN_{tot}-(n_i-1)N_{mob}} \quad \text{and}$$

$$\begin{aligned} &N_{mob} = N_{app}\left(\frac{B_{app}}{B}\right)^2 \\ &n_iN_{tot}-(n_i-1)N_{mob} = N_{app}\frac{B_{app}}{B} = \frac{F_{tot}}{B} \\ &\Rightarrow \frac{n_iN_{tot}-(n_i-1)N_{mob}}{N_{mob}} = \frac{B}{B_{app}} = \frac{n_iN_{tot}}{N_{mob}}-(n_i-1) \\ &\Rightarrow x_{mob} = \frac{N_{mob}}{N_{tot}} = n_i\left(\frac{B}{B_{app}}+n_i-1\right)^{-1} = 1-x_{immob} \end{aligned} \tag{S5}$$

Provided translational diffusion is the only process leading to fluorescence fluctuations, e.g. for $n_i=1$ (identical brightness), the mobile fraction can easily be obtained from $x_{mob}=N_{mob}/N_{tot}=B_{app}/B$. Thus the apparent change in molecular brightness as determined by stationary FCS can give information about the portion of mobile species otherwise invisible to this method.

For the samples studied, in particular the A488-D10, only a minor change in fluorescence lifetime due to quenching upon entering the hydrogel was observed ($\tau_{gel}/\tau_{sol}\approx0.97$, approximately half of the effect being caused by refractive index changes. See main document and S1.6), suggesting that the average molecular brightness in a first approximation can be considered as unaffected by the hydrogel. From FCS investigations of different concentrations of A488-D10/H_2O in the hydrogel between 30 and 100 nM we obtained an apparent molecular brightness of $B_{app}\approx2.5$ kHz/molecule. With $B\approx6.8$ kHz/molecule as measured free in solution a completely immobile fraction of $x_{immob}\approx0.63$ would have to be concluded from eq. S5. Since higher labelled molecules are preferentially trapped (see main document) this must be considered as an upper limit. In case all immobile particles were doubly labelled and the mobile ones would carry one fluorophore ($B_{mob}=B^{A488}=4.5$ kHz/molecule$=0.5B_{immob}$) an estimation according to the above analysis would yield $x_{mob}=2/((B/B_{app})+1)$ and $x_{immob}\approx0.29$. This is higher than the estimated fraction of A488-D10 with $n_f>1$ (12 %, table S3) and could indicate an enrichment of higher labelled dextrans inside the hydrogel, consistent with the observation of a higher binding constant for those probe molecules (main document).

S1.6. *Refractive index mismatch – effect on fluorescence lifetime and diffusion measurements*:

Inside the PAAm hydrogel the refractive index, n, is reported to be slightly higher than in dilute aqueous solutions.[4] For the densities of hydrogels and the wavelength used in our study a linear dependence of $dn/dc'=0.188$ ml/g can be extracted, with c' being the mass of PAAm per ml hydrogel. With $n_0=1.3361$ for water ($\lambda=525$ nm and T=22 °C)[5] and the measured densities of the gels (see main document, converted using a density of $\rho_{(PAA)}=1.3$ g/cm^3) we estimate the refractive indices in table S4.

Based on the refractive index, changes in radiative lifetimes, τ_r, can be calculated according to Toptygin by a modified Strickler-Berg approach.[6] The empty spherical cavity model (ESC, Toptygin, eq. 59) was found to successfully describe radiative lifetimes of small fluorophores in solution (eq. S1.5):

$$\frac{\tau_{r,2}}{\tau_{r,1}}=\left(\frac{n_1}{n_2}\right)^5\left(\frac{2n_2^2+1}{2n_1^2+1}\right)^2 \qquad \text{(S6)}$$

$\tau_{r,1}$ and n_1 are radiative lifetime and index of refraction in water, $\tau_{r,2}$ and n_2 the corresponding quantities in the gel (table S.4).

hydrogel	c [ml/ml]	c' [g/ml]	n	$\tau_{r(gel)}/\tau_{r(sol)}$
pH7	0.038	0.049	1.3454	0.987
ph10	0.015	0.020	1.3398	0.995

Table S4. Index of refraction at λ=525 nm and T=22 °C for PAAm hydrogels and its estimated effect on radiative lifetimes.

For A488 and A488-D10 the observed changes in fluorescence lifetimes are bigger than the predicted changes in radiative lifetime, suggesting additional fluorescence quenching due to matrix effects (see main document).

The relative small deviation of n from n_0 (H_2O) is well within the range of the correction collar of current water immersion objectives. This was shown for a Zeiss CApo40x/1.2 W objective,[7] comparable to our Olympus UPlanSApo 60x/1.2 W, and verified by experiment. Furthermore, in a calibration measurement we confirmed that for our conditions (wavelength, depth of the focal point in the sample) no readjustment of the correction collar setting was required after switching the sample from pure water to hydrogel.

S1.7. Binding model

A simple binding model was applied to describe the observed equilibrium fractions of mobile and trapped probe molecules:

$$\begin{aligned} K_d &= \frac{a_{bound}}{a_{free} \cdot a_{sites}} \\ K_d^{'} &\approx K_d \cdot a_{sites} = \frac{a_{bound}}{a_{free}} \approx \frac{c_{bound}}{f_{free} c_{free}} \\ &\Rightarrow \frac{c_{bound}}{c_{free}} = f_{free} K_d^{'} \\ &\Rightarrow \frac{c_{bound}}{c_{free} + c_{bound}} = x_{bound} = \frac{f_{free} K_d^{'}}{1 + f_{free} K_d^{'}} \end{aligned} \tag{S7}$$

Here, K_d is the binding constant, a the activity for free (a_{free}) and bound (a_{bound}) molecules with the respective concentration (c_{bound} and c_{free}). The number of binding sites in the matrix a_{sites} defines the effective binding constant K_d'.

Results

S2. *Image integrated normalized correlations curves measured in hydrogel for A488-Dx and TMR-Dx in water and for FLU-Dx in carbonate buffer 20 mM pH 10*

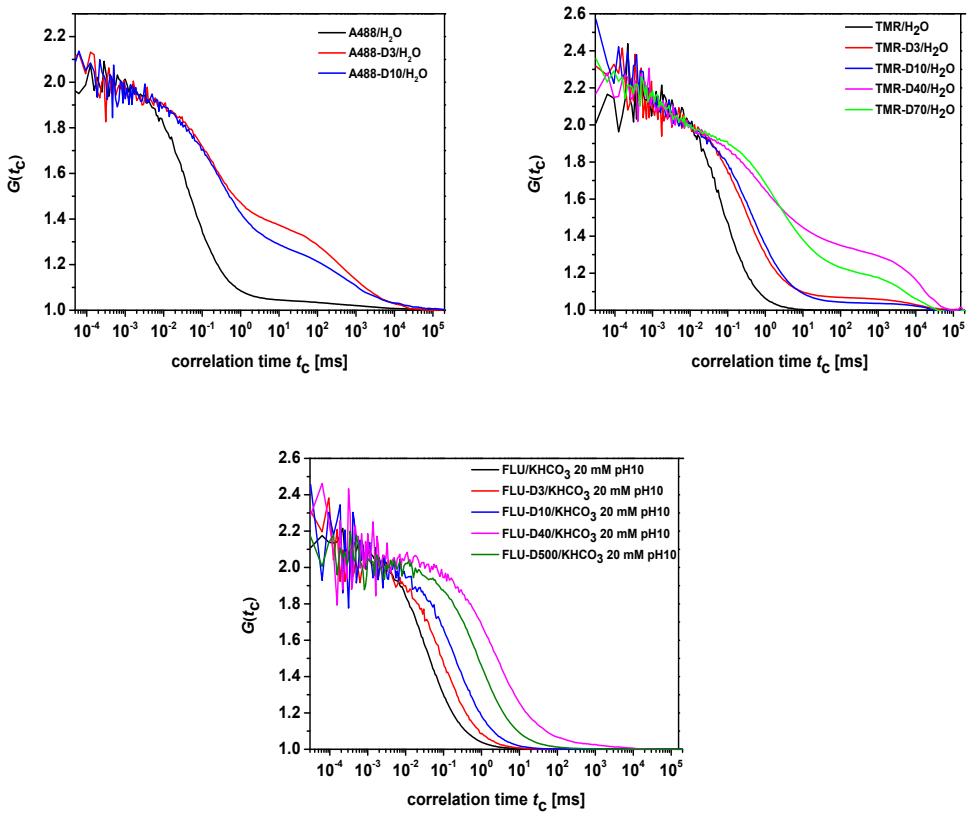

Figure S1. Image integrated normalized correlations curves for A488 and TMR free dye and with dextran in hydrogel in water conditions. In this case, more than one diffusion time is clearly visible, indicating the presence of temporarily trapped molecules in the hydrogel. FLU samples were measured in carbonate buffer 20 mM, pH 10, in this case the bound molecules are much less, only for samples D40 and D500 trapping is visible and amounts to about 1%.

S3. *Diffusion times from FCS experiments in the hydrogel at standard conditions*

Table S5 shows the diffusion times for A488, TMR and FLU for free dye and with dextran at standard conditions: water for A488 and TMR, carbonate buffer pH 10 for FLU in the hydrogel.

Dye	**Sample**	**Solvent**	**fast component**		**slow component**	
			t_d **[ms]**	**fraction x**	t_d **[ms]**	**fraction x**
A488	Free dye	H_2O	0.049 ± 0.002	0.991	200-500	0.009
A488	D3	H_2O	0.220 ± 0.007	0.626	10-2000	0.374
A488	D10	H_2O	0.410 ± 0.017	0.704	10-6000	0.296
TMR	Free dye	H_2O	0.065 ± 0.001	1	-	0
TMR	D3	H_2O	0.272 ± 0.010	0.873	10-8000	0.127
TMR	D10	H_2O	0.363 ± 0.011	0.962	1000-10000	0.038
TMR	D40	H_2O	1.699 ± 0.105	0.688	20-10000	0.312
TMR	D70	H_2O	2.026 ± 0.079	0.719	40-12000	0.281
FLU	Free dye	$KHCO_3$ 20 mM pH 10	0.036 ± 0.001	1	-	0
FLU	D3	$KHCO_3$ 20 mM pH 10	0.116 ± 0.001	1	-	0
FLU	D10	$KHCO_3$ 20 mM pH 10	0.263 ± 0.004	1	-	0
FLU	D40	$KHCO_3$ 20 mM pH 10	0.823 ± 0.032	0.992	10-140	0.008
FLU	D500	$KHCO_3$ 20 mM pH 10	3.664 ± 0.470	0.988	20-3000	0.012

Table S5. Results of FCS fits for A488, TMR and FLU (free dye and labelled dextran) in hydrogel. For some samples fitting the model function to the data required two or more diffusion times. In the latter case the fraction of the slow component (last column) is the sum of two terms that in total represent the fraction of trapped molecules. The diffusion times of fast components are the averages from different pixels. For the slow component, t_d is given as range because it significantly differs from pixel to pixel.

S4. *Diffusion times from FCS experiments for Rh110, A488, TMR and FLU free dye and labelled D10 at different salt conditions in the hydrogel.*

Sample	**Solvent**	**fast component**		**slow component**	
		t_d [ms]	**fraction x**	**t_d [ms]**	**fraction x**
Rh110	H_2O	0.036	1	-	0
A488	H_2O	0.049	0.991	200-500	0.009
A488-D10	H_2O	0.410	0.704	10-6000	0.296
A488-D10	$KClO_4$ 10 mM	0.384	0.832	10-6000	0.168
A488-D10	$KClO_4$ 20 mM	0.383	0.875	10-6000	0.125
A488-D10	KCl 20 mM	0.352	0.904	400-6000	0.096
A488-D10	$KClO_4$ 40 mM	0.401	0.900	10-6000	0.100
A488-D10	$KClO_4$ 60 mM	0.352	0.910	10-6000	0.090
A488-D10	$KHCO_3$ 20 mM pH 7	0.345	0.924	400-6000	0.076
A488-D10	$KHCO_3$ 20 mM pH 10	0.354	0.930	400-6000	0.070
TMR-D10	H_2O	0.363	0.960	500-7000	0.040
TMR-D10	$KHCO_3$ 20 mM pH 10	0.303	1	-	0
TMR-D10	TRIS 50 mM pH 7.5	0.212	1	-	0
FLU-D10	$KHCO_3$ 20 mM pH 10	0.265	1	-	0
FLU-D10	H_2O	0.260	1	-	0
FLU-D10	TRIS 50 mM pH 7.5	0.262	1	-	0

Table S6. Results of FCS fits for the reference Rh110, A488, A488-D10, TMR-D10 and FLU-D10 in solution and in the hydrogel at different salt conditions. For some samples fitting the model function to the data required two or more diffusion times. In the latter case the fraction of the slow component (last column) is the sum of two terms that in total represent the fraction of trapped molecules. The diffusion times of the fast components are the averages obtained from different pixels. For the slow component, t_d is given as range because it significantly differs from pixel to pixel.

S5. *Trace analysis*

The fluorescence time trace was split into small segments and sorted according to their approximated mean count rate employing a special feature of the binary single photon data format *.ht3 (PicoQuant, Berlin, Germany). Depending on the inter-photon time (i.e. the inverse count rate) in addition to the photon information extra entries are generated to store each overflow of the macroscopic time counter. Thus, sections containing the same total number of entries (as were generated upon splitting the recorded file) can be sorted by their content of photons and extra entries and thereby by their mean count rate. The produced subsets of split files were subsequently correlated and analyzed.

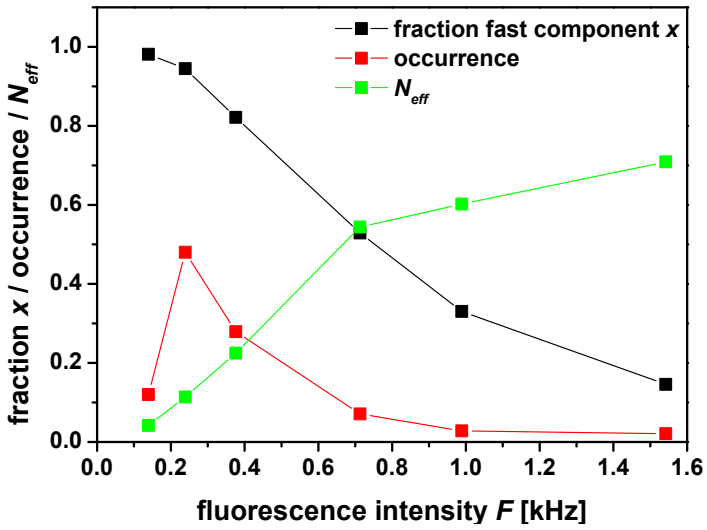

Figure S2. Fraction of fast component x, effective mean fluorophore number N_{eff} and occurrence of different count-rate based sections in time trace (Main document Figure 4). N_{eff} is the inverse correlation amplitude at τ_c=0 and corresponds to the total number of diffusing molecules in case of equal brightness for all components. Temporary accumulation of particles due to trapping is clearly visible.

S6. *Fluorescence intensity ratio between gel and the solution surrounding the gel plotted against experimental concentration for A488-D10 in H_2O from FCS measurements*

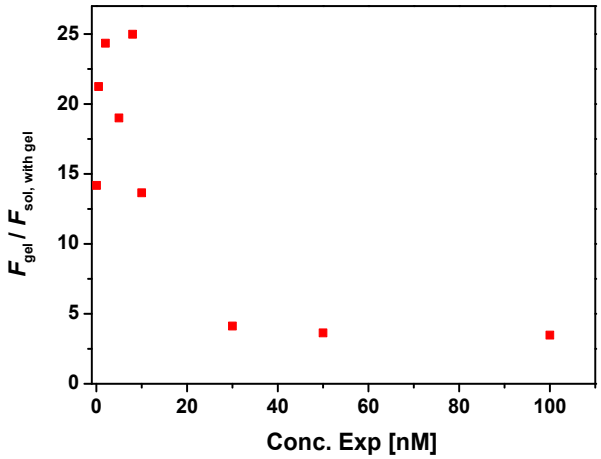

Figure S3. The plot shows that the fluorescence intensity ratio between gel and the solution surrounding the gel, F_{gel} / $F_{sol\ with\ gel}$, is decreasing with increasing experimental concentration. The enrichment of the fluorophores inside the gel, as indicated by the fluorescence intensity ratio is concentration dependent and strongest for small concentrations until high-affinity trap sites are saturated.

S7. *Fluorescence anisotropies of A488-D10, TMR-D10 and FLU-D10 in solution and hydrogel*

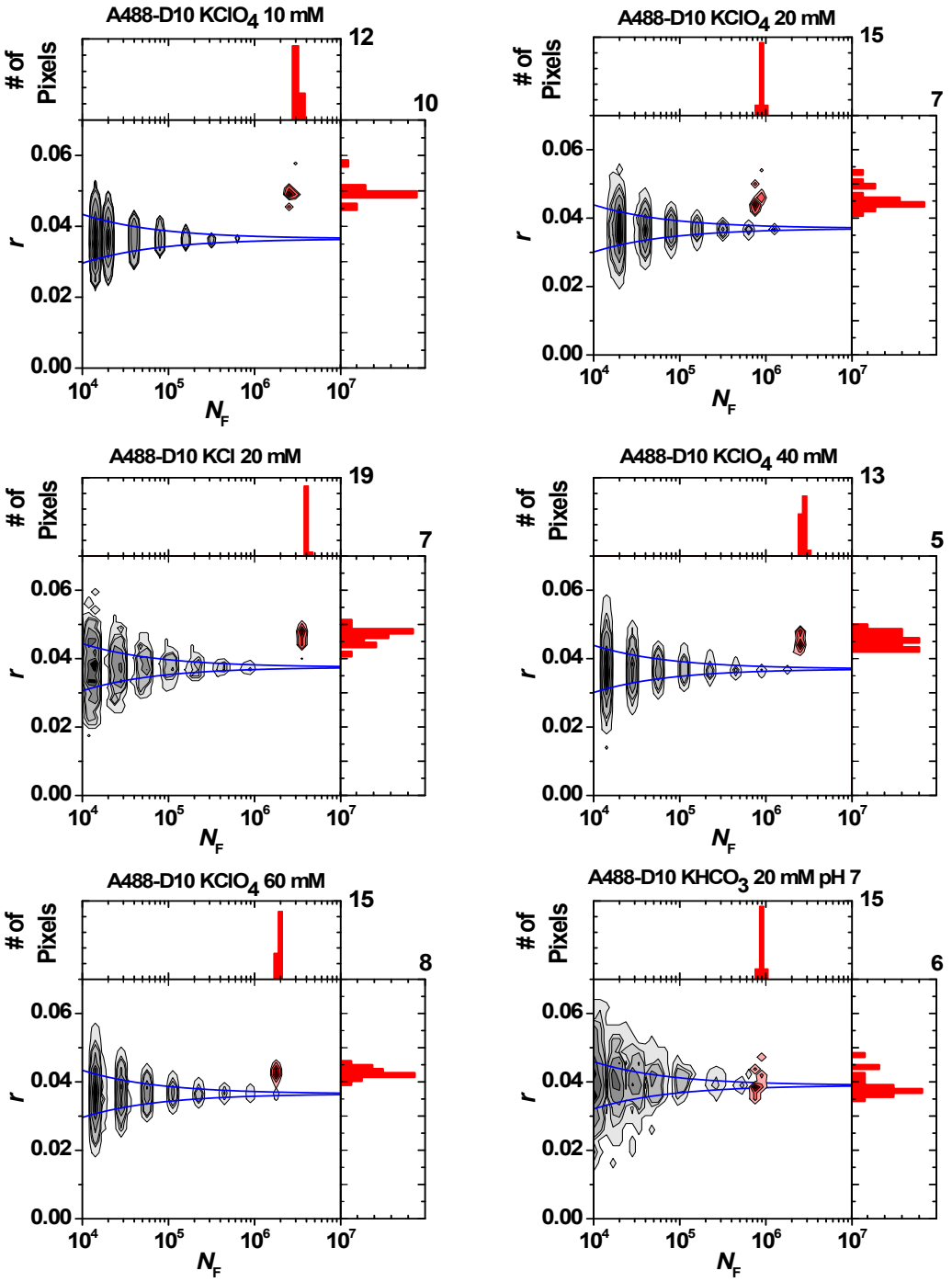

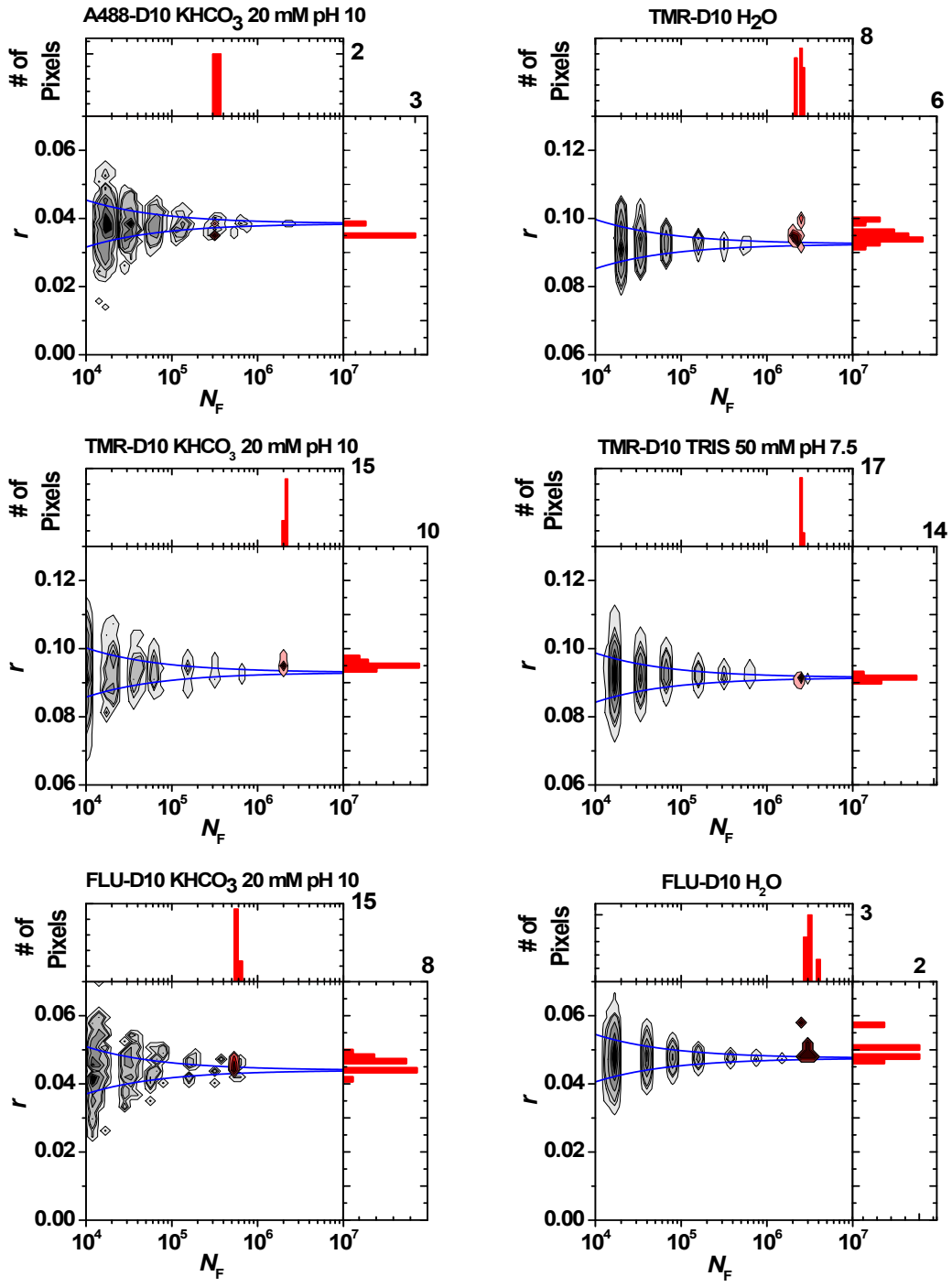
A488-D10 KHCO3 20 mM pH 10
TMR-D10 H2O
TMR-D10 KHCO3 20 mM pH 10
TMR-D10 TRIS 50 mM pH 7.5
FLU-D10 KHCO3 20 mM pH 10
FLU-D10 H2O
# of Pixels
r
NF

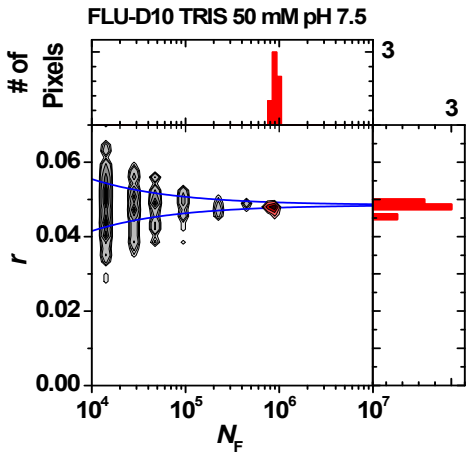

Figure S4. 2D plots of anisotropy r vs. photon number N_F for A488-D10, TMR-D10 and FLU-D10 in solution (gray contour lines) and in hydrogel (red contour lines) with 1D projections for the gel data.

For A488-D10 the plots show markedly different anisotropies inside the hydrogel for different solvent conditions. In case of $KClO_4$ 10 mM, 20 mM, 40 mM and KCl 20 mM the anisotropy in the gel is higher as compared to the solution value, in these cases the trapped fraction is≥10 %. The decrease in anisotropy starts with higher ionic strength: 60 mM $KClO_4$ and 20 mM in carbonate buffer pH 7 and 10, clearly correlated with the trapped fraction of the molecules as determined by FCS. For TMR-D10 and FLU-D10 the anisotropy is slightly higher or equal in comparison to solution measurements in different conditions (trapped fraction≤4%).

S8. *Fluorescence anisotropy A488-D10, TMR-D10 and FLU-D10*

Sample	**Solvent**	***r***		**Trapped fraction**
		Solution	**Hydrogel**	**x**
Rh110	H_2O	0.010	0.010	0
A488	H_2O	0.014	0.018	0.011
A488-D10	H_2O	0.037	0.049	0.296
A488-D10	$KClO_4$ 10 mM	0.037	0.049	0.168
A488-D10	$KClO_4$ 20 mM	0.037	0.046	0.125
A488-D10	KCl 20 mM	0.037	0.046	0.096
A488-D10	$KClO_4$ 40 mM	0.037	0.045	0.100
A488-D10	$KClO_4$ 60 mM	0.036	0.041	0.090
A488-D10	$KHCO_3$ 20 mM pH 7	0.039	0.040	0.076
A488-D10	$KHCO_3$ 20 mM pH 10	0.037	0.037	0.070
TMR-D10	H_2O	0.093	0.096	0.040
TMR-D10	$KHCO_3$ 20 mM pH 10	0.093	0.094	0
TMR-D10	TRIS 50 mM pH 7.5	0.092	0.092	0
FLU-D10	$KHCO_3$ 20 mM pH 10	0.044	0.046	0
FLU-D10	H_2O	0.047	0.049	0
FLU-D10	TRIS 50 mM pH 7.5	0.047	0.047	0

Table S7. Average anisotropy (*r*) for Rh110, A488, A488-D10, TMR-D10 and FLU-D10 in solution and in the hydrogel for different salt conditions.

S9. *Reference data*

Published experimental hydrodynamic radii for dextrans labelled with A488, TMR or fluorescein are compiled in Figure SI 5.

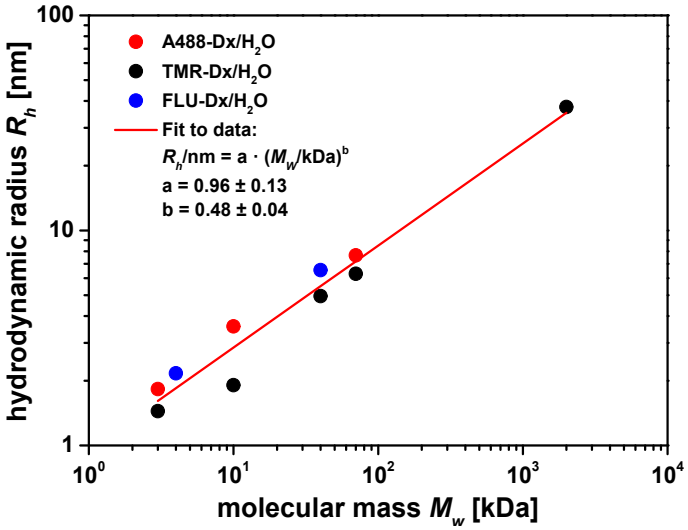

Figure S5. Fit of Flory scaling law to reference data for A488-D3 & A488-D10[8], A488-D70[9], TMR-Dx[10] and FLU-Dx[8]. R_h was taken as published or calculated via Stokes-Einstein equation. The systematic difference between TMR-Dx data (measured at 23 °C) and A488-Dx and Flu-Dx data (measured at 32 °C, except A488-D70 measured at 25 °C) is mainly attributed to calibration uncertainties. Reported temperature effects on R_h of dextrans in the relevant temperature and size range are about one order of magnitude smaller than the deviation of the two data sets and in the opposite direction: $-\Delta R_h/(R_h \Delta T) < 0.003\ \mathrm{K}^{-1}$ (extracted from Figure 1 in ref.[11]).

S10. *NMR Measurements*

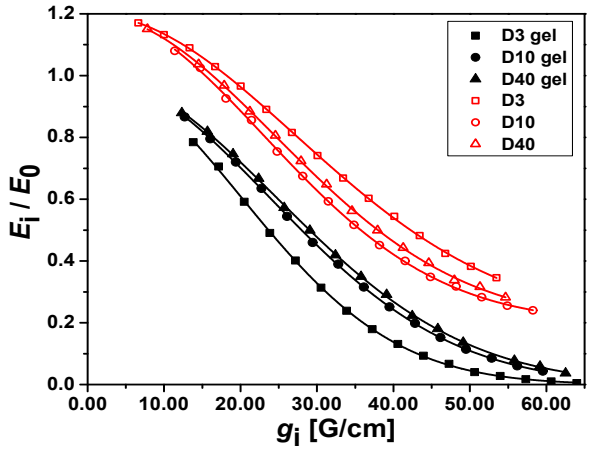

Figure S6. NMR data and fits for unlabelled dextrans (3 kDa, 10 kDa and 40 kDa) in hydrogels and in D_2O. Data was normalized and *xy* offset-corrected. For clarity reasons, the solution data (red) was vertically offset by 0.2.

The diffusion coefficients *D* were obtained by fitting the echo amplitudes (integral of the signals between 2.8 and 4.4 ppm) using Eq.7 (See main text). We performed several diffusion measurements with each sample, varying the key parameters δ and Δ_N and keeping constant the values of $\tau_N = 0.001$ s and γ=26752.22005 rad/s Gauss. Several combinations of Δ_N and δ were applied and the specific parameters are listed in the table S8.

	Solution			**Hydrogel**		
	δ [µs]	**Δ_N [s]**	**D_{sol} [10^{-10}m^2/s]**	**δ [µs]**	**Δ_N [s]**	**D_{gel} [10^{-10}m^2/s]**
D3	600	0.60	1.12	600	1.80	0.67
	800	0.30	1.15	700	1.40	0.65
	1000	0.10	1.16	800	1.00	0.68
D10	1000	0.30	0.97	750	1.70	0.30
	1200	0.25	0.96	1000	1.30	0.33
	1600	0.10	0.97	1500	0.50	0.31
D40	800	1.00	0.38	1200	1.60	0.096
	1000	0.80	0.38	1300	2.00	0.085
	1200	0.60	0.37	1400	1.80	0.096

Table S8. Parameters used for NMR measurements for unlabelled dextrans D3, D10 and D40. The fit provides the diffusion coefficient for each sample for the different experimental settings. The rows marked in yellow represent the curves shown in figure S6.

S11. *Technical details of the Brownian dynamics simulation*

General

In our Brownian dynamics simulation[12], we use a cubic simulation box with periodic boundary conditions containing 512 matrix particles and 1 tracer particle. About 200 independent simulation runs have been performed to generate typical trajectories for the statistical averages of the tracer's mean square displacements. The Brownian equations of motion were integrated with an Euler-algorithm. The time step Δt for the integration was chosen as $\Delta t < 2 \cdot 10^{-5}\ \tau_B$ (for model 1, 2 and 3a, TMR) and $\Delta t < 1.5 \cdot 10^{-6}\ \tau_B$ (for model 3b, TMR). $\tau_B = a^2 / D_0$ denotes the Brownian time. Here, a is the lattice constant of the matrix and D_0 the diffusion constant of the tracer particle in a pure solvent as obtained from the experiments. For FLU, Δt had to be chosen 10 times smaller. We carefully checked that the results for the statistical averages did not change upon further decreasing the time step such that the magnitude of Δt was small enough.

Simulation protocol

In our simulations we used the following protocol:

- Generation of the underlying gel structure:
  - The gel obstacles were placed on a simple cubic lattice of lattice constant a.
  - The matrix particles were randomly shifted up to half the lattice constant in each direction in model 2, 3a and 3b.
  - Springs were attached between the centers of neighboring matrix particles which were all undistorted, i.e. the rest lengths equaled exactly the corresponding particle separations.
- The tracer particle was placed in a void.
- The BD simulation was started and the system was equilibrated for a typical time of $t_{eq} >= 1\ \tau_B$.
- Statistics for the dynamical correlations was gathered by storing at least 100000 snapshots of the tracer trajectory $\vec{s}(t)$ at equidistant times within a sufficiently large time window of $t_{max} >= 40\tau_B$. In this time window, the tracer moved on average a distance of several lattice constants a.

Calculation of the hindrance factors

It was carefully checked that the long-time limit of the tracer's mean square displacement $\Delta s^2(t) = \left\langle \left(\vec{s}(t_0 + t) - \vec{s}(t_0)\right)^2 \right\rangle$ was reached. Here, <…> denotes the average over all $t_0 \in [0, t_{max} - t]$ and all independent simulation runs. The diffusion coefficient was obtained as $D = \lim_{t\to\infty} \frac{1}{6} \frac{d}{dt} \Delta s^2(t)$.[12, 13] As for an example, see Figure S7. We then performed a fitting procedure to describe the experimental hindrance factors $H=D/D_0$ as a function of R_h.

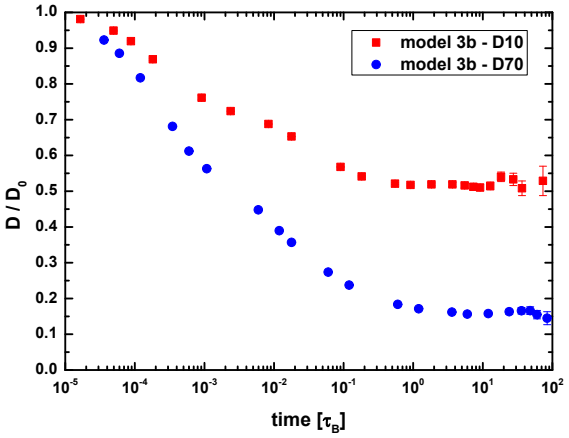

Figure S7. Hindrance factor D/D_0 versus time for two different tracers (D10 and D70) within model 3b. For very short times, the Diffusion coefficient approaches the Diffusion coefficient in solution D_0, as no collisions occur during these times. The long-time-limes is reached before 1 τ_B, as the diffusion coefficient does not decrease any further

Parameters

All model parameters were fixed according to Table S9 except the lattice constant a, which sets the pore size, and the obstacle radius R_{obst}, which was scaled with a factor such that the constraint of the experimentally prescribed volume fraction, φ, (measured by swelling analysis, see main text Sec.2.1.1) was fulfilled: $R_{obst} = \sqrt[3]{\frac{3\varphi}{4\pi}} a$. This leads to a coarse-grained obstacle radius comparable to the tracer size at least of the same order of magnitude. The additive diameters σ_{ij} used in Eq. (8), (10), (11) were therefore also fixed by $\sigma_{ij}=2\ R_{obst}$ for the obstacle-obstacle-interaction and $\sigma_{ij}=R_{obst} + R_h$ for the interaction between a matrix obstacle and a tracer of radius R_h. For the guest particle radii

R_h, we used our experimental values (see R_h in Table 3 in the results, 3.2.1). The short-time diffusivity of the obstacles was calculated via the Stokes-Einstein relation $D_{obst} = \frac{k_B T}{6\pi\eta R_{obst}}$. Here, η = 0.00095 Pa s is the viscosity of the solvent at T = 295 K (= 22 °C). We used ε_s=1 k_BT for the WCA-potential used in model 1, 2 and 3b. In model 3a, we used ε_G =12 k_BT since this value is above the value of 2 k_BT, which is found for self-avoiding polymers [14] but we expect our system to be stiffer. We have changed ε_G within the range of 4 k_BT and 20 k_BT and did not obtain an improved fit to the experimental data.

In conclusion, out of the 12 parameters shown in Table S9, 9 are fixed by physical constraints, namely the obstacle radius R_{obst}, and consequently also the obstacle self-diffusion constant D_{obst} and the additive diameters $\sigma_{obst,\ obst}$, $\sigma_{obst,\ D0}$, $\sigma_{obst,\ D3}$, $\sigma_{obst,\ D10}$, $\sigma_{obst,\ D40}$, $\sigma_{obst,\ D70}$, $\sigma_{obst,\ D500}$. Hence only 3 parameters are left: The lattice constant a, the spring constant k and the interaction parameters ε_s, resp. ε_G, (plus possibly the parameter ε_a in model 3b). ε_a and a are real fit parameters. We have checked that a change of k and the interaction parameters ε_s, resp. ε_G give indifferent fit quality.

Fitting and conclusion

For the fixed choice of a, the whole hindrance factors H were simulated as a function of R_h, i.e. for all tracer radii used in the experiments. These sets of simulation data were compared to the experimental data and an optimal value of a was obtained by the best fit. For model 3b, two fit parameters were used, namely the lattice constant a and the attraction strength ε_a. This results in better fitting in particular for small R_h. We remark here that the attraction was essential. In a purely repulsive dextran-matrix interaction model, a second fit parameter would not give a significant improvement of the fit. Additional simulations performed within model 3b using a Gaussian softened core showed a similar fit quality as that with a WCA-core such that we conclude that the attraction itself rather than the details of the repulsion is crucial to describe the experimental data properly.

Dye	Model	initial gel simple cubic lattice constant [10^{-9}m]	obstacle radius [10^{-9}m]	obstacle self diffusion constant [10^{-11}m^2/s]	spring constant [10^{-4}N/m]	Matrix-dextran-interaction parameters (at T=20 °C) [10^{-20}J]	$\sigma_{obst,obst}$ [10^{-9}m]	$\sigma_{obst,D0}$ [10^{-9}m]	$\sigma_{obst,D3}$ [10^{-9}m]	$\sigma_{obst,D10}$ [10^{-9}m]	$\sigma_{obst,D40}$ [10^{-9}m]	$\sigma_{obst,D70}$ [10^{-9}m]	$\sigma_{obst,D500}$ [10^{-9}m]
TMR	**1**	11.75	2.48	0	inf	$\varepsilon_s = 1k_BT \approx 0.405$	4.95	3.03	4.19	5.55	8.48	10.34	
	2	11.75	2.48	9.18	6.17	$\varepsilon_s = 1k_BT \approx 0.405$	4.95	3.03	4.19	5.55	8.48	10.34	
	3a	10.03	2.11	10.77	6.17	$\varepsilon_G = 12k_BT \approx 4.86$	4.23	2.66	3.82	5.18	8.11	9.97	
	3b	14.35	3.02	7.52	6.17	$\varepsilon_s = 1k_BT \approx 0.405$ $\varepsilon_a = 3k_BT \approx 1.21$	6.05	3.57	4.73	6.09	9.02	10.88	
FLU	**1**	31.73	4.86	0	inf	$\varepsilon_s = 1k_BT \approx 0.405$	9.73	5.41	6.57	7.93	10.86		25.16
	2	31.73	4.86	4.68	6.17	$\varepsilon_s = 1k_BT \approx 0.405$	9.73	5.41	6.57	7.93	10.86		25.16
	3a	30.29	4.64	4.90	6.17	$\varepsilon_G = 12k_BT \approx 4.86$	9.29	5.19	6.35	7.71	10.64		24.94
	3b	44.71	6.85	3.32	6.17	$\varepsilon_s = 1k_BT \approx 0.405$ $\varepsilon_a = 3k_BT \approx 1.21$	13.71	7.40	8.56	9.92	12.85		27.15

	D0	D3	D10	D40	D70	D500
radius [10^{-9}m]	0.55	1.7	3.1	6.0	7.9	20

Table S9. Parameters used for Brownian dynamics simulations for model 1 (fixed gel matrix, steric interaction), model 2 (flexible gel matrix, steric interaction), model 3a (flexible gel matrix, soft interaction), model 3b (flexible gel matrix, steric interaction and attractive shell).

References

1. D. Magde, R. Wong and P. G. Seybold, *Photochem. Photobiol.*, 2002, **75**, 327-334.
2. X.-F. Zhang, Y. Zhang and L. Liu, *J. Lumin.*, 2014, **145**, 448-453.
3. N. L. Thompson, in *Topics in Fluorescence Spectroscopy*, ed. J. R. Lakowicz, Plenum Press, New York, 1991, vol. 1, pp. 337-378.
4. J. Stejskal and J. Horská, *Makromol. Chem.*, 1982, **183**, 2527-2535.
5. *Release on the Refractive Index of Ordinary Water Substance as a Function of Wavelength, Temperature and Pressure*, The International Association for the Properties of Water and Steam, Erlangen, Germany, 1997.
6. D. Toptygin, *J. Fluoresc.*, 2003, **13**, 201-219.
7. E. Banachowicz, A. Patkowski, G. Meier, K. Klamecka and J. Gapinski, *Langmuir*, 2014, **30**, 8945-8955.
8. T. Kihara, J. Ito and J. Miyake, *PLoS One*, 2013, **8**, e82382.
9. S. Lehmann, S. Seiffert and W. Richtering, *J. Am. Chem. Soc.*, 2012, **134**, 15963-15969.
10. Z. Zhang, E. Nadezhina and K. J. Wilkinson, *Antimicrob. Agents Chemother.*, 2011, **55**, 1075-1081.
11. M. A. Masuelli, *J. Polym. Biopolym. Phys. Chem.*, 2013, **1**, 13-21.
12. M. P. Allen and D. J. Tildesley, *Computer Simulation of Liquids (Oxford Science Publications)*, Oxford University Press, 1989.
13. B. J. Alder, D. M. Gass and T. E. Wainwright, *J. Chem. Phys*, 1970, **53**, 3813-3826.
14. A. A. Louis, P. G. Bolhuis, E. J. Meijer and J. P. Hansen, *J. Chem. Phys*, 2002, **117**, 1893-1907.

Veröffentlichung II Hard rectangles near curved hard walls: Tuning the sign of the Tolman length

C. E. Sitta, F. Smallenburg, R. Wittkowski & H. Löwen
Hard rectangles near curved hard walls: Tuning the sign of the Tolman length,
J. Chem. Phys. **145**, 204508 (2016),
veröffentlicht durch *AIP Publishing*.

Digital Object Identifier (DOI): 10.1063/1.4967876

Stellungnahme zum eigenen Beitrag

H.L., R.W. und ich haben das Forschungsprojekt entwickelt.
H.L. und R.W. haben das Forschungsprojekt betreut.
F.S. hat die MC Simulationen implementiert und durchgeführt.
Ich habe die analytischen Rechnungen in Kapitel II.A durchgeführt.
F.S. hat die analytischen Rechnungen in Kapitel II.B durchgeführt.
Ich habe die numerische Minimierung der Dichtefunktionaltheorie implementiert und durchgeführt.
R.W. hat Abb. 1 erstellt.
R.W., F.S. und ich haben Abb. 2 erstellt.
R.W. und ich haben Abb. 3-6 erstellt.
Alle Autoren haben die Ergebnisse interpretiert und das Manuskript geschrieben.

Lizenzhinweise und Copyright

THE JOURNAL OF CHEMICAL PHYSICS **145**, 204508 (2016)

Hard rectangles near curved hard walls: Tuning the sign of the Tolman length

Christoph E. Sitta, Frank Smallenburg, Raphael Wittkowski,[a] and Hartmut Löwen
Institut für Theoretische Physik II: Weiche Materie, Heinrich-Heine-Universität Düsseldorf, D-40225 Düsseldorf, Germany

(Received 7 September 2016; accepted 3 November 2016; published online 30 November 2016)

Combining analytic calculations, computer simulations, and classical density functional theory we determine the interfacial tension of orientable two-dimensional hard rectangles near a curved hard wall. Both a circular cavity holding the particles and a hard circular obstacle surrounded by particles are considered. We focus on moderate bulk densities (corresponding to area fractions up to 50%) where the bulk phase is isotropic and vary the aspect ratio of the rectangles and the curvature of the wall. The Tolman length, which gives the leading curvature correction of the interfacial tension, is found to change sign at a finite density, which can be tuned via the aspect ratio of the rectangles. *Published by AIP Publishing.* [http://dx.doi.org/10.1063/1.4967876]

I. INTRODUCTION

When a fluid is in contact with a wall, the interfacial tension (also called "wall tension") γ measures the free-energy cost per boundary area due to the presence of the wall. Many boundary and interfacial effects are governed and controlled by the interfacial tension γ. For example, the wetting properties of a wall by a liquid droplet in the bulk gas phase depend crucially on the wall-gas, wall-liquid, and bulk liquid-gas interfacial tensions as described by Young's famous equation for the contact angle.[1,2] Moreover, heterogeneous nucleation at the wall is strongly affected by the interfacial tension.[3] Simple classical theory for heterogeneous nucleation[4,5] predicts that the size of the critical nucleus is determined by the degree of undercooling and the interfacial tensions between the wall, the bulk phase, and the nucleating phase.[6]

In the simplest case, the wall is planar in three spatial dimensions or a straight line in a two-dimensional system. However, in many practical situations the wall is curved. Examples are provided by spherical obstacles or impurities which can act as a seed for heterogeneous nucleation, by porous materials with a lot of inner curved walls and cavities, and by a rough or patterned substrate.[7,8] This raises the question of the curvature dependence of the interfacial tension γ. For weak curvature, Tolman suggested the asymptotic series expansion[9]

$$\gamma(R) = \gamma(\infty)\left(1 - \frac{2\ell_\mathrm{T}}{R} + \mathcal{O}(R^{-2})\right), \tag{1}$$

where R is the radius of curvature of the wall, $\gamma(\infty)$ is the interfacial tension for an uncurved wall, and the constant ℓ_T, which has the dimensions of a length, is referred to as the *Tolman length*.[10] Of particular importance is the sign of the Tolman length. If it is negative, there is a free-energy penalty upon bending the wall, whereas a positive Tolman length implies a free-energy decrease for a curved wall. For a flexible wall which can change shape, a positive Tolman length would induce a spontaneous curvature of the wall under appropriate conditions.

Therefore, there is a need to understand the sign of the Tolman length on a microscopic (i.e., particle-resolved) level. This is achieved best for simple model systems of classical statistical mechanics. Hard objects have been studied extensively in this respect as temperature scales out and density is the only relevant thermodynamic parameter.[11–13] In three spatial dimensions, hard spheres near a hard wall have received considerable attention.[14,15] The interfacial tension between a planar hard wall and a fluid hard-sphere bulk phase has been explored by computer simulations[16–20] and provides an ideal testing ground for the performance of approximations in classical density functional theory (DFT) of inhomogeneous fluids.[21–26] Subsequent analytic calculations,[27] simulations,[28] and DFT calculations[29–31] have considered a curved wall exposed to a hard-sphere fluid and found a negative sign of the Tolman length for hard spheres around a spherical obstacle. Moreover, the Tolman length has been accessed for other interactions such as (modified) Lennard-Jones potentials[20,32–38] or Yukawa potentials,[32,39] at phase boundaries[37,40] and in lattice models.[41] In some systems with not only excluded volume interactions, such as a Lennard-Jones fluid, the magnitude and sign of the Tolman length are still under debate.[33,35,36,38,39,92,93]

However, no studies have been done so far for the Tolman length of orientable shape-anisotropic particles, which have a nontrivial rotational degree of freedom. These particles show more complex structuring near walls as both translational and orientational degrees of freedom are coupled. Although one of the simplest of such systems, namely, orientable hard rectangles in two spatial dimensions near a wall, has been intensely studied by means of experiments,[42–45] simulations,[46–49] DFT calculations,[45,49–52] and other theories,[53] the curvature dependence of the interfacial tension in this system has not yet been explored. Here we close this gap. At moderate aspect ratios, hard rectangles exhibit a stable isotropic phase at densities up to at least 50% in area fraction (also called "packing fraction")

[a] Present address: Institut für Theoretische Physik, Westfälische Wilhelms-Universität Münster, D-48149 Münster, Germany.

but display significantly more complex ordering at higher densities.[54] For various aspect ratios and particle number densities corresponding to a bulk isotropic state, we explore in detail the effects of both a concave and a convex wall, corresponding, respectively, to a circular cavity holding the rectangles and a hard circular obstacle surrounded by rectangles.

Our results are threefold: first, we show that this model yields an *analytic expression* for the Tolman length at low densities. This is remarkable as any analytic result is helpful in testing approximative theories and understanding qualitative trends directly. Second, we calculate the Tolman length for a range of densities and aspect ratios in the isotropic phase by Monte Carlo (MC) computer simulations and thermodynamic integration. Interestingly, we find a zero in the Tolman length at finite density. This implies that the Tolman length is *tunable* to a large extent via particle shape and density. Finally, we perform DFT calculations for the Tolman length and discuss their performance by comparing the DFT results with our simulation data. For all investigated aspect ratios, we observe good agreement between MC simulations and DFT calculations up to moderate densities.

The paper is organized as follows: in Sec. II, analytic expressions for the Tolman length in systems with a concave and a convex wall, respectively, are derived. Our MC simulations and DFT calculations are described in Sec. III. The results of our analytic and numerical calculations are presented and discussed in Sec. IV. Finally, we conclude in Sec. V.

II. ANALYTIC CALCULATIONS

We study a two-dimensional system of orientable hard rectangular particles with length $L \geq \sigma$ and width σ in the presence of a hard unstructured wall. The wall has a constant radius of curvature R so that it forms either a circular cavity (concave wall) containing the rectangular particles (see Fig. 1(a)) or a circular obstacle (convex wall) surrounded by the particles (see Fig. 1(b)). In the latter case, we assume periodic boundary conditions far away from the circular obstacle. We define the domain $\mathcal{A}$ of the system as the total area accessible to any part of a rectangle (i.e., the light blue areas in Fig. 1). The limiting case $R \to \infty$ of an infinite wall curvature radius corresponds to a system with a flat wall, which has already been studied in detail.[3,16,18–20,44,46,48,50,55] For the three situations of a flat wall, a cavity containing the particles, and an obstacle surrounded by the particles, we are interested in the particle number density $\rho(\vec{r}, \phi)$, which denotes the probability to find a particle with orientation ϕ at center-of-mass position $\vec{r} = (x, y)$, the interfacial tension $\gamma(R)$, and the Tolman length ℓ_T. While for high particle concentrations the quantities $\rho(\vec{r}, \phi)$, $\gamma(R)$, and ℓ_T are difficult to determine analytically, in the low-density limit, interactions between the particles can be neglected and analytic results can be obtained. Therefore, in this section we will focus on low densities. We start with considering the ideal-gas limit where particle-particle interactions are completely negligible. Afterwards we extend our results to higher but still small densities on the level of a second-order virial expansion.

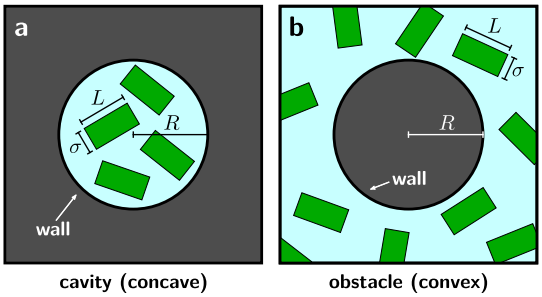

FIG. 1. A two-dimensional system of hard rectangular particles with length L and width σ either (a) confined by a circular hard wall that forms a cavity with radius R or (b) surrounding a circular hard wall that forms an obstacle with radius R.

Note that we define the interfacial tension γ, and therefore the Tolman length ℓ_T, in the grand-canonical ensemble, i.e.,[29]

$$\gamma = \frac{\Omega_{\text{wall}} - \Omega_{\text{bulk}}}{L_{\text{wall}}}, \tag{2}$$

using the grand-canonical free energy of the system in the presence (Ω_{wall}) and absence (Ω_{bulk}) of a wall of length L_{wall}, at fixed temperature T and chemical potential μ. Similar definitions can be written down in other ensembles (using, e.g., the Helmholtz free energy), which are equivalent in the thermodynamic limit for both flat walls and circular obstacles. However, in the case of a circular cavity, the length and curvature of the wall are inherently linked to the system size, which leads to an ensemble-dependence of the apparent Tolman length if Eq. (1) is followed directly.

A. Tolman length in the ideal-gas limit

In the ideal-gas limit, where particle-particle interactions can be completely neglected, the particle number density in the grand-canonical ensemble is given by

$$\rho(\vec{r}, \phi) = \frac{\rho_0}{2\pi} e^{-\beta U(\vec{r}, \phi)} \tag{3}$$

with the constant bulk particle number density $\rho_0 = e^{\beta\mu}/\Lambda^2$. Here, $\beta = 1/(k_B T)$ is the inverse thermal energy with Boltzmann's constant k_B and Λ is the thermal de Broglie wavelength corresponding to the particles. $U(\vec{r}, \phi)$ is the wall potential that describes the interaction of a particle with center-of-mass position $\vec{r}$ and orientation ϕ with the hard wall. This potential is ∞ if $\vec{r} \notin \mathcal{A}$ or if the particle and the wall (partially) overlap and 0 otherwise. The wall potential $U(\vec{r}, \phi)$ and thus the particle number density $\rho(\vec{r}, \phi)$ can therefore be determined by simple geometrical considerations. (For analogous calculations for spherocylinders in three spatial dimensions see Ref. 94.) If $\rho(\vec{r}, \phi)$ is known, one can calculate the interfacial tension γ from Eq. (2). Since particle-particle interactions can be neglected in the ideal-gas limit, the grand-canonical free energies Ω_{wall} and Ω_{bulk} are here given by the exact analytic expressions[56]

$$\Omega_{\text{wall}} = \frac{1}{\beta} \int_{\mathcal{A}} \mathrm{d}^2 r \int_0^{2\pi} \mathrm{d}\phi\, \rho(\vec{r}, \phi) \Big(\ln(2\pi\Lambda^2 \rho(\vec{r}, \phi)) - 1 + \beta U(\vec{r}, \phi) - \beta\mu \Big), \tag{4}$$

$$\Omega_{\text{bulk}} = -\frac{A e^{\beta\mu}}{\beta\Lambda^2} \tag{5}$$

with the domain area $A = |\mathcal{A}|$.

Together with Eq. (3), inserting Eqs. (4) and (5) into Eq. (2) leads to the interfacial tension

$$\gamma = -\frac{p}{L_{\text{wall}}}\left(\frac{1}{2\pi}\int_{\mathcal{A}} \mathrm{d}^2 r \int_0^{2\pi} \mathrm{d}\phi\, e^{-\beta U(\vec{r},\phi)} - A\right) \tag{6}$$

with the bulk pressure

$$p = \frac{e^{\beta\mu}}{\beta\Lambda^2}. \tag{7}$$

From γ the Tolman length ℓ_{T} is obtained by expansion (1). In the following, the quantities $U(\vec{r},\phi)$, which gives $\rho(\vec{r},\phi)$ when inserted into Eq. (3), $\gamma(R)$, and ℓ_{T} are given both for circular and rectangular particles in systems with a flat wall, a cavity (concave wall), and an obstacle (convex wall).

1. Hard disks

For disk-shaped particles of radius R_0, the orientation ϕ of the particles is trivial due to their full rotational symmetry.

a. Flat wall. We consider a flat wall at $x = 0$ and circular particles with center-of-mass positions at $x > 0$. The wall potential is then given by

$$U(\vec{r},\phi) = \begin{cases} \infty, & \text{if } x \le R_0, \\ 0, & \text{if } R_0 < x. \end{cases} \tag{8}$$

Using Eq. (6), one obtains the interfacial tension

$$\gamma = \gamma(\infty) = pR_0 \tag{9}$$

with the bulk pressure p for a circular particle given by Eq. (7).

b. Cavity (concave wall). If a circular particle is inside a circular cavity of radius R centered at $\vec{r} = \vec{0}$, its interaction with the wall of length $2\pi R$ is described by the potential

$$U(\vec{r},\phi) = \begin{cases} 0, & \text{if } r < R - R_0, \\ \infty, & \text{if } R - R_0 \le r, \end{cases} \tag{10}$$

with $r = |\vec{r}|$ denoting the distance of the particle's center of mass from the center of the cavity. Using Eq. (6), one obtains the interfacial tension

$$\gamma(R) = \gamma(\infty)\left(1 - \frac{R_0}{2}\frac{1}{R}\right). \tag{11}$$

Note that this expression is exact and no higher-order terms appear. The corresponding Tolman length is $\ell_{\text{T}} = R_0/4$.

c. Obstacle (convex wall). A circular obstacle with radius R centered at $\vec{r} = \vec{0}$ interacts with a circular particle via the potential

$$U(\vec{r},\phi) = \begin{cases} \infty, & \text{if } r \le R + R_0, \\ 0, & \text{if } R + R_0 < r, \end{cases} \tag{12}$$

with $r = |\vec{r}|$ denoting the distance of the particle's center of mass from the center of the obstacle. The integral

$$A_{\text{f}} = \frac{1}{2\pi}\int_{\mathcal{A}} \mathrm{d}^2 r \int_0^{2\pi} \mathrm{d}\phi\, e^{-\beta U(\vec{r},\phi)} \tag{13}$$

in Eq. (6) is basically the angle-averaged free area that is accessible for a particle's center of mass. Its calculation simplifies significantly when using $A_{\text{f}} - A = -(A_{\text{ov}} - A_{\text{o}})$ and the following expression for the overlap area A_{ov} of an arbitrary convex particle with area A_{p} and circumference O_{p} and an arbitrary convex obstacle with area A_{o} and circumference O_{o}:[57]

$$A_{\text{ov}} = A_{\text{p}} + A_{\text{o}} + \frac{O_{\text{p}} O_{\text{o}}}{2\pi}. \tag{14}$$

For the special case of a circular obstacle with radius R, the interfacial tension for any convex particle reads according to Eq. (6)

$$\gamma(R) = p\frac{A_{\text{p}} + O_{\text{p}} R}{2\pi R}. \tag{15}$$

Inserting $A_{\text{p}} = \pi R_0^2$ and $O_{\text{p}} = 2\pi R_0$ into Eq. (15) and using Eq. (9), this simplifies to the interfacial tension for circular particles

$$\gamma(R) = \gamma(\infty)\left(1 + \frac{R_0}{2}\frac{1}{R}\right). \tag{16}$$

The corresponding Tolman length is $\ell_{\text{T}} = -R_0/4$.

2. Hard rectangles

The calculation of the free area A_{f} becomes more complicated for rectangular particles with length L and width σ as their orientation ϕ must be considered. Due to the discrete rotational symmetry of the rectangles, only angles $\phi \in [0, \pi/2]$ need to be taken into account. In the following, the diameter of the rectangles is denoted as $D = \sqrt{L^2 + \sigma^2}$ and the angle between the long side of a rectangle and its diagonal is denoted as $\alpha = \arctan(\sigma/L)$.

a. Flat wall. We consider the same situation as in Sec. II A 1 a, but now for rectangular particles. The angle ϕ is defined as the angle between the wall, i.e., the y axis, and the long side of the rectangle. Depending on the rectangle's distance to the wall, only certain angles are allowed for ϕ, i.e., correspond to $U(\vec{r},\phi) < \infty$. The rectangle's center of mass at distance x from the wall must not approach the wall closer than $\sigma/2$. For $x > \sigma/2$ all angles between 0 and a threshold angle

$$\phi_1(x) = \arcsin(2x/D) - \alpha \tag{17}$$

are allowed, at which a rectangle's corner touches the wall. Additionally, for $x > L/2$ the rectangle can be orthogonal to the wall ($\phi = \pi/2$) and also rotate around this orientation up to another threshold angle

$$\phi_2(x) = -\arcsin(2x/D) + \pi - \alpha \tag{18}$$

at which the same corner collides with the wall again. For $x \ge D/2$ the particle cannot overlap with the wall. This results in the following wall potential (with $0 \le \phi \le \pi/2$):

$$U(\vec{r},\phi) = \begin{cases} 0, & \text{if } \sigma/2 < x \le L/2 \wedge \phi \in [0, \phi_1(x)], \\ 0, & \text{if } L/2 < x \le D/2 \\ & \quad \wedge \phi \in [0, \phi_1(x)] \cup [\phi_2(x), \pi/2], \\ 0, & \text{if } D/2 < x, \\ \infty, & \text{otherwise.} \end{cases} \tag{19}$$

The interfacial tension is then according to Eq. (6)

$$\gamma = \gamma(\infty) = p\frac{L + \sigma}{\pi}, \tag{20}$$

with the bulk pressure p for a rectangular particle given by Eq. (7).

b. Cavity (concave wall). The wall potential for a rectangular particle in a cavity with radius R centered at $\vec{r} = \vec{0}$ can be written as

$$U(\vec{r},\phi) = \begin{cases} 0, & \text{if } r < R - \frac{D}{2}, \\ 0, & \text{if } R - \frac{D}{2} \le r < \sqrt{R^2 - \frac{\sigma^2}{4}} - \frac{L}{2} \\ & \quad \wedge \phi \in [0, \phi_3(r)] \cup \left[\phi_4(r), \frac{\pi}{2}\right], \\ 0, & \text{if } \sqrt{R^2 - \frac{\sigma^2}{4}} - \frac{L}{2} \le r < \sqrt{R^2 - \frac{L^2}{4}} - \frac{\sigma}{2} \\ & \quad \wedge \phi \in [0, \phi_3(r)], \\ \infty, & \text{otherwise}, \end{cases} \tag{21}$$

with $r = |\vec{r}|$ denoting the distance of the rectangle's center of mass from the center of the cavity and ϕ defined as the angle between $\vec{r}$ and a short side of the rectangle. The contact angles of the rectangle's corner with the wall are in analogy to Sec. II A 2 a

$$\phi_3(r) = \arccos\Big(\frac{r^2 + \frac{D^2}{4} - R^2}{Dr}\Big) - \frac{\pi}{2} - \alpha, \tag{22}$$

$$\phi_4(r) = \frac{3\pi}{2} - \alpha - \arccos\Big(\frac{r^2 + \frac{D^2}{4} - R^2}{Dr}\Big). \tag{23}$$

In a circular cavity, the accessible area for a rectangle's center of mass is independent of the orientation ϕ due to the rotational symmetry of the cavity. This simplifies the integration in Eq. (6) and the interfacial tension reads

$$\begin{aligned} \gamma(R) = \frac{p}{2\pi R}\Big(&\pi R^2 - L\sigma + L\sqrt{R^2 - \frac{L^2}{4}} + \sigma\sqrt{R^2 - \frac{\sigma^2}{4}} \\ &+ 2R^2 \arctan\Big(\frac{\sigma}{\sqrt{4R^2 - \sigma^2}}\Big) \\ &- 2R^2 \arctan\Big(\sqrt{\frac{4R^2}{L^2} - 1}\Big)\Big). \end{aligned} \tag{24}$$

The series expansion

$$\begin{aligned} \gamma(R) = \gamma(\infty)\Big(1 &- \frac{L\sigma}{2(L+\sigma)}\frac{1}{R} - \frac{L^3 + \sigma^3}{24(L+\sigma)}\frac{1}{R^2} \\ &- \frac{L^5 + \sigma^5}{640(L+\sigma)}\frac{1}{R^4} + \mathcal{O}(R^{-6})\Big) \end{aligned} \tag{25}$$

with respect to $1/R$ at $R \to \infty$ results in the Tolman length $\ell_T = L\sigma/(4(L+\sigma))$.

c. Obstacle (convex wall). The wall potential for a rectangular particle outside of a circular obstacle with radius R centered at $\vec{r} = \vec{0}$ is given by

$$U(\vec{r},\phi) = \begin{cases} 0, & \text{if } R + \frac{\sigma}{2} \le r < \sqrt{R^2 + \frac{D^2}{4} + R\sigma} \\ & \quad \wedge \phi \in [0, \phi_5(r)], \\ 0, & \text{if } \sqrt{R^2 + \frac{D^2}{4} + R\sigma} \le r < R + \frac{D}{2} \\ & \quad \wedge \phi \in [0, \phi_6(r)], \\ 0, & \text{if } R + \frac{L}{2} < r \le \sqrt{R^2 + \frac{D^2}{4} + RL} \\ & \quad \wedge \phi \in \left[\phi_7(r), \frac{\pi}{2}\right], \\ 0, & \text{if } \sqrt{R^2 + \frac{D^2}{4} + RL} < r \le R + \frac{D}{2} \\ & \quad \wedge \phi \in \left[\phi_8(r), \frac{\pi}{2}\right], \\ 0, & \text{if } R + \frac{D}{2} < r, \\ \infty, & \text{otherwise}, \end{cases} \tag{26}$$

with $r = |\vec{r}|$ denoting the distance of the rectangle's center of mass from the center of the obstacle, ϕ defined as the angle between $\vec{r}$ and a short side of the rectangle, and the contact angles

$$\phi_5(r) = \arccos\Big(\frac{R + \frac{\sigma}{2}}{r}\Big), \tag{27}$$

$$\phi_6(r) = \arcsin\Big(\frac{r^2 + \frac{D^2}{4} - R^2}{Dr}\Big) - \alpha, \tag{28}$$

$$\phi_7(r) = \arcsin\Big(\frac{R + \frac{L}{2}}{r}\Big), \tag{29}$$

$$\phi_8(r) = \arccos\Big(\frac{r^2 + \frac{D^2}{4} - R^2}{Dr}\Big) - \alpha + \frac{\pi}{2}. \tag{30}$$

Here, the rectangle is not restricted to touch the wall with a corner (corresponding to the contact angles $\phi_6(r)$ and $\phi_8(r)$). It can also touch the wall with its edges. Therefore, additional cases appear in the potential, where $\phi = \phi_5(r)$ corresponds to a collision with a long edge and $\phi = \phi_7(r)$ corresponds to a collision with a short edge. The interfacial tension can be calculated analogously to the situation for a circular particle in Sec. II A 1 c by inserting $A_p = L\sigma$ and $O_p = 2(L+\sigma)$ into Eq. (15) and is given by

$$\gamma(R) = \gamma(\infty)\Big(1 + \frac{L\sigma}{2(L+\sigma)}\frac{1}{R}\Big). \tag{31}$$

Note that this analytic result is exact and no terms of higher order in $1/R$ appear. The corresponding Tolman length is $\ell_T = -L\sigma/(4(L+\sigma))$.

Comparing the Tolman lengths for disks and rectangles derived above, two features are remarkable. First, the only difference between the Tolman lengths for the cavity and the obstacle is the sign. Second, for both a cavity and an obstacle, the magnitude of the Tolman length is related to the particle's area A_p and circumference O_p via $|\ell_T| = A_p/(2O_p)$. We note here that in ensembles other than the grand-canonical one, neither of these two features is reproduced. For example, in the canonical ensemble we can define the interfacial tension

$$\gamma_F = \frac{F_{wall} - F_{bulk}}{L_{wall}}, \tag{32}$$

where F denotes the Helmholtz free energy and the systems with and without wall are compared at equal particle number N, domain area A, and temperature T. For an ideal gas, we then have

$$\beta F = N \ln(N\Lambda^2/A_f) - N \tag{33}$$

with A_f as defined in Eq. (13). Note that in the canonical ensemble, the overall density N/A is fixed rather than the bulk density ρ_0. As a result, any change in local density near the walls has to be compensated by a change in the bulk density. This is in contrast to the grand-canonical ensemble, where the bulk density is set by the external chemical potential. For flat walls and circular obstacles, γ_F converges to γ in the thermodynamic limit, i.e., when the domain area A is much larger than the region where a particle interacts with the wall. However, in the case of a cavity, this limit is only reached when $R \to \infty$. Explicitly performing the series expansion of γ_F in $1/R$ for hard disks with radius R_0, we obtain

$$\gamma_F(R) = \gamma(\infty)\Big(1 + \frac{R_0}{2}\frac{1}{R} + \mathcal{O}(R^{-2})\Big). \tag{34}$$

Similarly, for rectangular particles we obtain

$$\gamma_{\mathrm{F}}(R) = \gamma(\infty)\left(1 + \left(\frac{L+\sigma}{\pi} - \frac{L\sigma}{2(L+\sigma)}\right)\frac{1}{R} + \mathcal{O}(R^{-2})\right). \quad (35)$$

Comparison to Eqs. (11) and (24) shows significant changes to the term proportional to $1/R$, which defines the Tolman length. In fact, for a cavity in the canonical ensemble, we obtain a positive Tolman length for both disks and rectangles (regardless of L/σ), which is in contrast to a negative one in the grand-canonical ensemble. As this is essentially a finite-size effect, we define the interfacial tension in the remainder of this paper in the grand-canonical ensemble.

B. Low-density expansion of the Tolman length

The grand-canonical partition function Ξ is given by

$$\Xi = \sum_{N=0}^{\infty} \frac{e^{\beta\mu N}}{\Lambda^{2N}} Q_N. \quad (36)$$

Here, we have defined the N-particle partition function Q_N as

$$Q_N = \frac{1}{(2\pi)^N N!} \int_{\mathcal{A}} \mathrm{d}^{2N} r \int_0^{2\pi} \mathrm{d}^N \phi \, e^{-\beta U(\vec{r}^N, \phi^N)} \quad (37)$$

with the N-particle interaction potential $U(\vec{r}^N, \phi^N)$. In the limit of low chemical potential μ, the first few terms in the sum over N in Eq. (36) dominate. Expanding up to second order in the fugacity $z = \exp(\beta\mu)/\Lambda^2$, we obtain

$$\begin{aligned}\beta\Omega = -\ln(\Xi) &= -\ln(1 + zQ_1 + z^2 Q_2 + \mathcal{O}(z^3)) \\ &= -zQ_1 + z^2\left(\frac{Q_1^2}{2} - Q_2\right) + \mathcal{O}(z^3).\end{aligned} \quad (38)$$

Using Eq. (2), we can now write the interfacial tension γ as

$$\begin{aligned}\beta L_{\mathrm{wall}}\gamma = z(Q_1^{\mathrm{bulk}} - Q_1^{\mathrm{wall}}) + z^2\Big(&Q_2^{\mathrm{bulk}} - Q_2^{\mathrm{wall}} \\ &- \frac{1}{2}((Q_1^{\mathrm{bulk}})^2 - (Q_1^{\mathrm{wall}})^2)\Big) + \mathcal{O}(z^3).\end{aligned} \quad (39)$$

Here, Q_1^{bulk} and Q_1^{wall} are equal to A and A_{f}, respectively, with A_{f} as defined in Eq. (13). Additionally, $Q_2^{\mathrm{bulk}} = A(A - A_{\mathrm{ex}}^{\mathrm{bulk}})/2$, with $A_{\mathrm{ex}}^{\mathrm{bulk}}$ the orientationally averaged excluded area between two particles in the bulk, which is given by Eq. (14) as

$$A_{\mathrm{ex}}^{\mathrm{bulk}} = 2L\sigma + 2(L+\sigma)^2/\pi. \quad (40)$$

Thus, the only remaining unknown quantity is Q_2^{wall}, which can be written as

$$Q_2^{\mathrm{wall}} = \frac{1}{2(2\pi)^2} \int_{\mathcal{A}} \mathrm{d}^2 r_1 \int_{\mathcal{A}} \mathrm{d}^2 r_2 \int_0^{2\pi} \mathrm{d}\phi_1 \int_0^{2\pi} \mathrm{d}\phi_2 \, e^{-\beta(U_1 + U_2 + U_{12})}, \quad (41)$$

where U_1 and U_2 represent the interactions of particles 1 and 2 with the wall, respectively, and U_{12} is the pair-interaction potential of the particles. Although this integral is too cumbersome to tackle analytically, it can be rewritten as

$$Q_2^{\mathrm{wall}} = \frac{A_{\mathrm{f}}}{2}\left\langle \frac{1}{2\pi} \int_{\mathcal{A}} \mathrm{d}^2 r_2 \int_0^{2\pi} \mathrm{d}\phi_2 \, e^{-\beta(U_2 + U_{12})} \right\rangle_1, \quad (42)$$

where $\langle\cdot\rangle_1$ denotes averaging over all positions $\vec{r}_1 \in \mathcal{A}$ and orientations ϕ_1 of particle 1 which do not correspond to a particle-wall interaction. The expression in the average in Eq. (42) simply represents the free area available to particle 2 for a given choice of $\vec{r}_1$ and ϕ_1. Thus, Q_2^{wall} can be written as

$$Q_2^{\mathrm{wall}} = \frac{A_{\mathrm{f}}}{2}\left(A_{\mathrm{f}} - \langle A_{\mathrm{ex}}^{\mathrm{wall}}\rangle\right), \quad (43)$$

where $\langle A_{\mathrm{ex}}^{\mathrm{wall}}\rangle$ is the orientationally and translationally averaged excluded area between two particles in the given wall geometry. As $\langle A_{\mathrm{ex}}^{\mathrm{wall}}\rangle/A_{\mathrm{f}}$ is simply the probability that two non-interacting particles overlap in the same wall geometry, it can be numerically measured in simple two-particle MC simulations.

Combining Eqs. (39) and (43), we obtain

$$\beta\gamma = \frac{A - A_{\mathrm{f}}}{L_{\mathrm{wall}}} z - \frac{AA_{\mathrm{ex}}^{\mathrm{bulk}} - A_{\mathrm{f}}\langle A_{\mathrm{ex}}^{\mathrm{wall}}\rangle}{2L_{\mathrm{wall}}} z^2 + \mathcal{O}(z^3). \quad (44)$$

Rewriting this expression in terms of the bulk density

$$\begin{aligned}\rho_0 = \frac{\langle N\rangle}{A} &= \frac{1}{A}\frac{\sum_{N=0}^{\infty} N z^N Q_N}{\sum_{N=0}^{\infty} z^N Q_N} \\ &= z + z^2(2Q_2^{\mathrm{bulk}} - A^2)/A + \mathcal{O}(z^3)\end{aligned} \quad (45)$$

yields

$$\begin{aligned}\beta\gamma = &\frac{A - A_{\mathrm{f}}}{L_{\mathrm{wall}}}\rho_0 \\ &+ \frac{(A - A_{\mathrm{f}})A_{\mathrm{ex}}^{\mathrm{bulk}} + A_{\mathrm{f}}(\langle A_{\mathrm{ex}}^{\mathrm{wall}}\rangle - A_{\mathrm{ex}}^{\mathrm{bulk}})}{2L_{\mathrm{wall}}}\rho_0^2 \\ &+ \mathcal{O}(\rho_0^3).\end{aligned} \quad (46)$$

Note that the first term here corresponds to the ideal-gas limit considered in Sec. II A 2 as

$$\frac{A - A_{\mathrm{f}}}{L_{\mathrm{wall}}} = \frac{L+\sigma}{\pi}\left(1 + \frac{L\sigma}{2(L+\sigma)}\frac{1}{R}\right) \quad (47)$$

for the obstacle (the corresponding expression for the cavity can be obtained by substituting $R \to -R$ and adding $\mathcal{O}(R^{-2})$ on the right-hand side of Eq. (47)). We calculate $\langle A_{\mathrm{ex}}^{\mathrm{wall}}\rangle$ and the resulting interfacial tensions γ for walls with various radii of curvature and for several different aspect ratios. On this basis, we extract from our results the (linear) low-density behavior of the Tolman length.

III. NUMERICAL METHODS

In the following, we define the orientation ϕ of a rectangular particle as the angle measured counterclockwise from the y axis to the long axis of the particle (i.e., the particle is parallel to the y axis for $\phi = 0$). To calculate the particle number density $\rho(\vec{r}, \phi)$ and interfacial tension γ at moderate particle densities, where analytic results are no longer possible, we perform MC simulations and numerical calculations based on DFT. The Tolman length ℓ_{T} is again determined from the wall-curvature dependence of the interfacial tension γ. In this section, we describe both numerical approaches in detail.

A. Monte Carlo simulations

We perform MC simulations of perfectly hard rectangular particles in the grand-canonical ensemble and employ thermodynamic integration to obtain the interfacial tensions.[11] The simulations are performed at constant domain area $A = |\mathcal{A}|$,

constant chemical potential μ, and constant temperature T in the presence of flat or curved walls, as well as in the absence of walls. During each simulation, we measure the average number of particles $\langle N\rangle$ in the simulation box as well as average density profiles $\rho(\vec{r},\phi)$. Overlaps between rectangles are detected using the separating axis theorem (see, e.g., Ref. 58). Simulations are run for at least 10^{10} MC steps. For simulations where the particles are not completely confined by a wall, the area of the simulation box is chosen such that $A = 2500\sigma^2$.

To calculate the interfacial tension γ, we take the derivative of Eq. (2) with respect to the chemical potential μ and obtain

$$L_{\text{wall}}\frac{\mathrm{d}\gamma}{\mathrm{d}\mu} = \langle N\rangle_{\mu}^{\text{bulk}} - \langle N\rangle_{\mu}^{\text{wall}}. \tag{48}$$

Here, $\langle N\rangle_{\mu}^{\text{bulk}}$ and $\langle N\rangle_{\mu}^{\text{wall}}$ indicate the average number of particles in a simulation at chemical potential μ without and with a wall, respectively. Integrating with respect to μ from the low-density limit $\mu = -\infty$, we obtain

$$\gamma = \frac{1}{L_{\text{wall}}}\int_{-\infty}^{\mu}\mathrm{d}\mu'\,\left(\langle N\rangle_{\mu'}^{\text{bulk}} - \langle N\rangle_{\mu'}^{\text{wall}}\right). \tag{49}$$

Note that no additional integration constant is required as $\gamma(\mu = -\infty) = 0$. Thus, in order to calculate $\gamma(\mu)$ in each wall geometry, we integrate a fit to the simulation results $\langle N\rangle_{\mu}^{\text{bulk}} - \langle N\rangle_{\mu}^{\text{wall}}$. We make use of our analytic results for the ideal-gas limit (see Sec. II A) in order to improve accuracy at low chemical potential. Finally, to convert $\gamma(\mu)$ to a function of the bulk density ρ_0, we simply measure

$$\rho_0(\mu) = \frac{\langle N\rangle_{\mu}^{\text{bulk}}}{A} \tag{50}$$

in the simulations without walls.

B. Density functional theory

In addition to MC simulations, we use DFT calculations in order to obtain density profiles $\rho(\vec{r},\phi)$ and free energies. The Helmholtz free energy $\mathcal{F}$ of the system can be written as the sum of an ideal-gas term $\mathcal{F}_{\text{id}}$ and an excess term $\mathcal{F}_{\text{exc}}$

$$\mathcal{F} = \mathcal{F}_{\text{id}} + \mathcal{F}_{\text{exc}}. \tag{51}$$

While the free energy for an ideal gas $\mathcal{F}_{\text{id}}$ is analytically known and given by

$$\mathcal{F}_{\text{id}} = k_{\text{B}}T\int_{\mathcal{A}}\mathrm{d}^2r\int_0^{2\pi}\mathrm{d}\phi\,\rho(\vec{r},\phi)\left(\ln(\Lambda^2\rho(\vec{r},\phi)) - 1\right), \tag{52}$$

the exact excess term $\mathcal{F}_{\text{exc}}$ is only known in rare cases (e.g., for a hard-rod fluid in one spatial dimension[59]) and usually needs to be approximated.

An expression for the excess free energy $\mathcal{F}_{\text{exc}} = k_{\text{B}}T\int_{\mathcal{A}}\mathrm{d}^2r\,\Phi_{\text{exc}}(\vec{r})$ for hard rectangles in two spatial dimensions was proposed by Martínez-Ratón *et al.*[60] It is based on an approximation for the rescaled excess free-energy density $\Phi_{\text{exc}}(\vec{r})$. In order to match both the low-density and the high-density limit, they combined the Onsager approximation[61] and fundamental-measure theory (FMT).[62] Their expression for $\Phi_{\text{exc}}(\vec{r})$ also recovers results from scaled particle theory in the uniform limit.

In the scope of FMT, weighted densities $n_i(\vec{r})$ are defined as the angle-integrated cross correlations

$$\begin{aligned} n_i(\vec{r}) &= \int_0^{2\pi}\mathrm{d}\phi\,\left[\rho\star\omega^{(i)}\right](\vec{r},\phi)\\ &= \int_0^{2\pi}\mathrm{d}\phi\int_{\mathcal{A}}\mathrm{d}^2r'\,\rho(\vec{r}',\phi)\omega^{(i)}(\vec{r}'-\vec{r},\phi)\end{aligned} \tag{53}$$

of the density profile $\rho(\vec{r},\phi)$ with the geometric weight functions

$$\omega^{(0)}(\vec{r},\phi) = \frac{1}{4}\delta\left(\frac{\sigma}{2} - |x_\phi|\right)\delta\left(\frac{L}{2} - |y_\phi|\right), \tag{54}$$

$$\omega^{(2)}(\vec{r},\phi) = \Theta\left(\frac{\sigma}{2} - |x_\phi|\right)\Theta\left(\frac{L}{2} - |y_\phi|\right). \tag{55}$$

Here, $\delta(x)$ is the Dirac delta function, $\Theta(x)$ is the Heaviside function, $x_\phi = x\cos(\phi) - y\sin(\phi)$, and $y_\phi = x\sin(\phi) + y\cos(\phi)$. The approximative rescaled excess free-energy density reads[60]

$$\begin{aligned}\Phi_{\text{exc}}(\vec{r}) &= -n_0(\vec{r})\ln(1-n_2(\vec{r})) - \frac{n_0(\vec{r})n_2(\vec{r})}{1-n_2(\vec{r})}\\ &\quad + \frac{1}{2}\int_0^{2\pi}\mathrm{d}\phi\,\rho(\vec{r},\phi)\left[(1-n_2)^{-1}\star\omega^{(0)}\right](\vec{r},\phi)\\ &\quad \times\int_{\mathcal{A}}\mathrm{d}^2r'\int_0^{2\pi}\mathrm{d}\phi'\,\rho(\vec{r}',\phi')f(\vec{r}-\vec{r}',\phi,\phi'),\end{aligned} \tag{56}$$

where $f(\vec{r}-\vec{r}',\phi,\phi')$ is the (negative) Mayer function

$$f(\vec{r}-\vec{r}',\phi,\phi') = \begin{cases}1, & \text{if particles with coordinates}\\ & (\vec{r},\phi)\text{ and }(\vec{r}',\phi')\text{ overlap,}\\ 0, & \text{otherwise.}\end{cases} \tag{57}$$

To obtain the equilibrium density $\rho_{\text{eq}}(\vec{r},\phi)$, we minimize the grand-canonical free-energy functional

$$\Omega[\rho(\vec{r},\phi)] = \mathcal{F}[\rho(\vec{r},\phi)] - \mu\int_{\mathcal{A}}\mathrm{d}^2r\int_0^{2\pi}\mathrm{d}\phi\,\rho(\vec{r},\phi) \tag{58}$$

in real space with respect to $\rho(\vec{r},\phi)$ using a Picard iteration scheme[24] in combination with direct inversion in the iterative subspace (DIIS).[63–66]

For fixed values of the chemical potential μ, we calculate the equilibrium densities in the bulk, allowing to translate μ into the corresponding bulk area fraction η. Then the equilibrium density profiles for flat and curved walls with several different radii of curvature R are calculated. From the equilibrium profiles, we determine the corresponding grand-canonical free energies using Eq. (4) in the presence and Eq. (5) in the absence of a wall. On this basis, the interfacial tensions $\gamma(R)$ are calculated using Eq. (2). According to Eq. (1), the Tolman length is proportional to the slope of $\gamma(1/R)$ in the limit $1/R \to 0$, which can be accessed by a polynomial fit through the data points for $\gamma(1/R)$. By considering various values of μ, we obtain the Tolman length $\ell_{\text{T}}(\eta)$ as a function of the bulk area fraction η. This procedure was repeated for the aspect ratios $L/\sigma = 1, 2, 3$, and 4. Further details on the density-functional minimization are given in the Appendix.

IV. RESULTS

Figure 2 shows typical snapshots from our MC simulations (top row) and density profiles from our DFT calculations

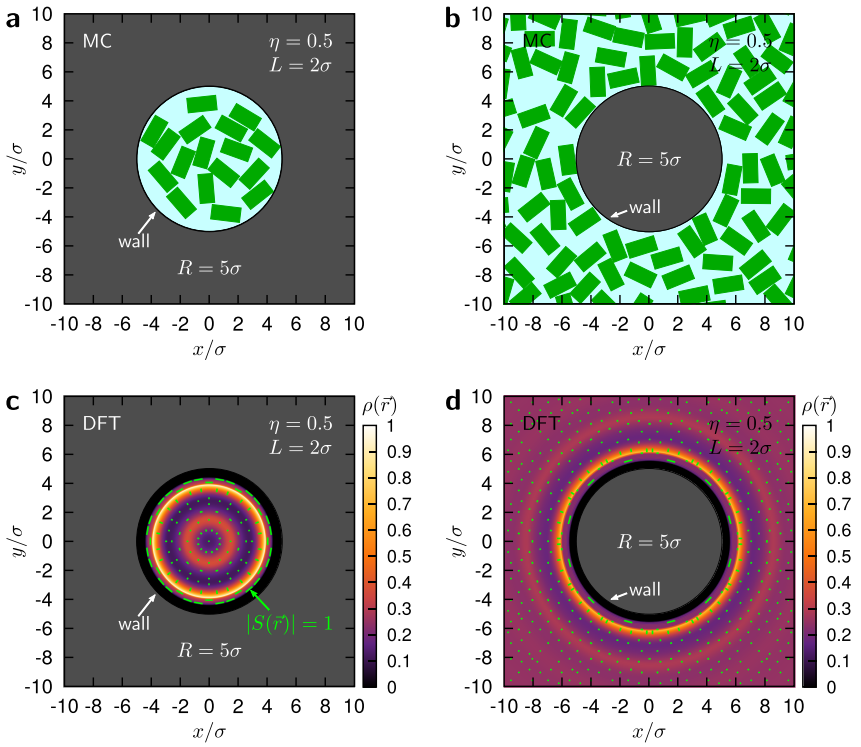

FIG. 2. Snapshots from MC simulations (top row) and equilibrium density profiles from DFT calculations (bottom row) are shown for rectangular particles with length $L = 2\sigma$ and bulk area fraction $\eta = 0.5$ in a cavity (left column) and around an obstacle (right column) with $R = 5\sigma$, respectively. For the DFT results, the orientation-integrated density $\rho(\vec{r})$ is shown by the density plots and the green dashes depict the local mean orientation of the particles as well as—through their length—the amount of local particle alignment $|S(\vec{r})|$ (a dash with length corresponding to $|S(\vec{r})| = 1$ is indicated in (c) for scale). Note that in (b) and (d) the full system is significantly larger than the region shown in these plots.

(bottom row)[67] for equilibrated systems of rectangular particles with $L = 2\sigma$ at bulk area fraction $\eta = 0.5$ in a circular cavity (left column) and around a circular obstacle (right column) with $R = 5\sigma$. For the DFT results, the orientation-integrated particle number density

$$\rho(\vec{r}) = \int_0^{2\pi} \mathrm{d}\phi\, \rho(\vec{r}, \phi) \tag{59}$$

is shown as a density plot and the orientation field of the particles is depicted with green dashes. The orientation of the dashes shows the local mean orientation of the particles and the length of the dashes is proportional to the absolute value of the orientational order-parameter field

$$S(\vec{r}) = 2\frac{\displaystyle\int_0^{2\pi} \mathrm{d}\phi \sin^2(\phi - \theta)\, \rho(r\hat{u}(\theta), \phi)}{\displaystyle\int_0^{2\pi} \mathrm{d}\phi\, \rho(r\hat{u}(\theta), \phi)} - 1 \tag{60}$$

with the polar angle θ and the parametrization $\vec{r} = r\hat{u}(\theta)$ with $\hat{u}(\theta) = (\cos(\theta), \sin(\theta))$. $S(\vec{r})$ describes the amount of local particle alignment relative to the wall with $|S(\vec{r})| = 1$ for a perfect alignment and $S(\vec{r}) = 0$ for a uniform distribution of the orientation ϕ. In Fig. 2, a layering of the particles near the wall is visible. Like the density field, also the orientation field is rotationally symmetric and shows a damped oscillation as a function of the distance from the wall. Near the wall, the local mean orientation of the particles is aligned parallel to the wall. When the distance from the wall is increased, the local mean particle orientation oscillates between an alignment perpendicular ($S(\vec{r}) < 0$) and parallel ($S(\vec{r}) > 0$) to the wall.

In order to compare the different approaches, we calculate from our analytic, MC, and DFT results the orientation-integrated density $\rho(d)$ and the orientational order parameter $S(d)$, where d is the distance of a rectangle's center of mass from the wall in units of σ, i.e., $d = (R - r)/\sigma$ with $r = |\vec{r}|$ for a cavity, $d = x/\sigma$ for a flat wall, and $d = (r - R)/\sigma$ for an obstacle. These profiles are shown in Fig. 3 for rectangular particles with $L = 2\sigma$ in the ideal-gas limit (analytic results, left) and at area fraction $\eta = 0.5$ for both MC simulations (middle) and DFT calculations (right). Both a cavity (orange) and an obstacle (blue) with $R = 5\sigma$ are considered and compared to the limiting case of a flat wall (green). The profiles for the cavity and the obstacle at $\eta = 0.5$ correspond to the snapshots and density profiles shown in Fig. 2.

In the ideal-gas limit (left column in Fig. 3), we find differences between the three systems, which can be explained by geometrical considerations. Clearly, the rectangle's center of mass cannot approach a wall closer than half the rectangle's width ($d = 0.5$). In the cavity, this inaccessible area is larger, due to the concave curvature of the wall, which prevents the rectangle from touching the wall with its edges. Therefore, this threshold shifts to $d_1^c = (\sigma/2 + R - \sqrt{R^2 - L^2/4})/\sigma$.

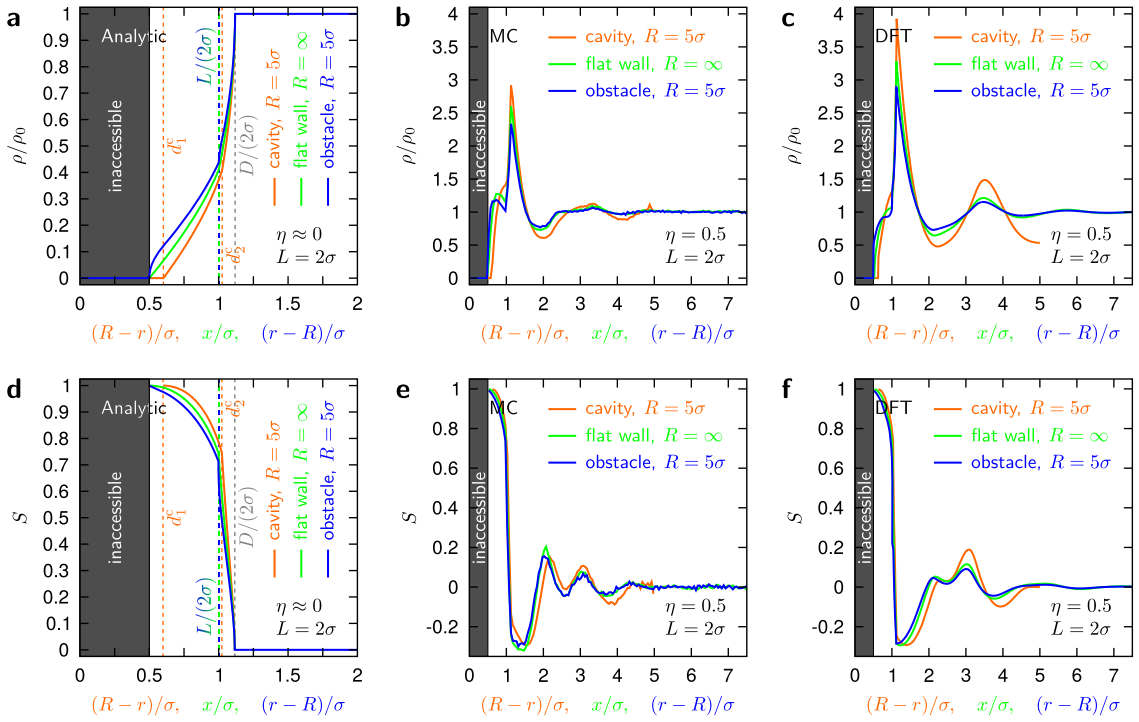

FIG. 3. (a)-(c) The orientation-integrated particle number density $\rho(\vec{r})$ and (d)-(f) the orientational order parameter $S(\vec{r})$ are shown for rectangular particles with $L = 2\sigma$ as a function of the distance from the wall for a circular cavity ($R = 5\sigma$, orange), a flat wall ($R = \infty$, green), and a circular obstacle ($R = 5\sigma$, blue). The columns correspond to (a) and (d) analytic results in the ideal-gas limit with $d_1^c = (\sigma/2 + R - \sqrt{R^2 - L^2/4})/\sigma$ and $d_2^c = (L/2 + R - \sqrt{R^2 - \sigma^2/4})/\sigma$, (b) and (e) MC results for $\eta = 0.5$, and (c) and (f) DFT results for $\eta = 0.5$. Note that the local mean particle alignment is either perpendicular ($S(\vec{r}) < 0$) or parallel ($S(\vec{r}) > 0$) to the wall.

At distances smaller than those threshold values, $\rho(d)$ vanishes and $S(d)$ is not defined. As the orientational freedom grows with increasing distance to the wall, $\rho(d)$ increases with d in all three systems. However, we find a qualitatively different behavior for the profiles near a cavity or flat wall, in comparison to that near an obstacle. While $\rho(d)$ is convex in the former two cases, meaning that its second derivative is always positive, we observe a sharp increase of $\rho(d)$ at $d = 0.5$ and then a transition from a concave to a convex curve in the latter case. In this concave regime of the density profile around an obstacle, the freedom of rotation of a rectangle is limited by the contact between one of its long edges and the obstacle, rather than its corners, allowing a significantly larger amount of orientational freedom. When looking at the orientational order parameter very closely to the wall, the rectangles are aligned exclusively parallel to the wall ($S(d) = 1$) as only this orientation is possible. Due to the increased orientational freedom further away from the wall, $S(d)$ decreases monotonically with d. As soon as the rectangle's distance from the wall reaches half its length ($d = L/(2\sigma)$) in case of the flat wall or obstacle, or $d_2^c = (L/2 + R - \sqrt{R^2 - \sigma^2/4})/\sigma$ in case of the cavity, the rectangles may also be aligned orthogonal to the wall and with further increasing distance they also rotate around this orientation. This gives rise to a kink in the profiles for both $\rho(d)$ and $S(d)$ in all systems under consideration. For larger distances to the wall, the density profiles increase monotonically with the same qualitative differences between the cavity and the flat wall on one side and the obstacle on the other side as observed very close to the wall (see above). This is accompanied with an ongoing monotonic decrease of $S(d)$. As all orientations are allowed for $d \geq D/(2\sigma)$, $\rho(d)$ reaches the bulk density ρ_0 and $S(d)$ reaches 0 at $d = D/(2\sigma)$. Both $\rho(d)$ and $S(d)$ are constant for $d \geq D/(2\sigma)$.

We now turn our attention to larger area fractions and focus on $\eta = 0.5$ (middle and right columns in Fig. 3). For both MC simulations and DFT calculations, the broadened inaccessible area for the cavity as explained for the ideal-gas limit is retrieved. As in the ideal-gas limit, we find kinks for $\rho(d)$ and $S(d)$ at $d \approx 1$ for both methods.[68] For larger distances d, an accumulation of particles close to the wall as well as a successive layering is clearly visible. Such a layering close to a hard wall is frequently reported in the literature.[29,46,55,69] Though the amplitudes of the density peaks slightly deviate between MC simulations and DFT calculations, we find very good qualitative agreement when comparing the different wall curvatures, as the relative amplitude differences between the different systems (amplitude for cavity > amplitude for flat wall > amplitude for obstacle) are in agreement. For large distances from the wall, these density fluctuations damp out and the bulk density ρ_0 is reached, if enough space is available. Note that in a small cavity (as shown for $R = 5\sigma$ in Fig. 3(c)), the bulk density is not reached in the center, which gives rise to strong finite-size effects; we therefore exclude those small cavities in the calculations of the Tolman length further below.

In contrast, the bulk reservoir for the flat wall and the obstacle can always be chosen sufficiently large to reach the bulk density in the isotropic phase. In our MC simulations and DFT calculations, we carefully confirmed that the bulk density was reached far away from the wall.

Based on our results for the equilibrium density profiles, we determine the interfacial tension γ for various aspect ratios L/σ, bulk area fractions η, and wall curvatures $\pm 1/R$, using Eq. (46) for our analytic calculations, Eq. (49) for our MC simulations, and Eq. (2) for our DFT calculations as described in Secs. II B and III. Figure 4 shows $\gamma(\eta)$ as obtained by analytic calculations, MC simulations, and DFT calculations for squares with $L = \sigma$ (top row) and rectangles with $L = 2\sigma$ (bottom row) in a circular cavity (left column) and around a circular obstacle (right column) with $R = 5\sigma$. In each plot, we also show the reference case of a flat wall for comparison. We find perfect agreement with our analytic results in the low-density limit. Additionally, at bulk area fractions up to $\eta \simeq 0.3$, we also observe good quantitative agreement between MC and DFT results. For both flat and curved walls, we find a monotonic increase in γ with the area fraction. At low densities, a concave curvature of the wall (left column) results in a clear decrease in γ, whereas a convex curvature (right column) increases γ, as one would expect from the signs of the Tolman lengths as predicted in the ideal-gas limit (see Sec. II A). However, at high densities, the interfacial tension for both the cavity and the obstacle appears to be higher than that for a flat wall. This surprising result occurs for both aspect ratios $L/\sigma = 1$ and $L/\sigma = 2$, and in both the MC simulations and DFT calculations for $R = 5\sigma$. We note here that for $R > 10\sigma$ the interfacial tension at high densities is lower for the obstacle than for the flat wall. Although this behavior clearly demonstrates that for $R = 5\sigma$ the first-order expansion of γ in terms of $1/R$ in Eq. (1) is no longer an accurate approximation, it also strongly suggests that the Tolman length may be strongly dependent on the particle density.

We therefore now consider the Tolman length in more detail. In both MC simulations and DFT calculations, we obtain the Tolman lengths at finite densities from polynomial fits to the interfacial tension $\gamma(R)$. Consistent with our analytic results, we expected the Tolman lengths for the cavity and the obstacle—also at higher densities—to differ only in sign and not in magnitude. Therefore, we plotted the data for both cavity and obstacle simultaneously, with the cavities corresponding to negative curvatures $-1/R$. Figure 5 shows an example for $L = 2\sigma$ and $\eta = 0.5$. In this representation, the Tolman length ℓ_T can be obtained from the slope of $\gamma(R)/\gamma(\infty)$ as a function of the wall curvature $\pm 1/R$, taken in the limit $1/R \to 0$, which we obtained using a single polynomial fit through the data for both the cavities and obstacles to optimize the fit accuracy. In

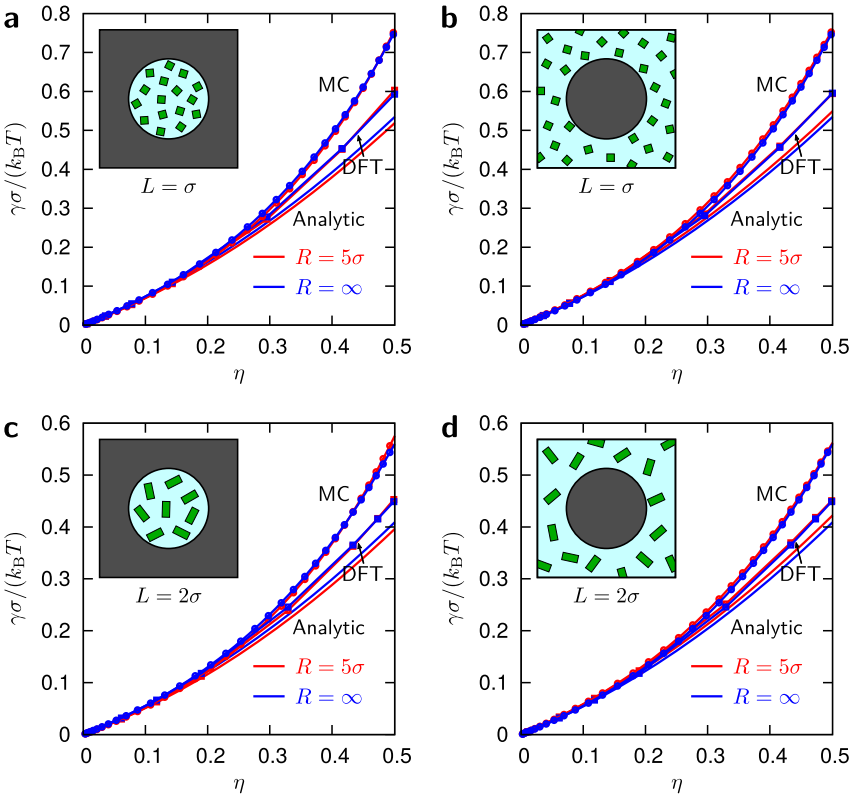

FIG. 4. Analytic results from our low-density expansion, MC results, and DFT results for the interfacial tensions γ are shown as a function of the bulk area fraction η for squares with $L = \sigma$ (top) and rectangles with $L = 2\sigma$ (bottom) in a circular cavity (left) and around a circular obstacle (right) with $R = 5\sigma$. For small area fractions, the agreement between the results is very good, whereas for larger area fractions, deviations become visible. In the case of the MC and DFT results, even the differences of the curves for $R = 5\sigma$ and $R = \infty$ are consistent for both methods.

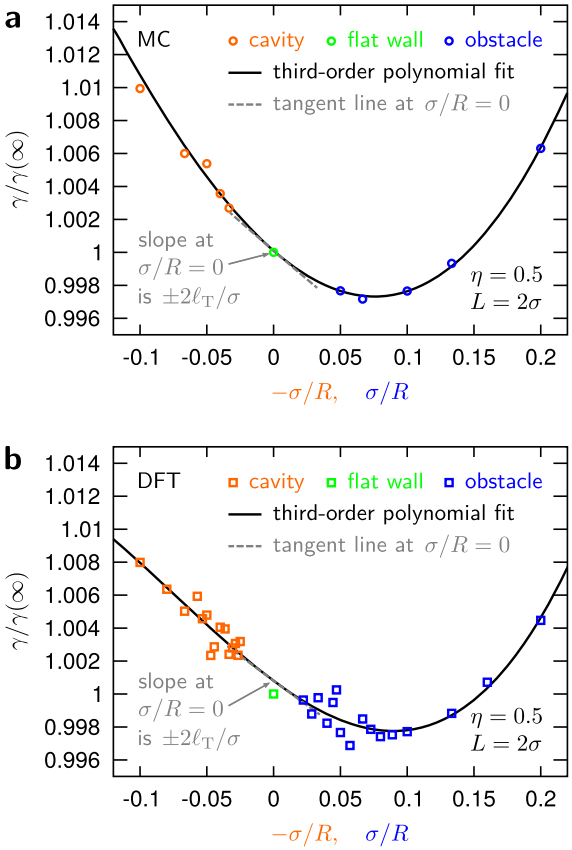

FIG. 5. For both (a) MC simulations and (b) DFT calculations, the normalized interfacial tension $\gamma(R)/\gamma(\infty)$ is shown for rectangular particles with $L = 2\sigma$ at bulk area fraction $\eta = 0.5$ in systems with cavities (orange) and obstacles (blue) with various radii of curvature R including a flat wall as limiting case (green, $R = \infty$). Note that the curvature of the cavity is $-1/R$, whereas the curvature of the obstacle is $1/R$. A third-order polynomial fit is also shown. Its slope at $\sigma/R = 0$ is $2\ell_T/\sigma$ for the cavity and $-2\ell_T/\sigma$ for the obstacle, which allows to determine the Tolman length ℓ_T.

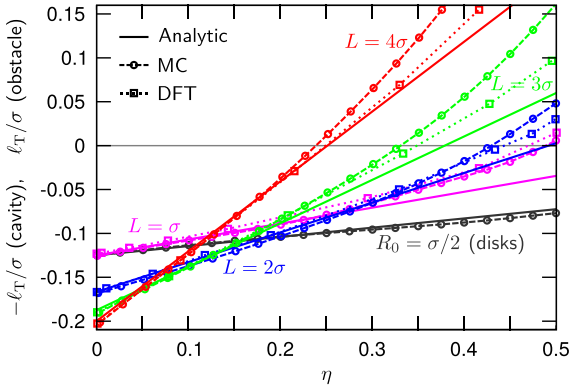

FIG. 6. Tolman lengths ℓ_T for a fluid inside a circular cavity and for a fluid surrounding a circular obstacle as a function of the bulk area fraction η. The data are obtained using MC simulations (circles with dashed lines) and DFT calculations (squares with dotted lines) for rectangular particles with aspect ratios $L/\sigma = 1$, 2, 3, and 4. In addition, MC results for disks with radii $R_0 = \sigma/2$ are shown. These MC and DFT results are compared with the analytic results from our low-density expansion (solid lines). The agreement is very good for low and intermediate densities. Especially in the ideal-gas limit, our analytic results (± 0.125 for disks and for $L = \sigma$, $\pm 1/6 \approx 0.1667$ for $L = 2\sigma$, ± 0.1875 for $L = 3\sigma$, and ± 0.2 for $L = 4\sigma$) match our numerical results precisely.

Fig. 5, γ shows a clear negative slope near $1/R = 0$ in both our MC and DFT results, resulting in a negative Tolman length for the cavity and a positive Tolman length for the obstacle.[70] This is in sharp contrast to the positive Tolman length we find at low densities for the cavity (or negative Tolman length at low densities for the obstacle) and indicates a sign change of the Tolman length as a function of the area fraction for this system. In other words, a bulk particle density exists at which $\ell_T = 0$, i.e., where the interfacial tension $\gamma(R)$ is, to first order in $1/R$, independent of the radius of curvature R.

In order to examine this intriguing behavior in more detail, we obtained the Tolman lengths for the aspect ratios $L/\sigma = 1$, 2, 3, and 4 for various area fractions using MC simulations and DFT calculations and compare these results in Fig. 6 with our theoretical results from Sec. II. For comparison, we also include MC results for disks of diameter σ. To maintain readability, we skip distinguishing between cavity and obstacle but instead focus on the obstacle in the following, as the Tolman lengths for the cavity and the obstacle only differ in sign. (The discussion for the Tolman length in the cavity is therefore obtained when exchanging the terms "positive" and "negative" as well as "increase" and "decrease," etc.) At low bulk area fractions η, we find negative Tolman lengths for all aspect ratios and observe very good agreement between analytic results, MC simulations, and DFT calculations. With increasing η, the Tolman length increases monotonically, with higher aspect ratios resulting in a stronger increase. This increase eventually leads to a sign change in ℓ_T for rectangular particles of all investigated aspect ratios. This sign switching is one of the main results of our article and can be observed for lower area fractions as the aspect ratio increases. To our knowledge, a dependence of the sign of the Tolman length on the bulk area fraction was not observed before, and indeed we do not observe this phenomenon for disk-shaped particles. Although the Tolman length for disks may change sign at area fractions higher than those investigated here, extrapolation would suggest that this does not occur before the onset of the hexatic phase around area fraction $\eta \approx 0.7$.[71,72] This observation for disks in two spatial dimensions is in agreement with previous works, in which no change of sign of the Tolman length was observed for spheres around a cylinder in three spatial dimensions.[28] When scaled accordingly, our results for disks are in qualitative agreement with Fig. 2 in Ref. 28. As we do not see a change of sign of the Tolman length for disks, we conclude that the change of sign of the Tolman length is caused by the anisotropy of the particle shape and not by the restriction to two spatial dimensions.

The effect of particle shape on the density-dependence of the Tolman length, as well as its sign change, is qualitatively captured by the second-order expansion of the interfacial tension in terms of the bulk density in Sec. II B. This suggests that this behavior can be explained by simple one- and two-particle arguments, even if it occurs at relatively high densities. We

recall that up to second order in the fugacity z, the interfacial tension can be written as

$$\beta L_{\text{wall}}\gamma = (A - A_{\text{f}})z - \left(AA_{\text{ex}}^{\text{bulk}} - A_{\text{f}}\langle A_{\text{ex}}^{\text{wall}}\rangle\right)\frac{z^2}{2} + \mathcal{O}(z^3). \tag{61}$$

On the right-hand side of this equation, only A_{f} and $\langle A_{\text{ex}}^{\text{wall}}\rangle$ depend on the radius of curvature of the wall R. The initial negative Tolman length at low density results from the first term of this expansion in z. Given the same total available area A and wall length L_{wall}, the effective free area A_{f} is smaller for convex than for flat walls, resulting in a higher interfacial tension γ. This corresponds to a negative Tolman length.

We now consider the second term on the right-hand side of Eq. (61). The term $\langle A_{\text{ex}}^{\text{wall}}\rangle$ represents the average area excluded by one particle to another particle within the relevant wall geometry. While far away from the wall, the area excluded by the first particle to the second is simply equal to the bulk value $A_{\text{ex}}^{\text{bulk}}$, close to the wall a part of this excluded area is inaccessible to the second particle due to its interaction with the wall, ensuring that $\langle A_{\text{ex}}^{\text{wall}}\rangle < A_{\text{ex}}^{\text{bulk}}$. Since A_{f} is also smaller than A in all cases, the second term on the right-hand side of Eq. (61) is always negative. Moreover, for convex walls, A_{f} is again smaller, and the particles are on average closer to the wall than for a concave wall (see Fig. 3), resulting in a smaller $\langle A_{\text{ex}}^{\text{wall}}\rangle$ as well. Thus, for convex walls, the z^2 term in Eq. (61) is more strongly negative, resulting in a positive contribution to the Tolman length, which becomes more important at higher fugacity z (i.e., at higher bulk density $\rho_0 \propto \eta$). This explains the positive slope of the Tolman length $\ell_{\text{T}}(\eta)$ as a function of the bulk area fraction η, which at sufficiently high density leads to a sign change. Finally, we note that for longer particles, the effect of the curvature on both A_{f} and $\langle A_{\text{ex}}^{\text{wall}}\rangle$ is stronger, resulting in a stronger positive slope in $\ell_{\text{T}}(\eta)$, consistent with our observations in Fig. 6.

V. CONCLUSIONS

In conclusion, we combined analytic calculations, computer simulations, and classical density functional theory to calculate the interfacial tension in a two-dimensional fluid of orientable hard rectangular particles near a curved hard wall. We considered particle densities where the bulk phase of the fluid is isotropic and found that the sign and magnitude of the Tolman length, which characterizes the leading-order curvature contribution to the interfacial tension, vary strongly with the particle shape and density. Specifically, we found a transition from negative to positive Tolman length for a fluid around a circular obstacle (and vice versa for a fluid in a cavity) at a density controlled by the aspect ratio of the rectangles. This sign change does not appear for hard disks in the same geometry.

Our results are in principle verifiable in experiments with sterically stabilized colloidal[42,45,73–77] or granular[43,78] particles on a two-dimensional substrate. However, it should be noted that the particle number density field near the wall is more direct to obtain than the interfacial tension itself, which requires a thermodynamic integration.

For future studies it would be interesting to generalize our results to various directions: first of all, other bulk phases different from the isotropic fluid such as nematic, smectic, and crystalline phases should be considered. This situation is much more complex and hardly explored, except for the case of the planar hard wall, which was investigated using a restricted-orientation approximation.[50] For complex bulk phases, the interfacial tension will depend also on the relative orientation of the wall with respect to the macroscopic nematic director. Second, other shapes of hard particles should be considered both in two and in three spatial dimensions. These will typically exhibit more complex phase diagrams (see, e.g., Ref. 79). Concomitantly, new classical density functional theories for shape-anisotropic hard particles[69,80–83] should be used to access the Tolman length for bodies of more complex shapes. Some of these were already used for planar hard walls[69] and could be applied to more general systems with curved walls. Finally, also other particle-particle or particle-wall interactions (such as Lennard-Jones potentials or homeotropic anchoring) could be considered.

ACKNOWLEDGMENTS

We thank A. Voigt for helpful discussions. Financial support from the Deutsche Forschungsgemeinschaft (Project No. LO418/20-1) is acknowledged. Moreover, F.S. gratefully acknowledges funding from the Alexander von Humboldt foundation.

APPENDIX: NUMERICAL DETAILS ON THE DENSITY FUNCTIONAL MINIMIZATION

The area of a rectangle with its center at position $\vec{r} = (x, y)$ and with orientation ϕ is denoted as $\mathfrak{A}(\vec{r}, \phi)$, whereas the corners of the rectangle $\mathfrak{A}(\vec{r}, \phi)$ are denoted as $\mathfrak{C}(\vec{r}, \phi)$. The cross correlations in the calculation of the weighted densities are performed in real space as they can be written as corner and area integrals

$$n_0(\vec{r}) = \int_0^{2\pi} \mathrm{d}\phi \int_{\mathfrak{C}(\vec{r},\phi)} \mathrm{d}^2 r' \rho(\vec{r}', \phi), \tag{A1}$$

$$n_2(\vec{r}) = \int_0^{2\pi} \mathrm{d}\phi \int_{\mathfrak{A}(\vec{r},\phi)} \mathrm{d}^2 r' \rho(\vec{r}', \phi), \tag{A2}$$

using the following notation for the corner and area integrals of a function $g(\vec{r}, \phi)$:

$$\int_{\mathfrak{C}(\vec{r},\phi)} \mathrm{d}^2 r'\, g(\vec{r}', \phi) = \int_{\mathcal{A}} \mathrm{d}^2 r'\, \omega^{(0)}(\vec{r}' - \vec{r}, \phi) g(\vec{r}', \phi), \tag{A3}$$

$$\int_{\mathfrak{A}(\vec{r},\phi)} \mathrm{d}^2 r'\, g(\vec{r}', \phi) = \int_{\mathcal{A}} \mathrm{d}^2 r'\, \omega^{(2)}(\vec{r}' - \vec{r}, \phi) g(\vec{r}', \phi). \tag{A4}$$

The functional derivative of the excess free-energy functional $\mathcal{F}_{\text{exc}}[\rho(\vec{r}, \phi)]$, which is needed for the minimization, is

given by

$$\frac{\delta\beta\mathcal{F}_{\text{exc}}}{\delta\rho(\vec{r},\phi)} = -\int_{\mathfrak{C}(\vec{r},\phi)} \mathrm{d}^2r' \left(\ln(1-n_2(\vec{r}')) + \frac{n_2(\vec{r}')}{1-n_2(\vec{r}')}\right) - \int_{\mathfrak{A}(\vec{r},\phi)} \mathrm{d}^2r' \frac{n_0(\vec{r}')n_2(\vec{r}')}{(1-n_2(\vec{r}'))^2} + m_1(\vec{r},\phi)m_2(\vec{r},\phi) + \int_0^{2\pi}\mathrm{d}\phi' \int_{\mathcal{A}} \mathrm{d}^2r'\, \rho(\vec{r}',\phi')m_2(\vec{r}',\phi')f(\vec{r}'-\vec{r},\phi',\phi) + \frac{1}{2}\int_0^{2\pi}\mathrm{d}\phi'' \int_{\mathcal{A}} \mathrm{d}^2r''\, \rho(\vec{r}'',\phi'')m_1(\vec{r}'',\phi'') \times \int_{\mathfrak{C}(\vec{r}'',\phi'')\cap\mathfrak{A}(\vec{r},\phi)} \mathrm{d}^2r' \frac{1}{(1-n_2(\vec{r}'))^2} \tag{A5}$$

with the auxiliary functions $m_1(\vec{r},\phi)$ and $m_2(\vec{r},\phi)$ defined as

$$m_1(\vec{r},\phi) = \int_0^{2\pi}\mathrm{d}\phi' \int_{\mathcal{A}} \mathrm{d}^2r'\, \rho(\vec{r}',\phi')f(\vec{r}-\vec{r}',\phi,\phi'), \tag{A6}$$

$$m_2(\vec{r},\phi) = \frac{1}{2}\int_{\mathfrak{C}(\vec{r},\phi)} \mathrm{d}^2r' \frac{1}{1-n_2(\vec{r}')}. \tag{A7}$$

The grand-canonical free-energy functional (58) is minimized in real space with respect to $\rho(\vec{r},\phi)$ using the Picard iteration scheme[24]

$$\rho^{(i+1)}(\vec{r},\phi) = (1-\alpha)\rho^{(i)}(\vec{r},\phi) + \alpha\frac{1}{\Lambda^2}\exp\left(\beta\mu - \frac{\delta\beta\mathcal{F}_{\text{exc}}}{\delta\rho(\vec{r},\phi)}\right) \tag{A8}$$

with the mixing parameter $\alpha \leq 0.02$ and Λ set to σ. As in previous works,[26,84] this iteration is combined with the DIIS[63–66] to improve the convergence significantly. The iteration is terminated when the relative change in the grand-canonical free energy during the last 50 iteration steps is less than 10^{-8}: $|\Omega[\rho^{(n)}(\vec{r},\phi)]/\Omega[\rho^{(n-50)}(\vec{r},\phi)] - 1| < 10^{-8}$. Reducing the threshold value from 10^{-8} to 10^{-9} does not affect the results. Alternatively, the functional $\Omega[\rho(\vec{r},\phi)]$ could also be minimized using algorithms based on the conjugate gradient method[85,86] or dynamical density functional theory.[87–91]

The discrete orientations ϕ_i of the particles are chosen in equidistant steps of $\Delta\phi = 2\pi/64$. The orientations are shifted by $\Delta\phi/2$ relative to the orientation of the spatial grid (so that $\phi_1 = \pi/64$) to avoid particle orientations parallel to the grid which might be numerically discriminated or favored. Making use of the particle's symmetries, only 16 (for $L = \sigma$) or 32 (for $L > \sigma$) different orientations have to be taken into account.

The step size of the spatial grid is chosen as $\Delta x = \Delta y \approx 0.03\sigma$. Increasing the resolution of the spatial grid has only a negligible effect on the results. For the corners and edges in the corner and area integrals, a bilinear interpolation is used.

For the bulk system, periodic boundary conditions in the x- and y-directions are used. In the case of the flat-wall system, the periodic boundaries in the x-direction are replaced by hard walls at the borders of the system. It is carefully checked that the bulk density is reached between the walls and that the results do not change upon further increasing the distance between the walls (e.g., a wall distance $L_x = 30\sigma$ is used for $L = 2\sigma$ and $\eta = 0.5$).

For systems with curved walls, we placed the center of the cavity or obstacle at $\vec{r} = \vec{0}$. Making use of the rotational symmetry of our system, we only consider a quarter of the full system ($x \geq 0$, $y \geq 0$) and "mirror" the density profiles at the edges of the system, which significantly speeds up the calculations. When calculating the equilibrium density profiles for an obstacle, we ensure that the domain $\mathcal{A}$ is sufficiently large so that all wall-induced fluctuations are damped out at the edges of the system.

We calculate equilibrium density profiles for various values of the chemical potential μ and consider at least 26 wall curvatures $\pm 1/R$ for each value of μ. To reduce finite-size effects, we limit the radii of curvature to $R > 10\sigma$ for the cavity and $R > 5\sigma$ for the obstacle. The interfacial tensions γ corresponding to the equilibrium density profiles are normalized by the interfacial tension for a flat wall $\gamma(\infty)$ and plotted as a function of the curvature $\pm 1/R$ as described in Sec. IV (see Fig. 5). To access the slope of the data at $\sigma/R = 0$ and thus to determine the Tolman length, we use a least-squares fit to a polynomial in σ/R (up to 3rd order for $L \leq 3\sigma$ and up to 4th order for $L = 4\sigma$). We do not force the fit to pass through the data point for the flat wall at $\sigma/R = 0$, i.e., the value of the polynomial at $\sigma/R = 0$ is not fixed to 1 but kept as a free fit parameter. In our calculations, this value never differs from 1 for more than 0.005, demonstrating internal consistency of the data.

[1] S. Dietrich, "Wetting phenomena," *Phase Transitions and Critical Phenomena*, Vol. 12, 3rd ed. (Academic Press, London, 1988), pp. 1–218.
[2] P.-G. de Gennes, F. Brochard-Wyart, and D. Quéré, *Capillarity and Wetting Phenomena: Drops, Bubbles, Pearls, Waves*, 1st ed. (Springer-Verlag, New York, 2004), p. 292.
[3] K. Sandomirski, E. Allahyarov, H. Löwen, and S. Egelhaaf, Soft Matter **7**, 8050 (2011).
[4] A. Cacciuto, S. Auer, and D. Frenkel, Nature **428**, 404 (2004).
[5] R. P. Sear, J. Phys.: Condens. Matter **19**, 033101 (2007).
[6] A. Cacciuto, S. Auer, and D. Frenkel, J. Chem. Phys. **119**, 7467 (2003).
[7] M. Heni and H. Löwen, Phys. Rev. Lett. **85**, 3668 (2000).
[8] E. Allahyarov, K. Sandomirski, S. U. Egelhaaf, and H. Löwen, Nat. Commun. **6**, 7110 (2015).
[9] R. C. Tolman, J. Chem. Phys. **17**, 333 (1949).
[10] In the original reference,[9] Tolman derived the expression $\gamma(R) = \gamma(\infty)/(1 + 2\ell_T/R)$ for a spherical droplet with $|\ell_T/R| \ll 1$, which corresponds to a fluid in a circular cavity here. Nevertheless, expansion (1) is also commonly applied for a fluid surrounding an obstacle.[28,29]
[11] D. Frenkel and B. Smit, *Understanding Molecular Simulation*, 1st ed. (Academic Press, San Diego, 2001).
[12] A. V. Ivlev, H. Löwen, G. E. Morfill, and C. P. Royall, *Complex Plasmas and Colloidal Dispersions: Particle-Resolved Studies of Classical Liquids and Solids*, Vol. 5, 1st ed. (World Scientific Publishing, Singapore, 2012), p. 336.
[13] M. Dijkstra, "Advances in chemical physics," *Entropy-Driven Phase Transitions in Colloids: From Spheres to Anisotropic Particles* (John Wiley & Sons, Hoboken, NJ, 2014), Chap. 2, pp. 35–71.
[14] D. J. Courtemanche and F. van Swol, Phys. Rev. Lett. **69**, 2078 (1992).
[15] M. Dijkstra, Phys. Rev. Lett. **93**, 108303 (2004).
[16] M. Heni and H. Löwen, Phys. Rev. E **60**, 7057 (1999).
[17] R. L. Davidchack and B. B. Laird, Phys. Rev. Lett. **85**, 4751 (2000).
[18] B. B. Laird and R. L. Davidchack, J. Phys. Chem. C **111**, 15952 (2007).
[19] B. B. Laird and R. L. Davidchack, J. Chem. Phys. **132**, 204101 (2010).
[20] R. Benjamin and J. Horbach, J. Chem. Phys. **137**, 044707 (2012).
[21] R. Evans, Adv. Phys. **28**, 143 (1979).
[22] R. Ohnesorge, H. Löwen, and H. Wagner, Phys. Rev. E **50**, 4801 (1994).
[23] J. M. Brader, M. Dijkstra, and R. Evans, Phys. Rev. E **63**, 041405 (2001).
[24] R. Roth, J. Phys.: Condens. Matter **22**, 063102 (2010).
[25] A. Gallardo, S. Grandner, N. G. Almarza, and S. H. L. Klapp, J. Chem. Phys. **137**, 014702 (2012).
[26] A. Härtel, M. Oettel, R. E. Rozas, S. U. Egelhaaf, J. Horbach, and H. Löwen, Phys. Rev. Lett. **108**, 226101 (2012).
[27] I. Urrutia, Phys. Rev. E **89**, 032122 (2014).

[28]B. B. Laird, A. Hunter, and R. L. Davidchack, Phys. Rev. E **86**, 060602 (2012).
[29]P. Bryk, R. Roth, K. R. Mecke, and S. Dietrich, Phys. Rev. E **68**, 031602 (2003).
[30]P.-M. König, R. Roth, and K. R. Mecke, Phys. Rev. Lett. **93**, 160601 (2004).
[31]E. M. Blokhuis, Phys. Rev. E **87**, 022401 (2013).
[32]T. V. Bykov and X. C. Zeng, J. Chem. Phys. **111**, 3705 (1999).
[33]Y. A. Lei, T. Bykov, S. Yoo, and X. C. Zeng, J. Am. Chem. Soc. **127**, 15346 (2005).
[34]M. C. Stewart and R. Evans, Phys. Rev. E **71**, 011602 (2005).
[35]J. C. Barrett, J. Chem. Phys. **124**, 144705 (2006).
[36]A. E. van Giessen and E. M. Blokhuis, J. Chem. Phys. **131**, 164705 (2009).
[37]B. J. Block, S. K. Das, M. Oettel, P. Virnau, and K. Binder, J. Chem. Phys. **133**, 154702 (2010).
[38]Ø. Wilhelmsen, D. Bedeaux, and D. Reguera, J. Chem. Phys. **142**, 064706 (2015).
[39]J. Barrett, J. Chem. Phys. **111**, 5938 (1999).
[40]A. Tröster, M. Oettel, B. Block, P. Virnau, and K. Binder, J. Chem. Phys. **136**, 064709 (2012).
[41]A. Tröster and K. Binder, Phys. Rev. Lett. **107**, 265701 (2011).
[42]J. Galanis, R. Nossal, W. Losert, and D. Harries, Phys. Rev. Lett. **105**, 168001 (2010).
[43]R. Cruz Hidalgo, I. Zuriguel, D. Maza, and I. Pagonabarraga, J. Stat. Mech.: Theory Exp. **2010**, P06025.
[44]M. Acevedo, R. C. Hidalgo, I. Zuriguel, D. Maza, and I. Pagonabarraga, Phys. Rev. E **87**, 012202 (2013).
[45]T. Müller, D. de las Heras, I. Rehberg, and K. Huang, Phys. Rev. E **91**, 062207 (2015).
[46]D. A. Triplett and K. A. Fichthorn, Phys. Rev. E **77**, 011707 (2008).
[47]D. de las Heras and E. Velasco, Soft Matter **10**, 1758 (2014).
[48]T. Geigenfeind, S. Rosenzweig, M. Schmidt, and D. de las Heras, J. Chem. Phys. **142**, 174701 (2015).
[49]M. Oettel, M. Klopotek, M. Dixit, E. Empting, T. Schilling, and H. Hansen-Goos, J. Chem. Phys. **145**, 074902 (2016).
[50]Y. Martínez-Ratón, Phys. Rev. E **75**, 051708 (2007).
[51]J. Z. Y. Chen, Soft Matter **9**, 10921 (2013).
[52]M. González-Pinto, Y. Martínez-Ratón, and E. Velasco, Phys. Rev. E **88**, 032506 (2013).
[53]J. C. Everts, M. T. J. J. M. Punter, S. Samin, P. van der Schoot, and R. van Roij, J. Chem. Phys. **144**, 194901 (2016).
[54]M. A. Bates and D. Frenkel, J. Chem. Phys. **112**, 10034 (2000).
[55]M. Schoen and S. H. L. Klapp, *Nanoconfined Fluids: Soft Matter Between Two and Three Dimensions, Review in Computational Chemistry*, Vol. 24 (John Wiley & Sons, Hoboken, NJ, 2007) pp. 1–517.
[56]H. Emmerich, H. Löwen, R. Wittkowski, T. Gruhn, G. I. Tóth, G. Tegze, and L. Gránásy, Adv. Phys. **61**, 665 (2012).
[57]T. Boublík, Mol. Phys. **29**, 421 (1975).
[58]S. Gottschalk, M. C. Lin, and D. Manocha, in *Proceedings of the 23rd Annual Conference on Computer Graphics and Interactive Techniques, SIGGRAPH'96* (ACM, New York, 1996), pp. 171–180.
[59]J. K. Percus, J. Stat. Phys. **15**, 505 (1976).
[60]Y. Martínez-Ratón, E. Velasco, and L. Mederos, J. Chem. Phys. **122**, 064903 (2005).
[61]L. Onsager, Ann. N. Y. Acad. Sci. **51**, 627 (1949).
[62]Y. Rosenfeld, Phys. Rev. Lett. **63**, 980 (1989).
[63]K. C. Ng, J. Chem. Phys. **61**, 2680 (1974).
[64]P. Pulay, Chem. Phys. Lett. **73**, 393 (1980).
[65]P. Pulay, J. Comput. Chem. **3**, 556 (1982).
[66]A. Kovalenko, S. Ten-no, and F. Hirata, J. Comput. Chem. **20**, 928 (1999).
[67]Though only a quarter of the systems was considered in the numerical DFT calculations, we make use of the boundary conditions and show here the full cavity and obstacle for a better illustration.
[68]In the DFT calculations, the orientations ϕ are not continuous but discretized, which causes a non-continuous increase in possible orientations and therefore small discontinuities in the profiles for $d < D/(2\sigma)$. As these discontinuities are numerical artifacts with known origin, they were smoothed in Fig. 3 to show the limit of a continuous ϕ.
[69]M. Marechal and H. Löwen, Phys. Rev. Lett. **110**, 137801 (2013).
[70]When using Eq. (1) to relate this slope to the Tolman lengths, one must take into account that in the representation shown in Fig. 5 the interfacial tension $\gamma(R)$ is plotted as a function of the wall curvature, which is $-1/R$ for a cavity and $1/R$ for an obstacle. Therefore, this slope must be multiplied with $\sigma/2$ for the cavity and with $-\sigma/2$ for the obstacle to determine the Tolman length ℓ_T.
[71]C. H. Mak, Phys. Rev. E **73**, 065104 (2006).
[72]E. P. Bernard and W. Krauth, Phys. Rev. Lett. **107**, 155704 (2011).
[73]K.-H. Lin, J. C. Crocker, V. Prasad, A. Schofield, D. A. Weitz, T. C. Lubensky, and A. G. Yodh, Phys. Rev. Lett. **85**, 1770 (2000).
[74]M. Hermes, E. C. M. Vermolen, M. E. Leunissen, D. L. J. Vossen, P. D. J. van Oostrum, M. Dijkstra, and A. van Blaaderen, Soft Matter **7**, 4623 (2011).
[75]O. Zvyagolskaya, A. J. Archer, and C. Bechinger, Europhys. Lett. **96**, 28005 (2011).
[76]T. H. Besseling, M. Hermes, A. Kuijk, B. de Nijs, T.-S. Deng, M. Dijkstra, A. Imhof, and A. van Blaaderen, J. Phys.: Condens. Matter **27**, 194109 (2015).
[77]L. Walsh and N. Menon, J. Stat. Mech.: Theory Exp. **2016**, 083302.
[78]S. Hernández-Navarro, J. Ignés-Mullol, F. Sagués, and P. Tierno, Langmuir **28**, 5981 (2012).
[79]P. Bolhuis and D. Frenkel, J. Chem. Phys. **106**, 666 (1997).
[80]H. Hansen-Goos and K. Mecke, Phys. Rev. Lett. **102**, 018302 (2009).
[81]H. Hansen-Goos and K. Mecke, J. Phys.: Condens. Matter **22**, 364107 (2010).
[82]M. Marechal, U. Zimmermann, and H. Löwen, J. Chem. Phys. **136**, 144506 (2012).
[83]R. Wittmann, M. Marechal, and K. Mecke, Europhys. Lett. **109**, 26003 (2015).
[84]M. Oettel, S. Dorosz, M. Berghoff, B. Nestler, and T. Schilling, Phys. Rev. E **86**, 021404 (2012).
[85]M. P. Hestenes and E. Stiefel, J. Res. Natl. Bur. Stand. **49**, 409 (1952).
[86]R. Fletcher and C. M. Reeves, Comput. J. **7**, 149 (1964).
[87]U. M. B. Marconi and P. Tarazona, J. Chem. Phys. **110**, 8032 (1999).
[88]U. M. B. Marconi and P. Tarazona, J. Phys.: Condens. Matter **12**, 413 (2000).
[89]A. J. Archer and R. Evans, J. Chem. Phys. **121**, 4246 (2004).
[90]P. Español and H. Löwen, J. Chem. Phys. **131**, 244101 (2009).
[91]R. Wittkowski and H. Löwen, Mol. Phys. **109**, 2935 (2011).
[92]E. M. Blokhuis and J. Kuipers, J. Chem. Phys. **124**, 074701 (2006).
[93]T. P. Bennett and J. C. Barrett, J. Chem. Phys. **137**, 124702 (2012).
[94]B. Groh and S. Dietrich, Phys. Rev. E **59**, 4216 (1999).

Veröffentlichung III Phase diagram of two-dimensional hard rods from fundamental mixed measure density functional theory

R. Wittmann*, C. E. Sitta*, F. Smallenburg & H. Löwen

Phase diagram of two-dimensional hard rods from fundamental mixed measure density functional theory,
J. Chem. Phys. **147**, 134908 (2017),
veröffentlicht durch *AIP Publishing*.

Digital Object Identifier (DOI): 10.1063/1.4996131

* Diese Autoren haben in gleichem Maß zur Publikation beigetragen und teilen die Erstautorschaft.

Stellungnahme zum eigenen Beitrag

H.L., R.W. und ich haben das Forschungsprojekt entwickelt.
H.L. hat das Forschungsprojekt betreut.
F.S. hat die MC Simulationen implementiert und durchgeführt.
R.W. hat die Dichtefunktionaltheorie hergeleitet.
Ich habe die numerische Minimierung der Dichtefunktionaltheorie implementiert und durchgeführt.
F.S. hat Abb. 1 erstellt.
Ich habe Abb. 2-5 erstellt.
Alle Autoren haben die Ergebnisse interpretiert und das Manuskript geschrieben.

Lizenzhinweise und Copyright

THE JOURNAL OF CHEMICAL PHYSICS **147**, 134908 (2017)

Phase diagram of two-dimensional hard rods from fundamental mixed measure density functional theory

René Wittmann,[1,a)] Christoph E. Sitta,[2,a)] Frank Smallenburg,[2] and Hartmut Löwen[2]
[1]*Department of Physics, University of Fribourg, CH-1700 Fribourg, Switzerland*
[2]*Institut für Theoretische Physik II, Weiche Materie, Heinrich-Heine-Universität Düsseldorf, D-40225 Düsseldorf, Germany*

(Received 14 July 2017; accepted 19 September 2017; published online 5 October 2017)

A density functional theory for the bulk phase diagram of two-dimensional orientable hard rods is proposed and tested against Monte Carlo computer simulation data. In detail, an explicit density functional is derived from fundamental mixed measure theory and freely minimized numerically for hard discorectangles. The phase diagram, which involves stable isotropic, nematic, smectic, and crystalline phases, is obtained and shows good agreement with the simulation data. Our functional is valid for a multicomponent mixture of hard particles with arbitrary convex shapes and provides a reliable starting point to explore various inhomogeneous situations of two-dimensional hard rods and their Brownian dynamics. *Published by AIP Publishing.* https://doi.org/10.1063/1.4996131

I. INTRODUCTION

Classical density functional theory (DFT) of inhomogeneous fluids[1] provides a microscopic theory for freezing, for reviews see Refs. 2–7. This has been exploited for spherical particles with radially symmetric pairwise potentials (such as hard or soft spheres) both in three[8–10] and two[11] spatial dimensions where the freezing line of liquids has been predicted with good accuracy. Density functional theory of freezing can also be formulated for orientational degrees of freedom as documented in Onsager's seminal work for the isotropic–nematic transition.[12] This has been applied to investigate the stability of liquid-crystalline phases (such as isotropic, nematic, and smectic) in three[13–22] and in two[22–30] dimensions. For both translational and orientational degrees of freedom, many different "meso-phases" with partial translational or orientational order are conceivable and therefore the resulting phase diagram is typically much more complex.[31]

The most elaborate DFTs were derived for hard particles which possess only steric or excluded-volume interactions. In these systems, temperature scales out such that the density (or packing fraction) is the only remaining parameter apart from the particle shape. In particular, the Fundamental Measure Theory (FMT) originally invented by Rosenfeld[32] has proven to be very successful for hard-body fluids in three dimensions, including the isotropic phase of particles with non-spherical shape.[33,34] The basic input into FMT is different weighted densities, which depend only on the geometry of a single body. This simple structure allows for an efficient numerical implementation. The versatile framework of Rosenfeld's FMT allows one to use the same building blocks to construct a new version yielding a more accurate equation of state[35] and, upon introducing additional weighted densities, to obtain generalized functionals for freezing[11,36] and liquid crystal phases.[18–20]

The usual first step to derive FMT is to take the low-density limit and decompose the Mayer function of the hard-core interaction. However, there is no exact representation based on a finite number of weighted densities in two (and other even) dimensions[37] or in any dimension if the shape of the freely rotating bodies is anisotropic.[33] Instead, for two-dimensional hard disks (HDs)[11] and arbitrary convex bodies in three dimensions,[18] an infinite series of tensorial weighted densities is necessary, which, for practical reasons, is usually truncated after the term including rank-two tensors. A more sophisticated expansion can be defined in terms of orthonormal functions, such as spherical harmonics in three dimensions.[38]

Regarding the ongoing progress in numerical techniques and computer speed, versions of FMT based on two-body weighted densities,[21,36,39,40] which are exact in the low-density limit, become a valid alternative to an approximate treatment, particularly in two dimensions. Another tractable functional involving many-body measures has been derived for infinitely thin disks in three dimensions.[41] The most general formulation of FMT for mixtures of arbitrary convex bodies in any dimension is the so-called Fundamental Mixed Measure Theory (FMMT).[21,40]

In this paper, we consider an explicit DFT based on FMMT for a simple model system of orientable hard rods in two spatial dimensions. We study particles with a "discorectangular" shape (the two-dimensional analog of spherocylinders) whose phase diagram is spanned by their packing fraction and aspect ratio only, while also considering the HD limit. Monte Carlo (MC) computer simulation[42] data are available for the bulk phase diagram of these discorectangles[43] and involve an isotropic, nematic, and crystalline phase. Here we evaluate our FMMT functional analytically and numerically and obtain a bulk phase diagram. In doing so, we also extend the previous MC data[43] and resolve between a two-dimensional smectic

[a)]R. Wittmann and C. E. Sitta contributed equally to this work.

and a full crystalline phase. Our DFT reproduces the topology of this enhanced phase diagram. It is therefore the first functional which gets the stability of four liquid-crystalline phases simultaneously in two dimensions. The FMMT functional is given in a general form for multicomponent mixtures of arbitrary convex hard particles. It can serve as an input for future DFT studies of two-dimensional liquid crystals at interfaces[44] and for Brownian dynamics of rods[45] similar in spirit as the FMT functional for HD proposed by Roth and co-workers.[11]

This paper is organized as follows: in Sec. II we derive an analytical expression for the DFT functional. Our MC simulations and our numeric DFT minimization are described in Sec. III and results of our calculations are presented and discussed in Sec. IV. We conclude in Sec.V.

II. DENSITY FUNCTIONAL THEORY

To tackle the general case first, we consider a two-dimensional system of κ components of anisotropic particles. The equilibrium configuration of the particles of each species i is described by a density profile $\rho_i(\mathcal{R}) \equiv \rho_i(\mathbf{r},\varphi)$ which depends on position $\mathbf{r}$ and orientation φ. For any external potential $V_i^{\text{ext}}(\mathcal{R})$ acting on the particles, the fundamental variational principle $\delta\Omega/\delta\rho_i(\mathcal{R}) = 0$ of DFT[1] states that the unique equilibrium densities minimize the functional

$$\Omega[\{\rho_i\}] = \mathcal{F}[\{\rho_i\}] + \sum_{i=1}^{\kappa}\int \mathrm{d}\mathcal{R}\rho_i(\mathcal{R})(V_i^{\text{ext}}(\mathcal{R}) - \mu_i), \quad (1)$$

which then equals the grand potential Ω of the system. The short notation $\int \mathrm{d}\mathcal{R}$ denotes the integral $\int_{\mathbb{R}^2}\mathrm{d}\mathbf{r}$ over all positions and the orientational average $\int_0^{2\pi}\frac{\mathrm{d}\varphi}{2\pi}$ and μ_i denote the chemical potentials of each species.

The intrinsic free energy

$$\beta\mathcal{F}[\{\rho_i\}] = \beta\mathcal{F}_{\text{id}} + \beta\mathcal{F}_{\text{exc}} = \int \mathrm{d}\mathbf{r}(\Phi_{\text{id}}(\mathbf{r}) + \Phi_{\text{exc}}(\mathbf{r})) \quad (2)$$

or its density $\Phi(\mathbf{r})$ is usually separated into excess ($\mathcal{F}_{\text{exc}}$) and ideal-gas ($\mathcal{F}_{\text{id}}$) contributions. The density of the latter reads as $\Phi_{\text{id}}(\mathbf{r}) = \sum_{i=1}^{\kappa}\int_0^{2\pi}\frac{\mathrm{d}\varphi}{2\pi}\rho_i(\mathbf{r},\varphi)\left(\ln(\rho_i(\mathbf{r},\varphi)\Lambda^2) - 1\right)$, with the thermal wavelength Λ and the inverse temperature $\beta^{-1} = k_{\text{B}}T$.

In order to derive the excess free energy density Φ_{exc} for a system with hard interactions along the lines of FMT,[32] we consider the exact functional

$$\beta\mathcal{F}_{\text{exc}} \to -\frac{1}{2}\sum_{i,j=1}^{\kappa}\iint \mathrm{d}\mathcal{R}_1\,\mathrm{d}\mathcal{R}_2\;\rho_i(\mathcal{R}_1)\,\rho_j(\mathcal{R}_2)f_{ij}(\mathcal{R}_1,\mathcal{R}_2) \quad (3)$$

in the dilute limit $\rho_i \to 0$, where only the interactions between two particles are relevant. These are represented by the Mayer function

$$f_{ij}(\mathcal{R}_1,\mathcal{R}_2) = e^{-\beta U_{ij}} - 1 = \begin{cases} 0 & \text{if } \mathcal{B}_i \cap \mathcal{B}_j = \emptyset \\ -1 & \text{if } \mathcal{B}_i \cap \mathcal{B}_j \neq \emptyset \end{cases} \quad (4)$$

of two hard bodies $\mathcal{B}_i$ and $\mathcal{B}_j$ with the pair interaction potential $U_{ij}(\mathcal{R}_1,\mathcal{R}_2)$. Since this interaction only depends on whether the intersection

$$\mathcal{I}_{ij}(\mathcal{R}_1,\mathcal{R}_2) \coloneqq \mathcal{B}_i(\mathcal{R}_1) \cap \mathcal{B}_j(\mathcal{R}_2) \quad (5)$$

is the empty set $\emptyset$ or not, Eq. (3) can be simplified using purely geometrical arguments to rewrite $f_{ij}(\mathcal{R}_1,\mathcal{R}_2)$ in terms of quantities that are functions of $\mathcal{R}_1$ or $\mathcal{R}_2$ only.

A. Mayer function of two-dimensional hard bodies

For two-dimensional HD mixtures, an exact decomposition of the Mayer function from Eq. (4) can be found by means of (i) simple geometrical considerations,[39] (ii) the Gauss-Bonnet theorem from differential geometry,[11] or (iii) the translative integral formula[21,40] from integral geometry.[46] Considering now mixtures of arbitrary convex bodies in two dimensions, we will show that both strategies (ii) and (iii) lead to the same decomposition as for HDs, in the sense that all terms are still present in the HD limit. Quite in contrast, the hard-sphere limit in three dimensions can be simplified to a deconvolution in terms of one-body weighted densities.[18,19,21,40] The origin of FMMT lies in strategy (iii) since it provides the proper mathematical foundation of employing two-body weighted densities. There are some alternative ways to derive such a functional from (iv) zero-dimensional cavities[47] or (v) an approximate virial series,[48] which imply the same decomposition of the Mayer function for anisotropic bodies.

Following Rosenfeld,[37] we define the three scalar weight functions

$$\begin{aligned}\omega_i^{(2)}(\mathcal{R}) &= \Theta\left(|\mathbf{R}_i(\hat{\mathcal{R}})| - |\mathbf{r}|\right),\\ \omega_i^{(1)}(\mathcal{R}) &= \frac{\delta(|\mathbf{R}_i(\hat{\mathcal{R}})| - |\mathbf{r}|)}{\mathbf{n}_i(\hat{\mathcal{R}})\cdot\hat{\mathbf{r}}},\\ \omega_i^{(0)}(\mathcal{R}) &= \frac{K_i(\hat{\mathcal{R}})}{2\pi}\,\omega_i^{(1)}(\mathcal{R})\end{aligned} \quad (6)$$

in the general form required for an anisotropic shape.[18] A point on the boundary $\partial\mathcal{B}_i$ of body $\mathcal{B}_i$ with orientation φ in the direction of the unit vector $\hat{\mathbf{r}} = \mathbf{r}/|\mathbf{r}|$ is denoted by $\mathbf{R}_i(\hat{\mathcal{R}})$, with $\hat{\mathcal{R}}$ short for $(\hat{\mathbf{r}},\varphi)$. At this point, $K_i(\hat{\mathcal{R}})$ is the curvature and $\mathbf{n}_i(\hat{\mathcal{R}})$ is the vector normal to the boundary. The orientation-dependence of the weight functions $\omega_i^{(\nu)}(\mathcal{R})$ can be treated as described for three dimensions[49,50] or by considering each discrete orientation as an individual species.

Here we briefly outline the idea behind FMMT.[21,40] For a more detailed description of the mathematical background, see Refs. 46 and 50. First we identify in any spatial dimension the Mayer function $-f_{ij} = \chi(\mathcal{I}_{ij})$ with the Euler characteristic $\chi(\mathcal{I}_{ij}) = \int\Phi_0(\mathcal{I}_{ij},\mathrm{d}\mathbf{r})$ of the intersection. The latter can be further written as the spatial integral of the local curvature measure Φ_0, which is closely related to the weight function $\omega_i^{(0)}$ when evaluated for a body $\mathcal{B}_i$.[40] Applying in two dimensions the translative integral formula (iii) to Eq. (3) results for any orientations φ_1 and φ_2 in the decomposition

$$\begin{aligned}-\iint f_{ij}(\mathcal{R}_1,\mathcal{R}_2)\,\mathrm{d}\mathbf{r}_1\,\mathrm{d}\mathbf{r}_2\\ = \iiint \mathrm{d}\mathbf{r}\sum_{k=0}^{2}\Phi_{k,2-k}^{(0)}(\bar{\mathcal{B}}_i(\mathbf{r},\varphi_1),\bar{\mathcal{B}}_j(\mathbf{r},\varphi_2);\mathrm{d}(\mathbf{r}_1,\mathbf{r}_2)),\end{aligned} \quad (7)$$

defining an inverted body as $\bar{\mathcal{B}}_i(\mathbf{r},\varphi_1) := 2\mathbf{r} - \mathcal{B}_i(\mathbf{r},\varphi_1)$ and introducing the mixed measures $\Phi^{(0)}_{k,2-k}$.[21,40] For the precise definitions of Φ_0 and $\Phi^{(0)}_{k,2-k}$, see Ref. 46.

It can be shown[40] that for $k = 0$ and $k = 2$, the expression on the right-hand side of Eq. (7) factorizes into a convolution product

$$\omega_i^{(\nu)} \otimes \omega_j^{(\mu)} = \int \mathrm{d}\mathbf{r}'\, \omega_i^{(\nu)}(\mathbf{r}' - \mathcal{R}_1)\, \omega_j^{(\mu)}(\mathbf{r}' - \mathcal{R}_2) \tag{8}$$

(integrated over $\mathrm{d}\mathbf{r}_1$ and $\mathrm{d}\mathbf{r}_2$) of the scalar weight functions with labels 0 and 2, where $(\mathbf{r} - \mathcal{R}_1)$ is short for $(\mathbf{r} - \mathbf{r}_1, \varphi_1)$. In a similar way, we can define from $\Phi^{(0)}_{1,1}$ the mixed weight function[40]

$$\Omega_{ij}^{(11)}(\mathcal{R}_1,\mathcal{R}_2) = \frac{\arccos(\mathbf{n}_i\cdot\mathbf{n}_j)}{2\pi}|\mathbf{n}_i\times\mathbf{n}_j| \times \omega_i^{(1)}(\mathcal{R}_1)\,\omega_j^{(1)}(\mathcal{R}_2), \tag{9}$$

where the vector product of the normals $\mathbf{n}_i = \mathbf{n}_i(\hat{\mathcal{R}}_1)$ and $\mathbf{n}_j = \mathbf{n}_j(\hat{\mathcal{R}}_2)$ can be calculated by adding a z component equal to zero or according to $|\mathbf{n}_i \times \mathbf{n}_j| = \sin(\arccos(\mathbf{n}_i \cdot \mathbf{n}_j))$. Thus we find the decomposition[21,40]

$$-f_{ij} = \omega_i^{(0)} \otimes \omega_j^{(2)} + \omega_i^{(2)} \otimes \omega_j^{(0)} + \Omega_{ij}^{(1\otimes1)} \tag{10}$$

of the Mayer function, where we define

$$\Omega_{ij}^{(1\otimes1)} = \int \mathrm{d}\mathbf{r}'\, \Omega_{ij}^{(11)}(\mathbf{r}' - \mathcal{R}_1, \mathbf{r}' - \mathcal{R}_2) \tag{11}$$

according to Eq. (8) for two one-body weights.

To show that the same decomposition can be obtained from the Gauss-Bonnet theorem (ii), we recall the result

$$-2\pi f_{ij} = \int_{\partial\mathcal{B}_i\cap\mathcal{B}_j} \mathrm{d}l_i\, K_i + \int_{\mathcal{B}_i\cap\partial\mathcal{B}_j} \mathrm{d}l_j\, K_j + \sum_{\partial\mathcal{B}_i\cap\partial\mathcal{B}_j} \phi \tag{12}$$

of Ref. 11, where $\phi = \arccos(\mathbf{n}_i \cdot \mathbf{n}_j)$ is the angle between the normal vectors at each intersection point and $\mathbf{n}_{i/j} = \mathbf{n}_{i/j}(\mathbf{r}' - \mathcal{R}_{1/2})$. The only difference is that we here consider an arbitrary convex body rather than a HD. This generalization does not violate the underlying assumption $-f_{ij} = \chi(\mathcal{I}_{ij})$.

The line integrals in Eq. (12) involving the curvature K_i at the boundary of the intersection can be deconvoluted in the standard way of FMT.[11] To see that the last term is equal to $\Omega_{ij}^{(1\otimes1)}$, we rewrite the sum as a pseudo three-dimensional line integral[19]

$$\int \frac{\phi\sin\phi\,\mathrm{d}s}{|\mathbf{n}_i\times\mathbf{n}_j|} = \int \mathrm{d}\mathbf{r}'\,\phi\sin\phi\,\omega_i^{(1)}(\mathbf{r}' - \mathcal{R}_1)\,\omega_j^{(1)}(\mathbf{r}' - \mathcal{R}_2), \tag{13}$$

where $\sin\phi = |\mathbf{n}_i \times \mathbf{n}_j|$. Thus we have shown that Eq. (12) also results in the decomposition given by Eq. (10).

The manner in which the Mayer function is rewritten in Eq. (12) depends on the dimensionality, as the Gauss-Bonnet theorem only applies to two-dimensional manifolds. In three dimensions, we set $-f_{ij} = \chi(\partial\mathcal{I}_{ij})/2$ for the two-dimensional boundary $\partial\mathcal{I}_{ij}$ of the three-dimensional intersection.[18] There is no obvious analog of strategy (ii) in other dimensions. In contrast, FMMT (iii) provides a formal decomposition of the Mayer function in an arbitrary dimension.[21,40] Finally, we note that although the last term in Eq. (10) still depends on two bodies simultaneously, the presented decomposition considerably facilitates the numerical implementation compared to the bare Mayer function. This is because the two-body weight functions exclusively depend on geometrical quantities of the single bodies, which, however, cannot be further simplified by factorization[21,40] without considering an approximate expansion.[11,18,19]

B. Excess free energy

Following the standard procedure in FMT, we define the weighted densities[18,32]

$$n_\nu(\mathbf{r}) = \sum_{i=1}^{\kappa} \int \mathrm{d}\mathcal{R}_1\, \rho_i(\mathcal{R}_1)\, \omega_i^{(\nu)}(\mathbf{r} - \mathcal{R}_1) \tag{14}$$

for the scalar weight functions in Eq. (6) and the mixed weighted density[21,40]

$$N(\mathbf{r}) = \sum_{i,j=1}^{\kappa} \iint \mathrm{d}\mathcal{R}_1\,\mathrm{d}\mathcal{R}_2\,\rho_i(\mathcal{R}_1)\,\rho_j(\mathcal{R}_2) \times \Omega_{ij}^{(11)}(\mathbf{r} - \mathcal{R}_1, \mathbf{r} - \mathcal{R}_2) \tag{15}$$

corresponding to Eq. (9). With the decomposition of the Mayer function from Eq. (10), we obtain the excess free energy density $\Phi_{\mathrm{exc}} = n_0 n_3 + \frac{1}{2}N$ in the low-density limit, Eq. (3), i.e., the FMT version of the Onsager functional in two dimensions. Following the procedure for the HD functional,[11,37] the extrapolation to higher densities results in

$$\Phi_{\mathrm{exc}} = -n_0\ln(1 - n_2) + \frac{N}{2(1 - n_2)}. \tag{16}$$

The uncommon choice of the prefactor in the second term stems from the definition of the mixed weight function according to the decomposition in Eq. (7) in terms of mixed measures.

Although we have the means to perform a free minimization of the functional in Eq. (16), an expansion in terms of tensorial one-body weighted densities as in three dimensions[18] might prove fruitful. Such an approximation can be obtained in a completely analog way as for HDs,[11] as the structure of the decomposition in Eq. (12) is exactly the same. Thus we Taylor expand the term $\arccos(\mathbf{n}_i\cdot\mathbf{n}_j)\sin(\arccos(\mathbf{n}_i\cdot\mathbf{n}_j))/(2\pi)$ in Eq. (9) up to quadratic order in $\mathbf{n}_i\mathbf{n}_j$ and identify the vectorial

$$\vec{\omega}_i^{(1)}(\mathbf{r}) = \mathbf{n}_i(\hat{\mathbf{r}})\,\omega_i^{(1)}(\mathbf{r}) \tag{17}$$

and tensorial

$$\overleftrightarrow{\omega}_i^{(1)}(\mathbf{r}) = \mathbf{n}_i(\hat{\mathbf{r}})\,\mathbf{n}_i^{\mathrm{T}}(\hat{\mathbf{r}})\,\omega_i^{(1)}(\mathbf{r}) \tag{18}$$

weight functions to factorize each term of this expansion. The corresponding one-body weighted densities $\vec{n}_1$ and $\overleftrightarrow{n}_1$ are then calculated according to Eq. (14). Note that it is important to write here $\mathbf{n}_i$ instead of $\hat{\mathbf{r}}$, which is only equivalent to $\mathbf{n}_i(\hat{\mathbf{r}})$ for HD parametrized in polar coordinates.

Following Ref. 11, we will consider the expansion coefficients as free parameters, which we adapt for a one-component system to ensure (I) the correct second virial coefficient of the homogeneous and isotropic fluid, (II) the correct dimensional crossover to one dimension, and (IIIa) the best fit to the Mayer

function of HDs. Conditions (I) and (II) do not depend on the specific shape, so we find

$$N \approx \frac{2+a}{6\pi} n_1 n_1 + \frac{a-4}{6\pi} \vec{n}_1 \cdot \vec{n}_1 + \frac{2-2a}{6\pi} \mathrm{Tr}\left[\overleftrightarrow{n}_1 \overleftrightarrow{n}_1\right], \quad (19)$$

in agreement with the approximation for HDs,[11] where (IIIa) results in $a_{\mathrm{HD}} = 11/4$.

For general convex bodies, we should demand a weaker criterion than (IIIa), as the excluded area of two bodies depending on their intermolecular angle is not exactly represented, which corresponds to the Mayer function integrated over the particle positions. Hence, we will determine the final, shape-dependent parameter a, as in three dimensions,[19] by requiring (IIIb) a minimal quadratic deviation from the exact excluded area. This criterion can be refined in various ways following the examples[19–21,51] in three dimensions. In order to further improve the general functional according to criteria (IIIa) and (IIIb), it becomes necessary to introduce additional parameters by including higher-order terms of the expansion of the mixed weight function, which we will not consider here.

III. NUMERICAL METHODS

In the following, we study the phase behavior of (one component, $\kappa = 1$) hard discorectangles of aspect ratio $l = L/D$ in two dimensions, i.e., capped rectangles of length L and width D equal to the diameter of the capping disks. The goal of our work is twofold. First, we demonstrate for the first time a free numerical minimization of a FMMT functional, which is exact in the low-density limit, including the transitions between spatially inhomogeneous phases of anisotropic hard particles. Second, we extend the available reference data[43] for a system of hard discorectangles by performing new detailed MC simulations, which resolve between smectic and crystalline phases at high density. The used numerical techniques are described below.

A. Monte Carlo simulations

We perform MC simulations of perfectly hard rods in the isobaric-isothermal ensemble, i.e., at constant pressure p, number of particles N, and temperature T. Each simulation contains $N = 5760$ particles in a rectangular simulation box with variable box lengths, and simulations were run for approximately 10^6 MC sweeps (consisting of a rotation and translation move per particle, as well as several volume moves). All simulations were started using a perfect crystalline lattice as the initial configuration. Overlaps were detected using the two-dimensional equivalent of the algorithm introduced by Vega and Lago for spherocylinders.[52]

In the simulations, we measure the pair correlation function $g_{\parallel}(r)$ along a crystalline or smectic layer, averaged over the width of a single layer. We then plot $g_{\parallel}(r) - 1$ as a function of the distance r and investigate how the oscillations decay towards zero at large distances. In particular, we associate exponential decay (indicating short-ranged positional order) with the smectic phase and algebraic decay (associated with quasi-long-range order) with the crystalline phase. Figure 1 shows typical examples of correlation functions for aspect ratio

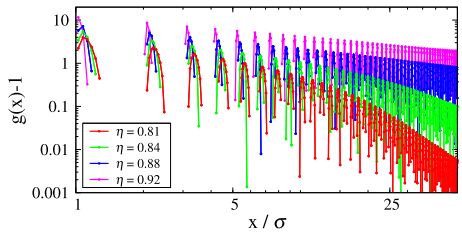

FIG. 1. Translational ordering in the high-density smectic and crystalline phases for aspect ratio $l = 4$. At lower packing fractions $\eta \lesssim 0.85$, we observe a fast (exponential) decay of the in-plane pair correlation function $g_{\parallel}(r) - 1$, while for higher η we find an algebraic decay.

$l = 4$. For all aspect ratios $l \geq 2$, we observe a crossover from exponential to algebraic decay in the correlation functions as the packing fraction increases. We estimate the transition line between the smectic and crystalline phases by extracting for each aspect ratio the packing fraction at which this crossover occurs.

In our simulations, we observe noticeable diffusion of particles between layers in the smectic phase, but essentially no diffusion in the crystal phase. This suggests that our observation of a transition to a crystalline phase might occur simply when our simulations are too short to sample the transfer of particles between layers. This would ensure that the number of particles per layer in our simulation is artificially fixed, favoring a crystalline state. To ensure that this effect does not meaningfully affect our result, we repeated simulations for several aspect ratios using shifted periodic boundary conditions, which facilitate transfer of particles between layers. Our results show no significant differences in the transition density measured using the two different approaches.

B. Density functional theory

Using the full expression (15) for $N(\mathbf{r})$ in the excess free energy density (16), we minimize the grand-canonical free energy functional in real space with respect to $\rho(\mathcal{R})$ by analogy with Ref. 53 using the following Picard iteration scheme:[7]

$$\rho^{(i+1)}(\mathcal{R}) = (1-\tilde{\alpha})\rho^{(i)}(\mathcal{R}) + \tilde{\alpha}\frac{1}{\Lambda^2}\exp\left(\beta\mu^{(i)} - \frac{\delta\beta\mathcal{F}_{\mathrm{exc}}}{\delta\rho(\mathcal{R})}\right) \quad (20)$$

with the mixing parameter $\tilde{\alpha} \leq 0.01$, Λ set to D, and the functional derivative $\frac{\delta\beta\mathcal{F}_{\mathrm{exc}}}{\delta\rho(\mathcal{R})}$ [see also Eq. (58) in Ref. 40]. The chemical potential $\mu^{(i)}$ is recalculated in every iteration step to maintain the desired area fraction and converges to a finite value in the iteration. As in previous studies,[53–55] we combine this iteration with a direct inversion in the iterative subspace (DIIS)[56–59] to improve the convergence. The resolution of the spatial grid was chosen as $\Delta x = \Delta y \approx 0.03D$ and the discrete orientations of the particles are chosen in equidistant steps of $\Delta\phi = 2\pi/48$.

IV. RESULTS FOR THE PHASE DIAGRAM OF HARD DISCORECTANGLES

The functional, Eq. (16), based on the expansion in Eq. (19) can be minimized analytically for hard discorectangles

when we assume a homogeneous density. Demanding that condition (IIIb) from Sec. II B holds, the remaining parameter becomes $a = 3$ for any aspect ratio l of the discorectangles. Note that in the HD limit, $l \to 0$, where there is no distinction between an isotropic and a nematic phase, condition (IIIb) is equivalent to (I) so that the parameter $a = a_{\mathrm{HD}} = 11/4$ can be used to fulfill (IIIa) instead.[11] However, the present choice $a = 3$ was found in Ref. 11 to be even more consistent with the simulation data for the bulk pressure of the HD crystal. Moreover, the excluded area of parallel discorectangles can be exactly represented by choosing $a = 4$.

By analogy with the functional in three dimensions, we expect that the choice $a = 3$ will provide reliable results for the isotropic and moderately ordered nematic phases but will not allow us to describe a stable smectic phase.[20,51] The latter is only possible qualitatively for $a = 4$, ensuring that the free energy per particle does not diverge in the limit $l \to \infty$. However, this parameter will result in a poor description of the homogeneous phases,[20,51] which is most apparent by comparing to a_{HD} in the HD limit.

To avoid the ambiguity of choosing a proper value of a, our main objective is to perform a free numerical minimization of the full functional from Eq. (16) with the mixed weighted density from Eq. (15), which is feasible in two dimensions. The employed algorithm is described in Sec. III. As a first step, however, we will demonstrate the utility of expanding the functional by calculating a closed expression for the isotropic–nematic transition line.

To characterize the homogeneous phases, we represent the density $\rho(\varphi) = \rho\, g(\cos\varphi)$ in terms of a normalized orientational distribution function $g(\cos\varphi)$. The two-dimensional nematic order parameter is conveniently defined as

$$S = \frac{2}{\pi}\int_0^{\pi/2} \mathrm{d}\varphi \left(2\cos^2\varphi - 1\right) g(\cos\varphi). \tag{21}$$

For discorectangles, we obtain the weighted densities

$$\begin{aligned} n_2 &= \rho\left(LD + \frac{\pi}{4}D^2\right) = \eta, \\ n_1 &= \rho\,(2L + \pi D), \quad n_0 = \rho, \\ (\overleftrightarrow{n}_1)_{11} &= \rho\left(L(1+S) + \frac{\pi}{2}D\right), \\ (\overleftrightarrow{n}_1)_{22} &= \rho\left(L(1-S) + \frac{\pi}{2}D\right), \end{aligned} \tag{22}$$

where η denotes the packing fraction. For a given aspect ratio l, the (nematic) free energy thus becomes a function of η and S when we use the approximation in Eq. (19).

Minimization with respect to the orientational distribution function[18] results in

$$g(\alpha, \cos\varphi) = \frac{\exp\left(\alpha^2(2\cos^2\varphi - 1)\right)}{I_0(\alpha^2)}, \tag{23}$$

where I_n denotes the modified Bessel function of the first kind, which follows from the normalization condition $\int_0^{\pi/2} \mathrm{d}\varphi\, g(\cos\varphi) = \pi/2$. The parameter $\alpha(\eta, l)$ then follows from the self-consistency equation

$$\alpha^2 := -\frac{\partial\Phi_{\mathrm{ex}}(\eta, S, l)}{\rho\,\partial S}. \tag{24}$$

Inserting Eq. (23) into Eq. (21), we obtain the nematic order parameter

$$S(\alpha) = \frac{I_1(\alpha^2)}{I_0(\alpha^2)} = \frac{1}{2}\alpha^2 - \frac{1}{16}\alpha^6 + \mathcal{O}(\alpha^{10}) \tag{25}$$

as a function of α.

A. Isotropic–nematic transition

In order to study the isotropic–nematic transition, one has to solve Eq. (24). For the functional from Eqs. (16) and (19), there is at most one (stable) solution to Eq. (24) at a given density, which is not the case in three dimensions. This can be easily seen by rewriting the condition in the generic form $\alpha^2 - CS(\alpha) = 0$ with a positive parameter $C \simeq C(\eta, l)$. The position $C_{\min}(\alpha)$ at which the expression on the left-hand side becomes minimal increases monotonously with increasing α. Therefore, at $\alpha = 0$ the isotropic and nematic solutions are indistinguishable, denoting a second-order phase transition, as it is expected from computer simulations,[43,60] although also first-order transitions between the isotropic and nematic phases are discussed in the literature.[25,61,62] Nevertheless, in three dimensions, the corresponding result for $S(\alpha)$ admits a non-monotonic behavior of $C_{\min}(\alpha)$, indicating that the nematic phase is only metastable at small order parameters, i.e., the isotropic–nematic transition is of first order.[18]

Solving Eq. (24) for η yields a closed expression for the packing fraction

$$\eta_{\mathrm{N}}(\alpha) = \left(1 + \frac{8l^2(a-1)I_1(\alpha^2)}{3\pi(4l+\pi)\alpha^2 I_0(\alpha^2)}\right)^{-1} \tag{26}$$

at which the nematic phase is stable for a given α. Numerically inverting $\eta_{\mathrm{N}}(\alpha)$ and comparing to Eq. (25), we can calculate the nematic order parameter $S(\eta)$ as a function of the packing fraction. In the limit of vanishing orientational order, we obtain the packing fraction

$$\eta_{\mathrm{IN}} := \lim_{\alpha\to 0}\eta_{\mathrm{N}}(\alpha) = \left(1 + \frac{4l^2(a-1)}{3\pi(4l+\pi)}\right)^{-1} \tag{27}$$

at the second-order isotropic–nematic transition of hard discorectangles in two dimensions for an arbitrary aspect ratio l and the parameter a. Obviously, with increasing the aspect ratio, the transition density decreases down to the scaled density

$$c_{\mathrm{N}} := \lim_{l\to\infty}\eta_{\mathrm{IN}} l = \frac{3\pi}{a-1} \tag{28}$$

obtained in the Onsager limit $l \to \infty$.

As the isotropic–nematic transition in two dimensions is of second order, the influence of higher-order terms in the expansion of the mixed weighted density from Eq. (19) is negligible, if the appropriate value $a = 3$ is chosen in a way that it ensures that the leading term in the order-parameter dependence is retained. Therefore, the result for η_{IN} given by Eq. (27) with $a = 3$ is equivalent to that obtained with the full functional from Eq. (19) based on the exact two-body representation. This is well confirmed for infinitely long rods where the Onsager result[63] for the transition density is

given by Eq. (28) with $a = 3$. A more detailed explanation has been given for the analogous three-dimensional case,[40,50] addressing the limit of metastability of the isotropic phase. Up to the first non-vanishing term in the parameter α, we can write

$$\eta_N(\alpha) - \eta_{IN} = \frac{6l^2\pi(4l+\pi)(a-1)}{(4l^2(a-1)+3\pi(4l+\pi))^2} S^2 + \mathcal{O}(\alpha^8) \quad (29)$$

with the help of Eq. (25). This result suggests that the nematic order parameter S approaches the critical point with a critical exponent of 1/2.

In Fig. 2 we show the density at the isotropic–nematic transition of hard discorectangles given by Eq. (27) as a function of the (inverse) aspect ratio D/L for different values of the parameter a. Our full minimization confirms the analytical finding that the transition is of second order. As discussed above, the results agree perfectly with those for $a = 3$ within the numeric error. For instance, at $l = 9$ we find $\eta_{IN} = 0.363$ and numerically $\eta_{IN} = 0.365 \pm 0.002$. However, compared to the simulation data,[43,60] the DFT predicts much smaller values. This discrepancy is comparable to the inaccuracy of the Onsager functional[63] due to disregarding the virial coefficients higher than the second, which do not vanish in two dimensions. From this perspective, Eq. (28) provides a simple method to fix the parameter a to recover the simulation result $c_{IN} \approx 7$ for $l \to \infty$,[60] which appears more reasonable than fitting to simulation data at finite aspect ratio, as proposed in three dimensions,[18] but is still empirical in nature. Indeed, accordingly choosing $a = 3\pi/7 + 1$ results in better agreement with the simulation data for rods of finite thickness but deviates more and more with decreasing aspect ratio. Since this purely empirical approach is also inconsistent with the proper implementation of FMMT, we will not further discuss it here. On the other hand, choosing $a = 4$ results in the poorest functional for the isotropic–nematic transition.

Now we study the nematic phase of discorectangles with aspect ratio $l = 9$ in more detail. For various densities close to the isotropic–nematic transition, we compare in Fig. 3 the nematic order parameter S obtained according to Eq. (21) from a minimization of the full functional (red) and the analytical approximation with $a = 3$ using Eqs. (25) and (26) (black). We observe that beyond the common (up to a horizontal shift due to the numeric error) transition point with $S(\eta_{IN}) = 0$, the numerical result for the order parameter increases faster than that of the approximation in terms of rank-two tensors. Fitting $b\sqrt{\eta - \eta_{IN}}$ with fit parameter $b \approx 3.22$ (gray) to the numeric data shows a very good agreement close to η_{IN} and also points to a critical exponent of 1/2. From Eq. (29) we find $\tilde{b} \approx 2.94 < b$ for the analytical approximation.

The reason for the stronger increase of the order parameter in the numerical data is that the orientational distribution, Eq. (23), and thus the expansion of the nematic order parameter S in Eq. (25) are only exact at leading order in the orientational anisotropy, i.e., up to the quadratic term in α. As demonstrated in three dimensions,[40,50] it is possible to include tensors of higher rank to the expansion from Eq. (19) in a systematic way (suitably chosen correction parameters). This results in the presence of additional order parameters and a more accurate analytic solution for the nematic orientational distribution. For example, the nematic order parameter in Fig. 3 calculated from such an approach would converge to the data from a free minimization of the full functional.

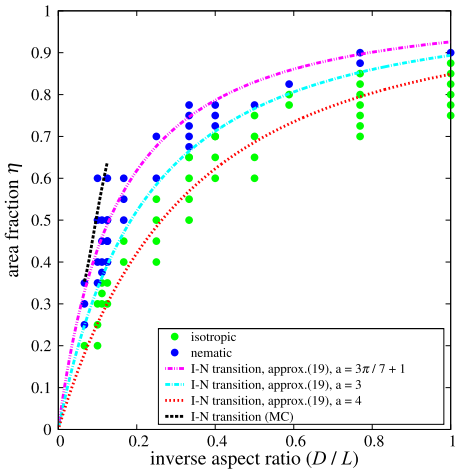

FIG. 2. Packing fraction at the second-order isotropic–nematic transition of two-dimensional hard discorectangles from the analytic prediction given by Eq. (27) (lines) for the parameters $a = 3\pi/7+1 \approx 2.35$ [obtained to fit Eq. (28) to the simulation result[60] in the Onsager limit, magenta], $a = 3$ (cyan), and $a = 4$ (red) as a function of the inverse aspect ratio $l^{-1} = D/L$. The approximation (19) with $a = 3$ matches the isotropic–nematic transition of the full functional with Eq. (15) (points), which was numerically evaluated under the constraint of a spatially homogeneous density. Data from MC simulations[43] are shown for comparison (black line).

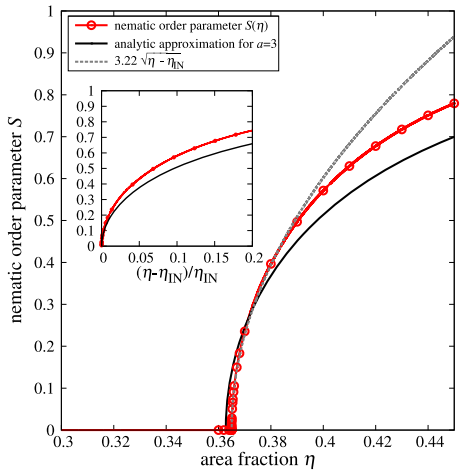

FIG. 3. Nematic order parameter $S(\eta)$ for discorectangles with aspect ratio $l = 9$ close to the area fraction of the isotropic–nematic transition η_l as a function of the area fraction η. Both numeric results for Eq. (15) (red) and analytic results for the approximation (19) with $a = 3$ (black) show a second-order transition between the isotropic and the nematic phases. Close to this transition, the nematic order parameter can be fitted with a square root function (gray), showing a critical exponent of 1/2, which agrees with that suggested by Eq. (29). The inset compares the shape of $S(\eta)$ for Eqs. (15) and (19) when rescaled.

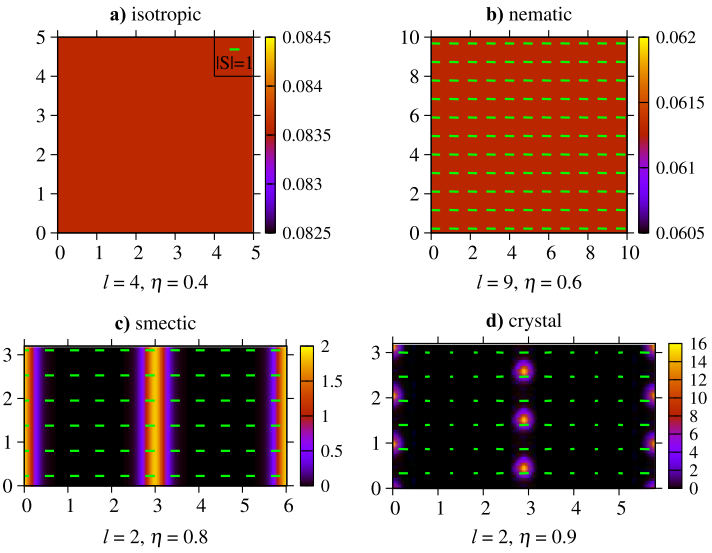

FIG. 4. Density and orientation profiles for various aspect ratios l and area fractions η. The orientation integrated center-of-mass density is shown in the color plot, while the local mean orientation is indicated with green dashes for (a) the isotropic phase at $l = 4$, $\eta = 0.4$, (b) the nematic phase at $l = 9$, $\eta = 0.6$, (c) the smectic phase at $l = 2$, $\eta = 0.8$, (d) the crystalline phase at $l = 2$, $\eta = 0.9$. For scale, a dash with length corresponding to perfect nematic order ($|S| = 1$) is drawn in (a).

B. Inhomogeneous phases

Taking now also spatially inhomogeneous phases into consideration, it is no longer possible to obtain an accurate analytic solution of the functional. Instead, we perform a full numerical minimization of the functional including the full expression, Eq. (15), for the mixed weighted density. We find in total four different phases for both DFT and MC: (a) an isotropic phase with neither orientational nor spatial order, (b) a nematic phase with orientational but no spatial order, (c) a smectic phase with orientational order and spatial order in one dimension, and (d) a crystalline phase with both orientational order and spatial order in two dimensions. Typical DFT profiles for these four phases are shown in Fig. 4 and particle resolved sketches for these phases are shown in the insets of Fig. 5. The phase diagram for varying aspect ratios ($l = L/D$) and area fractions (η) is shown in Fig. 5.

The isotropic phase (I, green) is dominating at low area fractions. For all aspect ratios at sufficiently high area fractions, the discorectangles freeze into a crystal (Cry, purple), with layers of discorectangles. Particles of adjacent layers are shifted by half a particle width, allowing the rounded caps of one particle to fill the voids between two rounded caps in each adjacent layer [see the density profile in Fig. 4(d) or the inset in Fig. 5]. Such a crystal allows for the closest packing (gray dotted line in Fig. 5). The closest packing η_{cp} as a function of the aspect ratio l is given by

$$\eta_{\mathrm{cp}} = \frac{l + \pi/4}{l + \sqrt{3}/2}. \tag{30}$$

For large aspect ratios, a nematic phase (N, blue) is found for intermediate area fractions for both DFT and MC, although the stability of the nematic phase is overestimated by DFT when compared with MC data (black dashed line, Ref. 43), as discussed in Sec. IV A.

For the first-order phase transition between a solid phase (either smectic or crystal) and a fluid phase (either isotropic or nematic), MC data are taken from the work of Bates and Frenkel.[43] These "melting/freezing lines" (black solid lines in Fig. 5) are coexistence lines, which were calculated via free energy calculations for $l \leq 7$ and extrapolated to larger aspect ratios.[43] For this phase transition, the agreement between the MC data and our DFT is very good. In particular, in the HD limit ($l = 0$), the transition density between the

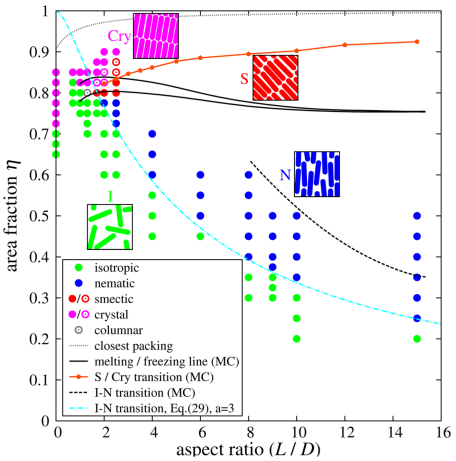

FIG. 5. The phase diagram for discorectangles as a function of aspect ratio and area fraction is shown for FMMT data (points) and compared with MC data (lines). For the transition between a solid phase (S or Cry) and a fluid phase (I or N), the corresponding melting and freezing lines for MC (black solid lines, adopted from Ref. 43) are in very good agreement with DFT. At sufficiently high aspect ratios, we find for the solid a transition from a smectic (red) to a crystalline (purple) phase for both MC (red line) and DFT. Close to this transition, the energy difference between the smectic and crystalline phases was close to our numeric error bars. Those points are displayed with open symbols for the slightly dominating phase. The stability of the nematic phase (blue) is overestimated when compared with MC data (black dashed line, adopted from Ref. 43). The topology is identical for both DFT and MC, except that we find a columnar phase once in the DFT (gray). The closest packing (gray dotted line) is shown for comparison. Sketches for the phases are shown in the insets.

isotropic and the crystalline phases matches the values found in early computer simulations[64] and DFT calculations based on Eq. (19).[11]

For small aspect ratios ($l \leq 1$), the discorectangles directly freeze into a crystal when increasing the area fraction. At higher aspect ratios ($l \geq 1.7$), the discorectangles freeze first into a smectic phase (S, red) with orientational and translational order in just one spatial dimension, before they cross over to the crystal at even higher area fractions. We find this behavior for both DFT and our refined MC. Close to this transition, the energy difference between the smectic and crystalline phases is close to our numeric error bars. This uncertainty is depicted in Fig. 5 with open symbols indicating the slightly dominating phase. At $l = 1.3$ (close to the isotropic–smectic–crystal triple point), we find in DFT a columnar phase, with particle alignment parallel to the density layer, instead of a smectic phase at a single state point between the isotropic and the crystal. We do not observe this in MC.

Note that the MC data in Fig. 5 for the melting of the solid does not take into account the possibility of melting via the Kosterlitz-Thouless (KT) dislocation unbinding mechanism, which would not be visible in DFT,[11] but could influence simulations. However, such a melting scenario is only likely to occur for very short rods, close to the HD limit where a KT crystal–hexatic transition and a first-order hexatic–isotropic transition are predicted.[65,66] Reference 43 reported no evidence of topological defects even for $l = 1$, and hence in the regime explored with simulations here, we do not expect this scenario. In contrast, the nematic–isotropic transition does occur via a continuous KT transition.[43]

V. CONCLUSIONS

In conclusion, we have predicted the bulk phase diagram of two-dimensional hard rods from fundamental mixed measure theory and found a stable isotropic, nematic, smectic, and crystalline phase depending on the particle aspect ratio and density. In general, it is mandatory to use a free minimization technique to obtain the correct minimizing equilibrium state in the density functional theory. At intermediate area fractions, the second-order isotropic–nematic transition is equally described by an analytical curve found from a simple expansion of the functional. The density functional results for the phase diagram agree well with our MC calculations, which also show a stable smectic phase.

For the first time, we have implemented a free minimization of the two-dimensional version of FMMT, which is not feasible in higher dimensions. In further contrast to the three-dimensional case, the mixed weighted density does not vanish in the HD limit,[36] and thus our approach also provides the most accurate way to study the crystallization of the HD fluid within the framework of FMT. Moreover, the value of the free parameter in the computationally more efficient expanded functional from Ref. 11 derived here appears to give better results for the HD crystal[11] and the liquid crystal surface tension.[67]

For the inhomogeneous phases of very long rods at high densities, a free minimization of FMMT becomes more demanding. Following the examples in three dimensions, this region of the phase diagram can be explored more efficiently by systematically expanding the mixed weighted density for intermediate aspect ratios[38] or by a linearization in the orientation-dependence for highly aligned systems of very long rods.[21,50] Another possible simplification would be to perform an (approximate) parametrized minimization, in combination with the decoupling approximation.[20] The latter is well justified for the smectic phase since Fig. 4(c) indicates that the orientational order is independent of the spatial coordinate. This procedure could allow for an analytic calculation in the limit of strong alignment.[21,50]

We have seen that the onset of crystallization is predicted very accurately for the aspect ratios considered here, which should also be the case for longer rods since FMMT recovers the cell theory limit.[51] Note that, for some versions of the cubic term in the density, the three-dimensional FMMT can diverge in an unphysical way when applied to highly aligned long rods.[20,51] There is no such pitfall for FMMT (and the expanded form with $a = 4$) in two dimensions. By construction, FMMT also reduces to scaled particle theory for a homogeneous fluid, which is known to overestimate the pressure at finite density, and to Onsager theory for infinitely long rods, which omits all relevant virial coefficients higher than the second. As a result, the nematic phase is severely overstabilized compared to the isotropic fluid, and we expect that the nematic–smectic transition of long rods predicted by FMMT will occur at smaller densities than found in computer simulations, which is also the case in three dimensions.[21]

In the future, the theory should be applied and generalized towards different situations: first of all, other particle shapes such as two-dimensional ellipses[68,69] or rectangles with sharp edges[53,70] can be considered, as well as mixtures between particles of different sizes[37,71] or shapes.[72] Second, our bulk phase diagram provides the starting point for a microscopic theory of interfaces[49,55] between two coexisting phases that show interesting translational and orientational structures.[73] Third, our density functional theory can be generalized towards dynamical density functional theory[74–80] describing translational and orientational Brownian dynamics of rods.[45] Finally our results for the phase diagram can in principle be verified by experiments using layers of monodisperse sterically stabilized colloidal rod-like particles.[29,81–86] Another macroscopic option is shaken granular rods[87,88] on a substrate which resemble equilibrium phase behavior.

ACKNOWLEDGMENTS

We thank Axel Voigt, Martin Oettel, and Shang-Chun Lin for helpful discussions. Financial support from the German Research Foundation (DFG) is gratefully acknowledged within Project No. LO 418/20-1. Moreover, R.W. gratefully acknowledges funding provided by the Swiss National Science Foundation and fruitful discussions with Joseph Brader and Matthieu Marechal.

[1] R. Evans, Adv. Phys. **28**, 143 (1979).
[2] D. Oxtoby, in *Liquids, Freezing and Glass Transition, Proceedings of the Les Houches Summer School, Course LI, 3–28 July 1989*, edited by J.-P. Hansen, D. Levesque, and J. Zinn-Justin (USMG, NATO Advanced Study Institute,

Elsevier Science Publishers B. V., North Holland, Amsterdam, 1991), Vol. 1, pp. 145–192.
[3]Y. Singh, Phys. Rep. **207**, 351 (1991).
[4]H. Löwen, Phys. Rep. **237**, 249 (1994).
[5]J. Wu and Z. Li, Annu. Rev. Phys. Chem. **58**, 85 (2007).
[6]P. Tarazona, J. A. Cuesta, and Y. Martínez-Ratón, in *Theory and Simulation of Hard-Sphere Fluids and Related Systems*, 1st ed., Lecture Notes in Physics Vol. 753, edited by Á. Mulero (Springer-Verlag, Berlin, 2008), Chap. 7, pp. 247–341.
[7]R. Roth, J. Phys.: Condens. Matter **22**, 063102 (2010).
[8]P. Bryk, R. Roth, K. R. Mecke, and S. Dietrich, Phys. Rev. E **68**, 031602 (2003).
[9]P.-M. König, R. Roth, and K. R. Mecke, Phys. Rev. Lett. **93**, 160601 (2004).
[10]A. Tröster, M. Oettel, B. Block, P. Virnau, and K. Binder, J. Chem. Phys. **136**, 064709 (2012).
[11]R. Roth, K. Mecke, and M. Oettel, J. Chem. Phys. **136**, 081101 (2012).
[12]L. Onsager, Ann. N. Y. Acad. Sci. **51**, 627 (1949).
[13]A. Poniewierski and R. Hołyst, Phys. Rev. Lett. **61**, 2461 (1988).
[14]R. van Roij, P. Bolhuis, B. Mulder, and D. Frenkel, Phys. Rev. E **52**, R1277 (1995).
[15]A. M. Bohle, R. Hołyst, and T. Vilgis, Phys. Rev. Lett. **76**, 1396 (1996).
[16]H. Graf and H. Löwen, J. Phys.: Condens. Matter **11**, 1435 (1999).
[17]G. Cinacchi and F. Schmid, J. Phys.: Condens. Matter **14**, 12223 (2002).
[18]H. Hansen-Goos and K. Mecke, Phys. Rev. Lett. **102**, 018302 (2009).
[19]H. Hansen-Goos and K. Mecke, J. Phys.: Condens. Matter **22**, 364107 (2010).
[20]R. Wittmann, M. Marechal, and K. Mecke, J. Chem. Phys. **141**, 064103 (2014).
[21]R. Wittmann, M. Marechal, and K. Mecke, Europhys. Lett. **109**, 26003 (2015).
[22]M. Oettel, M. Klopotek, M. Dixit, E. Empting, T. Schilling, and H. Hansen-Goos, J. Chem. Phys. **145**, 074902 (2016).
[23]S. Varga and I. Szalai, Mol. Phys. **95**, 515 (1998).
[24]Y. Martínez-Ratón, E. Velasco, and L. Mederos, J. Chem. Phys. **122**, 064903 (2005).
[25]H. H. Wensink and R. L. C. Vink, J. Phys.: Condens. Matter **19**, 466109 (2007).
[26]D. de las Heras, E. Velasco, and L. Mederos, Phys. Rev. E **79**, 061703 (2009).
[27]S. Varga, P. Gurin, J. C. Armas-Pérez, and J. Quintana-H, J. Chem. Phys. **131**, 184901 (2009).
[28]J. Z. Y. Chen, Soft Matter **9**, 10921 (2013).
[29]T. Müller, D. de las Heras, I. Rehberg, and K. Huang, Phys. Rev. E **91**, 062207 (2015).
[30]A. Díaz-De Armas and Y. Martínez-Ratón, Phys. Rev. E **95**, 052702 (2017).
[31]P. Bolhuis and D. Frenkel, J. Chem. Phys. **106**, 666 (1997).
[32]Y. Rosenfeld, Phys. Rev. Lett. **63**, 980 (1989).
[33]Y. Rosenfeld, Phys. Rev. E **50**, R3318 (1994).
[34]M. Marechal and H. Löwen, Phys. Rev. Lett. **110**, 137801 (2013).
[35]H. Hansen-Goos and R. Roth, J. Phys.: Condens. Matter **18**, 8413 (2006).
[36]P. Tarazona and Y. Rosenfeld, Phys. Rev. E **55**, R4873 (1997).
[37]Y. Rosenfeld, Phys. Rev. A **42**, 5978 (1990).
[38]M. Marechal, S. Dussi, and M. Dijkstra, J. Chem. Phys. **146**, 124905 (2017).
[39]Y. Martínez-Ratón, J. A. Capitán, and J. A. Cuesta, Phys. Rev. E **77**, 051205 (2008).
[40]R. Wittmann, M. Marechal, and K. Mecke, Phys. Rev. E **91**, 052501 (2015).
[41]A. Esztermann, H. Reich, and M. Schmidt, Phys. Rev. E **73**, 011409 (2006).
[42]M. P. Allen and D. J. Tildesley, *Computer Simulation of Liquids*, 1st ed., Oxford Science Publications (Oxford University Press, Oxford, 1989), p. 408.
[43]M. A. Bates and D. Frenkel, J. Chem. Phys. **112**, 10034 (2000).
[44]P. Patrício, J. M. Romero-Enrique, N. M. Silvestre, N. R. Bernardino, and M. M. Telo da Gama, Mol. Phys. **109**, 1067 (2011).
[45]M. Rex, H. H. Wensink, and H. Löwen, Phys. Rev. E **76**, 021403 (2007).
[46]R. Schneider and W. Weil, *Stochastic and Integral Geometry, Probability and its Applications* (Springer, Berlin, Heidelberg, 2008).
[47]M. Marechal, H. H. Goetzke, A. Härtel, and H. Löwen, J. Chem. Phys. **135**, 234510 (2011).
[48]M. Marechal, S. Korden, and K. Mecke, Phys. Rev. E **90**, 042131 (2014).
[49]R. Wittmann and K. Mecke, J. Chem. Phys. **140**, 104703 (2014).
[50]R. Wittmann, "Density functional theory for liquid Crystals: Refining fundamental measure theory for anisotropic bodies," Ph.D. thesis, Friedrich-Alexander-Universität Erlangen-Nürnberg, 2015.
[51]R. Wittmann, M. Marechal, and K. Mecke, J. Phys.: Condens. Matter **28**, 244003 (2016).
[52]C. Vega and S. Lago, Comput. Chem. **18**, 55 (1994).
[53]C. E. Sitta, F. Smallenburg, R. Wittkowski, and H. Löwen, J. Chem. Phys. **145**, 204508 (2016).
[54]M. Oettel, S. Dorosz, M. Berghoff, B. Nestler, and T. Schilling, Phys. Rev. E **86**, 021404 (2012).
[55]A. Härtel, M. Oettel, R. E. Rozas, S. U. Egelhaaf, J. Horbach, and H. Löwen, Phys. Rev. Lett. **108**, 226101 (2012).
[56]K. C. Ng, J. Chem. Phys. **61**, 2680 (1974).
[57]P. Pulay, Chem. Phys. Lett. **73**, 393 (1980).
[58]P. Pulay, J. Comput. Chem. **3**, 556 (1982).
[59]A. Kovalenko, S. Ten-no, and F. Hirata, J. Comput. Chem. **20**, 928 (1999).
[60]D. Frenkel and R. Eppenga, Phys. Rev. A **31**, 1776 (1985).
[61]R. L. C. Vink, Phys. Rev. Lett. **98**, 217801 (2007).
[62]J. M. Fish and R. L. C. Vink, Phys. Rev. E **81**, 021705 (2010).
[63]R. F. Kayser and H. J. Raveché, Phys. Rev. A **17**, 2067 (1978).
[64]B. J. Alder and T. E. Wainwright, Phys. Rev. **127**, 359 (1962).
[65]E. P. Bernard and W. Krauth, Phys. Rev. Lett. **107**, 155704 (2011).
[66]A. L. Thorneywork, J. L. Abbott, D. G. A. L. Aarts, and R. P. A. Dullens, Phys. Rev. Lett. **118**, 158001 (2017).
[67]M. Oettel and S.-C. Lin, private communication (2017).
[68]M. E. Foulaadvand and M. Yarifard, Phys. Rev. E **88**, 052504 (2013).
[69]G. Bautista-Carbajal and G. Odriozola, J. Chem. Phys. **140**, 204502 (2014).
[70]M. González-Pinto, Y. Martínez-Ratón, and E. Velasco, Phys. Rev. E **88**, 032506 (2013).
[71]M. Dijkstra, R. van Roij, and R. Evans, Phys. Rev. E **59**, 5744 (1999).
[72]F. M. van der Kooij and H. N. W. Lekkerkerker, Langmuir **16**, 10144 (2000).
[73]S. Praetorius, A. Voigt, R. Wittkowski, and H. Löwen, Phys. Rev. E **87**, 052406 (2013).
[74]U. M. B. Marconi and P. Tarazona, J. Chem. Phys. **110**, 8032 (1999).
[75]U. M. B. Marconi and P. Tarazona, J. Phys.: Condens. Matter **12**, A413 (2000).
[76]A. J. Archer and R. Evans, J. Chem. Phys. **121**, 4246 (2004).
[77]U. M. B. Marconi and S. Melchionna, J. Chem. Phys. **126**, 184109 (2007).
[78]P. Español and H. Löwen, J. Chem. Phys. **131**, 244101 (2009).
[79]R. Wittkowski and H. Löwen, Mol. Phys. **109**, 2935 (2011).
[80]B. D. Goddard, A. Nold, N. Savva, P. Yatsyshin, and S. Kalliadasis, J. Phys.: Condens. Matter **25**, 035101 (2013).
[81]K.-H. Lin, J. C. Crocker, V. Prasad, A. Schofield, D. A. Weitz, T. C. Lubensky, and A. G. Yodh, Phys. Rev. Lett. **85**, 1770 (2000).
[82]J. Galanis, R. Nossal, W. Losert, and D. Harries, Phys. Rev. Lett. **105**, 168001 (2010).
[83]M. Hermes, E. C. M. Vermolen, M. E. Leunissen, D. L. J. Vossen, P. D. J. van Oostrum, M. Dijkstra, and A. van Blaaderen, Soft Matter **7**, 4623 (2011).
[84]O. Zvyagolskaya, A. J. Archer, and C. Bechinger, Europhys. Lett. **96**, 28005 (2011).
[85]T. H. Besseling, M. Hermes, A. Kuijk, B. de Nijs, T.-S. Deng, M. Dijkstra, A. Imhof, and A. van Blaaderen, J. Phys.: Condens. Matter **27**, 194109 (2015).
[86]L. Walsh and N. Menon, J. Stat. Mech.: Theory Exp. **2016**, 083302.
[87]R. Cruz Hidalgo, I. Zuriguel, D. Maza, and I. Pagonabarraga, J. Stat. Mech.: Theory Exp. **2010**, P06025.
[88]S. Hernández-Navarro, J. Ignés-Mullol, F. Sagués, and P. Tierno, Langmuir **28**, 5981 (2012).

Veröffentlichung IV Liquid crystals of hard rectangles on flat and cylindrical manifolds

C. E. Sitta, F. Smallenburg, R. Wittkowski & H. Löwen
Liquid crystals of hard rectangles on flat and cylindrical manifolds,
Phys. Chem. Chem. Phys. (2018),
veröffentlicht als *accepted manuscript* durch *The Royal Society of Chemistry*.

Digital Object Identifier (DOI): 10.1039/C5CP07781H

Stellungnahme zum eigenen Beitrag

H.L. und ich haben das Forschungsprojekt entwickelt.
H.L. und R.W. haben das Forschungsprojekt betreut.
F.S. hat die MC Simulationen implementiert und durchgeführt.
Ich habe die neue Dichtefunktionaltheorie entwickelt sowie die numerische Minimierung implementiert und durchgeführt.
R.W. und ich haben Abb. 1-4 und 6 erstellt.
F.S. und R.W. haben Abb. 5 erstellt.
Alle Autoren haben die Ergebnisse interpretiert und das Manuskript geschrieben.

Copyright und Lizenzhinweise

Page 1 of 11 Physical Chemistry Chemical Physics

View Article Online
DOI: 10.1039/C7CP07026H

Liquid crystals of hard rectangles on flat and cylindrical manifolds

Christoph E. Sitta,[1] Frank Smallenburg,[1] Raphael Wittkowski,[2,3] and Hartmut Löwen[1]

[1] *Institut für Theoretische Physik II: Weiche Materie, Heinrich-Heine-Universität Düsseldorf, D-40225 Düsseldorf, Germany*

[2] *Institut für Theoretische Physik, Westfälische Wilhelms-Universität Münster, D-48149 Münster, Germany*

[3] *Center for Nonlinear Science (CeNoS), Westfälische Wilhelms-Universität Münster, D-48149 Münster, Germany*

Using the classical density functional theory of freezing and Monte Carlo computer simulations, we explore the liquid-crystalline phase behavior of hard rectangles on flat and cylindrical manifolds. Moreover, we study the effect of a static external field which couples to the rectangles' orientations, aligning them towards a preferred direction. In the flat and field-free case, the bulk phase diagram involves stable isotropic, nematic, tetratic, and smectic phases depending on the aspect ratio and number density of the particles. The external field shifts the transition curves significantly and generates a binematic phase at the expense of the tetratic phase. On a cylindrical manifold, we observe tilted smectic-like order, as obtained by wrapping a smectic layer around a cylinder. We find in general good agreement between our density functional calculations and particle-resolved computer simulations and mention possible setups to verify our predictions in experiments.

I. INTRODUCTION

There are many ways to control structural ordering and topological defects in liquid crystals. One way is to expose them to an external field which aligns the particle orientations and therefore favors the formation of orientationally ordered phases.[1–11] Another way is to confine liquid crystals on a curved manifold which enforces the formation of defects due to topological constraints.[11–23] Our fundamental understanding of the structuring of liquid crystals has been strongly aided by simulation studies of hard anisotropic particles, the minimal model required to obtain liquid-crystalline phase behavior.[24–32] Moreover, dating back to the seminal work of Onsager,[33] these systems have been studied extensively by the density functional theory of freezing (DFT).[26,32,34–47]

Although most studies on liquid crystals of hard particles are performed in three spatial dimensions, two-dimensional systems have been considered extensively as well.[27,28,32,35–37,39,41,43,48,49] In two dimensions, the phase behavior is often more subtle: even the phase behavior of hard disks differs significantly from that of hard spheres, due to the intervention of a hexatic phase between the fluid and crystalline states.[50,51] An additional source of complexity can be formed by the shape of the substrate supporting the particles. For example, two-dimensional sheets of liquid crystals can be constrained on a curved manifold resulting in liquid-crystalline shells[52,53] with many novel structural ordering phenomena.[54,55] These structures can be further tuned by aligning fields to, e.g., control the number of defects in the liquid-crystalline structure.[56] One of the simplest substrate shapes is a cylindrical manifold, where one of the principal curvatures vanishes. Interestingly, systematic studies for highly ordered liquid-crystalline phases (like smectics) on cylinders are not available for freely orientable rods or rectangles. Previous work addressed liquid crystals confined between two planar walls (see, e.g., Ref. 57) and the anisotropic dynamics of isotropic disks[58,59] or parallel cylinders[60] on a cylindrical manifold.

In this article we combine two aspects of controlling liquid-crystalline ordering, namely aligning external fields and constraints by curved manifolds. We do this for a two-dimensional system of hard rectangles and first study its bulk phase behavior in the flat and field-free case as a function of the particles' aspect ratio and number density. To tackle this problem, we propose a new DFT and perform complementary Monte Carlo (MC) computer simulations, showing stable isotropic,[36,49,61] nematic,[36,37,43,46,49,62] tetratic,[27–29,35–37,39,43,46,62–64] and smectic[36,41,43,62] phases. Upon applying an aligning external field, the phase transition curves are shifted significantly and a binematic phase occurs at the expense of the tetratic phase. We then consider the same system on a cylindrical manifold, adjusting the external field to favor orientation along the cylindrical perimeter. Interestingly, a new tilted smectic-like order is observed, which emerges from wrapping a smectic layer around a cylinder. This is similar in spirit to helical hard-sphere configurations inside cylinders.[65,66] In general, we find good agreement between our DFT calculations and the particle-resolved computer simulations. Our predictions can be verified in real-space experiments on strongly confined colloidal rods[67–74] and granulates.[62–64,75,76]

The paper is organized as follows: In Sec. II, we present our new DFT and describe the MC simulations. The results from the DFT calculations and MC simulations are presented in Sec. III, including the phase diagrams for the flat bulk system of hard rectangles with and without an external field as well as the extension towards a cylindrical manifold. Finally, we conclude in Sec. IV.

II. METHODS

A. Density functional theory

DFT[77–79] provides a versatile framework for determining the equilibrium density profile $\rho_{\mathrm{eq}}(\vec{r},\phi)$ of a system

Physical Chemistry Chemical Physics Page 2 of 11
View Article Online
DOI: 10.1039/C7CP07026H 2

of interacting particles. The one-particle density profile $\rho(\vec{r},\phi)$ represents the probability density for finding a particle with orientation ϕ at position $\vec{r}=(x,y)^{\mathrm{T}}$. For the rectangular particles considered in this work, ϕ denotes the angle measured counterclockwise from the positive x axis to the long axis of a particle. The key expression in DFT is the grand-canonical free-energy functional

$$\Omega[\rho(\vec{r},\phi)] = \mathcal{F}[\rho(\vec{r},\phi)] + \int_{\mathbb{R}^2}\mathrm{d}^2r \int_0^{2\pi}\mathrm{d}\phi\,\rho(\vec{r},\phi)(V_{\mathrm{ext}}(\vec{r},\phi)-\mu)\,, \tag{1}$$

which is minimized by $\rho_{\mathrm{eq}}(\vec{r},\phi)$ and whose value $\Omega[\rho_{\mathrm{eq}}(\vec{r},\phi)]$ matches the equilibrium value of the grand potential of the system. In Eq. (1), $\mathcal{F}[\rho(\vec{r},\phi)]$ is the Helmholtz free-energy functional, $V_{\mathrm{ext}}(\vec{r},\phi)$ is the external potential acting on the particles, and μ is the chemical potential. Unfortunately, $\mathcal{F}[\rho(\vec{r},\phi)]$ is rarely known except for a few special cases (e.g., for monodisperse hard particles in one spatial dimension[80]) and therefore usually needs to be approximated. It is commonly split as $\mathcal{F}=\mathcal{F}_{\mathrm{id}}+\mathcal{F}_{\mathrm{exc}}$ into a sum of the analytically known ideal-gas contribution $\mathcal{F}_{\mathrm{id}}$ and an unknown excess term $\mathcal{F}_{\mathrm{exc}}$. The ideal-gas term is given by

$$\beta\mathcal{F}_{\mathrm{id}} = \int_{\mathbb{R}^2}\mathrm{d}^2r \int_0^{2\pi}\mathrm{d}\phi\,\rho(\vec{r},\phi)\big(\ln(2\pi\Lambda^2\rho(\vec{r},\phi))-1\big) \tag{2}$$

with the inverse thermal energy β (also called thermodynamic beta) and the thermal de Broglie wavelength Λ.

For the excess term we propose a phenomenological approximation

$$\beta\mathcal{F}_{\mathrm{exc}} = \int_{\mathbb{R}^2}\mathrm{d}^2r\,\Phi(\vec{r}) \tag{3}$$

with the rescaled excess free-energy density $\Phi(\vec{r})$, which features all phases that were observed by simulations[27–29,37] and experiments[62–64] for a fluid of hard rectangles, i.e., an isotropic, a nematic, a tetratic, and a smectic phase. An illustration of the different phases is given by Fig. 1 further below. We write $\Phi(\vec{r})$ as a sum of four terms,

$$\Phi(\vec{r}) = \Phi_{\mathrm{Ons}}(\vec{r}) + \Phi_{\mathrm{FMT}}(\vec{r}) + \Phi_{\mathrm{T}}(\vec{r}) + \Phi_{\mathrm{P}}(\vec{r})\,, \tag{4}$$

which are explained and justified in detail in the following.

To equip our functional with an appropriate low-density limit, we start by using the Onsager approximation[33]

$$\Phi_{\mathrm{Ons}}(\vec{r}) = -\frac{1}{2}\int_0^{2\pi}\mathrm{d}\phi\,\rho(\vec{r},\phi)\int_{\mathbb{R}^2}\mathrm{d}^2r'\int_0^{2\pi}\mathrm{d}\phi'\rho(\vec{r}',\phi')f(\vec{r}-\vec{r}',\phi,\phi') \tag{5}$$

with the Mayer function

$$f(\vec{r}-\vec{r}',\phi,\phi') = \begin{cases} -1\,, & \text{if particles with coordinates} \\ & (\vec{r},\phi) \text{ and } (\vec{r}',\phi') \text{ overlap,} \\ 0\,, & \text{otherwise,} \end{cases} \tag{6}$$

which should perform well in the low-density limit of long rods. As this term scales with second order in density, our functional $\mathcal{F}_{\mathrm{exc}}$ will inherit this low-density behavior as long as all other terms on the right-hand side of Eq. (4) scale with third or higher order in density. The term $\Phi_{\mathrm{Ons}}(\vec{r})$ already yields an isotropic and a nematic phase but does not feature a stable tetratic phase except for squares. For high densities and spatial density modulations, which are necessary, e.g., for a smectic phase, functionals based on fundamental measure theory are known to perform better than the Onsager functional.[81]

Thus, another term is needed to model a smectic phase at high densities. As the particles should be well aligned at high densities, we adopt the excess free-energy functional for parallel hard rectangles, which was derived by Cuesta and Martínez-Ratón by a dimensional crossover,[82,83] and therefore introduce the term

$$\Phi_{\mathrm{FMT}}(\vec{r}) = n_2(\vec{r})\Big(-n_0(\vec{r})\ln\big(1-n_2(\vec{r})\big) + \frac{n_{1x}(\vec{r})\,n_{1y}(\vec{r})}{1-n_2(\vec{r})}\Big) \tag{7}$$

in our rescaled free-energy density. Here, the $n_i(\vec{r})$ with $i\in\{0,1x,1y,2\}$ are weighted densities as typical for fundamental measure theory.[79,84] In the case of freely orientable rectangles, they are defined as in Ref. 36 by the angle-integrated cross-correlations

$$\begin{aligned} n_i(\vec{r}) &= \int_0^{2\pi}\mathrm{d}\phi\,[\rho\star\omega^{(i)}](\vec{r},\phi) \\ &= \int_0^{2\pi}\mathrm{d}\phi\int_{\mathbb{R}^2}\mathrm{d}^2r'\,\rho(\vec{r}',\phi)\omega^{(i)}(\vec{r}'-\vec{r},\phi) \end{aligned} \tag{8}$$

of the one-particle density $\rho(\vec{r},\phi)$ with the geometric weight functions

$$\omega^{(0)}(\vec{r},\phi) = \frac{1}{4}\delta\Big(\frac{D}{2}-|x_\phi|\Big)\delta\Big(\frac{L}{2}-|y_\phi|\Big)\,, \tag{9}$$

$$\omega^{(1x)}(\vec{r},\phi) = \frac{1}{2}\delta\Big(\frac{D}{2}-|x_\phi|\Big)\Theta\Big(\frac{L}{2}-|y_\phi|\Big)\,, \tag{10}$$

$$\omega^{(1y)}(\vec{r},\phi) = \frac{1}{2}\Theta\Big(\frac{D}{2}-|x_\phi|\Big)\delta\Big(\frac{L}{2}-|y_\phi|\Big)\,, \tag{11}$$

$$\omega^{(2)}(\vec{r},\phi) = \Theta\Big(\frac{D}{2}-|x_\phi|\Big)\Theta\Big(\frac{L}{2}-|y_\phi|\Big)\,. \tag{12}$$

Here, $\delta(x)$ is the Dirac delta function and $\Theta(x)$ is the Heaviside function; D and L with $D<L$ denote the width and length of the rectangular particles, respectively, and x_ϕ and y_ϕ are defined as $x_\phi = x\cos(\phi) - y\sin(\phi)$ and $y_\phi = x\sin(\phi)+y\cos(\phi)$. Except for the prefactor $n_2(\vec{r})$, Eq. (7) is identical to the corresponding expression from Cuesta and Martínez-Ratón.[82,83] As their original expression scales with $\mathcal{O}(\rho^2)$, we need the dimensionless prefactor $n_2(\vec{r})$, which scales with order $\mathcal{O}(\rho)$, in Eq. (7) to maintain the low-density behavior from the Onsager term in Eq. (4).

Since the two previous terms do not feature a stable tetratic phase yet, we introduce an empirical term $\Phi_{\mathrm{T}}(\vec{r})$, which suppresses nematic order and favors tetratic order.

View Article Online
DOI: 10.1039/C7CP07026H 3

We make use of the squared Fourier coefficients $|A_2(\vec{r})|^2$ and $|A_4(\vec{r})|^2$, which are defined as

$$|A_n(\vec{r})|^2 = \frac{1}{\bar{\rho}(\vec{r})^2}\left(\int_0^{2\pi} \mathrm{d}\phi\, \rho(\vec{r},\phi)\, e^{-\mathrm{i}n\phi}\right)\left(\int_0^{2\pi} \mathrm{d}\phi\, \rho(\vec{r},\phi)\, e^{\mathrm{i}n\phi}\right) \tag{13}$$

with the angle-integrated center-of-mass density (i.e., concentration field) $\bar{\rho}(\vec{r}) = \int_0^{2\pi} \mathrm{d}\phi\, \rho(\vec{r},\phi)$. On the one hand, $|A_2(\vec{r})|^2 \to 1$ and $|A_4(\vec{r})|^2 \to 1$ holds for twofold nematic order in a perfect nematic phase. On the other hand, $|A_2(\vec{r})|^2 \to 0$ and $|A_4(\vec{r})|^2 \to 1$ holds for fourfold tetratic order in a perfect tetratic phase. Thus a term as simple as $\Phi_\mathrm{T} \propto a\,|A_2|^2 - |A_4|^2$ will favor tetratic order while suppressing nematic order if $a > 0$, whereas $a < 0$ will favor nematic order. Since tetratic order is present only in the tetratic phase, while the nematic and smectic phases include nematic order, we require the switching coefficient $a = a(L/D, n_2)$ to dependent on both the aspect ratio L/D and the weighted density $n_2(\vec{r})$ in order to adjust the phases at the correct positions in the phase diagram. Choosing $a = \chi_\mathrm{T}(L/D) - n_2(\vec{r})$ allows a to switch between negative values for local area fractions $n_2(\vec{r})$ above an aspect-ratio-dependent threshold area fraction $\chi_\mathrm{T}(L/D) > 0$ and positive values below this threshold. For the area fraction $\chi_\mathrm{T}(L/D)$ describing the transition between nematic and tetratic states, we shift a tanh to positive values by writing $\chi_\mathrm{T}(L/D) = 0.5c_1\big(1 + \tanh(c_2(c_3 - L/D))\big)$. The parameter c_1 corresponds to the largest area fraction where tetratic order is still possible, the parameter c_2 describes the steepness of $\chi_\mathrm{T}(L/D)$ at its inflection point, and the parameter c_3 sets the position of the inflection point. c_3 should be close to the largest aspect ratio where tetratic order is still observed. Testing several values for these parameters, the choice $c_1 = 0.85$, $c_2 = 2/3$, and $c_3 = 9$ resulted in the best agreement of the phase diagram obtained from the functional (1) and the MC simulation data.[85] The full tetratic term then reads

$$\Phi_\mathrm{T} = \frac{5}{2}\,\bar{\rho}(\vec{r})\, n_2(\vec{r})^2 \Big(1 + \big(\chi_\mathrm{T}(L/D) - n_2(\vec{r})\big)|A_2|^2 - \chi_\mathrm{T}(L/D)|A_4|^2\Big) \tag{14}$$

with the threshold area fraction

$$\chi_\mathrm{T}(L/D) = 0.425\left(1 + \tanh\big(\tfrac{2}{3}\,(9 - L/D)\big)\right). \tag{15}$$

In Eq. (14), the summand 1 in the outer parentheses and the positive prefactor $\chi_\mathrm{T}(L/D)$ in front of $|A_4|^2$ are included to improve numerical stability. The prefactor $(5/2)\bar{\rho}(\vec{r})\, n_2(\vec{r})^2$ with the angle-integrated local density $\bar{\rho}(\vec{r})$ ensures both that the dimensions of Φ_T are correct and that Φ_T scales with $\mathcal{O}(\rho^3)$ so that the low-density behavior of the Onsager term is maintained in Eq. (4). In this prefactor, the proportionality constant 5/2 is chosen to match the MC simulation data and constitutes the fourth fitted parameter in this model.

Finally, we add the penalty term

$$\Phi_\mathrm{P}(\vec{r}) = -\frac{n_2(\vec{r})^2}{D^2}\ln\big(1 - n_2(\vec{r})\big), \tag{16}$$

which diverges for local area fractions $n_2(\vec{r}) \to 1$, avoiding unphysical overlap of the hard particles and enhancing the numerical stability of the full functional. Again, a prefactor $(n_2(\vec{r})/D)^2$ is chosen for reasons of dimensionality and to maintain the low-density limit described by the Onsager term in Eq. (4) through $\Phi_\mathrm{P}(\vec{r})$ scaling with $\mathcal{O}(\rho^3)$.

After inserting Eqs. (5), (7), (14), and (16) into the rescaled excess free-energy density (4) and choosing an expression for the external potential $V_\mathrm{ext}(\vec{r},\phi)$, the equilibrium density $\rho_\mathrm{eq}(\vec{r},\phi)$ can be obtained by a free minimization of the functional (1) with respect to $\rho(\vec{r},\phi)$. When an aligning external field is taken into account, we choose the external potential as

$$V_\mathrm{ext}(\vec{r},\phi) = V_0 \sin(\phi)^2 \tag{17}$$

with the amplitude V_0. Otherwise, $V_\mathrm{ext}(\vec{r},\phi)$ is set to zero. Note that these expressions for V_ext maintain the $\phi \to \phi + \pi$ invariance of the system.

As in Refs. 61 and 86, the minimization of the functional (1) is performed numerically in real space by using a Picard iteration scheme[79]

$$\rho^{(i+1)}(\vec{r},\phi) = (1-\alpha)\rho^{(i)}(\vec{r},\phi) + \frac{\alpha}{2\pi\Lambda^2}\exp\left(\beta\Big(\mu^{(i)} - V_\mathrm{ext}(\vec{r},\phi) - \frac{\delta\mathcal{F}_\mathrm{exc}}{\delta\rho(\vec{r},\phi)}\Big)\right) \tag{18}$$

with the mixing parameter $\alpha \leq 0.01$, Λ set to $D/\sqrt{2\pi}$, and the functional derivative $\delta\mathcal{F}_\mathrm{exc}/\delta\rho(\vec{r},\phi)$. To maintain a constant area fraction, the chemical potential $\mu^{(i)}$ is recalculated in every iteration step i. It converges to a finite value during the iteration. As in previous works,[61,86–88] we combine this iteration with a direct inversion in the iterative subspace[89–92] to improve the convergence. The orientations of the rectangles are discretized in equidistant steps of $\Delta\phi \leq \pi/24$ and a spatial Cartesian grid with step sizes $\Delta x = \Delta y \approx 0.03D$ is used. For the simulation box, a rectangular domain with a size much larger than that of a particle and with periodic boundary conditions is used. When considering a flat system, we minimize the grand-canonical free energy per area also with respect to the width and length of the simulation box. In the case of particles on a cylindrical manifold, the width of the box is kept constant and equal to the circumference of the cylinder, while its length is varied. In both cases, the width and length of the box shall correspond to the x and y directions of our Cartesian coordinate system, respectively.

B. Monte Carlo simulations

In order to estimate the bulk phase behavior of hard rectangles in the regime of interest, we make use of MC

Physical Chemistry Chemical Physics Page 4 of 11
View Article Online
DOI: 10.1039/C7CP07026H 4

simulations. In particular, we simulate perfectly hard rectangular particles in rectangular boxes with periodic boundary conditions, at constant number of particles N, pressure P, and temperature $T \propto 1/\beta$. Overlaps between rectangles are detected using the separating axis theorem (see, e.g., Ref. 93). Simulations consist of single-particle translations and rotations, as well as cluster movements that collectively rotate all particles whose centers lie in a small circular region around the center of a random particle by 90 degrees. Additionally, in order to keep the pressure fixed, the simulations include volume changes which adapt the length of the simulation box along either the x or y direction. We estimate the isotropic-to-nematic and isotropic-to-tetratic transitions by measuring the average nematic and tetratic order parameters in the system, which are defined as

$$S_k = \left| \frac{1}{N} \sum_{j=1}^{N} \exp(\mathrm{i}k\phi_j) \right|^2 \tag{19}$$

with $k = 2$ for the nematic and $k = 4$ for the tetratic order parameter. Here, ϕ_j is the angle measured from the x axis of the system to the long axis of the jth particle. These order parameters are zero for an isotropic system. In a perfectly nematic phase, where all particles are aligned along one axis, $S_2 = 1$ and $S_4 = 1$, while in a perfectly tetratic phase $S_2 = 0$ and $S_4 = 1$. Since the boundary between the smectic phase and the lower-density phases is a first-order phase transition, the simulation results typically exhibit hysteresis. In particular, the transition from a tetratic to a smectic phase upon increasing density is often kinetically prevented, as the system gets trapped in a state with multiple small smectic domains. The effect of hysteresis is weaker on decompression, as the smectic phase always eventually transforms into a tetratic phase at sufficiently low density. Hence, to estimate the transition curve for the smectic phase, we start simulations in the smectic phase and determine at which density the layering disappears by visual inspection. This approach is expected to overestimate the stability range of the smectic phase, and hence will underestimate the transition density by up to a few percent. Note that while we refer to this phase as smectic in this work, we did not closely examine the decay of translational ordering in the system and hence do not resolve any distinction between a crystalline and a smectic phase, which would both show similar layering.

We follow the same approach for determining the phase diagram for rectangles in an aligning field, where we apply the external potential (17). To explore self-assembly on a cylindrical surface, we fix the width of the periodic simulation box to the desired circumference C of the cylinder and allow volume fluctuations only along the perpendicular direction. The length of the simulation box is always much larger than C. To compare more directly to the DFT results with constant area fraction, we first compress the system from a low-density isotropic fluid to the desired density by slowly ramping up the pressure, and then fix the volume once the desired volume is reached. In this effectively one-dimensional system, there are no true phase transitions. As a result, the system typically fluctuates between qualitatively different structures during a single simulation, and even forms domains with different structures in different parts of the simulation box. Hence, we usually find a variety of likely states for a given combination of the cylinder circumference in units of particle length C/L, the aspect ratio L/D of the particles, their total area fraction η, and the amplitude V_0 of the external potential. To address this ambiguity, we perform multiple independent simulation runs at each state point and collect data on the observed structures by visual inspection. The simulations involve $N = 1000$-4000 particles for the flat space and $N = 120$ particles on a cylindrical surface.

III. RESULTS

In this section, we explore the self-assembly of hard rectangles. We first test the developed functional on flat systems without an aligning external field and then apply it to both flat systems with an external field and to systems on a cylindrical manifold.

A. Phase behavior on a plane without an external field

For flat systems of hard rectangles in the absence of any aligning fields, we find four distinct phases in the parameter range considered here: an isotropic phase, a nematic phase, a tetratic phase, and a smectic phase. Typical equilibrated systems of rectangular particles obtained from DFT calculations and MC simulations are shown in Fig. 1 for all observed phases.

In the *isotropic* phase (see Fig. 1a), the particles are disordered with respect to both position and orientation. This phase is observed at low densities for all aspect ratios. Also the *nematic* and *tetratic* phases are disordered in space, but they show an anisotropic distribution of the orientation. We find a *nematic* phase (see Fig. 1b) at intermediate area fractions for large aspect ratios, which are $L/D \gtrsim 7$ in DFT calculations and $L/D \gtrsim 9$ in MC simulations. Although spatially disordered (i.e., spatial correlations are absent in DFT results and decay exponentially in MC simulations), the orientational distribution shows a twofold symmetry, indicating that most particles are aligned parallel to a certain axis. On the other hand, the *tetratic* phase (see Fig. 1d) shows a fourfold symmetry in the orientational distribution, which indicates alignment along two perpendicular axes. This phase is found at intermediate area fractions for small aspect ratios. For high area fractions, we observe a transition to a spatially ordered *smectic* phase (see Fig. 1e), where aligned particles form layers, with their orientations perpendicular to the layers. This is also known as

View Article Online
DOI: 10.1039/C7CP07026H 5

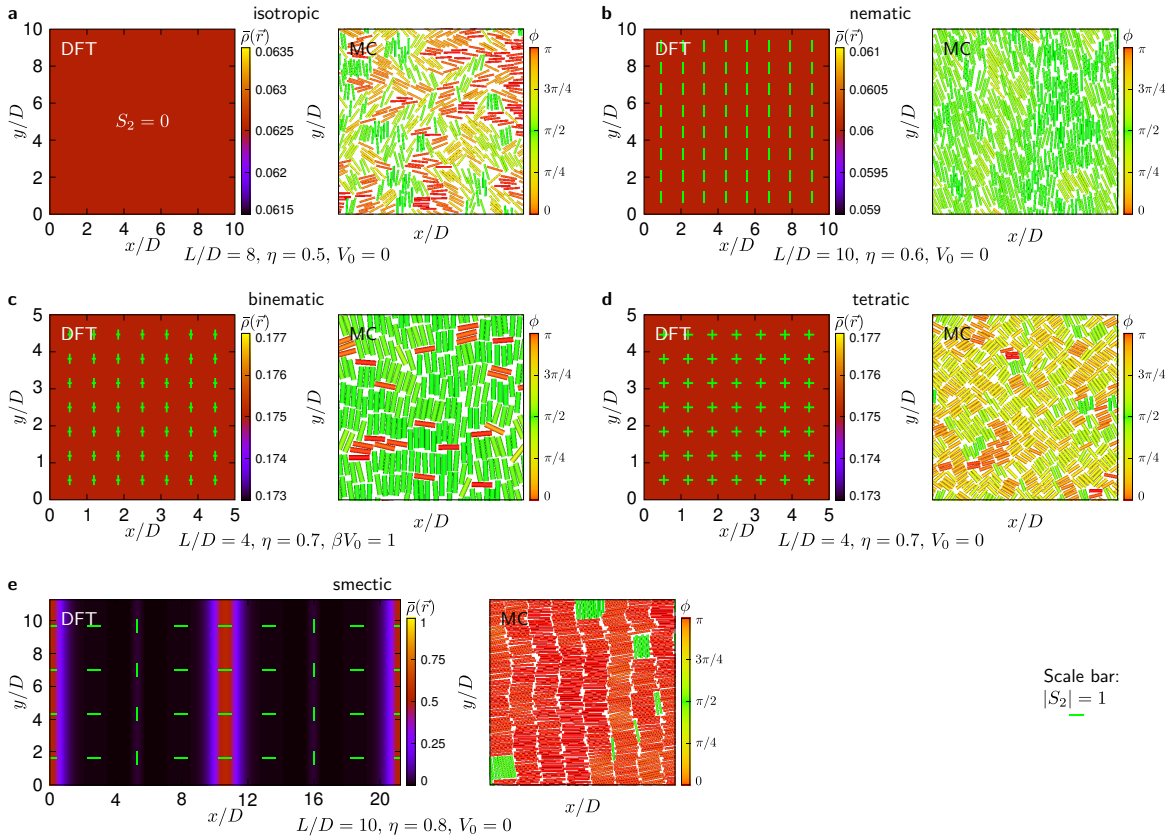

FIG. 1. Typical equilibrium density profiles $\bar{\rho}(\vec{r})$ and orientation fields indicating the local particle alignment (green dashes) obtained from DFT calculations as well as snapshots of MC simulations are shown for all observed types of structures of hard rectangular particles in two spatial dimensions. When $V_0 \neq 0$, an external field that aligns the particles in parallel to the x axis is present. Perfect isotropic and tetratic phases were only found without such an external field, while a binematic phase was only found in the presence of an external field.

a smectic A phase. In this phase, we also find particles that are located between and oriented parallel to the layers, which is in agreement with observations in three spatial dimensions.[26]

Figure 2 shows the DFT and MC results for the phase diagram of rectangular particles on a plane. Both approaches lead to qualitatively similar phase diagrams that include the same phases. Note that, in principle, we expect crystalline phases at very high area fractions for all aspect ratios, including a solid where the particles are tetratically ordered[27] and a periodic crystal of aligned particles on a rectangular lattice. However, it is difficult to distinguish these phases from the tetratic fluid and smectic phases, respectively. Hence, we do not attempt to distinguish between the tetratic solid and fluid or between the orientationally ordered crystal and smectic phase in this work. Instead, we refer to them simply as tetratic and smectic phases, respectively.

B. Phase behavior on a plane with an external field

We now extend our approach to systems of hard rectangles on a plane that are exposed to an aligning external potential (see Eq. (17)), which acts purely on the orientation of each particle. To investigate the effect of the potential's amplitude V_0 on the phase diagram, we now keep the aspect ratio of the particles fixed at $L/D = 4$ and show the phase diagram for varying potential amplitudes V_0 and area fractions η in Fig. 3. A striking effect of the aligning field is the complete absence of the isotropic and tetratic phases for potential amplitudes $V_0 > 0$. As the field favors alignment of the particles along the x axis, it makes a purely isotropic phase impossible. Likewise, the tetratic phase with four equally pronounced peaks in the orientational distribution is no longer possible, as the probability of alignment along the x axis will always be larger than the probability of alignment along the y axis. When considering, for example, a system with $L/D = 4$

Physical Chemistry Chemical Physics Page 6 of 11
View Article Online
DOI: 10.1039/C7CP07026H 6

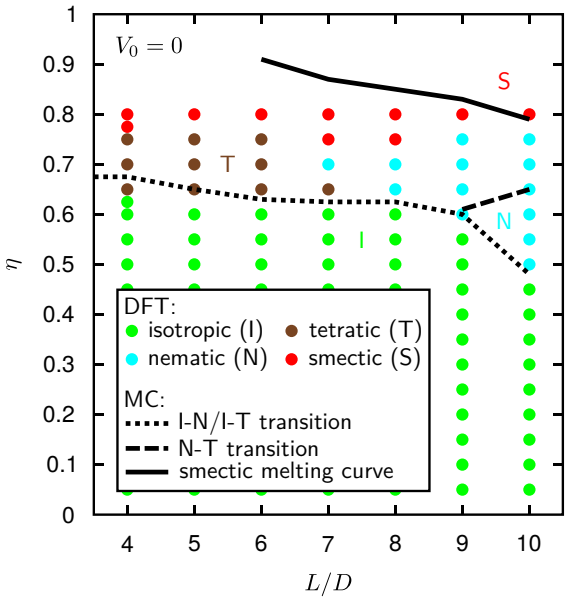

FIG. 2. Bulk phase diagram of freely orientable hard rectangular particles on a plane without an external field obtained from both DFT calculations and MC simulations. The aspect ratio L/D and area fraction η of the particles are varied.

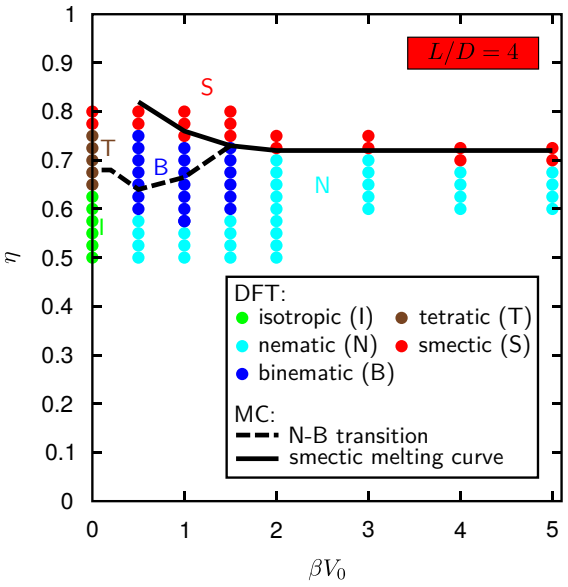

FIG. 3. Phase diagram of freely orientable hard rectangular particles on a plane in the presence of an aligning external field for both DFT calculations and MC simulations. The aspect ratio of the particles is now $L/D = 4$, whereas the amplitude V_0 of the external potential and the particles' area fraction η are varied. Perfect isotropic or tetratic phases are found only for $V_0 = 0$.

and $\eta = 0.7$, the tetratic phase is stable without an external field, but turns smoothly into a nematic phase (with preferred orientation along the x axis) when increasing the potential amplitude V_0. During this transition, the peaks in the orientational distribution that correspond to the y direction gradually decrease. As long as the height of the former tetratic peaks is still at least 10% of the height of the main peaks corresponding to the x direction, we call this intermediate phase *binematic* (see Fig. 1c). Note that these isotropic-nematic and tetratic-binematic transitions are no true thermodynamic phase transitions, since they do not involve jumps in the order parameters.

In the phase diagram (see Fig. 3), the results of the DFT calculations and MC simulations show the same trends. When increasing the external field from $V_0 = 0$ to $\beta V_0 \leq 1$, the binematic phase becomes stable at lower densities for low aspect ratios. At $V_0 = 0$, the tetratic phase should be more stable than the nematic phase but less stable than the isotropic phase for densities just below the isotropic-tetratic transition density. When imposing an external field, which helps the particles to align parallel or antiparallel to the x axis, at this density, some tetratic order is maintained if the field is weak enough, giving rise to a minimum in the nematic-binematic transition curve found for both methods. As the external field is further increased, it eventually causes (nearly) full alignment of the particles and a purely nematic phase becomes stable. Similarly, increasing the field strength enhances the stability of the smectic phase, where the particles are aligned along one axis. At large field strengths with $\beta V_0 \geq 4$ in the case of DFT calculations and $\beta V_0 \geq 2$ for MC simulations, this effect saturates and no further stabilization of the smectic phase is observed. In this parameter region, the particles in both the nematic and smectic phases are essentially fully aligned, and hence further increasing the field strength has no effect on the relative stability of the phases. It is important to note that while the parameters of our density functional were chosen in Eq. (14) to improve the agreement with the MC simulation data for systems without an external field, we made no adaptations to the functional for the case with an aligning field. Therefore, it is remarkable that the phase behavior predicted by our DFT calculations and MC simulations still shows good agreement when an aligning external field is present.

C. Phase behavior on a cylinder with an external field

We now turn our attention from rectangles on the plane to rectangles on the lateral surface of an infinitely long cylinder, whose axis is parallel to the y axis. To investigate the effect of the periodic confinement on a cylinder, we vary the radius of the cylinder such that

View Article Online
DOI: 10.1039/C7CP07026H 7

its circumference C ranges between $9D = 2.25L$ and $21D = 5.25L$ for a fixed aspect ratio $L/D = 4$ of the rectangles. The lower limit is sufficiently large to avoid cases where two particles could interact with each other on both sides of the cylinder. In order to prevent the system from simply forming nematic and smectic phases with the preferred particle orientation parallel to the axis of the cylinder, which would result in a phase diagram quite similar to that for the flat case, we include an external field to align the particles along the x direction. This promises interesting results, because it favors the formation of smectic phases where the particles are aligned along the (short) circumference of the cylinder. Such an alignment results in a competition between the favored layer spacing of the smectic phase and the fixed circumference C, leading to more complex self-assembled structures that attempt to satisfy both constraints.

As on a plane, we observe a binematic phase without spatial order and a smectic phase where the particles are aligned according to the external field. In the latter phase, the layers are parallel to the axis of the cylinder. In addition to these phases, we observe two new phases that occur only on a cylinder: firstly, a *tilted smectic* phase with layers along any other direction than the cylinder axis and particle orientations still orthogonal to the layers (see Fig. 4a) and, secondly, a *smectic C* phase, where the particles are no longer oriented perpendicular to the layers (see Fig. 4b). We observe these two phases in both DFT calculations and MC simulations. In the MC simulations, two further phases are found: a columnar phase and a tilted columnar phase with particle layers parallel to the particle orientation.

Figure 5 displays the phase behavior close to the transition between the binematic and the smectic phase obtained from DFT calculations and MC simulations for different cylinder radii. As one might expect, the smectic phase is most stable for circumferences C just above an integer number of particle lengths L and least stable for circumferences equal to or just below an integer number of particle lengths. These circumferences correspond to cases where an integer number of smectic layers fits, or does not fit, onto the cylinder in the direction preferred by the field, respectively. Although observed at $\eta = 0.75$ on a plane, no inhomogeneous density profiles with smectic layers are found at circumferences $2.75L$, $3L$, and $4L$, when using the DFT. In the MC simulations, we observe multiple competing states for most choices of the circumference and area fraction, indicated by the presence of multiple colored slices at the same state point in Fig. 5a. These fluctuations are a result of the quasi-one-dimensional nature of our system: since the system size is limited in the direction perpendicular to the cylinder axis, multiple structures can form in the same system without macroscopically large interfaces between them. Hence, fluctuations allow the system to partly or fully transform to a different structure without large free-energy penalties. Note that, since in the finite systems considered here there are no true phase boundaries between different states, classification of different phases is partially subjective.

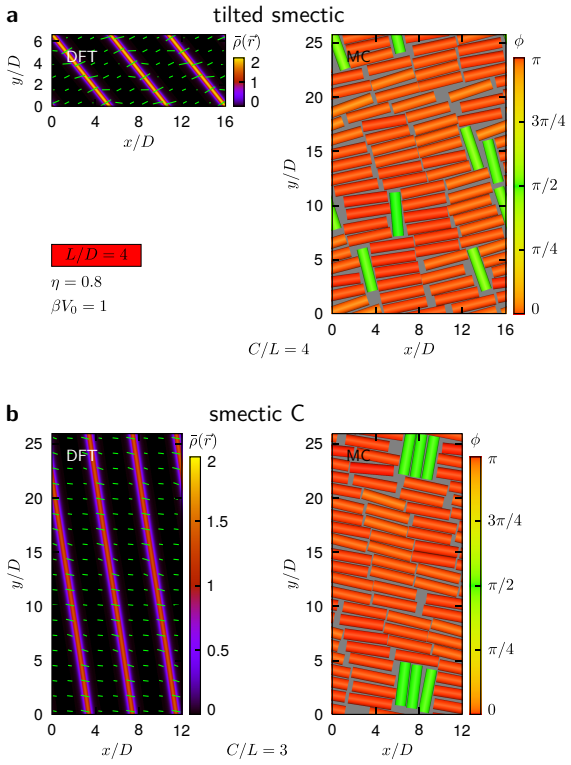

FIG. 4. As in Fig. 1, but now for a (a) tilted smectic phase and a (b) smectic C phase, which are observed only on a cylinder in the presence of an external field that favors particle alignment along the x direction. The plots show the unrolled cylindrical surface (see Fig. 5b for the snapshots of MC simulations on a cylinder). In both cases, the aspect ratio of the particles is $L/D = 4$, their area fraction is $\eta = 0.8$, and the amplitude of the external potential is $V_0 = 1/\beta$.

Interestingly, for increasing area fractions we observe an increasing tilt of the smectic layers away from the cylinder axis. This is understandable, as at lower area fractions the system can more easily distort or incorporate defects that allow for a better total alignment of the system. The observed increasing tilt of the particles is further characterized by Fig. 6. There, we show the average particle orientation $\phi_{\text{avg}} \in [0, \pi)$ (see Fig. 6a) relative to the x axis, i.e., to the direction along the circumference, for the area fractions $\eta = 0.75$ and 0.8 and for both the DFT calculations and MC simulations. As extracting the average particle orientation is difficult in MC simulations, where the system continually shifts between configurations with different average tilt angles, which can be both positive and negative, we also show the average potential energy per particle V_{avg} (see Fig. 6b). We typically find larger tilting and a higher potential energy

Physical Chemistry Chemical Physics Page 8 of 11
View Article Online
DOI: 10.1039/C7CP07026H 8

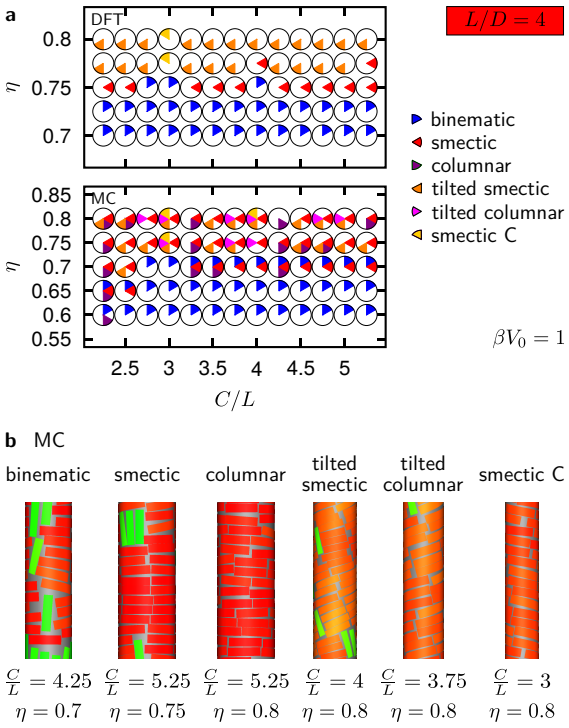

FIG. 5. (a) Phase diagrams obtained from DFT calculations and MC simulations as well as (b) MC snapshots illustrating the individual phases for hard rectangular particles of aspect ratio $L/D = 4$ on a cylinder, where an external field with $\beta V_0 = 1$ is present. We focus here on circumferences C and area fractions η close to the transition between spatially ordered and disordered phases.

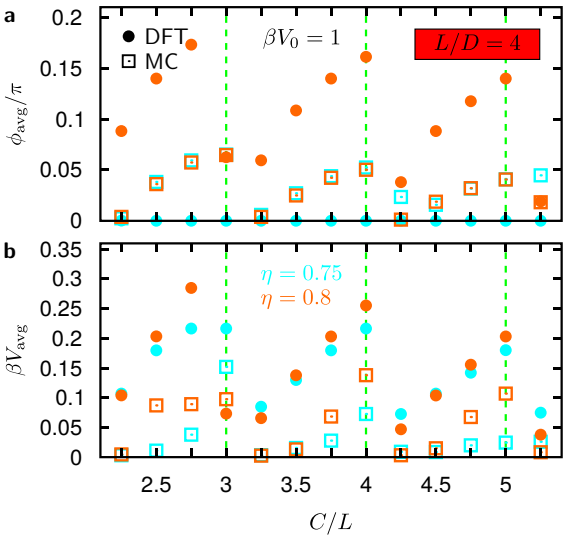

FIG. 6. (a) The average orientation angle $\phi_{\mathrm{avg}} \in [0, \pi)$ due to the particle alignment in the external field and (b) the average potential energy per particle V_{avg} in a system of hard rectangular particles with aspect ratio $L/D = 4$ on a cylinder are shown as a function of the cylinder circumference C for different area fractions η and the potential amplitude $V_0 = 1/\beta$. Circumferences that are exactly an integer multiple of the particle length L are indicated by dashed lines.

when we approach, but not exceed, an integer ratio C/L from below. This effect is tendentially stronger at larger area fractions. We observe these trends for both methods. The tilting allows the system to reduce the size of the gaps between the smectic layers. At larger area fractions, the lack of free space makes gaps between the smectic layers even more unfavorable, further favoring tilting over the formation of defects.

IV. CONCLUSIONS

We combined DFT and MC computer simulations to investigate the phase behavior of two-dimensional orientable hard rectangular particles both on a plane and on a cylindrical manifold for systems with and without aligning external fields. As a basis for our DFT calculations, we designed a new density functional that yields all liquid-crystalline phases observed in experiments with layers of hard rectangular particles.[62–64] The resulting phase diagrams agree well with our particle-resolved simulations.

Depending on the aspect ratio and number density of the particles, we found stable isotropic, nematic, tetratic, and smectic phases in the flat and field-free case. Applying an aligning external field shifts the transition curves and enhances nematic order at the expense of tetratic order, which generates a binematic phase. For a cylindrical manifold, we observed in our DFT calculations both untilted and tilted smectic-like order around the cylinder. Additionally, the MC simulations showed both untilted and tilted columnar phases.

Future studies could generalize our DFT towards a dynamical density functional theory,[94–101] which would provide insights into the nonequilibrium Brownian dynamics of such systems. It would also be interesting to consider other two-dimensional manifolds like cones and spheres or other particle interactions like those of ionic liquid crystals[102] and magnetic nanorods.[103] Our results can be verified in experiments using sterically-stabilized rectangular colloidal particles[67–72,74,103] or shaken granular particles.[75,76]

CONFLICTS OF INTEREST

There are no conflicts of interest to declare.

View Article Online
DOI: 10.1039/C7CP07026H 9

ACKNOWLEDGMENTS

We thank Axel Voigt for helpful discussions. R.W. and H.L. are funded by the Deutsche Forschungsgemeinschaft (DFG, German Research Foundation) – WI 4170/3-1; LO 418/20-1. F.S. gratefully acknowledges funding from the Alexander von Humboldt foundation.

[1] J. Hanus, Physical Review **178**, 420 (1969).
[2] P. J. Wojtowicz and P. Sheng, Physics Letters A **48**, 235 (1974).
[3] A. R. Khokhlov and A. N. Semenov, Macromolecules **15**, 1272 (1982).
[4] A. J. Nicastro and P. H. Keyes, Physical Review A **30**, 3156 (1984).
[5] R. M. Hornreich, Physics Letters A **109**, 232 (1985).
[6] I. Lelidis, M. Nobili, and G. Durand, Physical Review E **48**, 3818 (1993).
[7] J. Tang and S. Fraden, Physical Review Letters **71**, 3509 (1993).
[8] S. Varga, G. Jackson, and I. Szalai, Molecular Physics **93**, 377 (1998).
[9] H. Graf and H. Löwen, Journal of Physics: Condensed Matter **11**, 1435 (1999).
[10] F. Kimura, T. Kimura, M. Tamura, A. Hirai, M. Ikuno, and F. Horii, Langmuir **21**, 2034 (2005).
[11] G. Napoli and L. Vergori, Physical Review Letters **108**, 207803 (2012).
[12] J. Dzubiella, M. Schmidt, and H. Löwen, Physical Review E **62**, 5081 (2000).
[13] H. Stark, Physics Reports **351**, 387 (2001).
[14] A. R. Bausch, M. J. Bowick, A. Cacciuto, A. D. Dinsmore, M. F. Hsu, D. R. Nelson, M. G. Nikolaides, A. Travesset, and D. A. Weitz, Science **299**, 1716 (2003).
[15] A. Fernández-Nieves, V. Vitelli, A. S. Utada, D. R. Link, M. Márquez, D. R. Nelson, and D. A. Weitz, Physical Review Letters **99**, 157801 (2007).
[16] H. Shin, M. J. Bowick, and X. Xing, Physical Review Letters **101**, 037802 (2008).
[17] M. A. Bates, G. Skačej, and C. Zannoni, Soft Matter **6**, 655 (2010).
[18] T. Araki, M. Buscaglia, T. Bellini, and H. Tanaka, Nature Materials **10**, 303 (2011).
[19] H.-L. Liang, S. Schymura, P. Rudquist, and J. Lagerwall, Physical Review Letters **106**, 247801 (2011).
[20] T. Lopez-Leon, V. Koning, K. B. S. Devaiah, V. Vitelli, and A. Fernandez-Nieves, Nature **7**, 1745 (2011).
[21] H.-L. Liang, J. Noh, R. Zentel, P. Rudquist, and J. P. F. Lagerwall, Philosophical Transactions of the Royal Society A: Mathematical, Physical and Engineering Sciences **371**, 20120258 (2013).
[22] G. Napoli and L. Vergori, International Journal of Non-Linear Mechanics **49**, 66 (2013).
[23] A. Martinez, M. Ravnik, B. Lucero, R. Visvanathan, S. Žumer, and I. I. Smalyukh, Nature Materials **13**, 258 (2014).
[24] G. J. Vroege and H. N. W. Lekkerkerker, Reports on Progress in Physics **55**, 1241 (1992).
[25] P. Bolhuis and D. Frenkel, Journal of Chemical Physics **106**, 666 (1997).
[26] R. van Roij, P. Bolhuis, B. Mulder, and D. Frenkel, Physical Review E **52**, R1277 (1995).
[27] A. Donev, J. Burton, F. H. Stillinger, and S. Torquato, Physical Review B **73**, 054109 (2006).
[28] D. A. Triplett and K. A. Fichthorn, Physical Review E **77**, 011707 (2008).
[29] J. Geng and J. V. Selinger, Physical Review E **80**, 011707 (2009).
[30] H. H. Wensink, H. Löwen, M. Marechal, A. Härtel, R. Wittkowski, U. Zimmermann, A. Kaiser, and A. M. Menzel, European Physical Journal Special Topics **222**, 3023 (2013).
[31] M. Dijkstra, "Advances in chemical physics," (John Wiley & Sons, Hoboken, NJ, 2014) Chap. 2. Entropy-driven phase transitions in colloids: from spheres to anisotropic particles, pp. 35–71.
[32] M. Oettel, M. Klopotek, M. Dixit, E. Empting, T. Schilling, and H. Hansen-Goos, Journal of Chemical Physics **145**, 074902 (2016).
[33] L. Onsager, Annals of the New York Academy of Sciences **51**, 627 (1949).
[34] A. Poniewierski and R. Hołyst, Physical Review Letters **61**, 2461 (1988).
[35] H. Schlacken, H.-J. Mogel, and P. Schiller, Molecular Physics **93**, 777 (1998).
[36] Y. Martínez-Ratón, E. Velasco, and L. Mederos, Journal of Chemical Physics **122**, 064903 (2005).
[37] Y. Martínez-Ratón, E. Velasco, and L. Mederos, Journal of Chemical Physics **125**, 014501 (2006).
[38] H. Hansen-Goos and K. Mecke, Physical Review Letters **102**, 018302 (2009).
[39] Y. Martínez-Ratón and E. Velasco, Physical Review E **79**, 011711 (2009).
[40] H. Hansen-Goos and K. Mecke, Journal of Physics: Condensed Matter **22**, 364107 (2010).
[41] S. Belli, M. Dijkstra, and R. van Roij, Journal of Chemical Physics **137**, 124506 (2012).
[42] M. Marechal, U. Zimmermann, and H. Löwen, Journal of Chemical Physics **136**, 144506 (2012).
[43] D. de las Heras, Y. Martínez-Ratón, L. Mederos, and E. Velasco, Journal of Molecular Liquids **185**, 13 (2013).
[44] M. Marechal and H. Löwen, Physical Review Letters **110**, 137801 (2013).
[45] R. Wittmann, M. Marechal, and K. Mecke, Europhysics Letters **109**, 26003 (2015).
[46] A. Díaz-De Armas and Y. Martínez-Ratón, Physical Review E **95**, 052702 (2017).
[47] M. Marechal, S. Dussi, and M. Dijkstra, Journal of Chemical Physics **146**, 124905 (2017).

Physical Chemistry Chemical Physics Page 10 of 11
View Article Online
DOI: 10.1039/C7CP07026H10

[48] M. A. Bates and D. Frenkel, Journal of Chemical Physics **112**, 10034 (2000).
[49] R. L. C. Vink, Physical Review Letters **98**, 217801 (2007).
[50] S. C. Kapfer and W. Krauth, Physical Review Letters **114**, 035702 (2015).
[51] A. L. Thorneywork, J. L. Abbott, D. G. A. L. Aarts, and R. P. A. Dullens, Physical Review Letters **118**, 158001 (2017).
[52] C. Knorowski and A. Travesset, Europhysics Letters **100**, 56004 (2012).
[53] X. Xing, H. Shin, M. J. Bowick, Z. Yao, L. Jia, and M.-H. Li, Proceedings of the National Academy of Sciences U.S.A. **109**, 5202 (2012).
[54] D. Coursault, B. Zappone, A. Coati, A. Boulaoued, L. Pelliser, D. Limagne, N. Boudet, B. H. Ibrahim, A. de Martino, M. Alba, M. Goldmann, Y. Garreau, B. Gallas, and E. Lacaze, Soft Matter **12**, 678 (2016).
[55] R. Zhang, Y. Zhou, M. Rahimi, and J. J. de Pablo, Nature Communications **7**, 13483 (2016).
[56] G. Skačej and C. Zannoni, Physical Review Letters **100**, 197802 (2008).
[57] T. Geigenfeind, S. Rosenzweig, M. Schmidt, and D. de las Heras, Journal of Chemical Physics **142**, 174701 (2015).
[58] A. Mughal and D. Weaire, Physical Review E **89**, 042307 (2014).
[59] R. Kusters, S. Paquay, and C. Storm, Soft Matter **11**, 1054 (2015).
[60] Y. Martínez-Ratón and E. Velasco, Physical Review E **87**, 052314 (2013).
[61] C. E. Sitta, F. Smallenburg, R. Wittkowski, and H. Löwen, Journal of Chemical Physics **145**, 204508 (2016).
[62] V. Narayan, N. Menon, and S. Ramaswamy, Journal of Statistical Mechanics: Theory and Experiment **2006**, 01005 (2006).
[63] K. Zhao, C. Harrison, D. Huse, W. B. Russel, and P. M. Chaikin, Physical Review E **76**, 040401 (2007).
[64] R. Sánchez and L. A. Aguirre-Manzo, Physica Scripta **09**, 095002 (2016).
[65] A. Mughal, H. K. Chan, and D. Weaire, Physical Review Letters **106**, 115704 (2011).
[66] E. C. Oğuz, R. Messina, and H. Löwen, Europhysics Letters **94**, 28005 (2011).
[67] K.-H. Lin, J. C. Crocker, V. Prasad, A. Schofield, D. A. Weitz, T. C. Lubensky, and A. G. Yodh, Physical Review Letters **85**, 1770 (2000).
[68] J. Galanis, R. Nossal, W. Losert, and D. Harries, Physical Review Letters **105**, 168001 (2010).
[69] M. Hermes, E. C. M. Vermolen, M. E. Leunissen, D. L. J. Vossen, P. D. J. van Oostrum, M. Dijkstra, and A. van Blaaderen, Soft Matter **7**, 4623 (2011).
[70] O. Zvyagolskaya, A. J. Archer, and C. Bechinger, Europhysics Letters **96**, 28005 (2011).
[71] T. H. Besseling, M. Hermes, A. Kuijk, B. de Nijs, T.-S. Deng, M. Dijkstra, A. Imhof, and A. van Blaaderen, Journal of Physics: Condensed Matter **27**, 194109 (2015).
[72] T. Müller, D. de las Heras, I. Rehberg, and K. Huang, Physical Review E **91**, 062207 (2015).
[73] P. Guillamat, J. Ignés-Mullol, and F. Sagués, Proceedings of the National Academy of Sciences U.S.A. **113**, 5498 (2016).
[74] L. Walsh and N. Menon, Journal of Statistical Mechanics: Theory and Experiment **2016**, 083302 (2016).
[75] R. Cruz Hidalgo, I. Zuriguel, D. Maza, and I. Pagonabarraga, Journal of Statistical Mechanics: Theory and Experiment **2010**, P06025 (2010).
[76] S. Hernández-Navarro, J. Ignés-Mullol, F. Sagués, and P. Tierno, Langmuir **28**, 5981 (2012).
[77] R. Evans, Advances in Physics **28**, 143 (1979).
[78] R. Evans, "Fundamentals of inhomogeneous fluids," (Marcel Dekker, New York, 1992) Chap. 3: Density Functionals in the Theory of Nonuniform Fluids, pp. 85–176, 1st ed.
[79] R. Roth, Journal of Physics: Condensed Matter **22**, 063102 (2010).
[80] J. K. Percus, Journal of Statistical Physics **15**, 505 (1976).
[81] Y. Martínez-Ratón, J. A. Cuesta, R. van Roij, and B. Mulder, "Nematic to smectic: A "hard" transition," in *New Approaches to Problems in Liquid State Theory: Inhomogeneities and Phase Separation in Simple, Complex and Quantum Fluids*, edited by C. Caccamo, J.-P. Hansen, and G. Stell (Springer Netherlands, Dordrecht, 1999) pp. 139–150.
[82] J. A. Cuesta and Y. Martínez-Ratón, Physical Review Letters **78**, 3681 (1997).
[83] J. A. Cuesta and Y. Martínez-Ratón, Journal of Chemical Physics **107**, 6379 (1997).
[84] Y. Rosenfeld, Physical Review Letters **63**, 980 (1989).
[85] In its current form, $\chi_{\mathrm{T}}(L/D)$ constitutes a compromise between a small number of free parameters and a good agreement with the MC simulation data.
[86] R. Wittmann, C. E. Sitta, F. Smallenburg, and H. Löwen, Journal of Chemical Physics **147**, 134908 (2017).
[87] M. Oettel, S. Dorosz, M. Berghoff, B. Nestler, and T. Schilling, Physical Review E **86**, 021404 (2012).
[88] A. Härtel, M. Oettel, R. E. Rozas, S. U. Egelhaaf, J. Horbach, and H. Löwen, Physical Review Letters **108**, 226101 (2012).
[89] K. C. Ng, Journal of Chemical Physics **61**, 2680 (1974).
[90] P. Pulay, Chemical Physics Letters **73**, 393 (1980).
[91] P. Pulay, Journal of Computational Chemistry **3**, 556 (1982).
[92] A. Kovalenko, S. Ten-no, and F. Hirata, Journal of Computational Chemistry **20**, 928 (1999).
[93] S. Gottschalk, M. C. Lin, and D. Manocha, in *Proceedings of the 23rd Annual Conference on Computer Graphics and Interactive Techniques*, SIGGRAPH '96 (ACM, New York, 1996) pp. 171–180.
[94] U. M. B. Marconi and P. Tarazona, Journal of Chemical Physics **110**, 8032 (1999).
[95] U. M. B. Marconi and P. Tarazona, Journal of Physics: Condensed Matter **12**, 413 (2000).
[96] A. J. Archer and R. Evans, Journal of Chemical Physics **121**, 4246 (2004).
[97] U. M. B. Marconi and S. Melchionna, Journal of Chemical Physics **126**, 184109 (2007).
[98] M. Rex, H. H. Wensink, and H. Löwen, Physical Review E **76**, 021403 (2007).
[99] P. Español and H. Löwen, Journal of Chemical Physics **131**, 244101 (2009).
[100] R. Wittkowski and H. Löwen, Molecular Physics **109**, 2935 (2011).
[101] B. D. Goddard, A. Nold, N. Savva, P. Yatsyshin, and S. Kalliadasis, Journal of Physics: Condensed Matter **25**, 035101 (2013).
[102] H. Bartsch, M. Bier, and S. Dietrich, preprint **arXiv:1708.07295** (2017).

View Article Online
DOI: 10.1039/C7CP07026H 11

[103] K. Slyusarenko, D. Constantin, and P. Davidson, Journal of Chemical Physics **140**, 104904 (2014).

Kapitel 3

Zusammenfassung

In diesem Kapitel werden die wichtigsten Forschungsbeiträge der dieser Dissertation zugrunde liegenden Publikationen zusammengefasst:

Im Rahmen dieser Arbeit wurden zwei unterschiedliche Systeme im Bereich der weichen Materie erforscht.

Auf der einen Seite wurde die Diffusion von Makromolekülen durch ein Hydrogel untersucht: Dabei ist es durch Kombination dreier unterschiedlicher experimenteller Methoden meiner Co-Autoren sowie mit Hilfe der von mir durchgeführten Brownsche Dynamik Simulationen gelungen, präzise Werte für die Diffusionskoeffizienten in diesen Systemen zu ermitteln und die mittlere Porengröße im untersuchten Hydrogel zu bestimmen. Des Weiteren wurden starke Hinweise auf eine nicht-triviale anziehende Wechselwirkung zwischen den Makromolekülen und der Polymer-Gelmatrix gefunden.

Auf der anderen Seite wurden Systeme anisotroper Teilchen auf zweidimensionalen Mannigfaltigkeiten untersucht: Von methodischer Seite her wurden mit Dr. René Wittmanns Adaption der FMMT auf zwei Raumdimensionen und der von mir entwickelten Beschreibung harte Rechtecke in zwei Raumdimensionen zwei neue Dichtefunktionaltheorien hergeleitet. Beide wurden von mir numerisch ausgewertet und mit Monte-Carlo-Simulationen von Dr. Frank Smallenburg verglichen. Dadurch konnten in der Ebene sowohl für Stäbchen als auch für Rechtecke die Phasendiagramme in Abhängigkeit der Teilchendichte und des Länge-Breite-Verhältnisses bestimmt werden. Für Rechtecke wurde darüber hinaus das Phasenverhalten unter Einwirkung eines externen Potentials untersucht und das Phasendiagramm in Abhängigkeit der Teilchendichte und der Potentialstärke in der Ebene ermittelt. Ebenso wurde das Phasendiagramm von Rechtecken auf einer Zylinderoberfläche in Abhängigkeit der Teilchendichte und des Zylinderumfanges bestimmt. Zuletzt wurde das Verhalten von Rechtecken in der Nähe gekrümmter Wände untersucht und dabei erstmals eine Dichteabhängigkeit des Vorzeichens der Tolman-Länge entdeckt.

Literaturverzeichnis

[1] P.-G. de Gennes, *Soft matter*, Reviews of Modern Physics **64**, 645 (1992)

[2] H. Löwen, *Colloidal soft matter under external control*, Journal of Physics: Condensed Matter **13**, R415–R432 (2001)

[3] I. W. Hamley, *Introduction to soft matter: synthetic and biological self-assembling materials*. John Wiley & Sons, Chichester (2013).

[4] M. Doi, *Soft matter physics*. Oxford University Press, Oxford (2013).

[5] P. A. Kralchevsky, K. D. Danov & N. D. Denkov, *Handbook of surface and colloid chemistry*, Kap. 5: Chemical physics of colloid systems and interfaces, 137–344. CRC Press, Boca Raton, 2 ed. (1997).

[6] M. N. Albarghouthi & A. E. Barron, *Polymeric matrices for DNA sequencing by capillary electrophoresis*, Electrophoresis **21**, 4096–4111 (2000)

[7] S. T. Balke, A. E. Hamielec, B. P. LeClair & S. L. Pearce, *Gel permeation chromatography*, Industrial & Engineering Chemistry Product Research and Development **8**, 54–57 (1969)

[8] F. Chen, P. W. Tillberg & E. S. Boyden, *Expansion microscopy*, Science **347**, 543–548 (2015)

[9] V. E. Barsky, A. M. Kolchinsky, Y. P. Lysov & A. D. Mirzabekov, *Biological microchips with hydrogel-immobilized nucleic acids, proteins, and other compounds: properties and applications in genomics*, Molecular Biology **36**, 437–455 (2002)

[10] T.-O. Peulen & K. J. Wilkinson, *Diffusion of nanoparticles in a biofilm*, Environmental Science and Technology **45**, 3367–3373 (2011)

[11] O. Wichterle & D. Lím, *Hydrophilic gels for biological use*, Nature **185**, 117–118 (1960)

[12] R. Morita, R. Honda & Y. Takahashi, *Development of oral controlled release preparations, a PVA swelling controlled release system (SCRS). II. In vitro and in vivo evaluation*, Journal of Controlled Release **68**, 115 (2000)

[13] P. Gupta, K. Vermani & S. Garg, *Hydrogels: from controlled release to pH-responsive drug delivery*, Drug discovery today **7**, 569 (2002)

[14] A. S. Hoffman, *Hydrogels for biomedical applications*, Advanced drug delivery reviews **54**, 3–12 (2002)

[15] N. Murthy, Y. X. Thng, S. Schuck, M. C. Xu & J. M. Fréchet, *A novel strategy for encapsulation and release of proteins: hydrogels and microgels with acid-labile acetal cross-linkers*, Journal of the American Chemical Society **124**, 12398 (2002)

[16] S. Sershen & J. West, *Implantable, polymeric systems for modulated drug delivery*, Advanced drug delivery reviews **54**, 1225–1235 (2002)

[17] D. T. Eddington & D. J. Beebe, *Flow control with hydrogels*, Advanced drug delivery reviews **56**, 199–210 (2004)

[18] R. Zolfaghari, A. A. Katbab, J. Nabavizadeh, R. Y. Tabasi & M. H. Nejad, *Preparation and characterization of nanocomposite hydrogels based on polyacrylamide for enhanced oil recovery applications*, Journal of Applied Polymer Science **100**, 2096–2109 (2006)

[19] A. Z. Abidin, T. Puspasari & W. A. Nugroho, *Polymers for enhanced oil recovery technology*, Procedia Chemistry **4**, 11–16 (2012)

[20] H. W. Kang, Y. Tabata & Y. Ikada, *Fabrication of porous gelatin scaffolds for tissue engineering*, Biomaterials **20**, 1339–1344 (1999)

[21] L. Haggerty, J. H. Sugarman & R. K. Prud'homme, *Diffusion of polymers through polyacrylamide gels*, Polymer **29**, 1058–1063 (1988)

[22] A. Stellwagen & N. C. Stellwagen, *Anomalously slow electrophoretic mobilities of DNA restriction fragments in polyacrylamide gels are not eliminated by increasing the gel pore size*, Biopolymers **30**, 309–324 (1990)

[23] D. L. Holmes & N. C. Stellwagen, *Estimation of polyacrylamide gel pore size from Ferguson plots of normal and anomalously migrating DNA fragments. I. Gels containing 3% N, N′-methylenebisacrylamide*, Electrophoresis **12**, 253–263 (1991)

[24] M. Kremer, E. Pothmann, T. Roessler, J. Baker, A. Yee, H. Blanch & J. M. Prausnitz, *Pore-size distributions of cationic polyacrylamide hydrogels varying in initial monomer concentration and cross-linker/monomer ratio*, Macromolecules **27**, 2965–2973 (1994)

[25] J. Tong & J. Anderson, *Partitioning and diffusion of proteins and linear polymers in polyacrylamide gels*, Biophysical Journal **70**, 1505–1513 (1996)

[26] S. M. Russell & G. Carta, *Mesh size of charged polyacrylamide hydrogels from partitioning measurements*, Industrial & Engineering Chemistry Research **44**, 8213–8217 (2005)

[27] A. Vagias, R. Raccis, K. Koynov, U. Jonas, H.-J. Butt, G. Fytas, P. Košovan, O. Lenz & C. Holm, *Complex tracer diffusion dynamics in polymer solutions*, Physical Review Letters **111**, 088301 (2013)

[28] J. S. Fawcett & C. J. O. R. Morris, *Molecular-sieve chromatography of proteins on granulated polyacrylamide gels*, Separation Science **1**, 9–26 (1966)

[29] J. Wang, A. D. Gonzalez & V. M. Ugaz, *Tailoring bulk transport in hydrogels through control of polydispersity in the nanoscale pore size distribution*, Advanced Materials **20**, 4482–4489 (2008)

[30] M. P. Tombs, *The interpretation of gel electrophoresis*, Analytical Biochemistry **13**, 121–132 (1965)

[31] N. C. Stellwagen, *Anomalous electrophoresis of deoxyribonucleic acid restriction fragments on polyacrylamide gels*, Biochemistry **22**, 6186–6193 (1983)

[32] D. L. Holmes & N. C. Stellwagen, *Estimation of polyacrylamide gel pore size from Ferguson plots of normal and anomalously migrating DNA fragments. II. comparison of gels with different crosslinker concentrations, added agarose and added linear polyacrylamide*, Electrophoresis **12**, 612–619 (1991)

[33] Z. Blank & A. C. Reimschuessel, *Structural studies of organic gels by SEM*, Journal of Materials Science **9**, 1815–1822 (1974)

[34] R. Rüchel & M. D. Brager, *Scanning electron microscopic observations of polyacrylamide gels*, Analytical Biochemistry **68**, 415–428 (1975)

[35] L. M. Lira, K. A. Martins & S. I. C. de Torresi, *Structural parameters of polyacrylamide hydrogels obtained by the equilibrium swelling theory*, European Polymer Journal **45**, 1232–1238 (2009)

[36] M. Maaloum, N. Pernodet & B. Tinland, *Agarose gel structure using atomic force microscopy: gel concentration and ionic strength effects*, Electrophoresis **19**, 1606–1610 (1998)

[37] L. Kisley, R. Brunetti, L. J. Tauzin, B. Shuang, X. Yi, A. W. Kirkeminde, D. A. Higgins, S. Weiss & C. F. Landes, *Characterization of porous materials by fluorescence correlation spectroscopy super-resolution optical fluctuation imaging*, ACS Nano **9**, 9158–9166 (2015)

[38] L. Kisley, K. A. Serrano, D. Guin, X. Kong, M. Gruebele & D. E. Leckband, *Direct imaging of protein stability and folding kinetics in hydrogels*, ACS Applied Materials & Interfaces **9**, 21606–21617 (2017)

[39] A. G. Ogston, B. N. Preston & J. D. Wells, *On the transport of compact particles through solutions of chain-polymers*, Proceedings of the Royal Society of London. Series A, Mathematical and Physical Sciences **333**, 297–316 (1973)

[40] B. Amsden, *Solute diffusion within hydrogels. mechanisms and models*, Macromolecules **31**, 8382–8395 (1998)

[41] L. Johansson & J.-E. Löfroth, *Diffusion and interaction in gels and solutions. 4. Hard sphere Brownian dynamics simulations*, Journal of Chemical Physics **98**, 7471–7479 (1993)

[42] P. A. Netz & T. Dorfmüller, *Computer simulation studies of diffusion in gels: Model structures*, Journal of Chemical Physics **107**, 9221–9233 (1997)

[43] P. Licinio & A. V. Teixeira, *Anomalous diffusion of ideal polymer networks*, Physical Review E **56**, 631–634 (1997)

[44] T. Miyata, A. Endo, T. Ohmori, M. Nakaiwa, M. Kendo, K.-i. Kurumada & M. Tanigaki, *Brownian dynamics simulation study of self-diffusion of a charged particle in swollen counter-charged hydrogel modeled as cubic lattice*, Journal of chemical engineering of Japan **35**, 640–648 (2002)

[45] S. Schneider & P. Linse, *Monte Carlo simulation of defect-free cross-linked polyelectrolyte gels*, Journal of Physical Chemistry B **107**, 8030–8040 (2003)

[46] S. Edgecombe, S. Schneider & P. Linse, *Monte Carlo simulations of defect-free cross-linked gels in the presence of salt*, Macromolecules **37**, 10089–10100 (2004)

[47] B. A. Mann, R. Everaers, C. Holm & K. Kremer, *Scaling in polyelectrolyte networks*, Europhysics Letters **67**, 786–792 (2004)

[48] S. Schneider & P. Linse, *Discontinuous volume transitions in cross-linked polyelectrolyte gels induced by short-range attractions and strong electrostatic coupling*, Macromolecules **37**, 3850–3856 (2004)

[49] B. A. Mann, C. Holm & K. Kremer, *Swelling of polyelectrolyte networks*, Journal of Chemical Physics **122**, 154903 (2005)

[50] H. Pei, S. Allison, B. M. H. Haynes & D. Augustin, *Brownian dynamics simulation of the diffusion of rods and wormlike chains in a gel modeled as a cubic lattice: application to DNA*, Journal of Physical Chemistry B **113**, 2564–2571 (2008)

[51] H. Zhou & S. B. Chen, *Brownian dynamics simulation of tracer diffusion in a cross-linked network*, Physical Review E **79**, 021801 (2009)

[52] B. A. F. Mann, K. Kremer, O. Lenz & C. Holm, *Hydrogels in poor solvents: a molecular dynamics study*, Macromolecular theory and simulations **20**, 721–734 (2011)

[53] P. Cremer, H. Löwen & A. M. Menzel, *Superelastic stress-strain behavior in ferrogels with different types of magneto-elastic coupling*, Physical Chemistry Chemical Physics **18**, 26670–26690 (2016)

[54] D. Sandrin, D. Wagner, C. E. Sitta, R. Thoma, S. Felekyan, H. E. Hermes, C. Janiak, N. de Sousa Amadeu, R. Kühnemuth, H. Löwen, S. U. Egelhaaf & C. A. M. Seidel, *Diffusion of macromolecules in a polymer hydrogel: from microscopic to macroscopic scales*, Physical Chemistry Chemical Physics **18**, 12860–12876 (2016)

[55] S. Weidtkamp-Peters, S. Felekyan, A. Bleckmann, R. Simon, W. Becker, R. Kühnemuth & C. A. M. Seidel, *Multiparameter fluorescence image spectroscopy to study molecular interactions*, Photochemical & Photobiological Sciences **8**, 470–480 (2009)

[56] R. Kühnemuth, H. Hornen, S. Felekyan, S. Weidtkamp-Peters, E. Knus, & C. A. M. Seidel, *Multiparameter fluorescence image spectroscopy*, Biophysical Journal **100**, 139a (2011)

[57] D. Wagner, M. Börgardts, C. Grünzweig, E. Lehmann, T. J. J. Müller, S. U. Egelhaaf & H. E. Hermes, *Neutron, fluorescence, and optical imaging: An in situ combination of complementary techniques*, Review of Scientific Instruments **86**, 093706 (2015)

[58] D. Wagner, J. Burbach, C. Grünzweig, S. Hartmann, E. Lehmann, S. U. Egelhaaf & H. E. Hermes, *Solvent and solute ingress into hydrogels resolved by a combination of imaging techniques*, Journal of Chemical Physics **144**, 204903 (2016)

[59] J. Jonas & H. S. Gutowsky, *NMR in chemistry-an evergreen*, Annual Review of Physical Chemistry **31**, 1–28 (1980)

[60] J. N. Shoolery, *The development of experimental and analytical high resolution NMR*, Progress in Nuclear Magnetic Resonance Spectroscopy **28**, 37–52 (1995)

[61] M. Scardigli, C. Crocini, C. Ferrantini, T. Gabbrielli, L. Silvestri, R. Coppini, C. Tesi, E. A. Rog-Zielinska, P. Kohl, E. Cerbai, C. Poggesi, F. S. Pavone & L. Sacconi, *Quantitative assessment of passive electrical properties of the cardiac t-tubular system by frap microscopy*, Proceedings of the National Academy of Sciences U.S.A. **114**, 5737 (2017)

[62] A. J. Smith, X. Yao, J. A. Dix, B.-J. Jin & A. S. Verkman, *Test of the 'glymphatic' hypothesis demonstrates diffusive and aquaporin-4-independent solute transport in rodent brain parenchyma*, eLife **6**, e27679 (2017)

[63] D. Helbing, A. Johansson & H. Z. Al-Abideen, *Dynamics of crowd disasters: An empirical study*, Physical Review E **75**, 046109 (2007)

[64] M. Moussaêd, D. Helbing & G. Theraulaz, *How simple rules determine pedestrian behavior and crowd disasters*, Proceedings of the National Academy of Sciences U.S.A. **108**, 6884–6888 (2011)

[65] J. L. Silverberg, M. Bierbaum, J. P. Sethna & I. Cohen, *Collective motion of humans in mosh and circle pits at heavy metal concerts*, Physical Review Letters **110**, 228701 (2013)

[66] S. J. Singer & G. L. Nicolson, *The fluid mosaic model of the structure of cell membranes*, Science **175**, 720–731 (1972)

[67] J. D. Watson & F. H. C. Crick, *Molecular structure of nucleic acids: A structure for deoxyribose nucleic acid*, Nature **171**, 737–738 (1953)

[68] J. D. Watson, *The structure of tobacco mosaic virus: I. X-ray evidence of a helical arrangement of sub-units around the longitudinal axis*, Biochimica et biophysica acta **13**, 10–19 (1954)

[69] G. Lebeurier, A. Nicolaieff & K. E. Richards, *Inside-out model for self-assembly of tobacco mosaic virus*, Proceedings of the National Academy of Sciences U.S.A. **74**, 149–153 (1977)

[70] R. B. Meyer, L. Liebert, L. Strzelecki & P. Keller, *Ferroelectric liquid crystals*, Journal de Physique Lettres **36**, 69–71 (1975)

[71] D. E. Moncton & R. Pindak, *Long-range order in two- and three-dimensional smectic-B liquid-crystal films*, Physical Review Letters **43**, 701–704 (1979)

[72] R. Pindak, D. E. Moncton, S. C. Davey & J. W. Goodby, *X-ray observation of a stacked hexatic liquid-crystal B phase*, Physical Review Letters **46**, 1135–1138 (1981)

[73] R. van Roij, P. Bolhuis, B. Mulder & D. Frenkel, *Transverse interlayer order in lyotropic smectic liquid crystals*, Physical Review E **52**, R1277–R1280 (1995)

[74] G. P. Crawford & S. Zumer, *Liquid crystals in complex geometries: formed by polymer and porous networks.* Taylor & Francis, London, UK (1996).

[75] C. Bahr & H.-S. Kitzerow, *Chirality in liquid crystals.* Springer-Verlag, New York (2001).

[76] V. Narayan, N. Menon & S. Ramaswamy, *Nonequilibrium steady states in a vibrated-rod monolayer: tetratic, nematic, and smectic correlations*, Journal of Statistical Mechanics: Theory and Experiment **2006**, 01005 (2006)

[77] K. Zhao, C. Harrison, D. Huse, W. B. Russel & P. M. Chaikin, *Nematic and almost-tetratic phases of colloidal rectangles*, Physical Review E **76**, 040401 (2007)

[78] R. Sánchez & L. A. Aguirre-Manzo, *Concentric tetratic orientational order in a confined quasi-2d tubular system*, Physica Scripta **09**, 095002 (2016)

[79] G. J. Vroege & H. N. W. Lekkerkerker, *Phase transitions in lyotropic colloidal and polymer liquid crystals*, Reports on Progress in Physics **55**, 1241–1309 (1992)

[80] P. Bolhuis & D. Frenkel, *Tracing the phase boundaries of hard spherocylinders*, Journal of Chemical Physics **106**, 666–687 (1997)

[81] M. A. Bates & D. Frenkel, *Phase behavior of two-dimensional hard rod fluids*, Journal of Chemical Physics **112**, 10034–10041 (2000)

[82] A. Donev, J. Burton, F. H. Stillinger & S. Torquato, *Tetratic order in the phase behavior of a hard-rectangle system*, Physical Review B **73**, 054109 (2006)

[83] D. A. Triplett & K. A. Fichthorn, *Monte Carlo simulation of two-dimensional hard rectangles: confinement effects*, Physical Review E **77**, 011707 (2008)

[84] J. Geng & J. V. Selinger, *Theory and simulation of two-dimensional nematic and tetratic phases*, Physical Review E **80**, 011707 (2009)

[85] H. H. Wensink, H. Löwen, M. Marechal, A. Härtel, R. Wittkowski, U. Zimmermann, A. Kaiser & A. M. Menzel, *Differently shaped hard body colloids in confinement: from passive to active particles*, European Physical Journal Special Topics **222**, 3023–3037 (2013)

[86] M. Dijkstra, *Advances in chemical physics*, **156**, Kap. 2: Entropy-driven phase transitions in colloids: from spheres to anisotropic particles, 35–71. John Wiley & Sons, Hoboken, NJ (2014).

[87] M. Oettel, M. Klopotek, M. Dixit, E. Empting, T. Schilling & H. Hansen-Goos, *Monolayers of hard rods on planar substrates: I. Equilibrium*, Journal of Chemical Physics **145**, 074902 (2016)

[88] A. Poniewierski & R. Hołyst, *Density-functional theory for nematic and smectic-a ordering of hard spherocylinders*, Physical Review Letters **61**, 2461–2464 (1988)

[89] H. Schlacken, H.-J. Mogel & P. Schiller, *Orientational transitions of two-dimensional hard rod fluids*, Molecular Physics **93**, 777–787 (1998)

[90] Y. Martínez-Ratón, E. Velasco & L. Mederos, *Effect of particle geometry on phase transitions in two-dimensional liquid crystals*, Journal of Chemical Physics **122**, 064903 (2005)

[91] Y. Martínez-Ratón, E. Velasco & L. Mederos, *Orientational ordering in hard rectangles: The role of three-body correlations*, Journal of Chemical Physics **125**, 014501–014501 (2006)

[92] H. Hansen-Goos & K. Mecke, *Fundamental measure theory for inhomogeneous fluids of nonspherical hard particles*, Physical Review Letters **102**, 018302 (2009)

[93] Y. Martínez-Ratón & E. Velasco, *Enhanced stability of the tetratic phase due to clustering*, Physical Review E **79**, 011711 (2009)

[94] H. Hansen-Goos & K. Mecke, *Tensorial density functional theory for non-spherical hard-body fluids*, Journal of Physics: Condensed Matter **22**, 364107 (2010)

[95] S. Belli, M. Dijkstra & R. van Roij, *Free minimization of the fundamental measure theory functional: Freezing of parallel hard squares and cubes*, Journal of Chemical Physics **137**, 124506–124506 (2012)

[96] M. Marechal, U. Zimmermann & H. Löwen, *Freezing of parallel hard cubes with rounded edges*, Journal of Chemical Physics **136**, 144506 (2012)

[97] D. de las Heras, Y. Martínez-Ratón, L. Mederos & E. Velasco, *Two-dimensional nematics in bulk and confined geometries*, Journal of Molecular Liquids **185**, 13–19 (2013)

[98] M. Marechal & H. Löwen, *Density functional theory for hard polyhedra*, Physical Review Letters **110**, 137801 (2013)

[99] R. Wittmann, M. Marechal & K. Mecke, *Fundamental mixed measure theory for non-spherical colloids*, Europhysics Letters **109**, 26003 (2015)

[100] A. Díaz-De Armas & Y. Martínez-Ratón, *Role of length polydispersity in the phase behavior of freely rotating hard-rectangle fluids*, Physical Review E **95**, 052702 (2017)

[101] M. Marechal, S. Dussi & M. Dijkstra, *Density functional theory and simulations of colloidal triangular prisms*, Journal of Chemical Physics **146**, 124905 (2017)

[102] R. L. C. Vink, *Liquid crystals in two dimensions: first-order phase transitions and nonuniversal critical behavior*, Physical Review Letters **98**, 217801 (2007)

[103] S. C. Kapfer & W. Krauth, *Two-dimensional melting: From liquid-hexatic coexistence to continuous transitions*, Physical Review Letters **114**, 035702 (2015)

[104] A. L. Thorneywork, J. L. Abbott, D. G. A. L. Aarts & R. P. A. Dullens, *Two-dimensional melting of colloidal hard spheres*, Physical Review Letters **118**, 158001 (2017)

[105] J. Dzubiella, M. Schmidt & H. Löwen, *Topological defects in nematic droplets of hard spherocylinders*, Physical Review E **62**, 5081–5091 (2000)

[106] H. Stark, *Physics of colloidal dispersions in nematic liquid crystals*, Physics Reports **351**, 387–474 (2001)

[107] A. R. Bausch, M. J. Bowick, A. Cacciuto, A. D. Dinsmore, M. F. Hsu, D. R. Nelson, M. G. Nikolaides, A. Travesset & D. A. Weitz, *Grain boundary scars and spherical crystallography*, Science **299**, 1716–1718 (2003)

[108] A. Fernández-Nieves, V. Vitelli, A. S. Utada, D. R. Link, M. Márquez, D. R. Nelson & D. A. Weitz, *Novel defect structures in nematic liquid crystal shells*, Physical Review Letters **99**, 157801 (2007)

[109] H. Shin, M. J. Bowick & X. Xing, *Topological defects in spherical nematic*, Physical Review Letters **101**, 037802 (2008)

[110] M. A. Bates, G. Skačej & C. Zannoni, *Defects and ordering in nematic coatings on uniaxial and biaxial colloids*, Soft Matter **6**, 655 (2010)

[111] T. Araki, M. Buscaglia, T. Bellini & H. Tanaka, *Memory and topological frustration in nematic liquid crystals confined in porous materials*, Nature Materials **10**, 303–309 (2011)

[112] H.-L. Liang, S. Schymura, P. Rudquist & J. Lagerwall, *Nematic-smectic transition under confinement in liquid crystalline colloidal shells*, Physical Review Letters **106**, 247801 (2011)

[113] T. Lopez-Leon, V. Koning, K. B. S. Devaiah, V. Vitelli & A. Fernandez-Nieves, *Frustrated nematic order in spherical geometries*, Nature **7**, 1745–2473 (2011)

[114] C. Knorowski & A. Travesset, *Nanorods in functionalized block-copolymer gels: Flexible ladders and liquid crystalline order in curved geometries*, Europhysics Letters **100**, 56004 (2012)

[115] X. Xing, H. Shin, M. J. Bowick, Z. Yao, L. Jia & M.-H. Li, *Morphology of nematic and smectic vesicles*, Proceedings of the National Academy of Sciences U.S.A. **109**, 5202–5206 (2012)

[116] Y. Martínez-Ratón & E. Velasco, *Dimensional crossover of hard parallel cylinders confined on cylindrical surfaces*, Physical Review E **87**, 052314 (2013)

[117] H.-L. Liang, J. Noh, R. Zentel, P. Rudquist & J. P. F. Lagerwall, *Tuning the defect configurations in nematic and smectic liquid crystalline shells*, Philosophical Transactions of the Royal Society A: Mathematical, Physical and Engineering Sciences **371**, 20120258–20120258 (2013)

[118] A. Martinez, M. Ravnik, B. Lucero, R. Visvanathan, S. Žumer & I. I. Smalyukh, *Mutually tangled colloidal knots and induced defect loops in nematic fields*, Nature Materials **13**, 258–263 (2014)

[119] A. Mughal & D. Weaire, *Theory of cylindrical dense packings of disks*, Physical Review E **89**, 042307 (2014)

[120] R. Kusters, S. Paquay & C. Storm, *Confinement without boundaries: anisotropic diffusion on the surface of a cylinder*, Soft Matter **11**, 1054–1057 (2015)

[121] D. Coursault, B. Zappone, A. Coati, A. Boulaoued, L. Pelliser, D. Limagne, N. Boudet, B. H. Ibrahim, A. de Martino, M. Alba, M. Goldmann, Y. Garreau, B. Gallas & E. Lacaze, *Self-organized arrays of dislocations in thin smectic liquid crystal films*, Soft Matter **12**, 678–688 (2016)

[122] R. Zhang, Y. Zhou, M. Rahimi & J. J. de Pablo, *Dynamic structure of active nematic shells*, Nature Communications **7**, 13483 (2016)

[123] S. Dietrich, *Wetting phenomena*, **12** aus *Phase Transitions and Critical Phenomena*. Academic Press, London, 3rd ed. (1988).

[124] P.-G. de Gennes, F. Brochard-Wyart & D. Quéré, *Capillarity and wetting phenomena: Drops, bubbles, pearls, waves*. Springer-Verlag, New York, 1st ed. (2004).

[125] W. Barthlott & C. Neinhuis, *Purity of the sacred lotus, or escape from contamination in biological surfaces*, Planta **202**, 1–8 (1997)

[126] A. Marmur, *The lotus effect: superhydrophobicity and metastability*, Langmuir **20**, 3517–3519 (2004)

[127] N. A. Patankar, *Mimicking the lotus effect: influence of double roughness structures and slender pillars*, Langmuir **20**, 8209–8213 (2004)

[128] M. Heni & H. Löwen, *Surface freezing on patterned substrates*, Physical Review Letters **85**, 3668–3671 (2000)

[129] A. Cacciuto, S. Auer & D. Frenkel, *Solid-liquid interfacial free energy of small colloidal hard-sphere crystals*, Journal of Chemical Physics **119**, 7467–7470 (2003)

[130] E. Allahyarov, K. Sandomirski, S. U. Egelhaaf & H. Löwen, *Crystallization seeds favour crystallization only during initial growth*, Nature Communications **6**, 7110 (2015)

[131] R. C. Tolman, *The effect of droplet size on surface tension*, Journal of Chemical Physics **17**, 333–337 (1949)

[132] J. Barrett, *First-order correction to classical nucleation theory: a density functional approach*, Journal of Chemical Physics **111**, 5938–5946 (1999)

[133] T. V. Bykov & X. C. Zeng, *A patching model for surface tension and the Tolman length*, Journal of Chemical Physics **111**, 3705–3713 (1999)

[134] M. Heni & H. Löwen, *Interfacial free energy of hard-sphere fluids and solids near a hard wall*, Physical Review E **60**, 7057–7065 (1999)

[135] R. L. Davidchack & B. B. Laird, *Direct calculation of the hard-sphere crystal /melt interfacial free energy*, Physical Review Letters **85**, 4751–4754 (2000)

[136] P. Bryk, R. Roth, K. R. Mecke & S. Dietrich, *Hard-sphere fluids in contact with curved substrates*, Physical Review E **68**, 031602 (2003)

[137] P.-M. König, R. Roth & K. R. Mecke, *Morphological thermodynamics of fluids: shape dependence of free energies*, Physical Review Letters **93**, 160601 (2004)

[138] Y. A. Lei, T. Bykov, S. Yoo & X. C. Zeng, *The Tolman length: is it positive or negative?*, Journal of the American Chemical Society **127**, 15346–15347 (2005)

[139] M. C. Stewart & R. Evans, *Wetting and drying at a curved substrate: long-ranged forces*, Physical Review E **71**, 011602 (2005)

[140] J. C. Barrett, *Some estimates of the surface tension of curved surfaces using density functional theory*, Journal of Chemical Physics **124**, 144705 (2006)

[141] E. M. Blokhuis & J. Kuipers, *Thermodynamic expressions for the Tolman length*, Journal of Chemical Physics **124**, 074701 (2006)

[142] B. B. Laird & R. L. Davidchack, *Wall-induced prefreezing in hard spheres: a thermodynamic perspective*, Journal of Physical Chemistry C **111**, 15952–15956 (2007)

[143] A. E. van Giessen & E. M. Blokhuis, *Direct determination of the Tolman length from the bulk pressures of liquid drops via molecular dynamics simulations*, Journal of Chemical Physics **131**, 164705 (2009)

[144] B. J. Block, S. K. Das, M. Oettel, P. Virnau & K. Binder, *Curvature dependence of surface free energy of liquid drops and bubbles: a simulation study*, Journal of Chemical Physics **133**, 154702 (2010)

[145] B. B. Laird & R. L. Davidchack, *Calculation of the interfacial free energy of a fluid at a static wall by Gibbs-Cahn integration*, Journal of Chemical Physics **132**, 204101 (2010)

[146] R. Benjamin & J. Horbach, *Wall-liquid and wall-crystal interfacial free energies via thermodynamic integration: a molecular dynamics simulation study*, Journal of Chemical Physics **137**, 044707 (2012)

[147] T. P. Bennett & J. C. Barrett, *Water nucleation: a comparison between some phenomenological theories and experiment*, Journal of Chemical Physics **137**, 124702 (2012)

[148] A. Tröster, M. Oettel, B. Block, P. Virnau & K. Binder, *Numerical approaches to determine the interface tension of curved interfaces from free energy calculations*, Journal of Chemical Physics **136**, 064709 (2012)

[149] E. M. Blokhuis, *Existence of a bending rigidity for a hard-sphere liquid near a curved hard wall: validity of the Hadwiger theorem*, Physical Review E **87**, 022401 (2013)

[150] I. Urrutia, *Bending rigidity and higher-order curvature terms for the hard-sphere fluid near a curved wall*, Physical Review E **89**, 032122 (2014)

[151] Ø. Wilhelmsen, D. Bedeaux & D. Reguera, *Tolman length and rigidity constants of the Lennard-Jones fluid*, Journal of Chemical Physics **142**, 064706 (2015)

[152] M. P. Allen & D. J. Tildesley, *Computer simulation of liquids*. Oxford Science Publications, Oxford University Press, Oxford, 1 ed. (1989).

[153] W. T. Coffey, Y. P. Kalmykov & J. T. Waldron, *The langevin equation: With applications to stochastic problems in physics, chemistry and electrical engineering*, **14** aus *World Scientific Series in Contemporary Chemical Physics*. World Scientific Publishing, Singapore, 2 ed. (2004).

[154] P. S. Doyle & P. T. Underhill, *Brownian dynamics simulations of polymers and soft matter* in *Handbook of materials modeling*, 2619–2630 (2005).

[155] B. J. Alder, D. M. Gass & T. E. Wainwright, *Studies in molecular dynamics. VIII. the transport coefficients for a hard-sphere fluid*, Journal of Chemical Physics **53**, 3813–3826 (1970)

[156] C. Ebner, W. F. Saam & D. Stroud, *Density-functional theory of simple classical fluids: I. Surfaces*, Physical Review A **14**, 2264–2273 (1976)

[157] W. F. Saam & C. Ebner, *Density-functional theory of classical systems*, Physical Review A **15**, 2566–2568 (1977)

[158] R. Evans, *The nature of the liquid-vapour interface and other topics in the statistical mechanics of non-uniform, classical fluids*, Advances in Physics **28**, 143–200 (1979)

[159] P. Hohenberg & W. Kohn, *Inhomogeneous electron gas*, Physical Review **136**, 864–871 (1964)

[160] W. Kohn & L. J. Sham, *Self-consistent equations including exchange and correlation effects*, Physical Review **140**, 1133–1138 (1965)

[161] N. D. Mermin, *Thermal properties of the inhomogeneous electron gas*, Physical Review **137**, 1441–1443 (1965)

[162] W. Kohn, *Nobel lecture: Electronic structure of matter-wave functions and density functionals*, Reviews of Modern Physics **71**, 1253–1266 (1999)

[163] R. Roth, *Fundamental measure theory for hard-sphere mixtures: a review*, Journal of Physics: Condensed Matter **22**, 063102 (2010)

[164] J. K. Percus, *Equilibrium state of a classical fluid of hard rods in an external field*, Journal of Statistical Physics **15**, 505–511 (1976)

[165] L. Tonks, *The complete equation of state of one, two and three-dimensional gases of hard elastic spheres*, Physical Review **50**, 955–963 (1936)

[166] L. Onsager, *The effects of shape on the interaction of colloidal particles*, Annals of the New York Academy of Sciences **51**, 627–659 (1949)

[167] S. Toxvaerd, *Perturbation theory for nonuniform fluids: Surface tension*, Journal of Chemical Physics **55**, 3116–3120 (1971)

[168] S. Nordholm, M. Johnson & B. C. Freasier, *Generalized van der Waals theory. III. The prediction of hard sphere structure*, Australian Journal of Chemistry **33**, 2139–2150 (1980)

[169] P. Tarazona, *A density functional theory of melting*, Molecular Physics **52**, 81–96 (1984)

[170] W. A. Curtin & N. W. Ashcroft, *Density-functional theory and freezing of simple liquids*, Physical Review Letters **56**, 2775–2778 (1986)

[171] T. V. Ramakrishnan & M. Yussouff, *First-principles order-parameter theory of freezing*, Physical Review B **19**, 2775–2794 (1979)

[172] R. Evans, *Fundamentals of inhomogeneous fluids*, Kap. 3: Density Functionals in the Theory of Nonuniform Fluids, 85–176. Marcel Dekker, New York, 1 ed. (1992).

[173] P. Tarazona, *Solid-fluid transition and interfaces with density functional approaches*, Surface Science **331**, 989–994 (1995)

[174] H. Löwen, *Density functional theory for inhomogeneous fluids ii: Statics, dynamics, and applications* in *3rd Warsaw School of Statistical Physics* (B. Cichocki, M. Napiórkowski & J. Piasecki, eds.), Kap. 3, 87–121, Warsaw University Press, Warschau (2010).

[175] Y. Rosenfeld, *Free-energy model for the inhomogeneous hard-sphere fluid mixture and density-functional theory of freezing*, Physical Review Letters **63**, 980–983 (1989)

[176] E. Kierlik & M. L. Rosinberg, *Free-energy density functional for the inhomogeneous hard-sphere fluid: Application to interfacial adsorption*, Physical Review A **42**, 3382–3387 (1990)

[177] S. Phan, E. Kierlik, M. L. Rosinberg, B. Bildstein & G. Kahl, *Equivalence of two free-energy models for the inhomogeneous hard-sphere fluid*, Physical Review E **48**, 618–620 (1993)

[178] Y. Rosenfeld, M. Schmidt, H. Löwen & P. Tarazona, *Dimensional crossover and the freezing transition in density functional theory*, Journal of Physics: Condensed Matter **8**, L577–L581 (1996)

[179] Y. Rosenfeld, M. Schmidt, H. Löwen & P. Tarazona, *Fundamental-measure free-energy density functional for hard spheres: dimensional crossover and freezing*, Physical Review E **55**, 4245–4263 (1997)

[180] P. Tarazona, *Density functional for hard sphere crystals: a fundamental measure approach*, Physical Review Letters **84**, 694–697 (2000)

[181] R. Wittmann, C. E. Sitta, F. Smallenburg & H. Löwen, *Phase diagram of two-dimensional hard rods from fundamental mixed measure density functional theory*, Journal of Chemical Physics **147**, 134908 (2017)

[182] C. E. Sitta, F. Smallenburg, R. Wittkowski & H. Löwen, *Hard rectangles near curved hard walls: Tuning the sign of the tolman length*, Journal of Chemical Physics **145**, 204508 (2016)

[183] C. E. Sitta, F. Smallenburg, R. Wittkowski & H. Löwen, *Liquid crystals of hard rectangles on flat and cylindrical manifolds*, Physical Chemistry Chemical Physics, DOI: 10.1039/C7CP07026H (2018)

[184] R. Roth, R. Evans, A. Lang & G. Kahl, *Fundamental measure theory for hard-sphere mixtures revisited: the White Bear version*, Journal of Physics: Condensed Matter **14**, 12063–12078 (2002)

[185] Y.-X. Yu & J. Wu, *Structures of hard-sphere fluids from a modified fundamental-measure theory*, Journal of Chemical Physics **117**, 10156–10164 (2002)

[186] H. Hansen-Goos & R. Roth, *Density functional theory for hard-sphere mixtures: the White Bear version mark II*, Journal of Physics: Condensed Matter **18**, 8413–8425 (2006)

[187] J. A. Cuesta & Y. Martínez-Ratón, *Dimensional crossover of the fundamental-measure functional for parallel hard cubes*, Physical Review Letters **78**, 3681–3684 (1997)

[188] J. A. Cuesta & Y. Martínez-Ratón, *Fundamental measure theory for mixtures of parallel hard cubes: I. general formalism*, Journal of Chemical Physics **107**, 6379–6389 (1997)

[189] R. Wittmann, M. Marechal & K. Mecke, *Elasticity of nematic phases with fundamental measure theory*, Physical Review E **91**, 052501 (2015)